EUROPEAN ORGANIZATION FOR NUCLEAR RESEARCH

CERN-PPE/93-31
February 22, 1993

Results from the L3 Experiment at LEP

The L3 Collaboration.

Abstract

In this report we summarize the major results from the first three years of running of the L3 detector at the Large Electron Positron collider (LEP). The L3 detector was designed to measure electrons, photons and muons with high precision; it has achieved $(\Delta E/E) \approx 1.4\%$ for electrons and photons at $E = 45$ GeV and $(\Delta p/p) \approx 2.5\%$ for muons at $p = 45$ GeV. Most of the experimental results presented are based on approximately 500,000 Z events. The data provide four independent checks of the Standard Model weak neutral currents to an accuracy of $\approx 1\%$. These are: the measurement of Z parameters; the measurement of the forward-backward charge asymmetry of lepton pairs; the measurement of asymmetry parameters from $Z \rightarrow b\bar{b}$ decays; and the measurement of the τ lepton polarization asymmetry. The data also provide information on weak charged currents from measurements of b hadrons – such as decay width, lifetime, and B^0-$\bar{B}^0$ mixing – and from measurements of τ leptons – such as their lifetime and branching ratios. The large number of Z events and the resolution of the L3 detector allow precision tests of QED and QCD, including the production of π^0, η and hard photons. Leptonic final states with hard isolated photons are analyzed and high mass photon pairs are observed. Higgs boson production has not been observed and limits are given in the context of the Standard Model and its supersymmetric extensions. We also present upper limits on rare Z decays such as $Z \rightarrow \gamma\gamma\gamma$ and on flavor violating decays such as $Z \rightarrow e\tau$, $\mu\tau$. Finally, upper limits obtained in the search for various new particles and new interactions are reported.

(Submitted to *Physics Reports*)

Contents

1 **Introduction** 6

2 **The L3 Detector at LEP** 8

2.1 General description of the L3 experiment 9

2.2 The magnet 9

2.3 The muon detector 9

2.4 The hadron calorimeter and muon filter 12

2.5 The scintillation counters 13

2.6 The electromagnetic calorimeter 14

2.7 The central track detector 16

2.8 The luminosity monitor 20

2.9 The trigger 20

2.10 The LEP collider complex 23

2.11 LEP collider energy calibration 25

3 **The Detector Simulation** **27**

3.1 SIL3: The L3 detector simulation 27

3.2 Quality of detector simulation 28

3.3 Simulation of detector imperfections 29

4 **Measurement of Luminosity** **30**

4.1 Event selection 30

4.2 Theoretical cross section 32

4.3 Luminosity determination 33

5 Production and Decay of Z Bosons **37**

5.1 The reaction $e^+e^- \to$ hadrons 38

5.2 The reaction $e^+e^- \to \mu^+\mu^-(\gamma)$ 40

5.3 The reaction $e^+e^- \to \tau^+\tau^-(\gamma)$ 45

5.4 The reaction $e^+e^- \to e^+e^-(\gamma)$ 50

5.5 The reaction $e^+e^- \to$ hadrons $+ \gamma$ 54

5.6 The reaction $e^+e^- \to \nu\bar{\nu}\gamma$ 56

6 Production and Decay of b Hadrons **61**

6.1 Signatures of b hadron events 61

6.2 b hadron decay properties 63

6.3 Weak neutral current interactions of b quarks 73

6.4 Determination of the Z partial width, $\Gamma_{b\bar{b}}$ 77

6.5 Production of J mesons 78

7 Production and Decay of Tau Leptons **83**

7.1 τ polarization in Z decay 83

7.2 τ decay properties 94

8 Determination of the Electroweak Parameters **101**

8.1 Lowest order cross sections and asymmetries 101

8.2 Parameters of the Standard Model 103

8.3 Radiative Corrections 103

8.4 Fitting Procedure and Effective Coupling Constants 104

8.5 Experimental systematic errors 105

8.6 Z mass, total width and partial widths 105

8.7 Effective weak neutral current coupling constants 107

8.8 Results in the framework of the Standard Model 110

8.9 Z resonance analysis with an S-matrix approach 112

9 Tests of Quantum Electrodynamics 115

10 Tests of Quantum Chromodynamics 119

10.1 Event selection and Monte Carlo programs 120

10.2 The strong coupling constant 123

10.3 Measurement of gluon properties 132

10.4 Isolated hard photons in hadronic events 134

10.5 Particle production and gluon interference effects 135

10.6 Summary 140

11 Leptonic Final States with Hard Photons 142

12 Search for the Higgs Boson 146

12.1 The Higgs boson in the Standard Model 146

12.2 Search for non-minimal Higgs bosons 152

13 Search for New Particles and New Interactions 159

13.1 Limits from line shape measurements 159

13.2 Limits on an additional heavy gauge boson Z' 160

13.3 Search for isodoublet heavy charged and neutral leptons 162

13.4 Search for isosinglet neutral heavy leptons 165

13.5 Search for supersymmetric particles 168

13.6 Search for compositeness 170

13.7 Z decay into a photon and a scalar meson 177

13.8 Flavor changing neutral currents 177

13.9 Leptoquarks 178

Chapter 1

Introduction

The discovery of weak neutral current interactions in neutrino physics [1] and the discovery of the bosons which mediate weak interactions, Z and $W^{\pm}$, in $p\bar{p}$ collisions [2] provided crucial evidence for the validity of the Standard Model [3]. Two e^+e^- colliders [4,5] were built in order to mass-produce Z bosons and to study their properties in detail. The production of large numbers of Z bosons makes the following measurements possible:

- determination of the properties (mass, total width) of the Z boson;
- measurement of the Z couplings to all leptons and quarks with a mass of less than half the Z mass;
- searches for new phenomena, new particles and new interactions; and
- study of strong interactions and/or weak charged current decays of the quarks and leptons abundantly produced in Z decays.

It was with these objectives in mind that the Large Electron Positron collider LEP at CERN [6] was built. The four experiments at this collider – ALEPH, DELPHI, L3 and OPAL [7–10] – have all run since the beginning of LEP operation in 1989 and had, at the end of 1991, each observed of the order of half a million Z decays.

In this report, we summarize the results from the L3 experiment mostly using data taken in 1989 to 1991. This detector conceptually differs from a standard e^+e^- collider detector by its emphasis on high resolution measurements of leptons, photons and jets. This is implemented in the experimental setup by a high-resolution muon spectrometer, a precision electromagnetic calorimeter as well as fine-grain hadron calorimetry. High resolution makes the recognition of exclusive final states straightforward. Furthermore, it is essential in:

- detecting rare new phenomena with sufficient signal-to-noise ratio;
- identifying exclusive and inclusive final states and rejecting backgrounds; and

- analyzing final state properties by measuring particle energy, momentum and reconstructing mass spectra.

In this review, we first give a brief description of the experimental apparatus, its principles of construction and the performance observed at LEP during its first three years of running. We then present physics results concerning the electroweak interaction of leptons and quarks, both their production by neutral currents and their decay by charged currents. Special emphasis is put on the heaviest quarks and leptons, i.e. the b quark and the τ lepton, and on final states containing hard photons.

Many different measurements of the properties of electroweak neutral currents by L3 provide independent determinations of its coupling constants. A stringent test of the Standard Model is thus provided. We devote a separate chapter to tests of this kind.

Measurements pertaining to the strong interactions of quarks and gluons follow. Redundancy as for example provided by the many different ways of measuring the strong coupling constant, tests Quantum Chromodynamics [11].

We then discuss the observation of leptonic final states with high mass photon pairs, including data from 1992.

The final chapters of the review are devoted to a summary of the searches which the L3 collaboration has made for new particles and new interactions, both inside and outside the framework of the Standard Model. Most important among those is clearly the search for Higgs bosons [12].

Chapter 2

The L3 Detector at LEP

The L3 detector shown in figure 2.1 is designed to study e^+e^- collisions up to 200 GeV with emphasis on high resolution energy measurements of electrons, photons, muons and jets [9]. The detectors are installed within a 7800 ton magnet providing a 0.5 T field. We have chosen a relatively low field in a large volume to optimize the muon momentum resolution, which improves linearly with the field but quadratically with the track length.

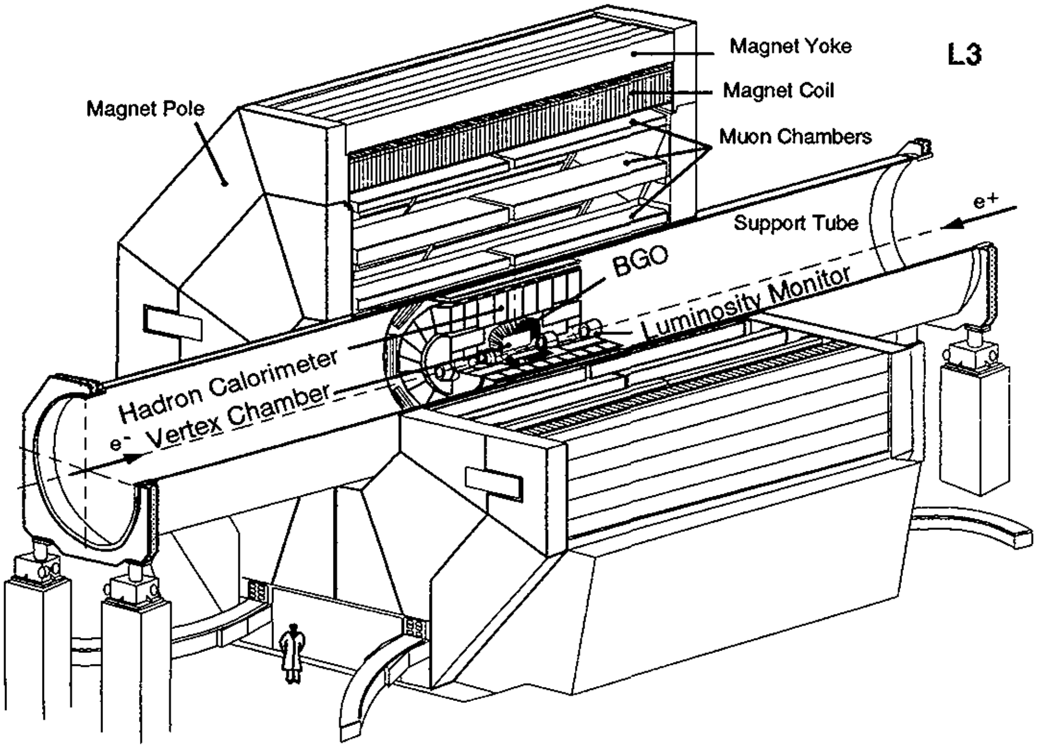

Figure 2.1: The L3 Detector

2.1 General description of the L3 experiment

The detectors are supported by a 32 m long, 4.45 m diameter steel tube. The tube is concentric with the LEP beam line and mechanically coupled to the elements of the low-β insertion, allowing alignment of all L3 detectors relative to the LEP beams. The muon spectrometer forms three concentric chamber layers around the beam, mounted on the outside of the support tube.

The central section of the support tube houses the inner detectors, arranged as "barrel" elements around the beam pipe and as "endcap" elements in the forward and backward directions. The barrel elements consist of muon filter, hadron calorimeter, electromagnetic calorimeter, vertex chamber and the beam pipe. The endcap elements consist of a hadron calorimeter, an electromagnetic calorimeter and a forward tracking chamber. The luminosity monitors are situated immediately in front of the low-β magnets.

2.2 The magnet

The coil (inside radius 5.93 m, total length 11.90 m) is made of aluminum plates welded together. Cooling is provided by two independent circuits made of an aluminum alloy with high resistance to corrosion. The 168 turn coil is divided into 28 packages, each weighing 40 tons, which are bolted together. An active thermal shield placed on the inside of the coil protects the detectors.

The magnetic structure is made of soft iron with 0.5% carbon content. The poles are made of 1100 tons of self-supporting structure giving the required rigidity and serving as a support and reference frame to mount the 5600 tons of filling material, which provides the mass needed for the magnetic flux return, both in the poles and in the barrel. Each pole has two 340 ton half-doors to allow installation and removal of the muon detectors. The magnetic field in the inner volume of the support tube was mapped with Hall probes. The field in the remaining volume has been mapped with about one thousand magnetoresistors, permanently installed on the muon chambers. In addition, five NMR probes monitor the absolute value of the field. The central field in the magnet is 0.5 T.

2.3 The muon detector

The muon detector consists of two ferris wheels, each weighing 86 tons and having eight independent units or octants. Each octant consists of a special mechanical structure supporting five precision (P) drift chambers. There are two chambers (MO) in the outer layer, each with 16 signal wires, two chambers (MM) in the middle layer, each with 24 signal wires, and one inner chamber (MI), with 16 signal wires. They measure track coordinates in the bending plane.

In addition, the top and bottom covers of the MI and MO chambers also consist of drift chambers which measure the z coordinate along the beam. In total there are 6 z-chambers per octant. We used thin aluminum honeycomb with an average of 0.9% of a radiation length per two layers to enclose the middle chambers. Using this design, a multiple scattering induced sagitta error of less than 30μm at 50 GeV is achieved.

Muons with more than 3 GeV energy are confined to a single octant. Therefore, alignment is only critical between chambers in the same octant. To achieve the design resolution, systematic errors in the internal octant alignment must be kept below 30 μm. The spectrometer covers scattering angles between 36° and 144°.

2.3.1 P- and z-chambers

Each P-chamber contains about 320 signal wires and a total of 3000 wires (including field shaping, cathode and guard wires). The signal and field shaping wires are positioned to about 10 μm in the bending direction and to better than 40 μm in the non-bending direction by precision Pyrex glass and carbon fiber bridges. The chamber cells have been designed to have a very uniform field throughout the active region. An internal alignment system is integrated to the structure of the bridges. This system consists of LED, lenses and quadrant photodiodes. Light from a LED mounted on one end bridge is focused by the lens in the middle bridge onto a quadrant photodiode at the opposite end bridge. The bridges are aligned when all four quadrants of the photodiode receive equal amounts of light. These systems allow us to position the bridges, and thereby the wires, to an accuracy of 10 μm.

The z-chambers consist of two layers of drift cells offset by one half cell with respect to each other to resolve left-right ambiguities. There are in total 96 z-chambers.

The octant stands (Figure 2.2) are precision structures supporting the chambers and maintaining long term chamber alignment to less than 30μm. The structures have been designed to avoid tensor force transmission, thus the octant behavior is fully predictable under all conditions of stress, load and temperature. Special materials, such as titanium and copper-beryllium have been used for chamber support feet, chamber tie-plates, torque-tube joints and other highly stressed areas.

2.3.2 Alignment system and resolution

Opto-mechanical straightness monitors (see figure 2.2) similar to those of the precision bridges are part of the octant alignment system. A precision piece containing two LEDs is attached to each end frame of an inner chamber. A brass pin referenced to the LED touches one wire of a signal plane. The end bridge can be moved so that the wire just makes or breaks its electrical contact to the pin. In this way, the end bridge positions are set to a few μm. The middle and outer chambers have a similar system of pins touching wires. The assembly between the middle chambers contains a lens and that between the outer chambers contains two quadrant diodes. The middle chamber can be moved to bring the chamber centers into a straight line with an error smaller than 10 μm.

The vertical alignment systems guarantee that the chambers line up at each end of the octant, but these two octant center lines must also be parallel to each other. We use a laser

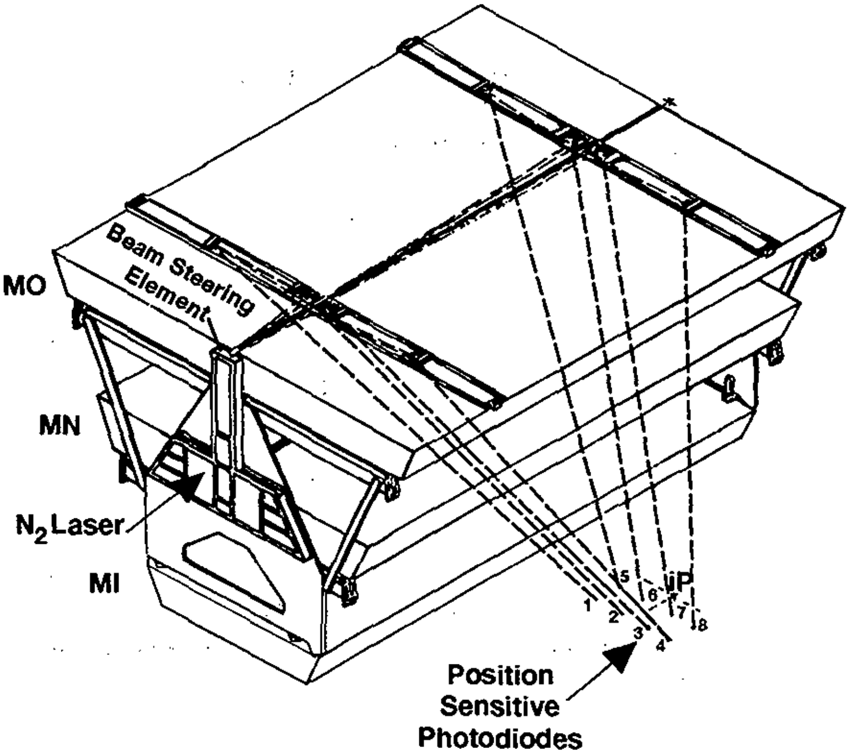

Figure 2.2: A muon chamber octant on its stand

beacon to measure the degree to which the two ends of the octant are parallel. The laser beacon can measure the angle between the two octant center lines to better than 25 μrad, corresponding to an error in the sagitta of less than 10 μm. The MO and MM chambers are adjusted so that this measured angle is zero.

Each of the 16 octants contains a two-stage nitrogen ultraviolet laser. The laser beam is directed up and across the top of the outer chamber layer by an addressable movable beam directional element (Figure 2.2). Mirrors direct the beam down through a quartz window into selected drift cells of all layers of an octant, which are connected by tubes pointing roughly to the interaction point. Photodiodes at the bottom of the MI chamber measure the intensity and position of the beam centroid. Each octant has eight laser beam trajectories, which simulate infinite momentum particles coming from the interaction point. The sagitta of laser events should be zero, and is used to verify the alignment. Two laser beams have movable mirrors and can produce parallel trajectories of exactly known separation, allowing us to measure and constantly monitor the electron drift velocity.

The accuracy of the L3 muon chamber system during the experiment is verified by an analysis of Z $\rightarrow$ $\mu^+\mu^-$ data, taking into account radiative corrections. The result shown in Figure 2.3. The observed resolution of $\sigma(E_{beam}/p_\mu) = 2.5\%$ agrees with the design value.

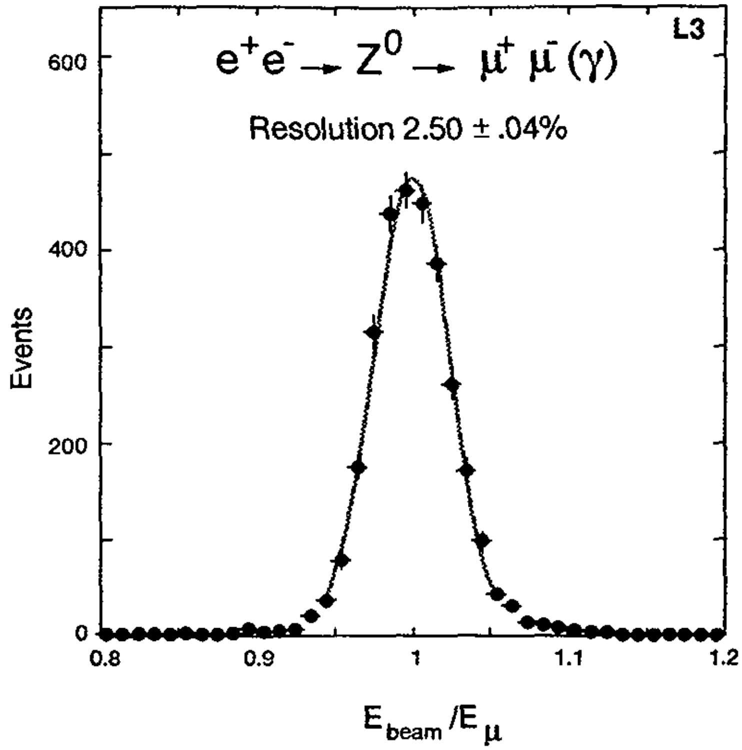

Figure 2.3: The measured momentum resolution of 45 GeV muons in the L3 experiment

2.4 The hadron calorimeter and muon filter

The energy of hadrons emerging from e^+e^- collisions is measured by the total absorption technique with an electromagnetic and a hadron calorimeter. The uranium hadron calorimeter is divided into a barrel part and a forward-backward part. The hadron calorimeter barrel covers the central region ($35° \leq \theta \leq 145°$); it is a fine sampling calorimeter made of depleted uranium absorber plates interspersed with 7968 proportional wire chambers and a total of 370'000 wires; it acts as a filter as well as a calorimeter, allowing only non-showering particles to reach the precision muon detector. The barrel hadron calorimeter has a modular structure consisting of 9 rings of 16 modules each (Figure 2.4).

The wires in each module are grouped to form readout towers. In the ϕ projection the towers point to the beam axis with a constant angular interval. The segmentation is 9 layers in ϕ and z and 10 (8) in the radial direction for the long (short) modules. Typically, a tower covers $\Delta\theta = 2°$, $\Delta\phi = 2°$. The thickness including electromagnetic calorimeter and support structure is at least six nuclear absorption lengths in the barrel part.

The endcaps of the hadron calorimeter cover the polar angle regions $5.5° \leq \theta \leq 35°$ and $145° \leq \theta \leq 174.5°$ over the full azimuthal range, and thus extend the coverage of the hadronic calorimetry to 99.5% of 4π. Each end-cap consists of three separate rings: an outer ring and two inner rings. Each ring is split vertically into half-rings, resulting in a total of 12 separate modules. The modularity of the endcap detectors permits their fast withdrawal to provide access to the other L3 central detector components. The endcaps consist of stainless steel

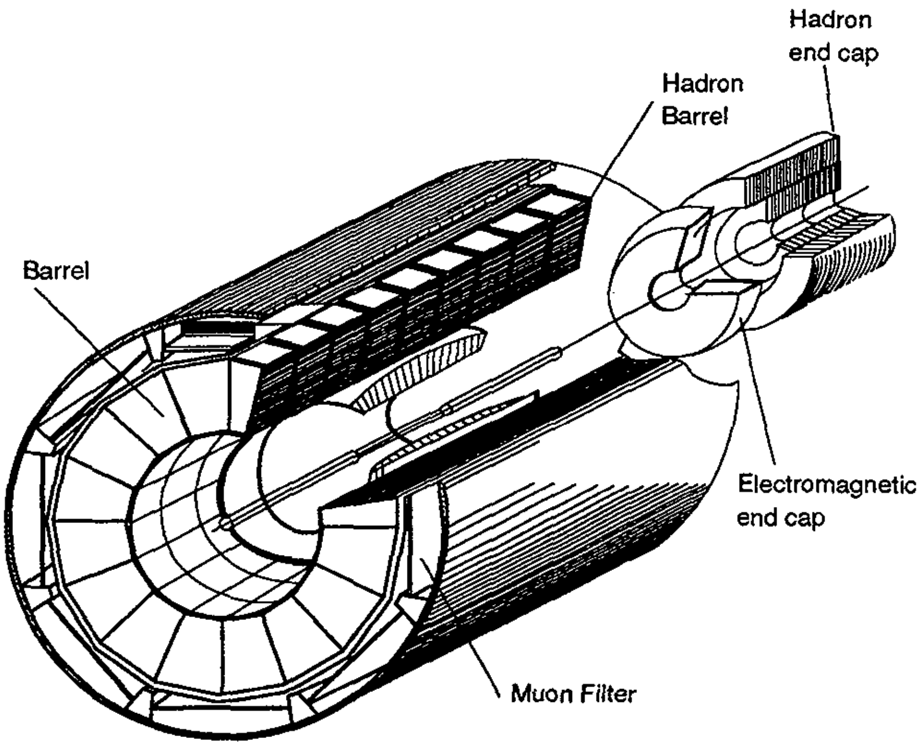

Figure 2.4: The hadron calorimeter

containers filled with alternating layers of brass tube proportional chambers and 5.5 mm thick absorber plates of depleted uranium. The amount of material traversed by a particle originating at the interaction point varies between 6 and 7 nuclear absorption lengths. The wire signals are grouped to form 3960 towers, with $\Delta\theta = 2°$, $\Delta\phi = 2°$.

A muon filter is mounted on the inside wall of the support tube and adds 1.03 absorption lengths to the hadron calorimeter. It consists of eight identical octants, each made of six 1 cm thick brass (65% Cu + 35% Zn) absorber plates, interleaved with five layers of proportional tubes and followed by 1.5 cm thick absorber plates matching the circular shape of the supporting tube.

The energy resolution of the calorimeter in conjunction with the other relevant subdetectors is shown in figure 2.12. The fine segmentation of the calorimeters allows the measurement of the axis of jets with an angular resolution of approximately 2.5°, and of the total energy of hadronic events from Z decay with a resolution of better than 10%.

2.5 The scintillation counters

The scintillation counter system consists of 30 single plastic counters and is located between the electromagnetic and hadronic calorimeters. A polar angle coverage corresponding to $|\cos\theta| < 0.83$ and an azimuthal coverage of 93% is achieved.

The scintillator hit multiplicity is used to trigger hadronic events. The system also records

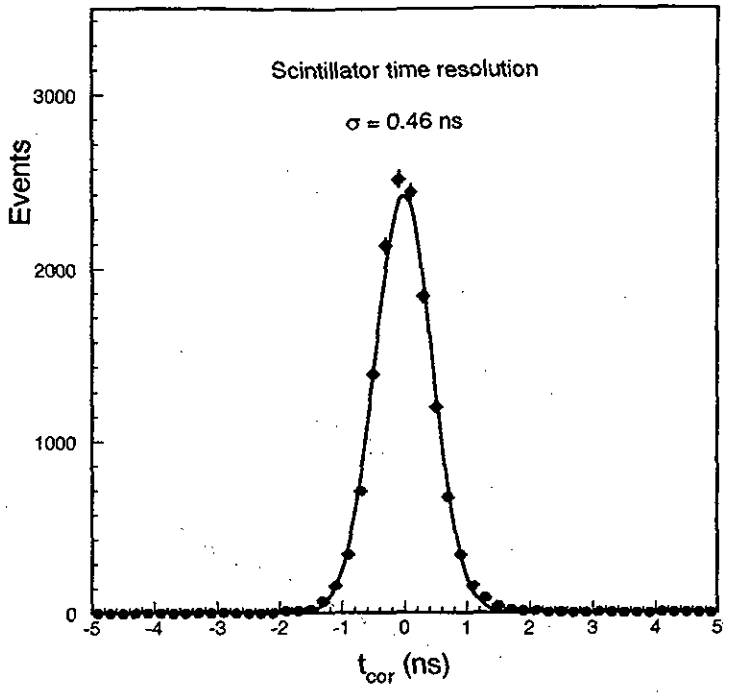

Figure 2.5: Scintillator time corrected for the expected time-of-flight for $e^+e^- \rightarrow \mu^+\mu^-$

the particle's time-of-flight which is used to distinguish dimuon events from cosmic ray background. A single cosmic muon which passes near the interaction point can fake a muon pair event produced in e^+e^- interaction. However, the time difference between opposite scintillation counters is 5.8 ns for cosmic muons and zero for muon pairs. The distribution of the measured time, corrected for the expected time-of-flight (t_{cor}) is shown in figure 2.5 for Z decays into muon pairs. A resolution of 460 ps is achieved.

2.6 The electromagnetic calorimeter

The electromagnetic detector has excellent energy and spatial resolution for photons and electrons over a wide energy range (from 100 MeV to 100 GeV). It uses bismuth germanium oxide (BGO) as both the showering and detecting medium. The electromagnetic calorimeter consists of about 11000 BGO crystals pointing to the interaction region. The detector (see. Figure 2.6) surrounds the central track detector and consists of:

- two half barrels of BGO crystals; the 7680 crystals of the barrel are arranged in two symmetrical half-barrels, giving a polar angle coverage $42° < \theta < 138°$;
- two endcaps, each made of 1527 BGO crystals, with a tracking chamber (FTC) in front, with polar angle coverage $11.6° < \theta < 38°$.

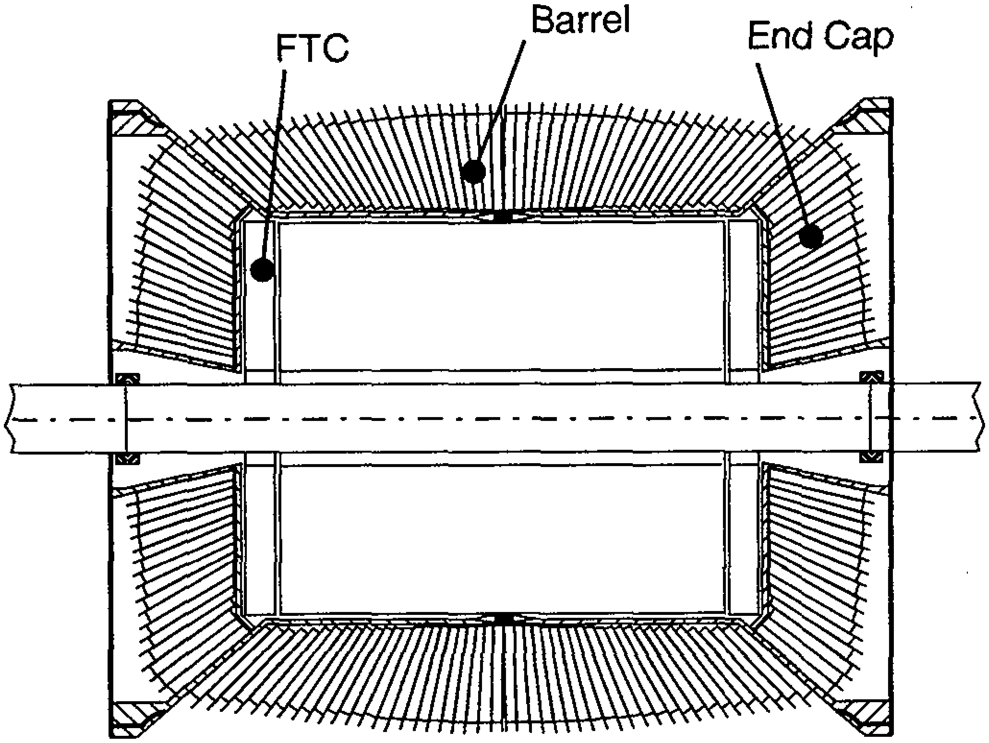

Figure 2.6: The BGO electromagnetic calorimeter

There is a Forward Trackingchambers (FTC) in front of each endcap, measuring the position and the direction of charged particles behind the central track detector's end flange with a spatial resolution of better than 200 μm and an angular precision better than 10 mrad.

2.6.1 BGO crystals and supporting structure

Each BGO crystal is 24 cm long and is a truncated pyramid of about $2 \times 2cm^2$ at the inner end and $3 \times 3cm^2$ at the outer end. All crystals point to the interaction region, with a small angular offset to suppress photon leakage. By coating the polished crystals with a 40 to 50 μm thick layer of high reflectivity paint, one obtains a nearly uniform light collection efficiency.

To achieve the best solid angle coverage and to minimize dead spaces between crystals, the structural material is confined to thin walls around the cells and to a cylindrical inner tube attached on each side to a conical funnel which carries the weight. Each crystal is held in a separate cell with clearances such that normal structural deformation does not affect any crystal and that the weight of a crystal is not transferred to its neighbors. Each crystal is separated from its neighbors by a composite wall, made of two layers of 100 μm pre-impregnated carbon cloth. Cellular walls and clearances represent about 1.75% of the solid angle covered by the barrel.

2.6.2 Readout electronics

Each crystal has two photodiodes glued to its rear face. We use $1.5cm^2$ photodiodes to detect the BGO scintillation light; they are insensitive to the magnetic field and have a quantum efficiency of about 70%. The charge sensitive amplifier is mounted directly behind each crystal. The analog-to-digital converter (ADC) has been designed to satisfy two basic requirements: to measure signals accurately over a wide range, from 10 MeV to 100 GeV and to have a short memory time so that tails from large signals do not mimic small signals in later beam crossings. The digitizing range of the ADC is equivalent to a 21 bit ADC, with a resolution at least 10 bits (i.e. 1000:1) for signals greater than 100 MeV. The linearity is better than 1% over the full range. The actual dynamic range achieved for BGO signals is 20000:1, from full scale to noise level.

2.6.3 Energy calibration and resolution

The barrel part of the calorimeter was calibrated at CERN in an SPS beam, where an accuracy better than 1% was obtained [9]. Sufficient statistical accuracy was achieved by recording about 1600 electrons for each crystal at 2, 10 and 50 GeV momenta. Since one of the most important parameters of the BGO detector is its resolution at low energy, this was tested at a specially designed beam line providing 180 MeV electrons at the LEP injector linac. The energy resolution is $\simeq$ 5% at 100 MeV and about 1.4% at high energies; the measured spatial resolution above 2 GeV is better than 2 mm and the hadron/electron rejection ratio is about 1000:1. The measured energy resolution for electrons from $Z \rightarrow e^+e^-$ is shown in figure 2.7.

The transparency of the BGO crystals is sensitive to ionizing radiation doses, for instance bursts of X-rays accidentally produced by the LEP beams. A typical beam loss close to the L3 apparatus deposits a few Grays on the inner end cap crystals. At room temperature, the crystals recover their transparency to within 80 to 90% over a few days.

A xenon light monitor [13] measures this transparency by means of light pulses injected into each crystal through a network of optical fibers. It also enables us to track the overall response (except for the scintillation efficiency) of a given crystal relative to its neighbors. The absolute calibration is maintained to within 0.9% by combining the Bhabha scattering information with the xenon monitor information.

In addition, cosmic muons are used to monitor the calibration constants as measured in the test beam and to perform periodic calibration in situ to ensure the stability of the calorimeter's energy response. Figure 2.8 shows reconstructed $\gamma\gamma$ mass spectra from hadronic events at LEP, demonstrating the performance of the electromagnetic calorimeter.

2.7 The central track detector

The total lever arm for coordinate measurement in the central tracking detector is 31.7 cm radially. The charge identification of 50 GeV particles with 95% confidence level requires 50

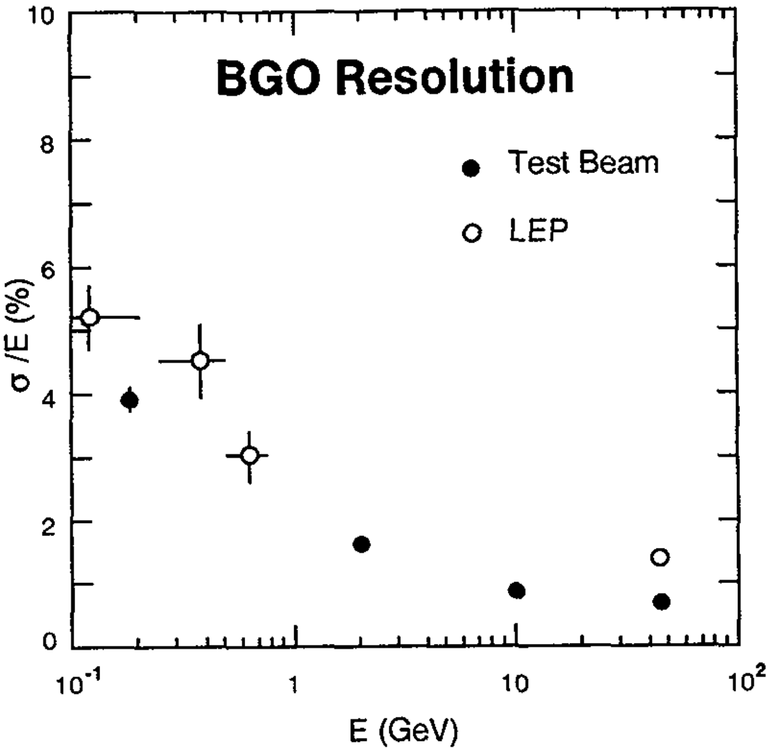

Figure 2.7: The barrel electromagnetic calorimeter energy resolution for electrons as a function of their energy in the L3 experiment.

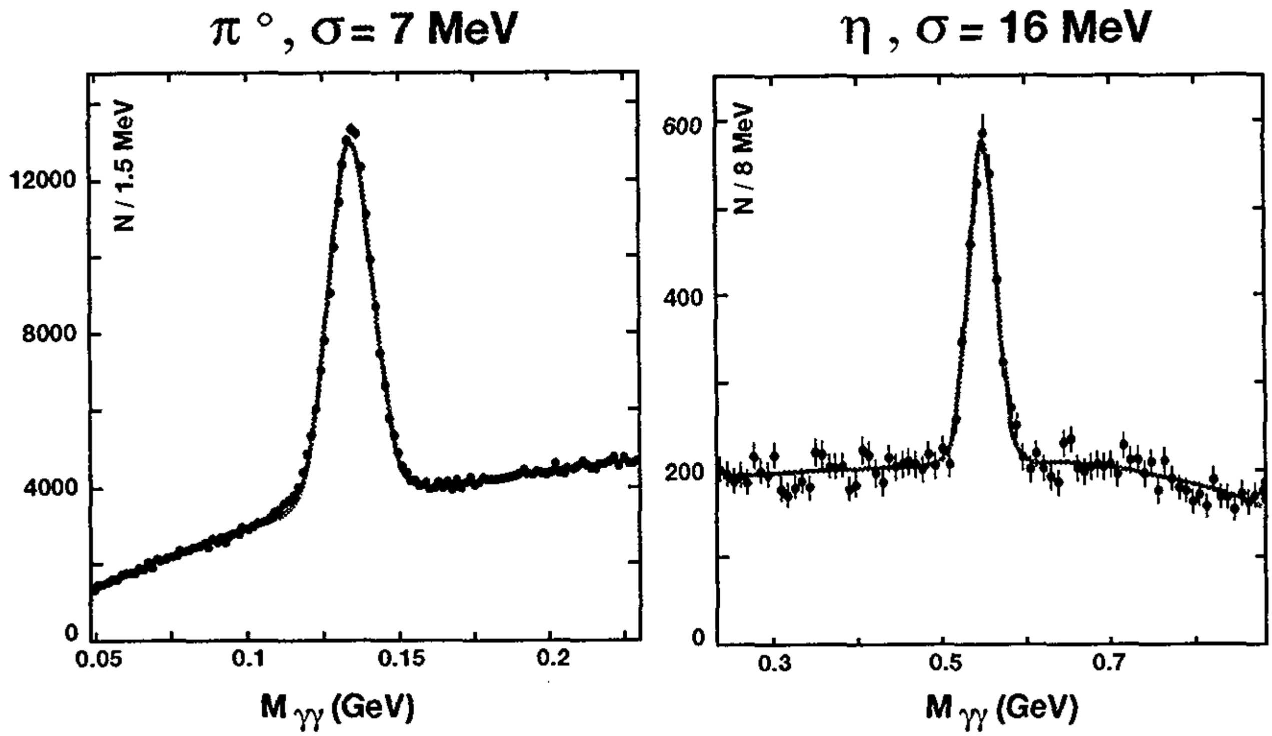

Figure 2.8: Measured $\gamma\gamma$ mass spectra from hadronic events at LEP

coordinate measurements with 50 μm resolution. This is accomplished by a ,Time Expansion Chamber (TEC), surrounded by two cylindrical proportional chambers with cathode strip readout, the z-detector (Figure 2.9). Following the TEC principle, the high field amplification region at the sense wire plane is separated from the low field drift region by an additional grid wire plane. This configuration allows to optimize the electron arrival time distribution as well as the track length seen by individual anode wires and choos a drift velocity in the drift region independent of gas amplification constraints. The TEC operates with a low diffusion 80% CO_2 and 20% iC_4H_{10} gas mixture at a pressure of 1.2 bar(abs) and a low drift velocity of 6μm/ns. Furthermore, this gas mixture has a small Lorentz angle of 2.3°. To reach the required resolution, determination of the drift time by a center of gravity method is mandatory. Thus the anode pulses are sampled by Flash Analog to Digital Converters (FADC) after shaping the analog pulses to cancel the ion tail. This principle has been tested by prototype chambers in test beams and in the MARK J experiment at PETRA.

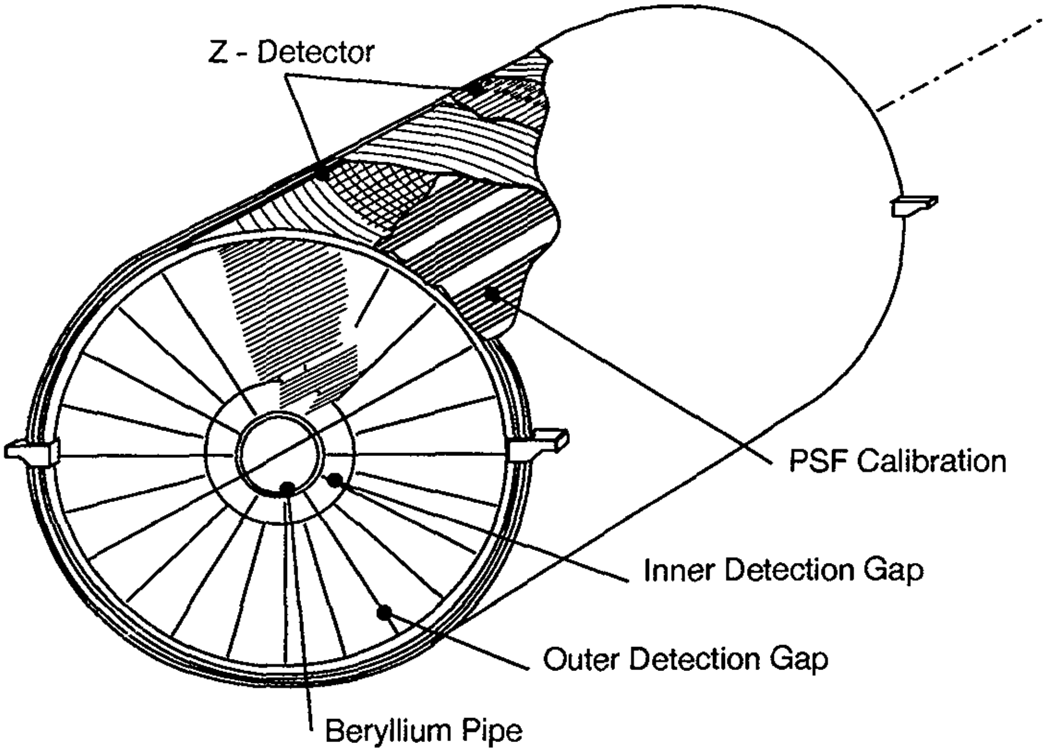

Figure 2.9: The Time Expansion Chamber

The z-detector consists of two thin cylindrical multiwire proportional chambers with cathode strip readout, covering the outer cylinder of the TEC. The cathode strips are inclined with respect to the beam (z-) direction by 69° and 90° for the inner chamber, and by −69° and 90° for the outer chamber.

Each TEC segment is equipped on its outer surface with a plastic scintillation fiber ribbon to monitor the drift velocity to an accuracy of 0.1%. The time-drift distance relationship is obtained for every anode by averaging over the fitted tracks using the e^+e^- interaction point and the fiber position.

Figure 2.10 shows the measured single point resolution of the TEC. The z-detector supplements these $R-\phi$ measurements with z-coordinates just outside the TEC. Its resolution was measured to be 320 μm (see Figure 2.11).

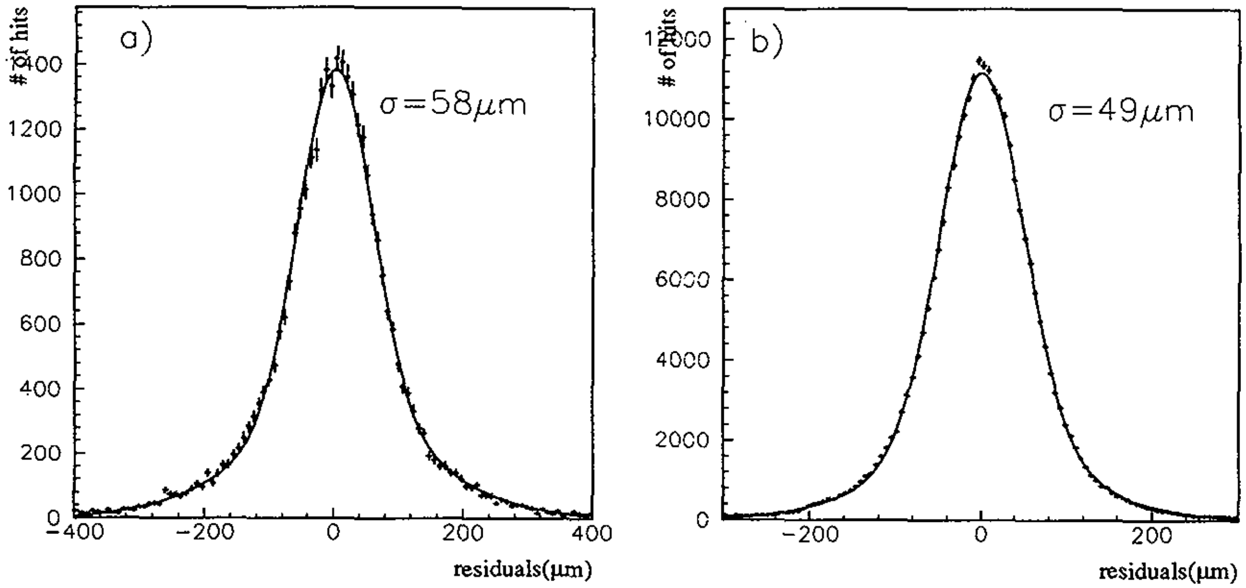

Figure 2.10: Single wire residuals for the TEC chamber in a) the inner and b) the outer ring.

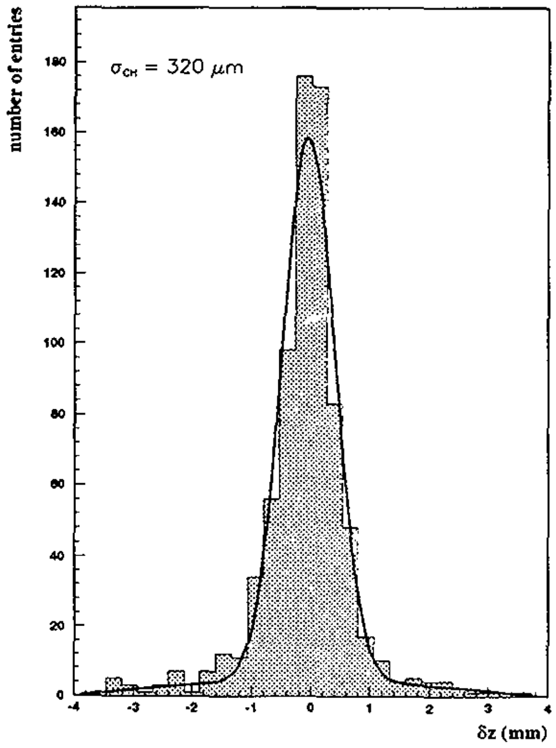

Figure 2.11: The measured z-chamber position resolution

Figure 2.12 shows that the 10.2% resolution of the L3 calorimeters for hadronic jets of 45 GeV improves to 8.4% when the momentum measurement from the central tracking detector is included.

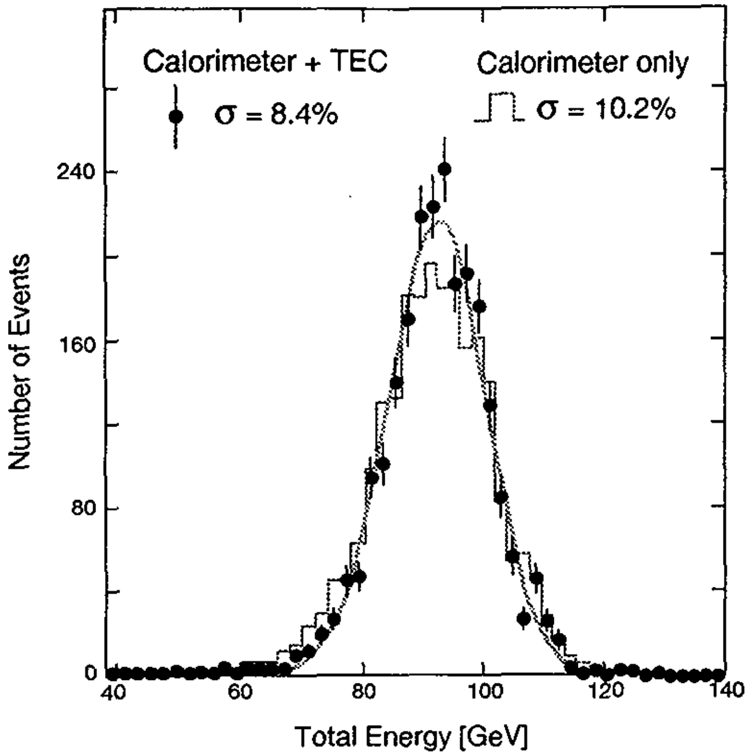

Figure 2.12: The energy resolution for the calorimeters, 10.2%, and its improvement to 8.4% on inclusion of the TEC information

2.8 The luminosity monitor

The luminosity monitor consists of two electromagnetic calorimeters and two sets of proportional wire chambers, situated symmetrically on either side of the interaction point. Each calorimeter is a finely segmented and azimuthally symmetric array of 304 BGO crystals covering the polar angular range $24.93 < \theta < 69.94$ mrad (or $(\pi - \theta)$) (with respect to the interaction point $x = y = z = 0$). Each crystal is read out by a photodiode and has a LED to monitor its stability. The analog photodiode signals are used for the luminosity triggers, and the digitized photodiode signals are used to determine the energy deposited in the crystals. The energy resolution of the calorimeters is about 2% at 45 GeV, and the angular resolution is 0.4 mrad in θ and $0.5°$ in ϕ.

2.9 The trigger

The overall goal of the L3 trigger system is to record the detector signals from each beam crossing in which particles came from the e^+e^- vertex. By design the only deadtime in the system is incurred during the digitization of the detector signals. This is achieved by a cascade of three digital trigger levels with intermediate buffering. To ensure good efficiency for each physics channel, each level has redundant selection criteria which are logically OR'd to arrive at a decision. To attain the highest precision in the event reconstruction the settings and calibrations of the accelerator, detector and trigger systems are frequently monitored and recorded. The functions of the three trigger levels are described below. All rates and thresholds noted are "typical".

2.9.1 Level-1 trigger

The level-1 has five triggers based on the calorimeters (electromagnetic and hadronic), luminosity monitors, scintillation counters, muon chambers and the TEC chamber. Each is gated by the beam crossing signal. On a positive result from any of the five, the fine digitization electronics commence operation. On a negative result, all electronics are cleared and readied for the next beam crossing. The level-1 rate of positive decisions is less than 8 Hz, with a dead time incurred from the fine digitizations of less than 5 %.

Calorimeter trigger

The level-1 calorimeter trigger is designed to select events which energy in the electromagnetic or hadronic calorimeters. This includes e^+e^-, $\tau^+\tau^-$, hadronic and $\nu\bar{\nu}\gamma$ final states.

The inputs are the analog sums of several BGO crystals or hadron calorimeter towers. The barrel and endcap BGO crystals are grouped into $32\ \phi \times\ 16\ \theta = 512$ superblocks. The hadron calorimeter is split into 2 radial layers and grouped into 16×11 (16×13) superblocks for the layer less than (greater than) about one absorption length in depth. The signals from a total of 896 channels are digitized and converted into GeV depositions. A series of memory stacks, arithmetic and memory lookup units then calculate several quantities which are compared to preset thresholds. Events with any of these values over threshold are accepted. The quantities used are: the total calorimeter energy; the energy in the electromagnetic calorimeter alone; and these two energies measured only in the barrel region. Typical thresholds are 25, 25, 15 and 8 GeV respectively. In addition θ and ϕ projections are formed to search for clusters, which are accepted with a threshold of 6 GeV. In spatial coincidence with a track from the TEC trigger, this threshold is reduced to 2.5 GeV. These projections are also used to search for events with only a single isolated electromagnetic cluster from single photon events with a threshold of 1 GeV.

The main source of background for this trigger is electronic noise. Typical total rates are 1 to 2 Hz.

Scintillator trigger

Trigger information from the scintillators is used to select high multiplicity events and, as described in the next section, to reject cosmic rays.

To be used as input, the mean time of a hit from any of the 30 scintillators is required to be within a loose gate of 30 ns. The rate of beam crossings with these good hits is about 3 kHz, owing to the proximity of the uranium in the barrel hadron calorimeter. High multiplicity events are selected by requiring 5 hits spread by over 90°. The rate of this trigger is typically 0.1 Hz and it is practically background free.

Muon trigger

The muon trigger selects events with at least one particle which penetrates the muon chambers.

Each wire in all of the muon chambers is scanned for a signal. Hits are formed if either of a pair of radially adjacent wires shows a signal. These hits are fed through a series of logic units and the event selected if the hits match any possible road from a track with a transverse momentum greater than 1 GeV as measured in either 2 out of 3 of the P-chamber layers or 3 out of 4 of the Z-chambers.

The trigger rate of 10 Hz is dominated by cosmic rays coincident with the beam crossing gate. By requiring in coincidence one good hit from the scintillator trigger this rate is reduced to less than 1 Hz.

TEC trigger

The TEC trigger is used to select events with charged tracks. This includes most of the physics of interest.

The split off signals from 14 anode wires spread radially over each of the outer 24 TEC sectors are used as input. Hits found in these signals are divided into 2 equal drift time bins. Logic units then scan each bin and its adjacent bins looking for tracks while allowing for the θ dependent chamber coverage and efficiency. The minimum transverse momentum selected is 150 MeV. Events are selected if at least two tracks are found with an acolinearity of less than 60°.

The trigger rate is dependent on the beam conditions, varying from 1 to 4 Hz.

Luminosity trigger

The luminosity trigger has as input the analog sums from the luminosity monitor. On each side the monitors are split into 16 ϕ segments and processed as like the calorimeter trigger. Any of three thresholds must be met to accept the event: Two back-to-back (within ± 1 sector) depositions with $\geq$ 15 GeV, total energy on one side greater than 25 GeV and on the other one greater than 5 GeV, or a total energy in either end greater than 30 GeV. The latter trigger is used to check the efficiency of the previous two and is prescaled by a factor of 20. As the statistical error does not dominate the luminosity determination the first two triggers are prescaled by a factor of two from the 1991 running period onward.

The typical trigger rate of 1.5 Hz depends primarily on the delivered luminosity but can increase in especially bad background conditions.

2.9.2 Level-2 trigger

The level-1 triggers attempt to select interesting events. In contrast, the function of the level-2 trigger is to reject background events selected by level-1. The input to the level-2 trigger are the coarse data used in level-1, the level-1 results and a few more data available for analysis at this step. The improvement on the level-1 results derives from the ability of level-2 to spend more time per event without incurring additional deadtime and on its ability to correlate subdetectors signals. This is especially effective in removing calorimeter triggers generated by electronic noise and TEC triggers generated by beam-gas, beam-wall interactions as well as synchrotron radiation. On a positive or negative result the level-2 results and all input is forwarded to an event builder memory. Other memories contain the zero suppressed fine digitizations from each subdetector. On a positive level-2 result the event builder collates the data for the entire event and transfers it to the level-3 trigger. On a negative level-2 result the event builder memories are reset. Events that fulfill more than one level-1 trigger condition pass the level-2 unhindered. The rejection power is typically 20 to 30% averaged over all level-1 triggers, such that the total rate after of level-2 is typically less than 6 Hz.

2.9.3 Level-3 trigger

To be effective level-3 applies criteria based on the complete digital data for the event. Several algorithms are used to examine the event, with the specific algorithm used being driven by the level-1 trigger which selected the event (calorimeter, luminosity, muon or TEC). As for level-2, events which were selected by more than one trigger at level-1 pass through unhindered. The calorimeter algorithm recalculates the event energies and applies similar criteria to those of the calorimeter trigger to pass the event. As the calculations are based on the fine digitizations the thresholds can be more precisely defined and electronic noise problems are further reduced. Luminosity triggers are passed through untouched. muon triggers are required to pass a more stringent scintillator coincidence in time, ±10ns, and space, ±60°. Tracks from TEC trigger events are correlated with at least 100 MeV of energy in the calorimeters and also examined for quality and a common vertex. Taken together these algorithms result in a rate reduction of 40 to 60%, with an output rate of 2 to 3 Hz.

The output from the level-3 trigger is delivered into a memory buffer on the main online computer. From this buffer all events are written to tape and selected events dispatched to ten separate monitoring programs. In addition, processes on this and the other online computers control the data taking, monitor, log and adjust detector settings, and calibrate the various detector and trigger elements.

2.10 The LEP collider complex

The Large Electron Positron collider LEP at CERN is situated in a tunnel of 27 km circumference on both sides of the border between France and Switzerland (see figure 2.13).

The main components of the collider are

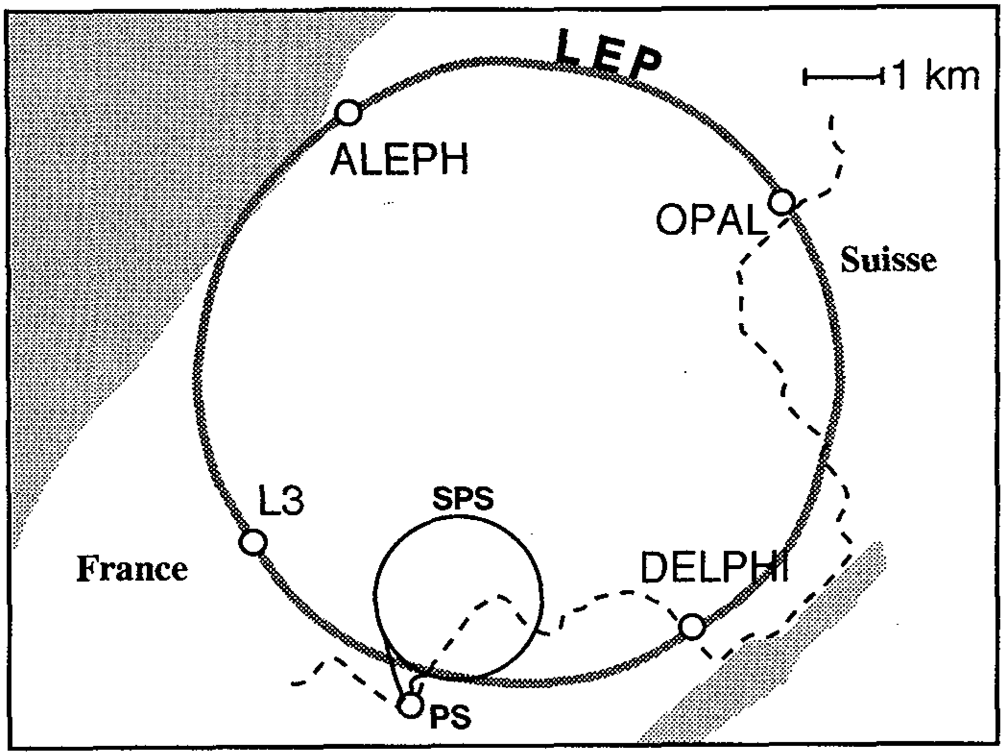

Figure 2.13: The LEP collider at CERN

- eight bending sections of 2840 m length each, with in total 3304 dipole magnets. At 45 GeV beam energy, the required field is 0.048 T.
- eight straight sections, four of which house the experiments ALEPH [7], DELPHI [8], L3 [9] and OPAL [10]. To both sides of each experiment, the beam is compressed with superconducting quadrupole magnets, increasing the luminosity.
- two straight sections containing the radiofrequency cavities with a total power of 16 MW, to accelerate the beam from injection energy to collision energy and to replace the energy lost by radiation on each turn.
- the existing accelerators PS and SPS, which are used as part of the injection system in addition to the linear accelerator LIL and an accumulation ring to enhance positron intensity.

At the beginning of each LEP fill, positrons and electrons are injected at an energy of 20 GeV. After ramping to collision energies, the beam lifetime is usually of the order of 20 hours at typical currents of up to 0.5 mA. The typical instantaneous luminosity delivered to L3 in 4 × 4 bunch operation during the later part of 1991 was $3 \times 10^{30} \mathrm{cm}^{-2}\mathrm{s}^{-1}$, with peak values reaching $5 \times 10^{30} \mathrm{cm}^{-2}\mathrm{s}^{-1}$.

In agreement with the originally proposed schedule of LEP, the collider has so far been run at energies at and around the Z resonance. Figure 2.14 shows the history of integrated luminosity delivered to the L3 experiment as a function of time. It is seen that in a short period after its commissioning, substantial improvements in luminosity have been achieved.

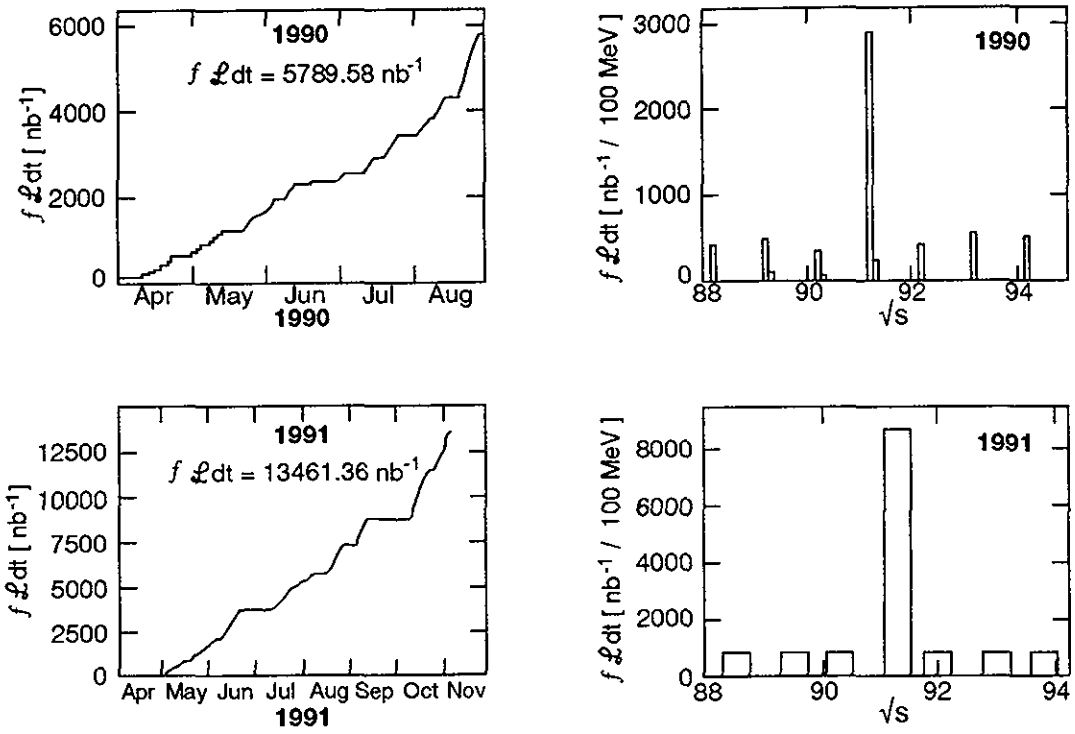

Figure 2.14: The history of integrated luminosity delivered to L3 in 1990 and 1991.

2.11 LEP collider energy calibration

The energy calibration of LEP is described in reference 14. The mass of the Z boson is a fundamental parameter of the Standard Model and its systematic error is dominated by the uncertainties in the LEP beam energies. Accordingly, four different methods have been used to provide information on the energy and to enable cross-checks to be made:

1. *The Field Display* uses a rotating coil to measure the magnetic field in reference dipoles powered in series with the main ring magnets. The reproducibility of the field display measurements is about 2.5×10^{-5}.

2. *The Flux Loop* consists of a closed electrical loop threading through all the dipoles; the integrated induced voltage when altering the dipole currents is a direct measure of the magnetic field generated by the main ring dipoles. However, it is insensitive to constant fields and does not take into account additional bending due to the quadrupoles and sextapoles on non-central orbits. Its absolute calibration has a precision of about 10^{-4}, but the additional corrections required reduce this precision.

3. *Proton Calibrations* are performed by filling the ring with 20 GeV protons which are not ultra-relativistic and thus their momentum can be measured by determination of the frequency of the RF acceleration voltage, this determines the momentum of positrons in a similar orbit. The precision of this method is high at 20 GeV but degrades to 2×10^{-4} after extrapolation to 45 GeV.

4. *Resonant Depolarization* determines the beam energy by measuring the frequency with which the spins of transversly polarized electrons precess around the vertical axis. This technique measures the beam energy under conditions very close to those of data-taking runs and is by far the most precise technique available.

In 1991 the absolute energy scale has been determined with a relative precision of 5.7×10^{-5} corresponding to ± 5.3 MeV at a center-of-mass energy of 93 GeV. In addition to the overall scale error, uncertainties in the local energy scale about the normalization point and in the fill-to-fill reproducibility of the beam energy lead to a total error due to energy uncertainties of ± 6.3 MeV on m_Z.

Chapter 3

The Detector Simulation

The L3 experiment is designed to search for 'new physics', and to perform precision tests of the Standard Model. Computer simulation is an essential part of the data analysis which allows us to understand the physics, the response of our detector, and the systematic errors, at a level which makes both precision tests and searches for rare new processes possible.

The Monte Carlo simulation program generates events in two steps:

- **event generation**, where events are created with a distribution according to a physical model, and where the results are stored as sets of energy-momentum four vectors and particle types;
- **detector Simulation**, where the generated particles are propagated through a detailed representation of the detector, including tracking and shower simulation in the detector materials, and the response of each active (chamber or calorimeter) element is simulated. This results in digitized events that are processed by the reconstruction program, and which are then compared directly to the reconstructed results from data.

Small disagreements between the reconstructed results obtained for Monte Carlo generated and real data samples cannot be taken as strong indicators of new physics, until high statistics standard physics data samples have been shown to be well represented, in all details, by the full detector simulation. The Monte Carlo can then (and only then) be used as an aid to develop criteria to separate the candidate rare event sample from the backgrounds as well as possible, and/or to determine the parameters of the new physics processes.

3.1 SIL3: The L3 detector simulation

The L3 detector simulation program SIL3 is based on GEANT3 [15], which is a general-purpose detector simulation program allowing for a general detector geometry and a detailed simulation of all particle interactions including electromagnetic and hadronic showers [15].. The program allows the detector geometry to be defined using a library of elementary shapes, and to be organized in a hierarchical tree structure. The physical properties such as material constants and magnetic field can be associated with the geometrical structures. Particles are tracked step by step through the detector, with all processes such as decay, energy loss, multiple scattering, nuclear interaction, bremsstrahlung, pair production and photofission simulated.

SIL3 includes a complete representation of the L3 detector, including the details of each subdetector geometry down to the required level of accuracy (typically 10 - 100 microns). Examples illustrating the complexity of this geometry are the hadron calorimeter, with 426,904 brass cells grouped into 11,252 chambers, and the electromagnetic calorimeter, with many different BGO crystal shapes and a thin-walled carbon fiber support structure. Both of these calorimeters are fully described. The survey information has been used to describe detector alignments with a high degree of accuracy.

Simulation of hadronic and electromagnetic showers in complex, non-uniform media requires tracking of low energy particles down to the sensitivity limit of the detectors. Thus particles are tracked down to $\sim$ 10 keV in the electromagnetic calorimeter and down to $\sim$ 1 MeV in the hadron calorimeter.

Fine tuning of parameters in the simulation has been done using results from test beam exposures of the calorimeters in 1986 to 1987 [9]. The tuning includes: an optimization of the step size for particle tracking in all subdetectors; an optimization of the medium dependent energy cut-off parameters; a parameterization of the saturation in light yield, the light collection efficiency and electronic noise in the electromagnetic calorimeter; and a simulation of uranium noise in the hadron calorimeter according to experimentally determined spectra.

All of this allows to reproduce to a high degree of accuracy not only global effects like the energy response and resolution for jets, but also more complex effects of the correlations in the longitudinal and transverse shower development for single particles and jets; the dependence of the response and resolution on polar angle; and the influence of boundary regions on energy and spatial resolution.

Hits in the central tracking chamber and in the muon chamber are simulated using the time-to-distance relation measured in the test beam data. Details of the response, such as multiple hits, cross talk and δ-rays are also included.

The scintillation counter ADC and TDC information are also simulated. Pulse heights are corrected for attenuation and times are corrected for particle flight time, scintillation light transmission time and time slewing due to varying pulse heights.

3.2 Quality of detector simulation

To give a examples of the high quality achieved in the detector simulation, each of the subsequent chapters contains comparisons of real and simulated data for many distributions. For example, in chapter 5 we show, for each Z decay channel, one of the key quantities used to identify the final state and distinuish it from others. L3's ability to assign small systematic errors to physics results is strongly dependent on the quality of the Monte-Carlo simulation.

3.3 Simulation of detector imperfections

The detector imperfections, e.g., the dead cells, noisy BGO crystals, disconnected sectors and inefficient wires, vary with time during data taking. For precise physics measurements, the time-dependent imperfections of the detector response must be fully simulated. Because the detector simulation is time consuming, these imperfections are simulated during the reconstruction of simulated events.

All information on the status and calibration of the detector is stored in the L3 data base. During reconstruction of real events, appropriate information is retrieved from the database using the time and date recorded in each event. Using this information, data from dead or noisy channels are discarded and appropriate calibrations are applied. During reconstruction of simulated data, each event is temporarily assigned a time and date such that the events are distributed over a data-taking period with the correct luminosity weighting.

To achieve the high degree of accuracy as required by this experiment, the simulation of a typical hadron event takes an average of 4.5 minutes of Apollo DN10000 CPU time (equivalent to 1.8 minutes of CPU time on an IBM 3090 Model J CPU). The computing time for a large angle e^+e^- final state is approximately 3.5 minutes on an Apollo DN10000.

Chapter 4

Measurement of Luminosity

Absolute cross section measurements of colliding beam reactions require a precise knowledge of the time integrated luminosity of the colliders. The definition of the luminosity $\mathcal{L}$ is given by $N = \mathcal{L} \times \sigma$ where N is the number of detected events, corrected for acceptance and background, and σ the cross section for the corresponding reaction.

In electron positron colliders one usually determines $\mathcal{L}$ from the measured number of small angle Bhabha scattering events, $e^+e^- \rightarrow e^+e^-(\gamma)$. For small scattering angles the reaction is dominated by t-channel exchange and the $\gamma - Z$ interference effects are small.

The experimental challenge lies in the precise definition of the geometrical acceptance. We note that the Bhabha cross section decreases sharply with increasing scattering angle θ, and hence is particularly sensitive to the minimum acceptance angle, θ_{min}. In addition, the theoretical uncertainty in the Bhabha cross section contributes significantly to the final uncertainty in the luminosity measurement.

4.1 Event selection

The Bhabha event selection is based on the energy deposits in the luminosity monitor described in section 2.8. A typical Bhabha event is shown in Figure 4.1. Adjacent crystals with more than 250 MeV of deposited energy are joined into clusters. The θ and ϕ impact coordinates of a cluster are determined from the observed energy sharing among the crystals. This is done by using an analytic function derived from the known average shape of electromagnetic showers. The same function is used to estimate the energy, E. of the incident particle by correcting the observed energy for lateral losses.

For most luminosity triggers one cluster is found in each calorimeter. For the events with multiple clusters we must differentiate between those with contributions from spurious beam-gas interactions and genuine radiative events. To do this, the clusters are ordered by energy and a vectorial sum of the individual cluster coordinates (E, θ, ϕ) is made. The summing is stopped when the difference between the energy of the cluster and the beam energy is minimal.

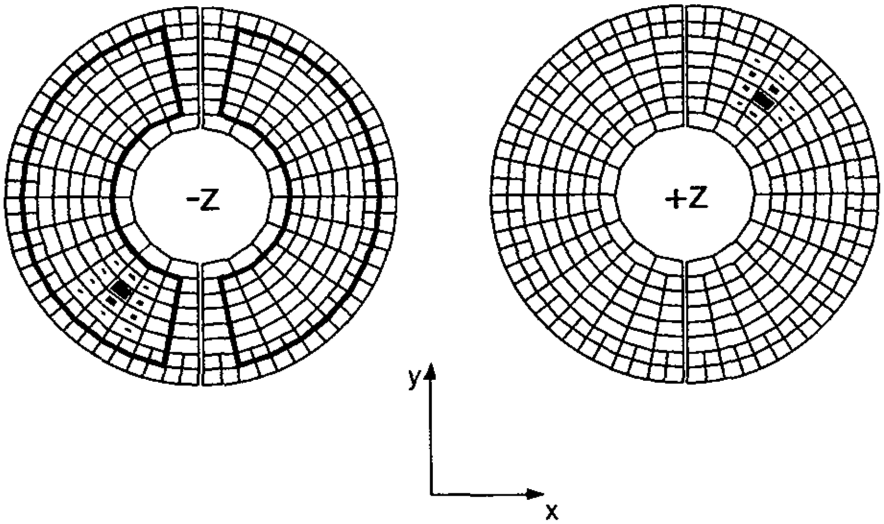

Figure 4.1: A Bhabha event as seen in the calorimeters of the luminosity monitor. Only energy deposits exceeding 250 MeV are shown. The size of each dark box is proportional to the energy deposit in the corresponding crystal. The tight fiducial volume corresponds to the outline shown in bold for the $-z$ calorimeter.

Two separate samples of Bhabha events are maintained. In the first (second) sample, a tight fiducial volume cut, as described in (1) below, is imposed on the calorimeter on the $+z$ ($-z$) side. The criteria used for selecting luminosity events are:

1. The cluster is required to have the reconstructed θ and ϕ impact coordinates more than one crystal away from the calorimeter edges (see Fig. 4.1):

   a. $\begin{cases} 30.92 < \theta < 64.41 \text{ mrad} & \text{for 1990} \\ 29.56 < \theta < 61.66 \text{ mrad} & \text{for 1991} \end{cases}$

   b. $|\phi - 90^\circ| > 11.25^\circ$ and $|\phi - 270^\circ| > 11.25^\circ$.

   No restrictions are imposed on the reconstructed impact coordinates on the opposite side.

2. The reconstructed energy on one side must be greater than $0.8E_{\text{beam}}$ and the that on the other side must be greater than $0.4E_{\text{beam}}$.

3. The coplanarity angle, $\Delta\phi$, of the two clusters must satisfy: $|\Delta\phi - 180^\circ| < 10^\circ$.

The asymmetric energy cut ensures that the acceptance is not sensitive to the effect of a few dead crystals, and in addition retains most of the radiative Bhabha events. Almost all the background from a coincidence of two beam-gas events has an energy of less than $0.8E_{\text{beam}}$ in each calorimeter and is, therefore, substantially reduced by requirement 2.

The coplanarity requirement is used to further suppress beam related background. The remaining background in the signal region is subtracted, on a fill-by-fill basis, using the sidebands of the coplanarity distribution, $10^\circ < |\Delta\phi - 180^\circ| < 30^\circ$, after imposing the requirement that the energy on neither side is within 5% of E_{beam}.

The residual background level of 0.1% is mainly due to random coincidences of beam-gas interactions. The systematic uncertainty due to the background subtraction is found to be negligible.

The average of the two Bhabha event samples is used to calculate the luminosity. The asymmetric fiducial volume cut and the averaging procedure greatly reduce the systematic effect on the luminosity measurement due to calorimeter misalignments and/or e^+e^- interaction point displacements. For example, a 2 mm displacement or a 1 mrad tilt of one calorimeter relative to the beam line increases the measured luminosity by only 0.1%. The colinearity of the Bhabha events is used to monitor relative displacements of the beam with a precision of 0.1 mm. The fill-to-fill variations of these displacements are less than 0.5 mm.

The effect of changes in the selection requirements on the integrated luminosity, $\mathcal{L}$, is shown in Figure 4.2. As can be seen a relatively large statistical uncertainty arises from increasing θ_{min} which strongly decreases the number of selected events. On the other hand, variations of the energy and coplanarity cuts hardly change the number of selected events. Within the statistical uncertainty, the value of $\mathcal{L}$ is stable against changes in the coplanarity, energy and fiducial volume cuts. Based on Figure 4.2, a 0.3% systematic uncertainty is assigned to $\mathcal{L}$ due to the event selection criteria.

4.2 Theoretical cross section

To determine the visible cross section, $e^+e^- \rightarrow e^+e^-(\gamma)$ events are generated at $\sqrt{s} = 91.18$ GeV using BHLUMI v2.01 [16,17]. At the generator level, the polar angles of the scattered electron and positron are required to be in the range $0.020 < \theta < 0.200$ rad. The generated events are passed through the L3 detector simulation program. For center of mass energies, $\sqrt{s}$, off the Z peak the visible cross section is rescaled by $(91.18\ \mathrm{GeV})^2/s$. Small $\sqrt{s}$ dependent electroweak interference effects ($\leq 0.2\%$) are also taken into account [18]. The contribution from $e^+e^- \rightarrow e^+e^-\gamma$ event configurations with the electron or the positron polar angle below 0.020 rad is estimated to be $(0.06 \pm 0.02)\%$.

The event selection does not differentiate between $e^\pm$ and γ. Thus, the contribution from the $e^+e^- \rightarrow \gamma\gamma(\gamma)$ process (0.02%) must be added to the visible cross section [19]. The small background from the double-tag mode of the two-photon process, $e^+e^- \rightarrow e^+e^-X$, is generally not coplanar and is therefore accounted for by the $\Delta\phi$ sideband background subtraction procedure.

Including all contributions, the visible cross section at the Z peak is 90.3 (84.7) pb for the 1991 (1990) analysis. The differences between the visible cross sections for the 1990 and 1991 selection are due to a change in the z location of the calorimeters. The systematic uncertainty in the visible cross section due to the limited Monte Carlo statistics is 0.1%. The theoretical uncertainty, resulting from the approximations used in the BHLUMI v2.01 calculation is estimated to be 0.3% [17]. The geometry of the calorimeters has been surveyed and has been checked independently using the proportional wire chambers mounted in front of the calorimeters. The uncertainty in the geometry measurements introduces a 0.4% systematic uncertainty in the visible cross section.

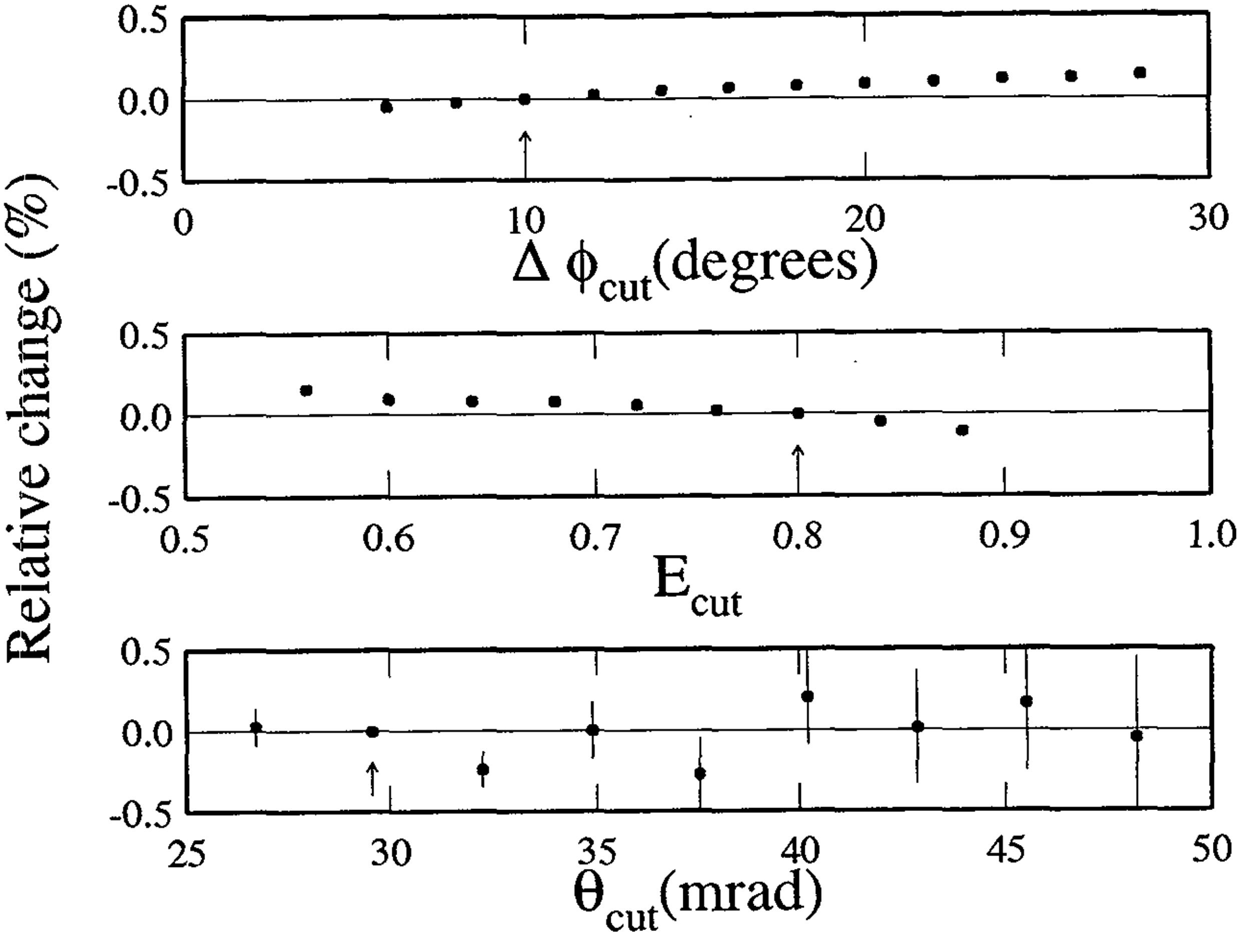

Figure 4.2: The relative change in the integrated luminosity as a function of (a) the coplanarity cut $|\Delta\phi - 180^\circ| < \Delta\phi_{cut}$; (b) the energy cut $E_{max}/E_{\rm beam} > E_{cut}$ and $E_{min}/E_{\rm beam} > \frac{1}{2}E_{cut}$; and (c) the smaller fiducial volume cut $\theta_{cut} < \theta < 61.66$ mrad. The arrows indicate the nominal cut values.

4.3 Luminosity determination

From the 1991 data sample approximately 6.3×10^5 events from the 2.0×10^6 recorded luminosity triggers pass the event selection criteria described above. The corresponding numbers of events for the 1990 data sample are 4.9×10^5 and 1.8×10^6, respectively. The measured coplanarity distribution, after the energy and the fiducial volume cuts, is compared to the Monte Carlo prediction in Figure 4.3a. Figures 4.3b-c show the measured energy and θ distributions for the selected Bhabha sample of 1991, together with the Monte Carlo predictions. Only the statistical errors on the data are shown; the statistical errors on the Monte Carlo simulation are approximately twice as large as those on the data. Apart from the tails of the energy distribution, the three distributions are in good agreement with the Monte Carlo simulations. The excess of data events at high energies is due to real Bhabha interactions contaminated with a spurious beam-gas interaction.

Radiative Bhabha events are used to further investigate the quality of the Monte Carlo

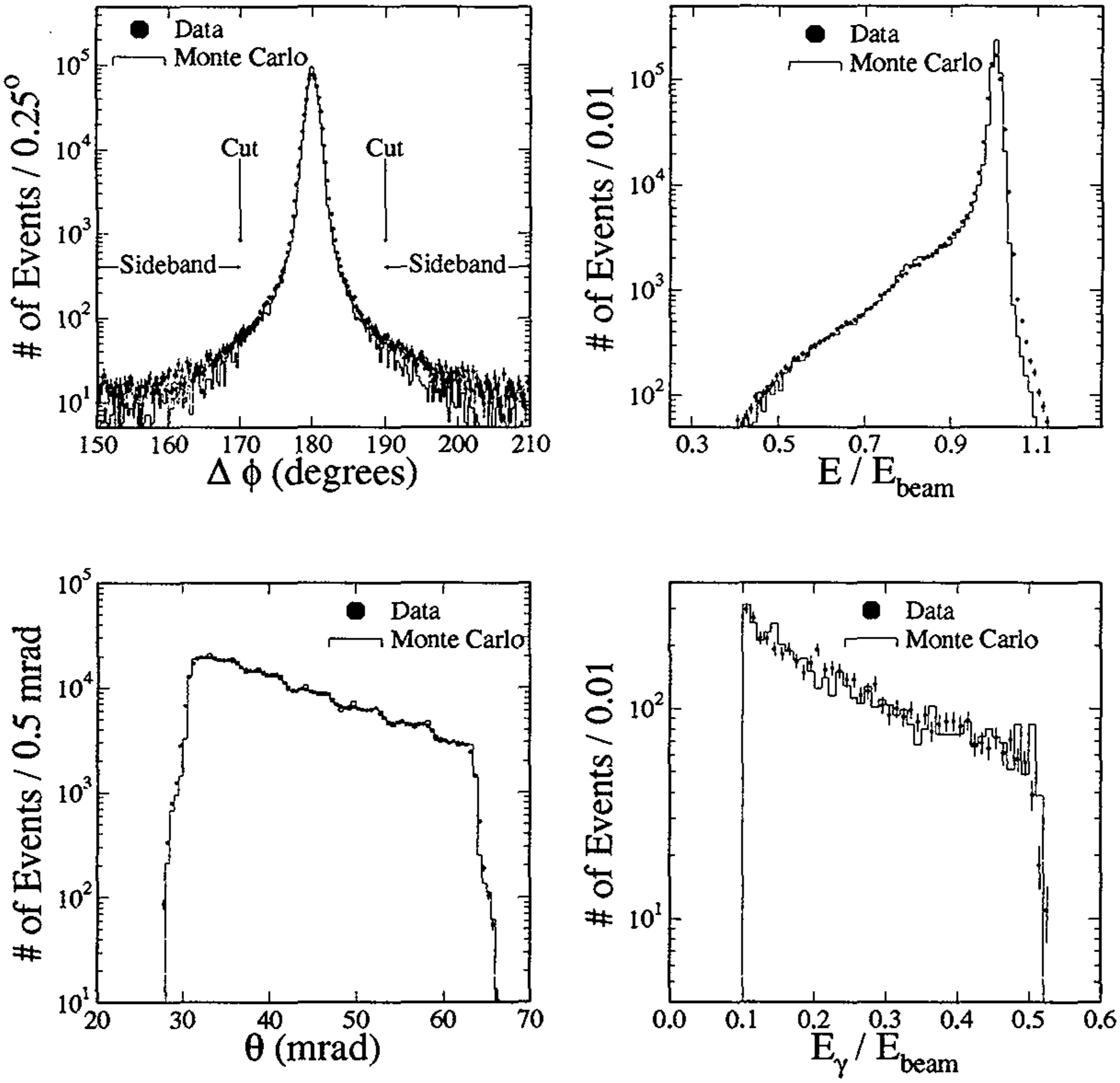

Figure 4.3: (a) The observed coplanarity distribution, $\Delta\phi$, compared to the Monte Carlo simulation for Bhabha event candidates. The cuts used to select Bhabha events, $|\Delta\phi - 180^\circ| < 10^\circ$, and the sidebands used for the background subtraction are indicated in the figure. (b) Distribution of the observed $E^\pm$ energies normalized to the beam energy, compared to the Monte Carlo simulation for Bhabha events. (c) Distribution of the observed polar scattering angle, θ, compared to the Monte Carlo simulation for Bhabha events. The structure in the distributions is due to the changing angular resolution across the face of each crystal. (d) Distribution of the observed photon energies, compared to the Monte Carlo simulation for Bhabha events.

simulation. The γ is identified as the smaller energy cluster in events with two separate clusters in one calorimeter. Requiring the γ energy, E_γ, to be larger than $0.1E_{\text{beam}}$, 5124 radiative Bhabha events are identified. Figure 4.3d shows the measured E_γ distribution and the Monte Carlo prediction. The agreement is satisfactory.

The various contributions to the systematic uncertainty in the luminosity are summarized in Table 4.1. The total systematic error of 0.6% is obtained by adding in quadrature the different contributions.

Source of Systematic Uncertainty	Contribution to $\Delta\mathcal{L}$ (%)
Luminosity Trigger Inefficiency	negligible
Geometry of the Calorimeters	0.4
Bhabha Event Selection Criteria	0.3
Background Subtraction	negligible
Monte Carlo Statistics	0.1
Total Experimental Systematic Uncertainty	0.5
Theoretical Systematic Uncertainty	0.3
Total Systematic Uncertainty	0.6

Table 4.1: The contributions to the systematic uncertainty in the luminosity measurement. The total systematic uncertainty is the quadratic sum of the various contributions.

Chapter 5

Production and Decay of Z Bosons

Operating the LEP storage ring in the vicinity of the Z mass with high luminosity permits a detailed study of the lineshape of the Z resonance. We have performed measurements of the following reactions:

1. $e^+e^- \to \text{hadrons}$,
2. $e^+e^- \to \mu^+\mu^-(\gamma)$,
3. $e^+e^- \to \tau^+\tau^-(\gamma)$,
4. $e^+e^- \to e^+e^-(\gamma)$,
5. $e^+e^- \to \text{hadrons} + \gamma$,
6. $e^+e^- \to \nu\bar{\nu}\gamma$.

The measured cross sections are used to extract the properties of the Z boson: the mass, the total width and its hadronic and leptonic decay widths. Further information on electroweak parameters such as the vector and axial vector coupling constants g_V and g_A is contained in the measurements of the forward-backward asymmetries of the leptonic decay channels of the Z. The difference between the total width and the sum of the observable partial widths, which in the Standard Model is attributed to the Z decays into neutrinos, leads to a determination of the number of light neutrino families. The process $Z \to \nu\bar{\nu}\gamma$ is also directly observed and its rate measured. Interpreted in terms of the predicted width per neutrino family this gives a second, independent measurement of the same quantity [20]. Hard isolated photons in hadronic events can be used to give a measurement of electroweak couplings to up-type and down-type quarks separately.

For all cross section and asymmetry measurements detailed studies of the systematic uncertainties have been carried out. The understanding of the systematic errors is very important to fully exploit the statistical precision achievable by the large number of events collected. The events for all reactions studied, except $\nu\nu\gamma$, are triggered by at least two independent level-1 triggers. For instance, hadronic Z decays are triggered by the energy, scintillation counter and charged particle triggers. Therefore, we can determine individual trigger efficiencies from selected events. From these analyses we find for all reactions a combined trigger efficiency larger than 99.9%. The systematic errors due to trigger inefficiencies are therefore negligible.

In this chapter we briefly describe the analysis methods used for reactions 1–6. More details can be found in reference 21. We present the cross sections and forward-backward asymmetries obtained in 1991 and the results of the re-analysis of the previously published [21] data taken in 1990 using similar selection criteria and cuts as for the analysis of the data taken in 1991.

5.1 The reaction $e^+e^- \longrightarrow$ hadrons

The selection of hadronic Z decays is based on the energy deposition in the electromagnetic and hadron calorimeters. For the measurement of the total cross section we use the following criteria:

1. $0.5 < E_{\text{vis}}/\sqrt{s} < 1.5$, where E_{vis} is the total calorimetric energy observed in the detector.
2. $|E_{\parallel}| / E_{\text{vis}} < 0.6$, where $E_{\parallel}$ is the energy imbalance along the beam direction.
3. $E_{\perp}/E_{\text{vis}} < 0.5$, where $E_{\perp}$ is the transverse energy imbalance.
4. The number of energy clusters, N_{cluster}, reconstructed in the calorimeters is required to satisfy:
    a. $N_{\text{cluster}} \geq 13$ for $|\cos\theta_t| < 0.74$ (barrel) or
    b. $N_{\text{cluster}} \geq 17$ for $|\cos\theta_t| > 0.74$ (endcap)
    ($N_{\text{cluster}} \geq 9$ for 1990 data)

    where θ_t is the polar angle of the event thrust axis (see equation 10.1) with respect to the beam line.

Figure 5.1 shows the distribution of $E_{\text{vis}}/\sqrt{s}$ after cuts 2–4 have been applied. The agreement between data and Monte Carlo generated events is very good in the signal region. The background in the sample of hadronic events selected by the above cuts is very small. From the analysis of $e^+e^- \to \tau^+\tau^-(\gamma)$ and $e^+e^- \to e^+e^-(\gamma)$ Monte Carlo simulations we derive a background contribution of $(0.10 \pm 0.02)\%$ and 0.02%, respectively. The non-resonant background from beam-gas interactions and two-photon events has been estimated by studying the observed event rate in the region $0.2 < E_{\text{vis}}/\sqrt{s} < 0.5$ at different center of mass energies. This leads to an additional contamination of (30 ± 10) pb which amounts to 0.1% of the cross section measured at the Z-peak.

Since the hadron calorimeter covers 99.5% of the full solid angle the acceptance for $e^+e^- \to$ hadrons events is very high, $(99.15 \pm 0.03)\%$ including all detector inefficiencies. This number has been determined with the JETSET 7.3 [22] Monte Carlo program. An alternative fragmentation model (HERWIG 5.3 [23]) gives the same result within errors. We estimate a 0.1% systematic uncertainty of the acceptance on the Z peak. The extrapolation of the acceptance to the off-peak energies adds a further 0.1% to the systematic error.

To study the dependence of the measured cross section on the selection criteria we have varied our cuts within reasonable limits. Due to the very good agreement of data and Monte Carlo distributions the uncertainty is estimated to be less than 0.15%. We have calculated the

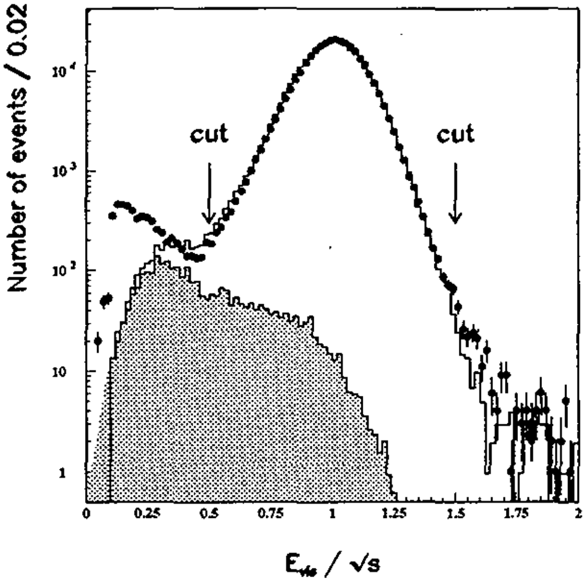

Figure 5.1: Total visible energy divided by the center of mass energy for $e^+e^- \rightarrow$ hadrons compared to Monte Carlo and background distributions from $e^+e^- \rightarrow \tau^+\tau^-(\gamma)$ and $e^+e^- \rightarrow e^+e^-(\gamma)$.

hadronic cross section for each LEP fill. The individual results are statistically compatible and we find no evidence for a time dependence of our measurements.

Adding all uncertainties in quadrature we assign a 0.2% (0.3% in 1990) systematic error to the corrected number of hadronic events.

For an integrated luminosity of 18.2 pb^{-1} we find 422585 $e^+e^- \rightarrow$ hadrons events. The cross sections around the Z resonance are listed in table 5.1. These cross sections have been corrected for acceptance and the finite energy spread of LEP (see section 2.10). The 1991 data are split into two parts reflecting the improved LEP energy calibration after August 14, 1991 [24]. The measurements are compared in figure 5.2a) to the result of the fit to all hadronic and leptonic cross sections as described in section 8.4. The resonance curve of the Z is very well described by our data which can be seen from figure 5.2b) where the ratio of the measured and fitted cross sections is plotted. The points agree within the statistical error.

Data 1990			
$\sqrt{s}$ (GeV)	N_{events}	$\mathcal{L}$ (nb^{-1})	σ_{tot} (nb)
88.231	1776	393.3	4.53±0.11
89.236	3841	453.7	8.50±0.14
90.238	6725	364.0	18.60±0.25
91.230	83835	2784.8	30.38±0.12
92.226	8637	399.5	21.78±0.26
93.228	6368	518.3	12.36±0.16
94.223	3915	480.0	8.20±0.14
Totals	115097	5393.6	

Data 1991			
$\sqrt{s}$ (GeV)	N_{events}	$\mathcal{L}$ (nb^{-1})	σ_{tot} (nb)
91.254	155091	5130.8	30.43±0.10
88.480	4050	782.9	5.17±0.09
89.470	8528	847.9	10.08±0.12
90.228	14333	794.3	18.12±0.18
91.222	90618	3014.8	30.26±0.13
91.967	16059	658.5	24.51±0.24
92.966	10864	759.2	14.36±0.16
93.716	7945	794.6	10.02±0.13
Totals	307488	12783.0	

Table 5.1: Results on the cross section for the reaction $e^+e^- \rightarrow$ hadrons. Quoted errors are statistical only; the overall systematic uncertainty in the cross section is 0.2% (0.3% for 1990 data) from the selection and acceptance of the hadronic events and 0.6% from the luminosity measurement.

5.2 The reaction $e^+e^- \rightarrow \mu^+\mu^-(\gamma)$

5.2.1 Cross section

The process $e^+e^- \rightarrow \mu^+\mu^-(\gamma)$ is identified as an event with two muons in the angular range $|\cos\theta| < 0.8$. In the L3 detector a muon is identified either by its track in the muon chambers or as a minimum ionizing particle in the calorimeters. To suppress cosmic ray background at least one of the muon candidates must have the corresponding scintillation counter fired within 3 ns of the beam crossing or a track in the central tracking chamber with a distance of closest approach to the interaction point of less than 2.5 mm in the $r\phi$ plane.

For events with two reconstructed muons in the muon chambers (81% of the total sample) one muon momentum must exceed $\frac{2}{3}E_{\text{beam}}$. Figure 5.3 shows the momentum distribution of the most energetic muon in the event compared to the Monte Carlo prediction [25] for data

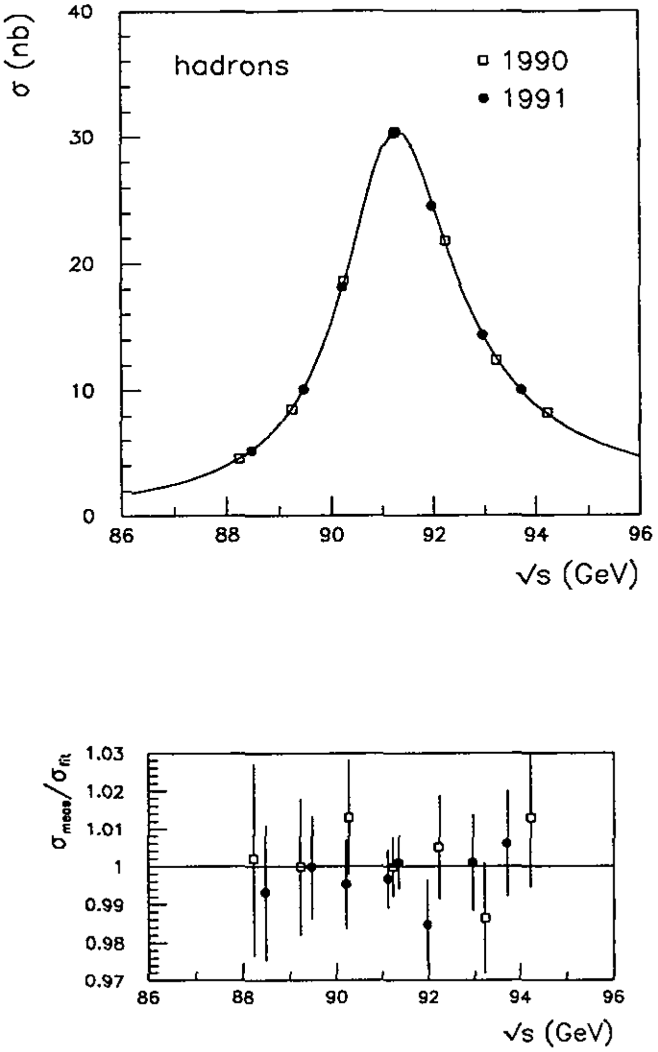

Figure 5.2: a) The total hadronic cross section. b) The ratio of the total hadronic cross section and the fit to all hadronic and leptonic cross sections.

at the Z peak. Good agreement between the data and the Monte Carlo is observed. The momentum cut removes most of the background from $e^+e^- \rightarrow \tau^+\tau^-(\gamma)$, two-photon processes and hadronic events. The remaining $e^+e^- \rightarrow$ hadrons events are rejected by a charged multiplicity requirement.

The background remaining in the event sample originates from Z decays into $\tau^+\tau^-$ and from cosmic rays. The $e^+e^- \rightarrow \tau^+\tau^-(\gamma)$ contamination has been determined to be $(1.7 \pm 0.1)\%$ by analyzing events generated with KORALZ [25]. We have estimated the cosmic ray background by extrapolating the observed rate of events with tracks in the central chamber not pointing to the vertex. We derive a contamination of $(0.7 \pm 0.1)\%$. Other possible background sources are found to be negligible.

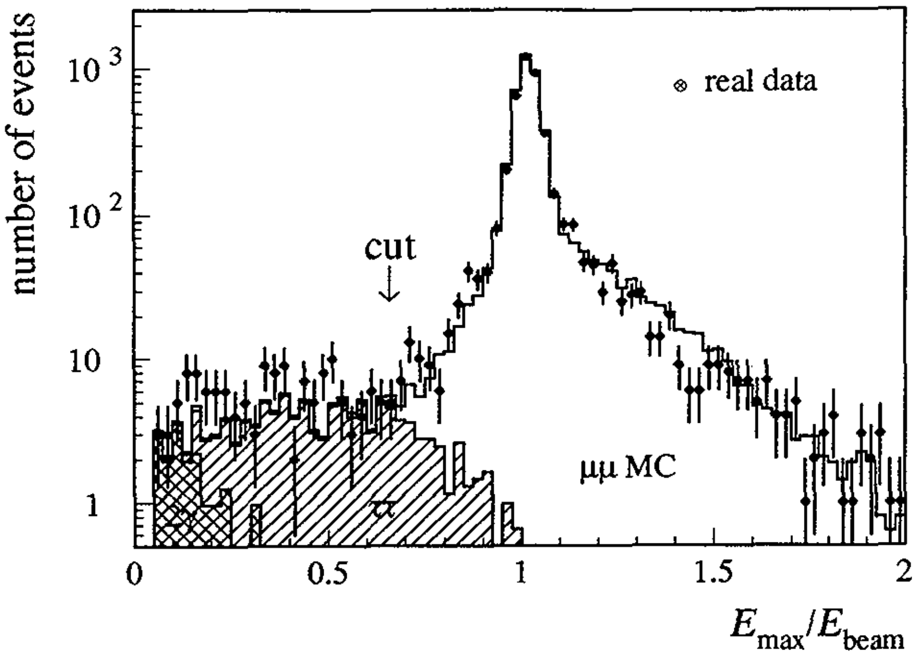

Figure 5.3: The measured momentum of the most energetic muon compared to $e^+e^- \to \mu^+\mu^-(\gamma)$ and background Monte Carlo.

The uncertainty in the event selection has been determined to 0.3% by varying our selection cuts. The acceptance inside the fiducial volume is $(97.58 \pm 0.08)\%$.

The cross section determined in the fiducial volume is extrapolated to the full $\cos\theta$ range. Since the contribution of hard initial state bremsstrahlung is different above and below the Z peak the $\cos\theta$ distribution of the events depends slightly on the center of mass energy. Hence, the fraction of events inside our fiducial volume changes by up to 2% over the energy range of our measurements. We assign a 0.2% error to the extrapolation.

After applying the above selection criteria, 14115 events are selected from the data sample with a total integrated luminosity of 18.1 pb^{-1}. The measured cross sections together with the number of events and the luminosity collected at each energy point are listed in Table 5.2. Figure 5.4 compares the measured cross sections to the result of a fit to all hadronic and leptonic data as described in section 8.4.

5.2.2 Forward-Backward Asymmetry

The forward-backward asymmetry, A_{fb}, is defined as follows:

$$A_{\text{fb}} \equiv \frac{\sigma_F - \sigma_B}{\sigma_F + \sigma_B} \tag{5.1}$$

where σ_F (σ_B) is the cross section for events with the μ^- scattered into the forward (backward) hemisphere with respect to the electron beam direction.

Data 1990			
$\sqrt{s}$ (GeV)	N_{events}	$\mathcal{L}$ (nb^{-1})	σ_{tot} (nb)
88.231	66	388.6	0.268±0.033
89.236	104	421.0	0.387±0.038
90.238	217	364.9	0.929±0.063
91.230	2675	2822.4	1.476±0.028
92.226	282	394.8	1.115±0.066
93.228	160	496.6	0.505±0.040
94.223	123	480.4	0.404±0.036
Totals	3627	5368.7	

Data 1991			
$\sqrt{s}$ (GeV)	N_{events}	$\mathcal{L}$ (nb^{-1})	σ_{tot} (nb)
91.254	5425	5041.9	1.497±0.020
88.480	130	780.4	0.235±0.021
89.470	290	851.1	0.478±0.028
90.228	492	794.3	0.866±0.039
91.222	2912	2933.8	1.381±0.026
91.967	585	700.9	1.165±0.048
92.966	372	759.2	0.686±0.036
93.716	282	830.9	0.478±0.028
Totals	10488	12692.4	

Table 5.2: Results on the cross section for the reaction $e^+e^- \rightarrow \mu^+\mu^-(\gamma)$. σ_{tot} is the cross section extrapolated to the full solid angle. Quoted errors are statistical only and the overall systematic uncertainty in the cross section is 0.5% (0.8% for 1990 data), excluding the 0.6% luminosity uncertainty.

For this measurement we use the subsample of events where both muon momenta are measured in the muon chambers. From the fraction of the events where both muons have the same reconstructed charge we determine the charge confusion rate to be $(1.2 \pm 0.2)\%$ for single muons. These events are removed from our sample. The main source for charge confusion are tracks passing close to the edges of the sensitive regions of the muon chambers. Studying the angular distribution of the same charge events we derive a probability of less than 0.2% that both muon charges are wrongly measured which translates into a systematic error of $0.004 A_{\text{fb}}$ due to charge reconstruction.

Events with hard initial state bremsstrahlung are removed from the sample by requiring that the acolinearity angle ζ of the $\mu^+\mu^-$ pair is less than 15°. This allows us to approximate the angular distribution for $|\cos\theta| < 0.8$ with the lowest order form:

$$\frac{d\sigma}{d\cos\theta} \propto \frac{3}{8}(1 + \cos^2\theta) + A_{\text{fb}} \cos\theta \tag{5.2}$$

From comparisons to the full electroweak calculations (ZFITTER [26]) we conclude that this approximation translates to a systematic error of less than 0.003 in the determination of the asymmetry. The asymmetry at a given energy point is then determined by a maximum like-

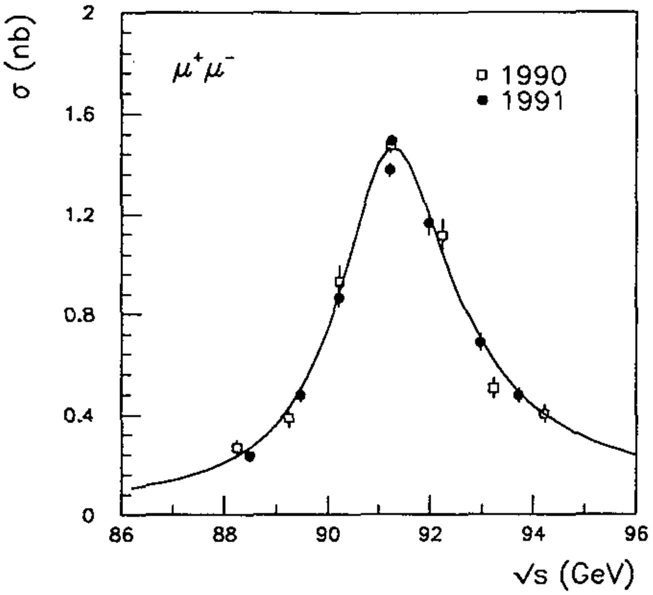

Figure 5.4: The measured muon pair cross section as a function of the center of mass energy.

lihood fit to our data where the likelihood is defined as the product over the selected events weighted with their $\cos\theta_i$ value:

$$L \equiv \prod_i \left(\frac{3}{8}(1 + \cos^2\theta_i) + A_{fb}\cos\theta_i \right). \tag{5.3}$$

This method does not require the exact knowledge of the acceptance as a function of the polar angle provided that the acceptance is independent of the muon charge. Comparing the momentum spectra of positively and negatively charged muons we can set a limit of 0.002 on the systematic error on the dimuon asymmetry induced by a possible charge dependence of the muon acceptance.

The background from the reaction $e^+e^- \to \tau^+\tau^-(\gamma)$ in the dimuon sample does not modify the asymmetry since these events have the same forward-backward asymmetry as $e^+e^- \to \mu^+\mu^-(\gamma)$ events. The systematic error from the small cosmic rays background is negligible. In summary, we assign a total systematic error of 0.005 to the asymmetry.

The results for the different center of mass energies are shown in table 5.3 and compared in figure 5.5 to the combined fit result (see section 8.4).

In figure 5.6 we show the angular distribution, corrected for the $\cos\theta$ dependent acceptance, for $\sqrt{s} = 91.22$ GeV. The result for the asymmetry (0.019 ± 0.015) obtained from a fit to this distribution agrees well with our result from the likelihood method.

Data 1990		Data 1991	
$\sqrt{s}$ (GeV)	$A_{\rm fb}$	$\sqrt{s}$ (GeV)	$A_{\rm fb}$
		91.254	0.018±0.015
88.231	-0.39±0.12	88.480	-0.15±0.10
89.236	-0.04±0.11	89.470	-0.20±0.07
90.238	-0.184±0.074	90.228	-0.041±0.052
91.230	0.006±0.021	91.222	0.013±0.021
92.226	0.110±0.066	91.967	0.060±0.045
93.228	0.095±0.091	92.966	0.122±0.058
94.223	0.134±0.099	93.716	0.084±0.067

Table 5.3: Measured forward-backward asymmetry, $A_{\rm fb}$, for the reaction $e^+e^- \to \mu^+\mu^-(\gamma)$ with $\zeta < 15°$. The quoted errors are statistical only. The systematic error is estimated to be less than 0.005.

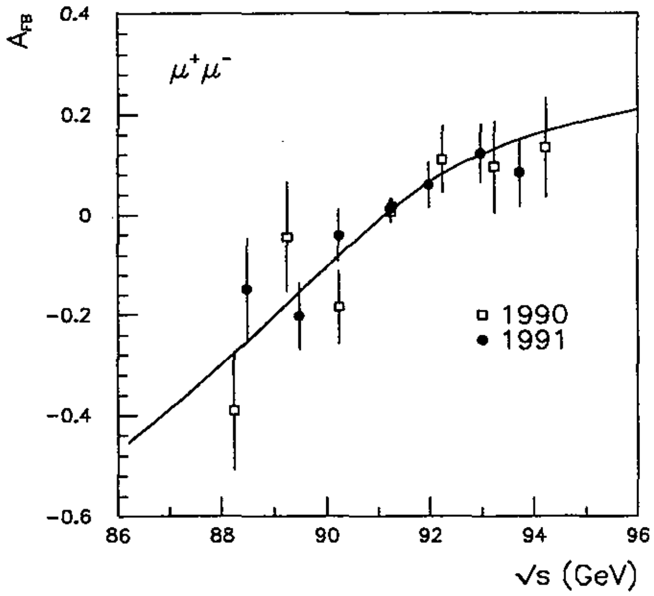

Figure 5.5: The $e^+e^- \to \mu^+\mu^-(\gamma)$ forward-backward asymmetry as a function of the center of mass energy.

5.3 The reaction $e^+e^- \to \tau^+\tau^-(\gamma)$

5.3.1 Cross section

The event selection for $e^+e^- \to \tau^+\tau^-(\gamma)$ is mainly based on calorimetric quantities. Tau pairs are selected in the fiducial volume defined by $|\cos\theta_t| < 0.73$ where the polar angle θ_t is given by the thrust axis of the event. The total energy measured in the electromagnetic and hadron

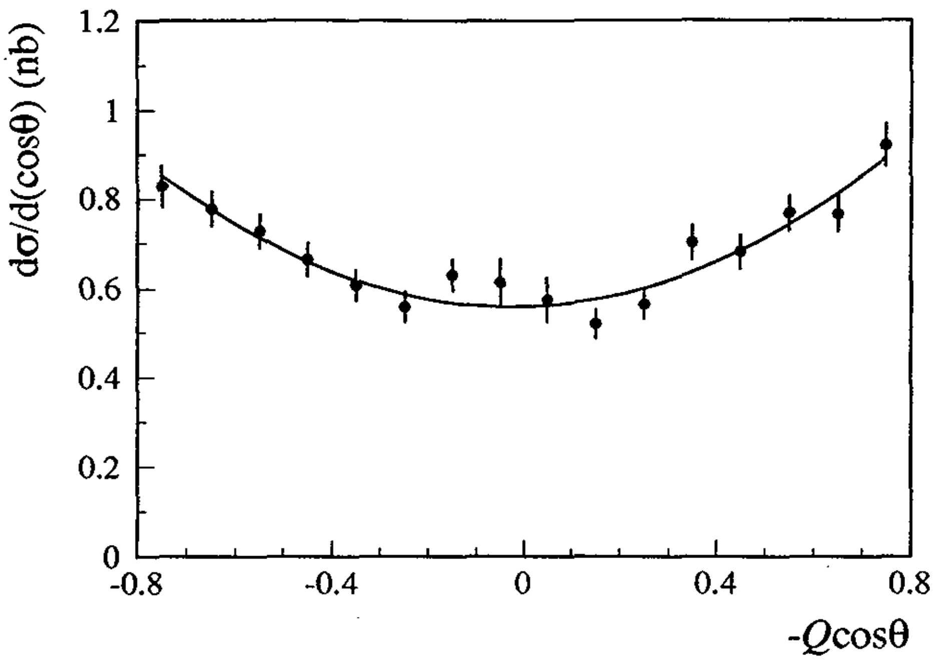

Figure 5.6: The differential cross section of $e^+e^- \rightarrow \mu^+\mu^-(\gamma)$ at the Z peak (91.22 GeV). The solid curve is the result of a fit using equation 5.2.

calorimeters must be above 7 GeV for the most energetic jet and above 3 GeV for the second most energetic jet. The acolinearity angle ζ between the two most energetic jets must be smaller than 250 mrad. To reject cosmic background we require a scintillator fired within 2.5 ns of the beam crossing. The two most energetic clusters in the electromagnetic calorimeter must have energies below 90% and 65% of the beam energy to reject events from $e^+e^- \rightarrow e^+e^-(\gamma)$. Similarly, the momentum measured in the muon chambers must be less than $0.9E_{\text{beam}}$ for the most energetic and $0.4E_{\text{beam}}$ for the second most energetic muon candidate in the event. Figure 5.7 shows the distributions of the most energetic cluster in the electromagnetic calorimeter and highest momentum muon track for $e^+e^- \rightarrow \tau^+\tau^-(\gamma)$ candidates and background. High multiplicity hadronic Z decays are removed by requiring less than 13 reconstructed energy clusters in the calorimeters. In addition, there should be no track in the central chamber with an azimuthal angle ϕ larger than 250 mrad to the axis of the nearest jet.

In this sample, a background of (2.70 ± 0.15)% remains from the other Z decay channels. Smaller contaminations originate from cosmic rays (0.25 ± 0.08)% and two-photon processes (0.12 ± 0.05)%, mainly $e^+e^- \rightarrow e^+e^-e^+e^-$. From varying the selection criteria we derive a systematic error of 0.6%.

The acceptance for $e^+e^- \rightarrow \tau^+\tau^-(\gamma)$ has been determined from Monte Carlo to (78.05 ± 0.12)% inside the fiducial volume. Because the acceptance depends on the decay mode, an additional error of 0.2% has to be added due to the uncertainties of the tau branching ratios. In total, we assign a systematic error of 0.7% to the number of $e^+e^- \rightarrow \tau^+\tau^-(\gamma)$ events.

For an integrated luminosity of 17.6 pb^{-1} we find 9943 events. Table 5.4 and figure 5.8 show

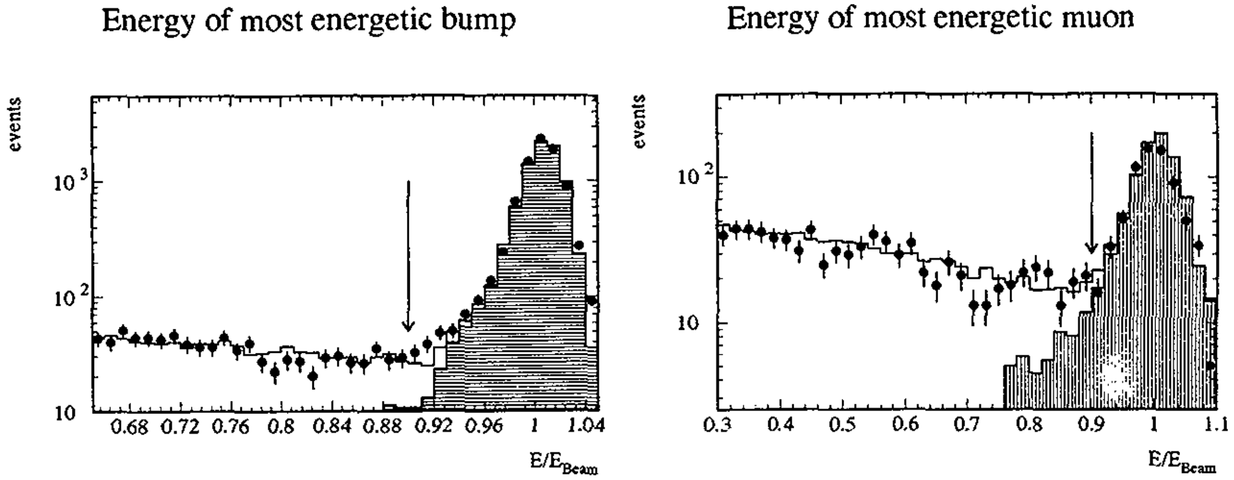
Energy of most energetic bump

Energy of most energetic muon

Figure 5.7: The energy of a) the most energetic electromagnetic cluster and b) of the highest momentum muon for $e^+e^- \to \tau^+\tau^-(\gamma)$ candidates compared to $e^+e^- \to \tau^+\tau^-(\gamma)$ and background Monte Carlo.

the results of the $e^+e^- \to \tau^+\tau^-(\gamma)$ cross section measurement. Again, the cross sections have been extrapolated to the full solid angle for each center of mass energy taking into account the variations of the acceptance ($\leq 2\%$).They are compared to the result of a fit to all hadronic and leptonic data as described in section 8.4.

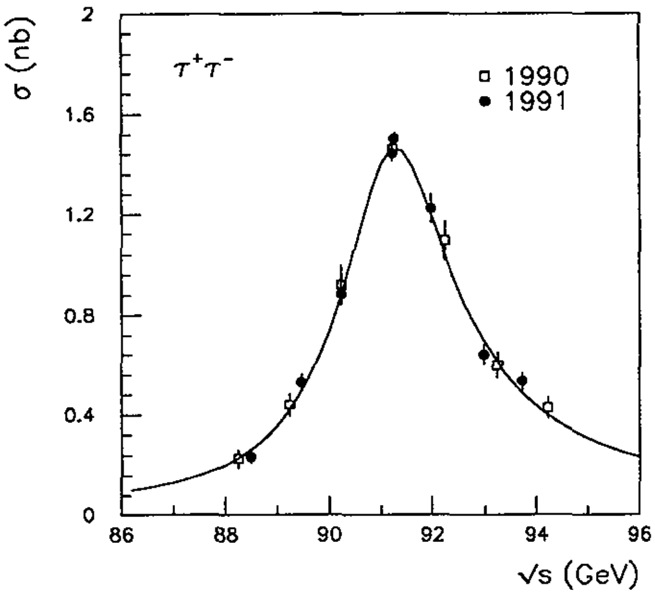

Figure 5.8: The measured tau pair cross section as a function of the center of mass energy.

Data 1990			
$\sqrt{s}$ (GeV)	N_{events}	$\mathcal{L}$ (nb^{-1})	σ_{tot} (nb)
88.231	36	337.8	0.228±0.037
89.236	83	404.7	0.439±0.047
90.238	138	319.9	0.920±0.077
91.230	1868	2721.3	1.463±0.033
92.226	188	366.3	1.095±0.078
93.228	132	472.2	0.599±0.051
94.223	95	477.4	0.427±0.043
Totals	2540	5099.6	

Data 1991			
$\sqrt{s}$ (GeV)	N_{events}	$\mathcal{L}$ (nb^{-1})	σ_{tot} (nb)
91.254	3720	4909.1	1.505±0.025
88.480	95	780.4	0.236±0.024
89.470	229	851.1	0.531±0.035
90.228	359	794.3	0.885±0.047
91.222	2102	2886.1	1.447±0.032
91.967	425	690.2	1.224±0.059
92.966	248	759.2	0.641±0.041
93.716	225	830.9	0.535±0.036
Totals	7403	12501.3	

Table 5.4: Results on the cross sections for the reaction $e^+e^- \to \tau^+\tau^-(\gamma)$. σ_{tot} is the cross section extrapolated to the full solid angle. Quoted errors are statistical only and the overall systematic uncertainty in the cross section is 0.7% (1.5% for 1990 data), excluding the 0.6% luminosity uncertainty.

5.3.2 Forward-Backward Asymmetry

The charge of a tau is determined from the charges of its decay products determined from the curvature of the tracks in the central tracking chamber or in the muon chambers. The sum of all charges in a jet gives the charge of a tau. For the determination of the forward-backward asymmetry we only take events where the two taus have opposite charge. 7441 tau pairs satisfy this additional requirement. We loose mainly events where particles pass through the low resolution regions of the central tracking chamber close to the cathode or anode wire planes. The charge confusion probability is $(10.2 \pm 0.3)\%$ for a single tau. We correct for this and estimate a residual systematic error for the $e^+e^- \to \tau^+\tau^-(\gamma)$ forward-backward asymmetry of $0.001 A_{\text{fb}}$.

The systematic uncertainty due to the subtraction of the $e^+e^- \to e^+e^-(\gamma)$ background is 0.005; due to the cosmic ray background it is 0.001. In total, we assign a systematic error of 0.006 to the measurement of the forward backward asymmetry.

Data 1990		Data 1991	
$\sqrt{s}$ (GeV)	A_{fb}	$\sqrt{s}$ (GeV)	A_{fb}
		91.254	0.037±0.021
88.231	-0.42±0.20	88.480	-0.11±0.13
89.236	-0.09±0.15	89.470	-0.152±0.083
90.238	-0.18±0.11	90.228	-0.137±0.070
91.230	0.07±0.03	91.222	-0.032±0.029
92.226	-0.04±0.10	91.967	0.042±0.063
93.228	0.11±0.12	92.966	0.161±0.079
94.223	0.02±0.13	93.716	0.058±0.082

Table 5.5: Measured forward-backward asymmetry, A_{fb}, of the reaction $e^+e^- \rightarrow \tau^+\tau^-(\gamma)$ for $\zeta < 250$ mrad. Quoted errors are statistical only. The systematic error is estimated to be less than 0.006 (0.01 for 1990 data).

The determination of the asymmetry is carried out in the same way as for the $e^+e^- \rightarrow \mu^+\mu^-(\gamma)$ events, i.e. independent of the acceptance at each value of $\cos\theta$ (see section 5.2.2). The results are summarized in table 5.5 for the different center of mass energies and compared in figure 5.9 to the result of the combined fit (see section 8.4).

Figure 5.10 shows the acceptance corrected angular distribution of the $e^+e^- \rightarrow \tau^+\tau^-(\gamma)$ events collected on the Z peak.

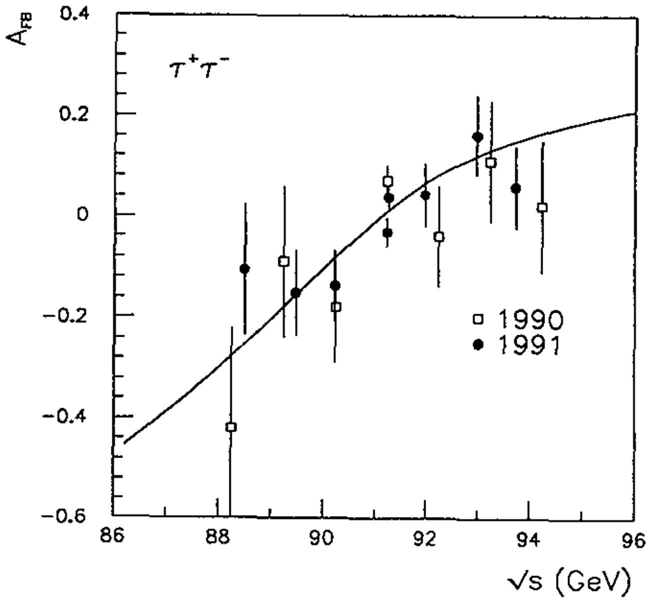

Figure 5.9: The $e^+e^- \rightarrow \tau^+\tau^-(\gamma)$ forward-backward asymmetry as a function of the center of mass energy.

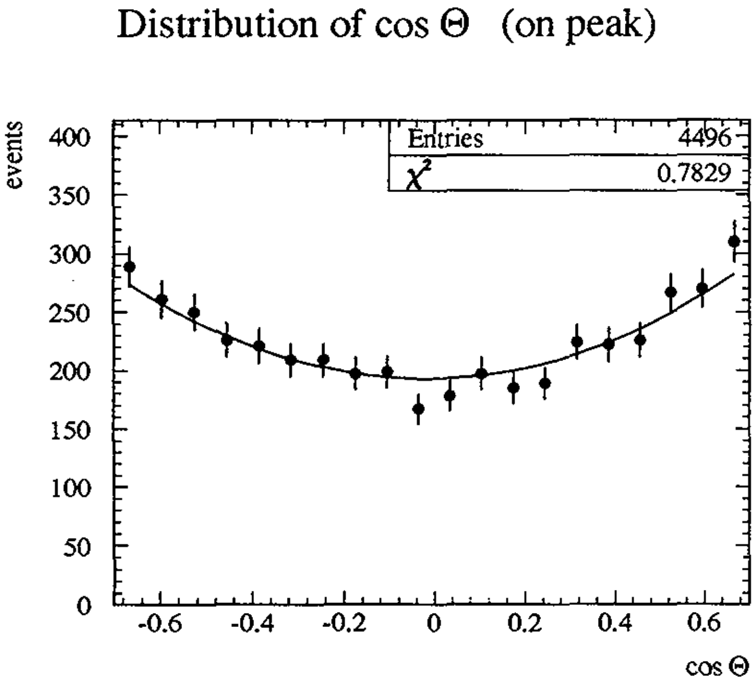

Figure 5.10: The angular distribution of $e^+e^- \rightarrow \tau^+\tau^-(\gamma)$ at the Z peak. The data are compared to the results of a fit using equation 5.2.

5.4 The reaction $e^+e^- \rightarrow e^+e^-(\gamma)$

5.4.1 Cross section

We select $e^+e^- \rightarrow e^+e^-(\gamma)$ events based on the energy deposition in the barrel part of the electromagnetic calorimeter. The fiducial volume for this analysis is thus defined by $44° < \theta < 136°$ which excludes crystals at the edges of the barrel calorimeter. Hadronic Z decays are suppressed requiring that the events have less than 8 reconstructed clusters in the electromagnetic calorimeter. To reject tau pair events, we require that $E_1 > 0.85E_{\text{beam}}$ and $E_2 > 2$ GeV, where E_1 and E_2 are the energies of the two most energetic clusters in the electromagnetic calorimeter. Figure 5.11 illustrates the cut on the most energetic cluster and the good agreement of our data and the Monte Carlo simulation. The acolinearity angle ζ between the two most energetic clusters must be less than 25° to reduce the effect of hard initial state bremsstrahlung. The only sizable background remaining after these cut is a $(1.5\pm0.1)\%$ contamination of $e^+e^- \rightarrow \tau^+\tau^-(\gamma)$ events and a 16.4 pb background of $e^+e^- \rightarrow \gamma\gamma(\gamma)$ events at the Z peak.

Inside the fiducial volume and for $\zeta < 25°$, the acceptance is determined for $e^+e^- \rightarrow e^+e^-(\gamma)$ using events generated with BABAMC [27, 28]. Including detector inefficiencies we find an acceptance of $(99.5 \pm 0.1)\%$. We use events generated with the program BHAGENE [29] to estimate the effects of double radiative events $e^+e^- \rightarrow e^+e^-\gamma\gamma$ on our selection efficiency. The cut on E_1 introduces an additional inefficiency of 0.3% due to the presence of a second hard photon. From variations of the energy, fiducial volume and acolinearity cut we derive a

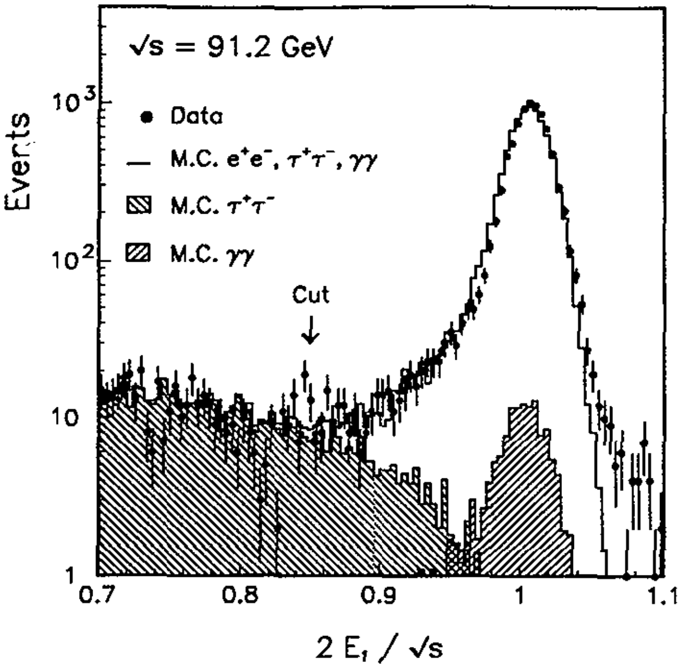

Figure 5.11: The most energetic cluster in the electromagnetic calorimeter compared to $e^+e^- \to e^+e^-(\gamma)$ and background Monte Carlos.

systematic error of 0.3% for the selection of events. Adding the uncertainties from background subtraction (0.1%) and Monte Carlo statistics (0.1%) we assign a systematic error of 0.4% to the corrected number of $e^+e^- \to e^+e^-(\gamma)$ events inside the fiducial volume. The measured cross sections are listed in table 5.6.

The exchange of time-like and space-like photons and Z bosons contribute to the cross section of $e^+e^- \to e^+e^-(\gamma)$. To extract the Z resonance contribution two methods can be used. The measured cross sections in a given fiducial volume can be directly compared to a theoretical calculation which includes all contributing Feynman diagrams, e.g. 40THIEVES [30], ALIBABA [31] or BHAGENE [29]. Alternatively, the ratio $\sigma_s/\sigma_{\mathrm{tot}}$ can be evaluated using the above programs to scale the measured cross sections. After this correction the Z decay into e^+e^- can be treated like the other decay channels. Both methods lead to consistent results.

We use the ALIBABA program to calculate the contributions from the t channel and the interference of the t and s channel. Figure 5.12 shows the total cross section for $44° < \theta < 136°$ and for an acolinearity angle of less than 25°. The measurements are compared to the calculation with ALIBABA using the Standard Model parameters determined in section 8.4. The calculated contributions from s channel and non-s channel are shown separately. Comparing different theoretical calculations we conclude that the non-s channel subtraction and the extrapolation to the full solid angle leads to a systematic error of 0.5%, including the 0.4% experimental error discussed above. The extrapolated cross sections can be found in table 5.6.

Data 1990				
$\sqrt{s}$ (GeV)	N_{events}	$\mathcal{L}$ (nb^{-1})	σ_{tot} (nb)	σ_s (nb)
88.231	120	380.1	0.334±0.030	0.188±0.053
89.236	237	466.3	0.532±0.034	0.473±0.057
90.238	310	359.3	0.894±0.050	1.034±0.082
91.230	3020	2960.9	1.052±0.019	1.462±0.031
92.226	276	397.4	0.715±0.043	1.135±0.071
93.228	198	505.5	0.405±0.029	0.660±0.048
94.223	104	485.7	0.223±0.022	0.348±0.037
Totals	4265	5555.2		

Data 1991				
$\sqrt{s}$ (GeV)	N_{events}	$\mathcal{L}$ (nb^{-1})	σ_{tot} (nb)	σ_s (nb)
91.254	5422	5244.3	1.031±0.014	1.437±0.023
88.480	316	783.5	0.400±0.023	0.291±0.040
89.470	498	862.3	0.573±0.026	0.528±0.044
90.228	632	795.0	0.792±0.032	0.866±0.053
91.222	3295	3080.8	1.067±0.019	1.484±0.030
91.967	591	731.7	0.798±0.033	1.239±0.054
92.966	336	759.9	0.430±0.024	0.701±0.040
93.716	261	832.1	0.302±0.019	0.486±0.032
Totals	11351	13089.6		

Table 5.6: Results on the cross section for the reaction $e^+e^- \to e^+e^-(\gamma)$. σ_{tot} is the acceptance corrected cross section for $44° < \theta < 136°$ and $\zeta < 25°$. σ_s is the s-channel corrected cross section extrapolated to the full solid angle as explained in the text. The quoted errors are statistical only and the overall systematic uncertainty, excluding the 0.6% luminosity uncertainty, in the cross section is 0.4% for σ_{tot} and 0.5% for σ_s.

5.4.2 Forward-Backward Asymmetry

For the measurement of the forward-backward asymmetry we use the polar angle θ of the scattered e^-, as determined from the reconstructed center of the energy cluster in the electromagnetic calorimeter. The angular resolution of 1.2° is dominated by the longitudinal extension of the LEP bunches of about ±1 cm.

The charges of the outgoing particles are determined in the central tracking chamber. We require the two electromagnetic clusters to be matched to tracks within 25 mrad, in the plane transverse to the beam direction. Since the length of an electron or positron track in the central tracking chamber is only $31\mathrm{cm}/\cos\theta$ a measurement of the curvature of each track leads to a momentum resolution of 100% at 45 GeV. This measurement is substantially improved by including the reconstructed impact points of the particles onto the electromagnetic calorimeter.

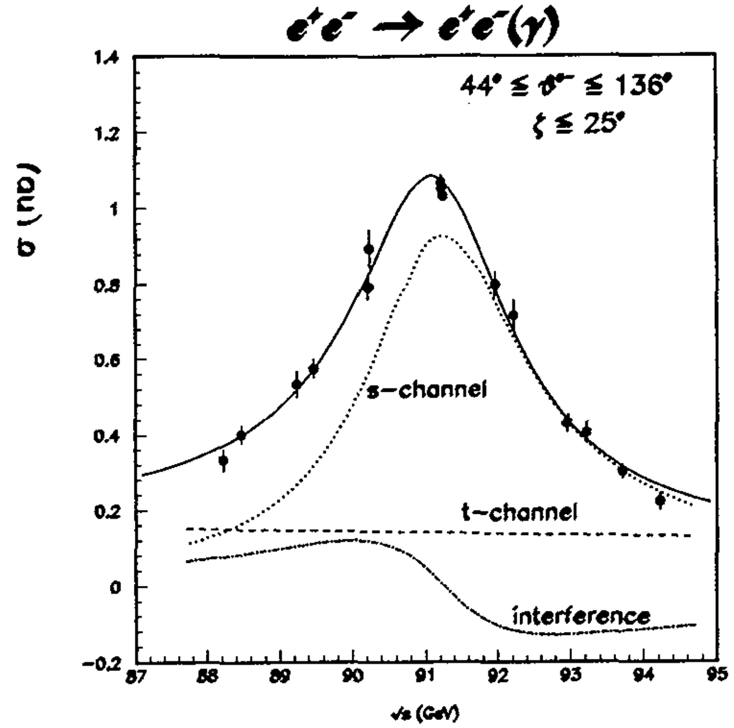

Figure 5.12: The $e^+e^- \rightarrow e^+e^-(\gamma)$ cross section for $44° < \theta < 136°$ and $\zeta < 25°$ compared to the ALIBABA calculation. The contributions from s and t channel are shown separately.

We check this method by applying the same procedure to the selected $e^+e^- \rightarrow \mu^+\mu^-(\gamma)$ sample and comparing the charge assignment of the events by the central tracking chamber and by the muon spectrometer. We find that in $(4.3 \pm 0.3)\%$ of the events the charge is assigned wrongly.

The asymmetry is defined by counting the events in the forward $(44° < \theta < 90°)$ and backward $(90° < \theta < 136°)$ hemispheres. The data are corrected bin-by-bin for the $\cos\theta$ dependent acceptance and charge confusion. The systematic error on the asymmetry is estimated to 0.004. In Table 5.7 the measured asymmetry is given at each energy point. In Figure 5.13 the differential cross section at the Z peak is shown as a function of $\cos\theta$.

The pure s channel forward-backward asymmetry A^s_{FB} can be extracted in a similar way to the muon and tau asymmetries using a likelihood fit. The non-s channel contribution to the angular distributions are parameterized by a function $\Omega(\cos\theta)$ calculated with the help of the ALIBABA program for each $\sqrt{s}$ point. We build the following likelihood function :

$$L \equiv \prod_i \left(\frac{3}{8}(1 + \cos^2\theta_i) + A^s_{FB}\cos\theta_i + \Omega(\cos\theta_i) \right). \tag{5.4}$$

The effects of the charge confusion are taken into account in the likelihood function. The precision of the ALIBABA program and the dependence of $\Omega(\cos\theta_i)$ on the Z and top quark masses lead to an additional systematic error of 0.003 on A^s_{FB}. The extrapolated s channel asymmetries are listed in table 5.7 and shown in Figure 5.14 as a function of $\sqrt{s}$., The numbers are corrected for the acolinearity cut.

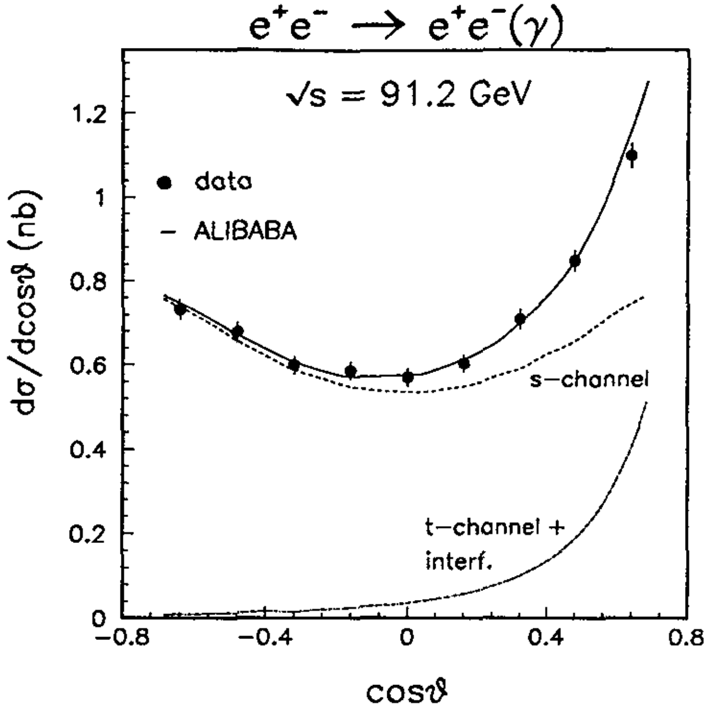

Figure 5.13: The differential cross section of $e^+e^- \rightarrow e^+e^-(\gamma)$ at the Z peak. The data are compared to the ALIBABA program. The contributions from s and t channel are shown separately.

5.5 The reaction $e^+e^- \rightarrow$ hadrons $+ \gamma$

Isolated hard photons produced in hadronic Z decays are mainly associated with radiation from the primary quark-antiquark pair. These events provide information about the electroweak couplings of quarks [32,33], and serve as probes of the short-distance structure of QCD. LEP is an ideal laboratory for this study because the background from photons radiated from the initial state electrons or positrons is strongly suppressed at the Z resonance. Nonetheless, one must still contend with a significant background from high-energy neutral hadrons, mainly π^0 mesons decaying into two unresolved photons.

We select hadronic events according to the criteria in section 5.1, with the additional requirement that the center-of-mass energy be in the range 91.0 – 91.5 GeV, in order to reduce the contribution from initial-state photons and interference between initial and final state radiation.

We identify photon candidates in hadronic events as clusters in the barrel region of the electromagnetic calorimeter where the contribution from initial-state photons is minimal, with energy greater than 5 GeV. We also require that photon candidates are not associated with a charged track, and are isolated by at least 15° from other electromagnetic-calorimeter clusters of energy greater than 500 MeV. Finally, jets are reconstructed from the hadronic part of the event (excluding the photon candidate) using the JADE algorithm [34] with the parameter $y_{\text{cut}} = 0.05$ (see section 10.2.1). We require that photon candidates be isolated by more than 20° from the axis of each reconstructed jet.

Data 1990		
$\sqrt{s}$ (GeV)	$A_{\rm fb}$	$A^s_{\rm fb}$
88.231	0.520±0.095	-0.034±0.276
89.236	0.296±0.070	-0.205±0.161
90.238	0.155±0.064	-0.111±0.107
91.230	0.101±0.021	-0.023±0.028
92.226	0.040±0.069	0.042±0.085
93.228	0.083±0.081	0.053±0.094
94.223	0.144±0.118	0.129±0.148

Data 1991		
$\sqrt{s}$ (GeV)	$A_{\rm fb}$	$A^s_{\rm fb}$
91.254	0.118±0.014	0.001±0.020
88.480	0.504±0.055	-0.013±0.157
89.470	0.312±0.048	-0.126±0.099
90.228	0.206±0.045	-0.100±0.075
91.222	0.129±0.019	0.019±0.027
91.967	0.161±0.047	0.103±0.055
92.966	0.107±0.064	0.098±0.072
93.716	0.185±0.070	0.165±0.085

Table 5.7: Results on the forward-backward asymmetry for the reaction $e^+e^- \to e^+e^-(\gamma)$. $A_{\rm fb}$ is the asymmetry determined from counting in angular range $44° < \theta < 136°$ and for $\zeta < 25°$. A^s_{FB} is the s channel contribution to the forward-backward asymmetry extrapolated to the full solid angle. The systematic error for each energy point is 0.004 on A_{FB} and 0.005 on A^s_{FB}, respectively.

We find 3202 events with isolated hard photon candidates. Monte Carlo studies indicate that in addition to final-state photons radiated from quarks, our sample includes neutral hadrons (mainly π^0) occurring either as single isolated particles or in tight groups of particles that decay into adjacent photons, as well as a smaller fraction of initial-state photons. We estimate the initial-state radiation contribution to be $69 \pm 5(stat) \pm 15(syst)$ events. To study the remaining background from neutral hadrons, we construct a cluster-shape parameter, C, sensitive to the detailed energy sharing between the BGO crystals in an electromagnetic energy cluster [35]. A fit of the C-distributions for JETSET 7.3 signal and background to the data determines a signal of 848 ± 55 events, corresponding to a direct photon ratio between data and JETSET 7.3 of $R_s = 1.14 \pm 0.06$ $(stat)$. For the background, we find $R_b = 1.88 \pm 0.08$ (stat).

The data distributions are corrected for detector effects, acceptance, and initial state radiation. We then correct for the remaining neutral hadron background by subtracting the JETSET prediction scaled by the factor $R_b = 1.88$ mentioned above. We obtain the fraction of hadronic events with photons isolated by more than 20° from jets and with energy greater than 5 GeV to be

$$\mathrm{Br}(\mathrm{Z} \to \mathrm{hadrons} + \gamma)/\mathrm{Br}(\mathrm{Z} \to \mathrm{hadrons}) = (5.2 \pm 0.3 \pm 0.4) \times 10^{-3}, \qquad (5.5)$$

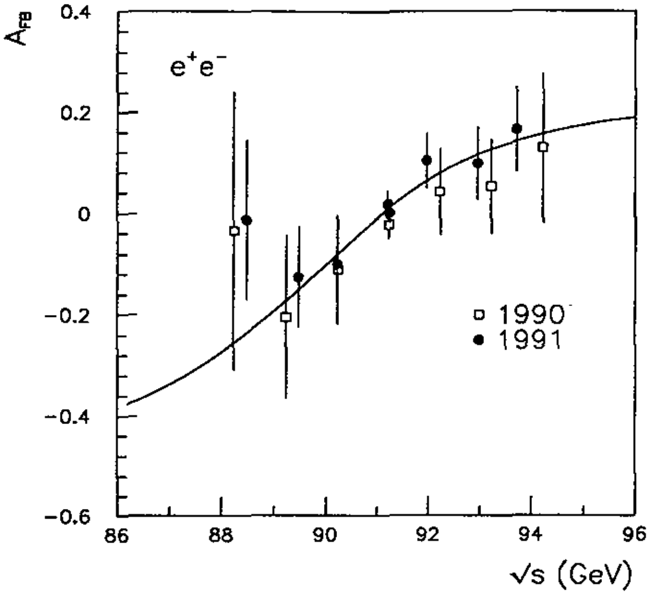

Figure 5.14: The s channel contribution to the $e^+e^- \rightarrow e^+e^-(\gamma)$ forward-backward asymmetry as a function of the center of mass energy.

where the first error is statistical and the second error is systematic. The main contribution to the systematic error stems from the uncertainty in the background subtraction [35]. Our result agrees with those of other LEP collaborations [36]. The measured rate will be used in section 8.7.2 to extract separate electroweak couplings to up-type and down-type quarks.

5.6 The reaction $e^+e^- \longrightarrow \nu\bar{\nu}\gamma$

A direct method for measuring the Z width into neutrinos and thus for counting the number of light neutrino types, is based on the measurement of the cross section for the radiative process $e^+e^- \rightarrow \nu\bar{\nu}\gamma$. The signature of such events is a single photon arising from initial state radiation. Around the Z pole the photons from $\nu\bar{\nu}\gamma$ have low energies with a rapidly falling spectrum.

The measurement is optimally carried out at energies at least 3 GeV above the Z mass where the ratio between the signal and QED background processes is maximum and the full width of the Z resonance is exploited [37, 38]. However, the LEP scanning strategy at the Z resonance [39] has given less favorable conditions for our first measurements, requiring a trigger efficient for low energy photons ($E > 1$ GeV), a good knowledge of the electromagnetic energy scale and tight control of backgrounds.

5.6.1 Experimental Procedure

The signature for the reaction $e^+e^- \rightarrow \nu\bar{\nu}\gamma$ is a single electromagnetic shower and nothing else observed in the detector. Candidates are selected by requiring:

- a single shower in the electromagnetic calorimeter barrel, with $E > 0.9$ GeV and the characteristics of an electromagnetic shower;
- no muon candidate, no track in the central detector and only small energy deposits in the other calorimeters, including the luminosity monitor;
- no cosmic muon emitting a hard bremsstrahlung and faking a single photon event.

These criteria leave us with 291 candidates from the 1991 running periods, corresponding to an integrated luminosity of 9.6 pb^{-1} [20].

Events of this kind are triggerd by the single photon trigger (see section 2.9). The efficiency for this trigger as a function of the photon energy has been calculated by Monte Carlo. The result is shown in Fig. 5.15. The calculation is verified in absolute value as well as energy dependence by observing events from the process $e^+e^- \rightarrow e^+e^-(\gamma)$ with a single large angle electron – selected with criteria analogous to those for the process above – in coincidence with a high energy electromagnetic shower in one of the luminosity monitor calorimeters. The trigger efficiency derived from this sample is also shown in Fig. 5.15 and agrees well with the calculation.

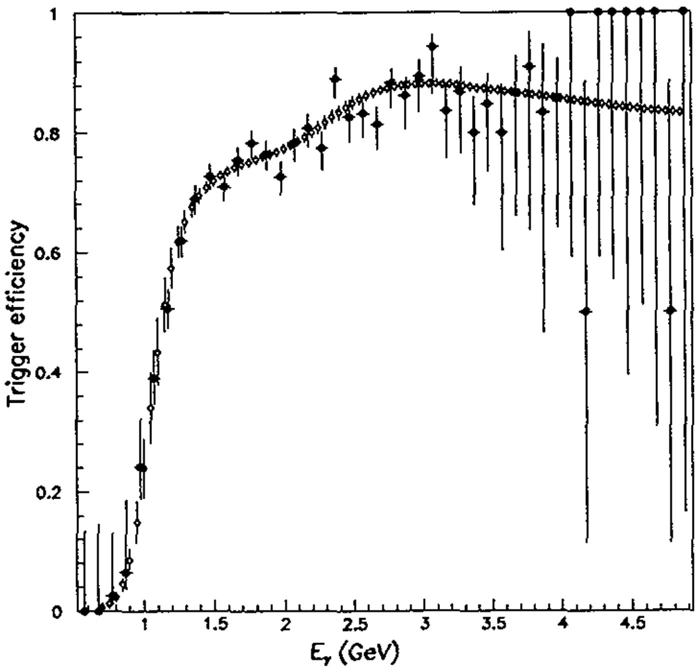

Figure 5.15: The trigger efficiency for $e^+e^- \rightarrow \nu\bar{\nu}\gamma$.

The measurement of this process also verifies the Monte Carlo program [40] used to calculate the dominant background, which comes from the process of radiative Bhabha scattering when only the photon is observed in the detector. It is found that a background of 94 ± 10 events is contained in the abovementioned sample.

Residual background from cosmic rays is estimated from a sample of events where cosmic ray rejection was released. Extrapolation to the tighter criteria used for the final selection leads to an estimated background of 1.0 ± 0.8 events. Other backgrounds from radiative processes are estimated by Monte Carlo calculation. These are photons coming from the decay of resonances produced via two-photon processes and the reactions $e^+e^- \to \gamma\gamma\gamma$ and $e^+e^- \to \mu^+\mu^-\gamma$ (15 ± 4 events). Other backgrounds are found to be negligible.

The measured single photon energy distribution for all center of mass energies is shown in Fig. 5.16 along with Monte Carlo predictions for the process $e^+e^- \to \nu\bar{\nu}\gamma$, assuming three families of light neutrinos, for the $e^+e^- \to e^+e^-\gamma$ background and the sum of all other backgrounds. There is good agreement between data and the prediction.

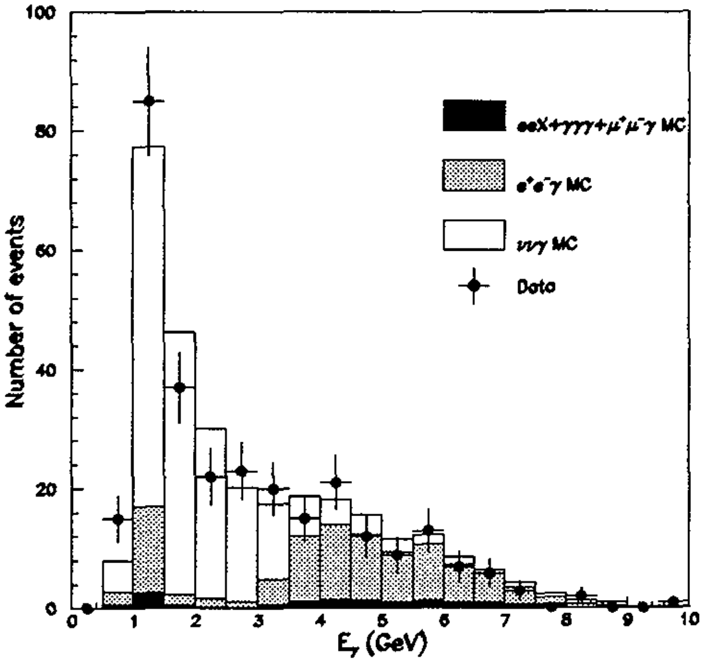

Figure 5.16: Photon energy distribution of $e^+e^- \to \nu\bar{\nu}\gamma$ events.

5.6.2 Cross Section Results

The total cross section is extracted from the number of candidates in the energy range $0.9 < E_\gamma < 3.5$ GeV, where the signal over background ratio is favorable.

For this energy range, table 5.8 shows the luminosity, the number of candidates and the $\nu\bar{\nu}\gamma$ expectations for 3 neutrino families computed with the Monte Carlo NNGSTR [41]. Also

E_{cm} (GeV)	$\mathcal{L}$ (nb^{-1})	N_{observed}	$N^{\nu\bar{\nu}\gamma}_{\mathrm{expected}}$	$N^{\mathrm{e^+e^-}}_{\mathrm{expected}}$	$N^{\mathrm{other\ back.}}_{\mathrm{expected}}$	σ (pb)
88.56	671	6	2.21	1.96	0.35	12^{+12}_{-5}
89.55	772	9	4.27	2.22	0.39	18^{+11}_{-6}
90.25	632	11	5.16	1.78	0.32	31^{+15}_{-8}
91.25	5763	116	92.41	14.42	2.96	37 ± 4
92.04	635	21	17.59	1.72	0.31	64^{+19}_{-12}
93.05	678	26	29.63	1.80	0.33	66^{+17}_{-12}
93.75	419	13	18.35	1.10	0.21	52^{+21}_{-12}
Total	9570	202	169.6	25.0	4.9	

Table 5.8: Luminosity, observed and expected number of events and corrected cross section for $\mathrm{e^+e^-} \to \nu\bar{\nu}\gamma$ at each center of mass energy.

shown is the expected background from radiative Bhabha events and, as other backgrounds, the total number of expected events from two-photon processes, from $\mathrm{e^+e^-} \to \gamma\gamma\gamma$ and from $\mathrm{e^+e^-} \to \mu^+\mu^-\gamma$.

The last column of table 5.8 shows the measured cross sections corrected for acceptances and detector efficiencies for the process $\mathrm{e^+e^-} \to \nu\bar{\nu}\gamma$ when one photon is emitted with energy above 0.9 GeV and a polar angle between 45° and 135° without restrictions on possibly additional photons. The errors are only statistical and take into account the uncertainty in the background subtraction.

We extract the number of light neutrino families N_ν by performing a maximum likelihood fit to the number of candidates shown in table 5.8. We use Poisson probabilities calculated as a function of the expected number of signal plus background events. We compute for each center of mass energy the cross section corresponding to different values of N_ν between 2 and 4 and use a straight line fit to get a parameterization of the cross section dependence on N_ν. We use an improved Born approximation of the analytical calculation of reference 42, which agrees with NNGSTR for $N_\nu = 3$ to better than 1% when a coherent set of input parameters is used. In this approach, we can allow the parameter N_ν to vary while keeping the total width fixed. The cross section $\sigma_0(s)$ can be written as

$$\sigma_0(s) = \frac{12\pi}{m_{\mathrm{Z}}^2} \frac{s\Gamma_{\mathrm{e}} N_\nu \Gamma_{\nu\bar{\nu}}}{(s - m_{\mathrm{Z}}^2)^2 + s^2\Gamma_{\mathrm{Z}}^2/m_{\mathrm{Z}}^2} + \mathrm{W\ terms} \tag{5.6}$$

where $\Gamma_{\nu\bar{\nu}}$ is the decay width of the Z in a neutrino pair with standard model couplings and m_{Z}, Γ_{Z}, and Γ_{e} are our measured values [21], respectively for the Z mass, the total width and the electron partial width. The terms due to W exchange in the t channel and interference between these and the s channel Z exchange contribute less than 3% to the total cross section in the energy range covered here. The results of the fit gives $N_\nu = 3.14 \pm 0.24$ (stat.).

The systematic errors in our analysis come from the determination of the trigger efficiency, which gives an uncertainty of $\Delta N_\nu = \pm 0.04$, from the luminosity measurement, $\Delta N_\nu = \pm 0.03$, the determination of the selection efficiency, $\Delta N_\nu = \pm 0.02$, the background subtraction, $\Delta N_\nu = \pm 0.09$, and the cosmic ray contamination, $\Delta N_\nu = \pm 0.02$. From the errors on our measurements of the Z parameters m_{Z}, Γ_{Z}, and Γ_{e}, from the top mass variation and the theoretical uncertainty on the parameterization of the cross section, we estimate a contribution to the systematic error of $\Delta N_\nu = \pm 0.05$. Adding all these systematic errors in quadrature, our final result is

$$N_\nu = 3.14 \pm 0.24(\text{stat.}) \pm 0.12(\text{syst.}). \tag{5.7}$$

This corresponds to an invisible width of the Z of

$$\Gamma_Z^{\text{inv}} = 524 \pm 40(\text{stat.}) \pm 20(\text{syst.}). \tag{5.8}$$

This is in agreement with our previously published result [43] and with the one published by the OPAL collaboration in a similar analysis [44]. The corrected cross section is shown in figure 5.17 as a function of the c.m. energy along with the expectations from $N_\nu = 2, 3, 4$ and from our best fit.

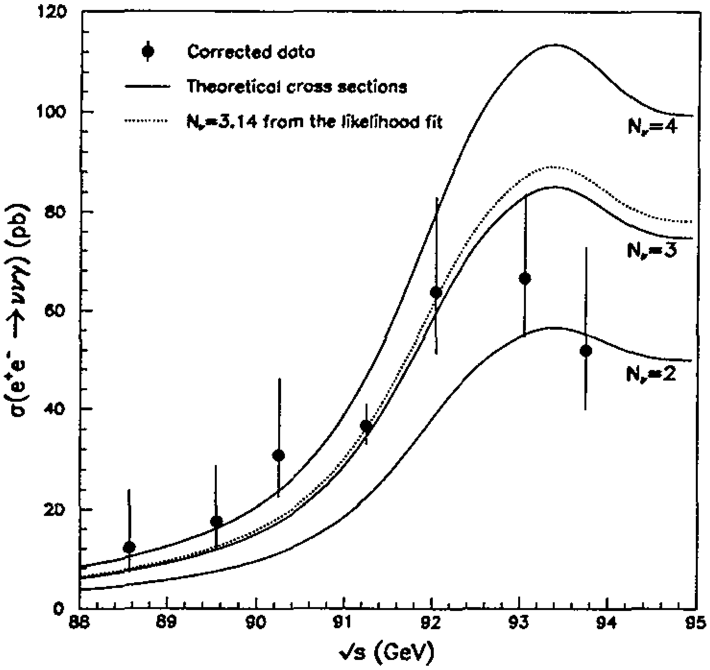

Figure 5.17: Cross section for $e^+e^- \rightarrow \nu\bar{\nu}\gamma$ as a function of the center of mass energy.

Chapter 6

Production and Decay of b Hadrons

The Z branching ratio to b quarks is predicted in the Standard Model to be large, roughly 15% of all Z decays. The Z is thus a copious source of b hadrons. A wide range of them are produced at LEP including B_d^0, B_s^0, $B^\pm$ mesons, and b baryons such as the Λ_b, together with excited b hadrons such as the B^*. In addition they have a large boost resulting in decay lengths of order 2 to 3 mm. In contrast, the B factories at the $\Upsilon(4S)$, CESR and DORIS, where most studies of B mesons have been carried out up to now, do not provide B_s^0 or b baryons and the mesons are produced almost at rest.

The b hadrons allow us to study topics which bear directly on the underlying electroweak theory, and thus to test and constrain the Standard Model. In particular the measurement of the Z partial width into $b\bar{b}$ pairs, $\Gamma_{b\bar{b}}$, provides a precise test of the weak neutral current coupling to b quarks, and of the forward-backward charge asymmetry, $A_{b\bar{b}}$, of b quark production, provides one of the best determinations of $\sin^2\overline{\theta}_W$. In addition, important constraints on the Cabibbo-Kobayashi-Maskawa matrix elements come from the determination of the b hadron lifetime, which together with $Br(b \rightarrow \ell\nu X)$ allows a determination of $|V_{cb}|$, and B^0-$\bar{B}^0$ mixing from the observation of same-sign dilepton events, since B_d^0-$\bar{B}_d^0$ and B_s^0-$\bar{B}_s^0$ rates are related to $|V_{td}|$ and $|V_{ts}|$ respectively. Heavy quark production and decay can also be investigated by measuring the process $b \rightarrow J + X$.

Finally, QCD inspired models developed to describe the hadronization of quark and gluon jets are investigated by measuring the b quark fragmentation function. The events identified as being $Z \rightarrow b\bar{b}$ can be used to measure the strong coupling constant, α_s, for b quarks. In three jet events, they allow a distinction between quark and gluon jets. These last two measurements are discussed in chapter 10.

6.1 Signatures of b hadron events

At LEP b hadrons are produced predominantly via the reaction $Z \rightarrow b\bar{b}$. Due to the hard fragmentation of the b quarks the resulting b hadrons carry typically 70% of the initial b quark momentum, the remainder being taken up by softer hadronic particles. The b quark decays via the weak charged current. In the case that the b decays semileptonically ($b \rightarrow \ell\nu X$), there will be a high momentum charged lepton and missing energy due to the undetected neutrino. Due to the high mass of the b quark the products of the b hadron decay have a large transverse momentum with respect to the initial parton direction, of order ~ 1.2 GeV.

To select $b\bar{b}$ events there are four main signatures:

- jets containing high momentum leptons having also high transverse momentum with respect to the remainder of the jet;
- jets with high momentum leading particles and missing energy;
- secondary vertices at a decay length of a few mm;
- jets containing J mesons identified by their leptonic decays, $J \rightarrow e^+e^-$ and $J \rightarrow \mu^+\mu^-$, since, at LEP energies, the J mesons are mainly produced in b decays.

We use the first of these signatures to select events containing b hadrons. In figure 6.1 we show the measured momentum, p, and transverse momentum, p_t distributions for electrons and muons for data and Monte Carlo events. The transverse momentum is defined with respect to the nearest jet, where the measured energy of the lepton is excluded from the jet. If there is no jet with an energy greater than 6 GeV remaining in the same hemisphere as the lepton, then the p_t is calculated relative to the thrust axis of the event. It can be seen that for leptons with momenta greater than ~ 4 GeV the high p_t sample arises predominantly from $b\bar{b}$ events. Depending on the analysis requirements, a p_t cut can be set to give a $b\bar{b}$ purity of more than 80%.

The Monte Carlo events have been generated using the parton shower program JETSET 7.3 [22] with string fragmentation [45] and full detector simulation [15]. For the simulation we have used the central values of the experimentally determined semileptonic branching ratios and fragmentation parameters for b and c quarks [46,47]: $\mathrm{Br}(b \rightarrow \ell\nu X) = 0.117$, $\mathrm{Br}(c \rightarrow \ell\nu X) = 0.096$, $\epsilon_b^z = 0.008$ and $\epsilon_c^z = 0.07$.

Muons are identified and measured in the muon chamber system by reconstructing a track with segments in at least two of the three layers The muon track should point back to within 4σ of the interaction point in transverse and longitudinal distance of closest approach. The measurement error is dominated by the multiple scattering in the calorimeters and has a typical value of $\sigma \approx 25$ mm. These requirements are very effective in reducing the backgrounds from hadron punchthrough and from π and K decays. We accept muons in the polar angle range $36° < \theta_\mu < 144°$.

Electrons are found by associating clusters in the electromagnetic calorimeter with charged tracks in the central tracking chamber. We require that the lateral shower shape of these clusters is consistent with that of an electromagnetic shower. The centroid of this cluster is required to be well matched in azimuthal angle with a charged track. A major source of background, that of charged particles overlapping with energetic photons or π^0's, is rejected by requiring that the cluster energy and the momentum of the track match to within 4σ. Finally, we further reject hadrons by requiring that the energy behind the electron candidate in the hadron calorimeter is small. We accept electrons in the polar angle range $42° < \theta_e < 138°$.

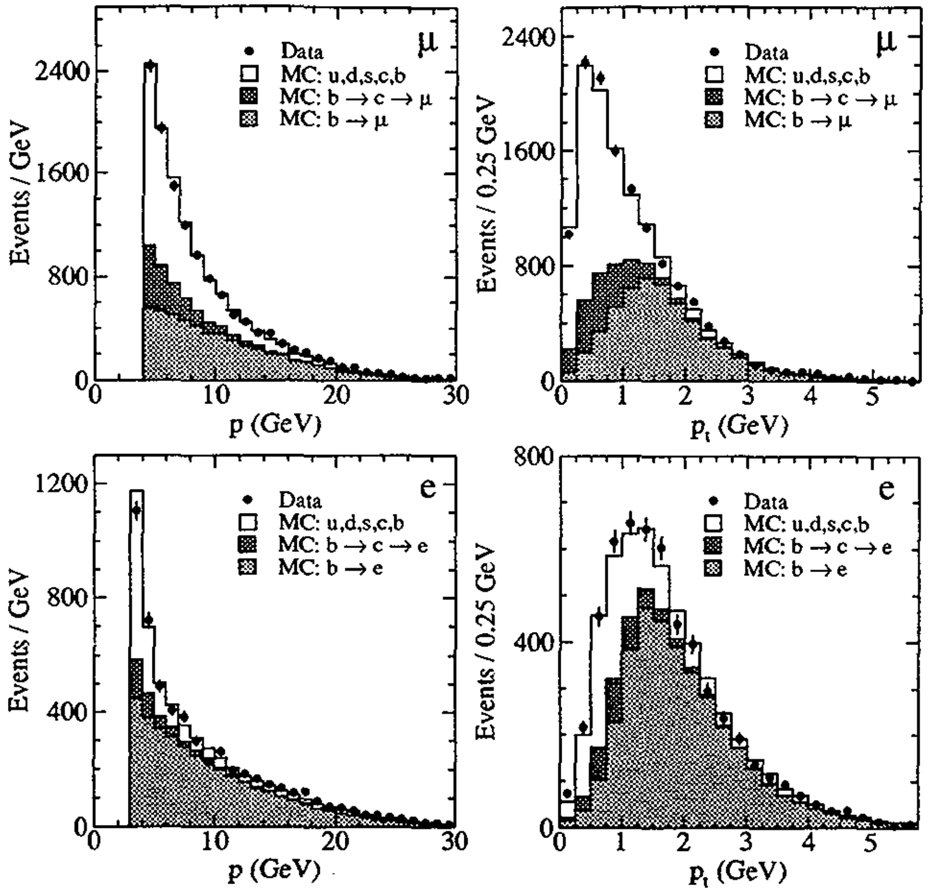

Figure 6.1: The p and p_t distributions for electrons and muons for data and Monte Carlo. Only leptons with a momentum greater than 3 GeV are entered into the p_t plots.

6.2 b hadron decay properties

6.2.1 Measurement of the fragmentation parameter

This analysis is based on approximately 115,000 hadronic Z decays recorded in the 1990 running period [47].

Fragmentation describes the process via which the primordial quark-antiquark pairs produced in the Z decay materialize as hadrons. This process is described by QCD, yet due to the presence of both perturbative and nonperturbative effects, is not rigorously understood quantitatively. Heavy quark processes are the simplest system in which to study hadronization mechanisms since heavy quark-pair production is suppressed in the jet evolution.

We use the lepton p and p_t distributions to determine the energy spectrum of the b hadrons [47]. The major source of systematic error in this determination comes from uncertainties in the mass spectrum of the b hadron decay products, which influences the lepton momenta. We have paid particular attention to the $D_2^*(2460)$ decay of the B mesons which, due to the high mass of the D_2^* meson, can substantially modify the lepton energy spectra. We determine the b hadron energy spectrum in terms of the scaled energy variable $x_E = 2E_{\text{hadron}}/\sqrt{s}$. We choose this variable as it can be directly measured and because its definition is independent of fragmentation models. We have found that the Peterson *et al.* [48] fragmentation function gives a reasonable parameterization of our observed scaled energy distribution, and for this reason we have used this function to determine $\langle x_E \rangle$ for b hadron production at the Z. The function was originally expressed in terms of the fractional "energy" of the primordial quark, $z = \frac{(E+p_{\parallel})_{hadron}}{(E+p_{\parallel})_{quark}}$:

$$f(z) = \frac{N}{z}\left(1 - \frac{1}{z} - \frac{\epsilon_q^z}{1-z}\right)^{-2} \tag{6.1}$$

where N is a normalization constant and ϵ_q^z is a free parameter. However, the primordial quark energy is difficult to determine experimentally as the quarks can radiate gluons before hadronizing. We therefore us the same form as equation 6.1, replacing z by x_E and ϵ_q^z by ϵ_q.

We first perform a study to check that the function $f(x_E)$ gives an adequate representation of the x_E distribution. We determine the b quark fragmentation function from the data without assuming a functional form and compare the result with the Peterson *et al.* function. For this test we use only the inclusive muon sample. The x_E distribution is approximated by a histogram with 7 bins, and the value for each bin is allowed to vary freely in the fit. The fit is constrained to enforce overall normalization of the fragmentation function. We perform a six parameter fit in the allowed range $x_E \geq 2m_b/\sqrt{s} \approx 0.1$. The points with error bars (statistical only) in figure 6.2 give the result of the fit. From this fit we obtain $\langle x_E \rangle = 0.680 \pm 0.011$, where the error is statistical only and includes correlations between all the points. Figure 6.2 also shows, for comparison, the Peterson *et al.* function for $\epsilon_b = 0.05$. The measured fragmentation function agrees, within errors, with this form.

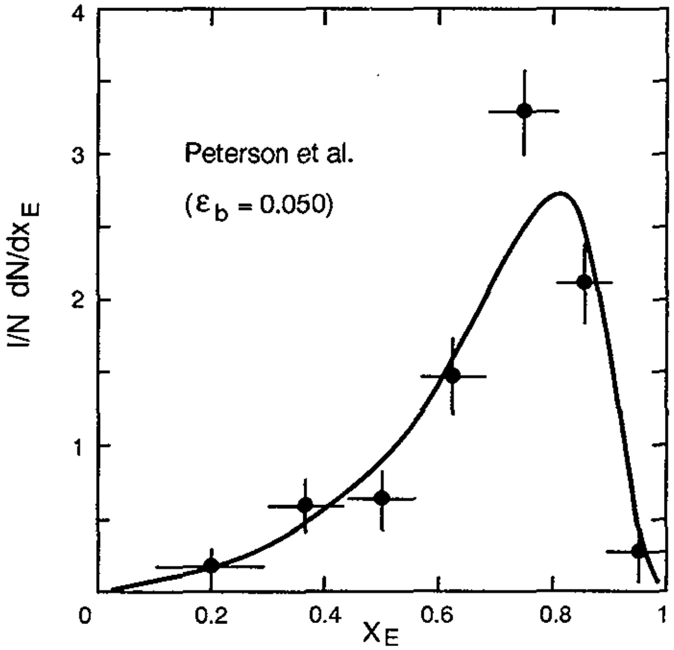

Figure 6.2: Measured b quark fragmentation function $f(x_E)$. The data points with errors are derived from a 6 parameter fit to the inclusive muon data. The solid line shows the Peterson *et al.* function for $\epsilon_b = 0.050$.

We have also performed a fit to our measured lepton momentum and transverse momentum spectra to determine the parameter ϵ_b. In the fit we vary ϵ_b and weight the x_E distribution of the Monte Carlo events accordingly. The result of the fit is

$$\epsilon_b = 0.050 \pm 0.004 \text{ (stat.)} \pm 0.010 \text{ (sys.)}, \tag{6.2}$$

which gives a determination of the average energy fraction of b hadrons:

$$\langle x_E \rangle = 0.686 \pm 0.006 \text{ (stat.)} \pm 0.016 \text{ (sys.)}. \tag{6.3}$$

The dominant source of error is the uncertainty in $\text{Br}(b \to \ell\nu X)$ which contributes 0.006 to the systematic error on ϵ_b [47].

We have also measured the b quark fragmentation function using events with J mesons, see section 6.5.3.

6.2.2 Measurement of the b hadron semileptonic branching ratio

This analysis is based on approximately 115,000 hadronic Z decays recorded in the 1990 running period [47].

The b semileptonic branching ratio, $\text{Br}(b \to \ell\nu X)$ has been measured in two ways:

- from the ratio of dilepton to single lepton events;
- from the total rate of lepton events, assuming the Standard Model value for $\Gamma_{b\bar{b}}$.

In the first method the ratio of dilepton to single lepton events is, to first order, proportional to the semileptonic branching ratio and independent of $\Gamma_{b\bar{b}}$. For dilepton events we require that the opening angle between the leptons be larger than 60°. We find the following results from this measurement:

$$\begin{aligned} \text{Br}(b \to \mu\nu X) &= 0.113 \pm 0.012 \text{ (stat.)} \pm 0.006 \text{ (sys.)} \quad (6.4) \\ \text{Br}(b \to e\nu X) &= 0.138 \pm 0.032 \text{ (stat.)} \pm 0.008 \text{ (sys.)}. \quad (6.5) \end{aligned}$$

The sources of the systematic errors are shown in table 6.1.

When we include the $e\mu$ events and perform a combined fit of the muon and electron events we obtain the average b semileptonic branching ratio:

$$\text{Br}(b \to \ell\nu X) = 0.113 \pm 0.010 \text{ (stat.)} \pm 0.006 \text{ (sys.)}. \tag{6.6}$$

This result agrees well with the results from PEP and PETRA measurements [46], and we have combined our measurements with these to obtain:

$$\text{Br}(b \to \ell\nu X) = 0.117 \pm 0.006 \tag{6.7}$$

where the statistical and systematic errors have been added in quadrature. This average is nearly independent of assumptions about neutral current couplings to b quarks. Our result

Parameter	Variation	$\Delta\mathrm{Br}(\mathrm{b} \to \mathrm{e}\nu\mathrm{X})$	$\Delta\mathrm{Br}(\mathrm{b} \to \mu\nu\mathrm{X})$
$\Gamma_{\mathrm{b\bar{b}}} = 378$ MeV	±40 MeV	±0.002	±0.002
$\mathrm{Br}(\mathrm{c} \to \ell\nu\mathrm{X}) = 0.096$	±0.006	±0.001	±0.002
ϵ_b=0.050	±0.004	±0.002	±0.002
ϵ_c=0.5	±0.1	< 0.001	< 0.001
background	±10%	±0.001	± 0.001
selection efficiencies (μ)	±0.5%	-	±0.001
selection efficiencies (e)	±3%	±0.006	-
p_t cut	±0.25 GeV	±0.003	±0.002
$\mathrm{D}_2^*(2460)$ fraction = 0.15	±0.15	±0.002	±0.002

Table 6.1: The contributions to the systematic error in the measurement of $\mathrm{Br}(\mathrm{b} \to \mathrm{e}\nu\mathrm{X})$ and $\mathrm{Br}(\mathrm{b} \to \mu\nu\mathrm{X})$ from the ratio of the number of dilepton to single lepton events.

depends only weakly on $\Gamma_{\mathrm{b\bar{b}}}$, and the PEP and PETRA results have been obtained at lower center of mass energies where electroweak effects contribute less than 3% to the $\mathrm{e^+e^-} \to \mathrm{b\bar{b}}$ cross section. It is this combined average that we use in section 6.4 to determine $\Gamma_{\mathrm{b\bar{b}}}$.

In the second method we perform a one-parameter fit to determine $\mathrm{Br}(\mathrm{b} \to \ell\nu\mathrm{X})$ using the Standard Model value for $\Gamma_{\mathrm{b\bar{b}}}$ of 378 MeV [26]. This method mainly relies on the number of single lepton events, in contrast to the first method, where the statistical error is dominated by the number of dilepton events.

The result of the fit is:

$$\begin{aligned} \mathrm{Br}(\mathrm{b} \to \mu\nu\mathrm{X}) &= 0.123 \pm 0.003\ (\mathrm{stat.}) \pm 0.006\ (\mathrm{sys.}), && (6.8) \\ \mathrm{Br}(\mathrm{b} \to \mathrm{e}\nu\mathrm{X}) &= 0.112 \pm 0.004\ (\mathrm{stat.}) \pm 0.008\ (\mathrm{sys.}). && (6.9) \end{aligned}$$

From a combined fit to electron and muon data we obtain:

$$\mathrm{Br}(\mathrm{b} \to \ell\nu\mathrm{X}) = 0.119 \pm 0.003\ (\mathrm{stat.}) \pm 0.006\ (\mathrm{sys.}). \tag{6.10}$$

6.2.3 Measurement of the average b hadron lifetime

This analysis is based on approximately 115,000 hadronic Z decays recorded in the 1990 running period [49].

We determine the lifetime of b hadrons from a maximum likelihood fit to the impact parameter distribution of the inclusive leptons from semileptonic b decays. Since the b hadrons are not fully reconstructed in this analysis, we measure their average lifetime, weighted by their production rates in the Z decay and by their semileptonic branching ratios. Measurements at lower center of mass energies [50] indicate that the lifetime difference between the B^0 and B^+ mesons is small, which is in agreement with the prediction of the spectator model [51].

The b hadron lifetime is determined from a measurement of the signed impact parameter of the selected lepton candidate tracks. The impact parameter is defined as the distance of closest approach of the lepton track to the estimated primary production vertex. We use the projected impact parameter, δ, in the plane transverse to the beam ($r-\phi$ projection), because the beam size is smaller and the spatial resolution of the tracking chamber is better in this plane than along the beam axis. An advantage of the impact parameter method is that the measured lifetime is not sensitive to the b hadron momentum and hence to a precise knowledge of the b quark fragmentation parameters. The b hadron direction is approximated by the thrust axis. The impact parameter is taken to be positive if the lepton track intersects with the event thrust axis in the apparent flight direction of the b hadron, and is taken to be negative if it intersects opposite to this direction. The negative values are a consequence of the experimental resolution and of the approximation of the b hadron direction by the thrust axis. Uncertainties in the measurement of the impact parameter can result from the following sources:

- the uncertainty in the position of the primary vertex;
- the error from the track reconstruction;
- the multiple scattering in the beryllium beampipe and TEC inner wall.

Since the e^+e^- collision point is not known on an event-by-event basis, its average position is taken to be the primary vertex. It is determined for each LEP fill from good quality tracks in hadronic events with a statistical precision of a few microns. From the variation in the measurement of the beam position within a LEP fill, which includes the effects of changes in the beam steering, we estimate an upper limit of 36 μm on the systematic error of the beam position determination.

The experimental resolution in δ and the size of the beam spot are found using high momentum tracks in the reactions $e^+e^- \to e^+e^-$ and $e^+e^- \to \mu^+\mu^-$. The resolution is determined by measuring the distance, d, in the $r-\phi$ plane between the two tracks at the primary vertex. From the r.m.s. of this distribution, σ_d, we obtain the average experimental resolution in the distance of closest approach, $<\sigma_{\rm exp}>=\sigma_d/\sqrt{2}=144\pm 1$ μm for particle momenta of ≈ 45 GeV, where the error is statistical only.

For a given azimuthal angle, the width of the impact parameter distribution of tracks originating from the primary vertex measures the projected size of the beam spot, folded with the resolution in δ. Subtracting in quadrature $<\sigma_{\rm exp}>$ from the r.m.s. of the δ distribution, we determine an r.m.s. beam spot size of $\sigma_x = 196\pm 5$ μm in the horizontal direction and $\sigma_y = 24\pm 25$ μm in the vertical direction. The determination of the b hadron lifetime is relatively insensitive to the exact value of the beam spot size.

For lower momentum tracks, a small additional contribution from multiple scattering in the beryllium tubes must be taken into account. This can be parameterized as a function of the track momentum p by $\sigma_{\rm mult} = 83\mu{\rm m}/p$ [GeV].

The total error on the measured distance of closest approach, σ_δ, can then be written as:

$$\sigma_\delta^2 = \sigma_{\rm exp}^2 + \sigma_{\rm mult}^2 + \sigma_x^2 sin^2\phi + \sigma_y^2 cos^2\phi, \tag{6.11}$$

where ϕ is the azimuthal angle of the track. The experimental error, $\sigma_{\rm exp}$, is taken from the covariance matrix of the track fit for each lepton candidate.

Category	muons	electrons
1: prompt b→ ℓ	82.1%	84.4%
2: cascade ℓ	5.3%	4.3%
3: prompt c→ ℓ	4.5%	1.7%
4: decay π,K → ℓ	1.2%	0.2%
5: misid. hadrons	6.9%	9.4%

Table 6.2: Monte Carlo estimates of the fraction of each lepton category in the data.

We determine the lifetime of b hadrons, τ_b, using a binned maximum likelihood fit to the measured impact parameter distribution, taking into account the expected contributions of the lepton categories listed in table 6.2.3. The impact parameter distributions for the prompt and cascade lepton sources depend on the lifetime of the parent hadrons. The impact parameter distributions for the five lepton sources are obtained from the data or from Monte Carlo simulations. The measured impact parameter distribution is shown in Figure 6.3. The preponderance of positive values, as seen from the measured mean of 176 ± 20 μm, is due to the lifetime of the b hadrons. The fit is performed simultaneously for the muon and electron δ distributions over the range $|\delta| < 3$ mm, using a bin size of 0.2 mm. The result of the fit is $\tau_b = 1.32 \pm 0.08$ ps, where the error is statistical only. The expected impact parameter distribution for this value of τ_b is shown in Figure 6.3 as a solid line, in good agreement with the measurement. The calculated χ^2 per degree of freedom is 54/59. The contributions from the different lepton sources are also shown in the figure.

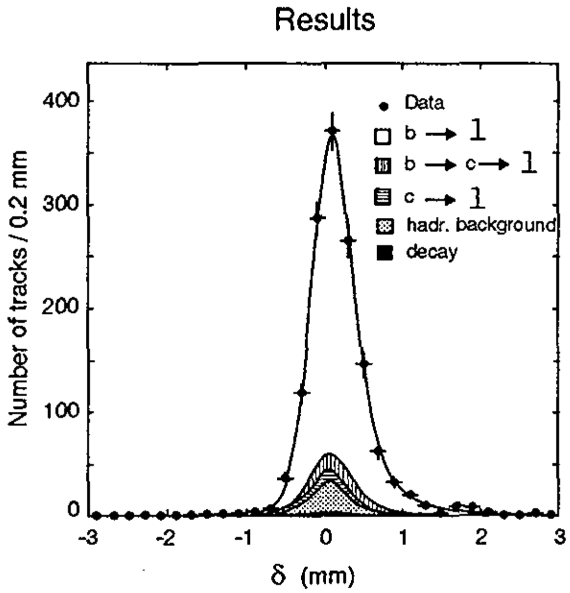

Figure 6.3: The impact parameter distribution of the lepton candidate tracks from the data, with the result of the fit superimposed. The contributions from the various lepton categories are shown by the shaded curves.

We have performed several consistency checks to verify the analysis and the fitting procedures. As a necessary check of the method, Monte Carlo events were generated with various b hadron lifetimes over a range from 0.5 to 1.5 ps. The events are analyzed in the same manner as the data. The measured b hadron lifetime obtained for each sample is found to be in good agreement with the generated lifetime. To check for biases, we also repeat the analysis for different subsets of the data. Within the statistical errors, all these subsample results are compatible with each other.

We estimate a total systematic error of 0.09 ps. The dominant source (±0.05 ps) is due to uncertainty in the parameterization of the prompt $b \rightarrow \ell$ decays. Thus the b hadron lifetime is determined to be:

$$\tau_b = 1.32 \pm 0.08 \text{ (stat.)} \pm 0.09 \text{ (sys.) ps.} \qquad (6.12)$$

6.2.4 Determination of the CKM matrix element $|V_{cb}|$

In the Standard Model, the dominant decay of hadrons containing a b quark proceeds through a flavor changing transition from the b quark to a c or u quark, with a strength described by the elements V_{cb} and V_{ub} of the Cabibbo-Kobayashi-Maskawa (CKM) matrix [52]. Our measurement of the b hadron lifetime, $\tau_b = 1.32 \pm 0.08 \pm 0.09$ ps, combined with that of the semileptonic branching ratio, $\text{Br}(b \rightarrow \ell\nu X) = 0.119 \pm 0.003 \pm 0.006$, can be used to extract the magnitude of the CKM matrix element $|V_{cb}|$.

The semileptonic decay width of b hadrons, which is obtained from the semileptonic branching ratio and the lifetime, is related to the CKM matrix elements by:

$$\Gamma(b \rightarrow \ell\nu X) = \frac{\text{Br}(b \rightarrow \ell\nu X)}{\tau_b} = \frac{G_F^2 m_b^5}{192\pi^3} \ (f_c \ |V_{cb}|^2 + f_u \ |V_{ub}|^2). \qquad (6.13)$$

The parameters $f_{q(q=u,c)}$ account for quark mass effects and QCD corrections, and can be approximated by [53]:

$$f_q \simeq (1 - 8\epsilon_q^2 + 8\epsilon_q^6 - \epsilon_q^8 - 24\epsilon_q^4 \ln \epsilon_q) \ (1 - \frac{2}{3}\frac{\alpha_s(m_b^2)}{\pi}[(\pi^2 - \frac{31}{4})(1 - \epsilon_q)^2 + \frac{3}{2}]), \qquad (6.14)$$

where $\epsilon_q = m_q/m_b$.

To calculate f_c and f_u, we use the following quark mass values, which were obtained by the ARGUS Collaboration in the framework of the ACCMM [54] model from a fit to the lepton momentum spectrum in semileptonic B meson decays [55]: $m_b = 4.95 \pm 0.07$ GeV and $m_b - m_c = 3.30 \pm 0.02$ GeV. In order to include uncertainties in the model, we increase the error on m_b to ±0.3 GeV and take $m_u = 0.2 \pm 0.2$ GeV, keeping the above error on $m_b - m_c$. We use the value $\alpha_s(m_b^2) = 0.20 \pm 0.03$, which has been obtained from extrapolating our measured value at $\sqrt{s} \approx m_Z$, $\alpha_s = 0.124 \pm 0.005$ (see section 10.2.6), to $Q^2 = m_b^2$. By using the ARGUS measurements, we assume that, in accordance with the spectator model, the light B mesons produced at the $\Upsilon(4S)$ have the same semileptonic widths as the heavier b hadrons that can be produced in the Z decays.

Taking our measured values for τ_b and the b hadron semileptonic branching ratio, we show in figure 6.4 the corresponding curve in the $|V_{ub}|$ versus $|V_{cb}|$ plane. The solid curved line corresponds to the central values of our measurements, and the dashed lines represent the one standard deviation errors, where the statistical and systematic errors have been added in quadrature. The systematic error has contributions from our measurements, from the uncertainties in the quark masses and α_s. Because of the anti-correlation between m_b and f_c, the factor ($m_b^5\, f_c$) in equation 6.13 varies by only ±12% over the m_b range from 4.65 to 5.25 GeV, for the above error of ±0.02 GeV on $m_b - m_c$. This is to be compared with the ±30% change in m_b^5 alone. However, there is much less of an anti-correlation between m_b and f_u. This explains the widening of the errors in Figure 6.4 when going from the $|V_{cb}|$ axis to the $|V_{ub}|$ axis.

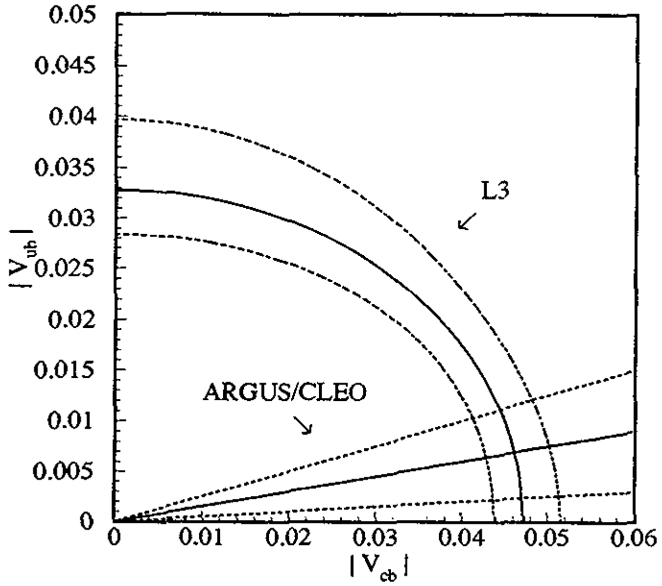

Figure 6.4: The contour plot of $|V_{ub}|$ versus $|V_{cb}|$. The solid curve comes from our measurement of the b hadron lifetime and the semileptonic branching ratio. The solid straight line corresponds to the ARGUS/CLEO measurement of $|V_{ub}|/|V_{cb}|$. The dashed lines are the one standard deviation errors, including the theoretical uncertainties.

To determine $|V_{cb}|$, one needs information about the ratio $|V_{ub}|/|V_{cb}|$. Measurements of the endpoint of the lepton momentum spectrum from B meson semileptonic decays [56, 57] determine this ratio to be small. Model dependent values for $|V_{ub}|/|V_{cb}|$ in the range from 0.1 to 0.2 are obtained. For our analysis, we use the value of $|V_{ub}|/|V_{cb}| = 0.15 \pm 0.10$. This ratio produces the solid straight line shown in Figure 6.4. The dashed lines again correspond to the estimated error on the ratio. The two solid curves meet at a value

$$|V_{cb}| = 0.046 \pm 0.002\ ^{+0.004}_{-0.003}, \qquad (6.15)$$

where the first error is due to our statistical and systematic errors added in quadrature, and the second is due to uncertainties in the theory, including the errors on $|V_{ub}|/|V_{cb}|$, the quark masses and α_s. This determination of $|V_{cb}|$ is relatively insensitive to the exact value of $|V_{ub}|/|V_{cb}|$. Varying the ratio from 0.05 to 0.25, changes the value of $|V_{cb}|$ by only $^{+0.001}_{-0.002}$.

6.2.5 Measurement of B^0-$\bar{B}^0$ mixing.

In the Standard Model the transformation of a B_d^0 or B_s^0 meson into its antiparticle proceeds via a weak flavor-changing box diagram, dominated by virtual top quark exchange. The rate of mixing depends on the Cabibbo-Kobayashi-Maskawa matrix elements, V_{td} and V_{ts}, and the top quark mass. A distinctive experimental signature of B^0-$\bar{B}^0$ mixing is the observation of like sign dileptons from the decays $B^0 \rightarrow \ell^+$ and $\bar{B}^0 \rightarrow B^0 \rightarrow \ell^+$. The amount of mixing may be expressed as

$$\chi_B = \frac{Br(b \rightarrow \bar{B}^0 \rightarrow B^0 \rightarrow \ell^+ X)}{Br(b \rightarrow b\ \text{hadron} \rightarrow \ell^\pm X)} \tag{6.16}$$

assuming equal semileptonic branching ratios for all hadrons containing a b quark. Measurements of χ_B at the Z resonance are sensitive to both B_d^0 and B_s^0 mixing, *i.e.* $\chi_B = f_d\chi_d + f_s\chi_s$, where χ_d and χ_s are the mixing parameters and f_d and f_s are the production fractions of B_d^0 and B_s^0 mesons. Previous measurements of the χ_B parameter have been made at proton colliders [58–60] and at e^+e^- colliders at the $\Upsilon(4S)$ [61–63] as well as at the Z [64–67]. At the $\Upsilon(4S)$ no B_s^0 mesons are produced, thus allowing an independent direct measurement of χ_d.

The signature of B^0-$\bar{B}^0$ mixing is hadronic events with two leptons of the same charge on opposite sides of the event. The angle between the two leptons is required to be larger than 60° to ensure that both leptons are from different b hadron decays. In our sample there are 1303 inclusive dilepton events; in 540 of these, both leptons have $p_t > 1$ GeV. We also observe 91 events with three inclusive leptons. They are considered in this analysis by using the two leptons with largest transverse momentum with respect to the nearest jet axis.

The number of events and their distribution in various categories is shown in table 6.3. More details are given in reference 68.

charges	$\mu\mu$	ee	$e\mu$	all
$\ell^+\ell^+$ all p_t	167	17	98	282
$\ell^+\ell^+$ $p_t > 1$ GeV	40	14	32	86
$\ell^-\ell^-$ all p_t	110	20	84	214
$\ell^-\ell^-$ $p_t > 1$ GeV	30	12	31	73
$\ell^+\ell^-$ all p_t	458	65	284	807
$\ell^+\ell^-$ $p_t > 1$ GeV	165	51	165	381
$\ell\ell$ all p_t	735	102	466	1303
$\ell\ell$ $p_t > 1$ GeV	235	77	228	540

Table 6.3: The numbers of dilepton events in the data.

From the Monte Carlo simulation of $Z \rightarrow b\bar{b}$ events we expect that the event sample of table 6.3 consists mainly of events with two prompt b hadron decays. The estimated fractions from various sources are listed in table 6.4 for $p_t > 1$ GeV.

We have reported [64,68] three different methods to measure the mixing parameter χ_B. One is based on counting the number of high p_t dilepton events with the same charge. We have also used two different fitting methods: a 4 dimensional fit to the p and p_t spectra of the dileptons, and a factorized two dimensional fit to the p_l and p_t distributions, where p_l is the component of the lepton momentum along the jet axis. The first fit uses the full information of the event, but requires large Monte Carlo statistics to accurately determine the probability functions. The second fit has the advantage that single lepton events can be used to determine the probability functions, so fewer Monte Carlo events are needed. We give results for this last method here.

	Category	$\mu\mu$	ee	$e\mu$
1	$b \to \ell$, $b \to \ell$	72.6	79.8	80.9
2	$b \to c \to \ell$, $b \to c \to \ell$	0.5	0.0	0.2
3	$b \to \ell$, $b \to c \to \ell$	16.1	11.2	11.6
4	$b \to \ell$, $b \to X$	7.2	8.2	5.2
5	$b \to c \to \ell$, $b \to X$	1.0	0.7	1.0
6	$b \to X$, $b \to X$	0.5	0.0	0.4
7	$c \to \ell$, $c \to \ell$	0.8	0.0	0.2
8	other sources	1.3	0.0	0.4

Table 6.4: Monte Carlo estimates of the fractions (in %) of various event categories for $p_t > 1$ GeV. X indicates a misidentified hadron or leptons from light hadron decays. The $b \to \ell$ fraction includes $b \to \tau \to \ell$ and $b \to \bar{c} \to \ell$ decays, which give a right sign lepton.

The other methods yield results compatible within errors, but the factorized fit method gives the smallest systematic error.

In this fit method, probability functions are assumed to factorize, and are therefore evaluated independently (using the single lepton data and Monte Carlo) for each lepton as a function of p_l and p_t, The p_l and p_t distributions for like sign and opposite sign dileptons are shown in figure 6.5.

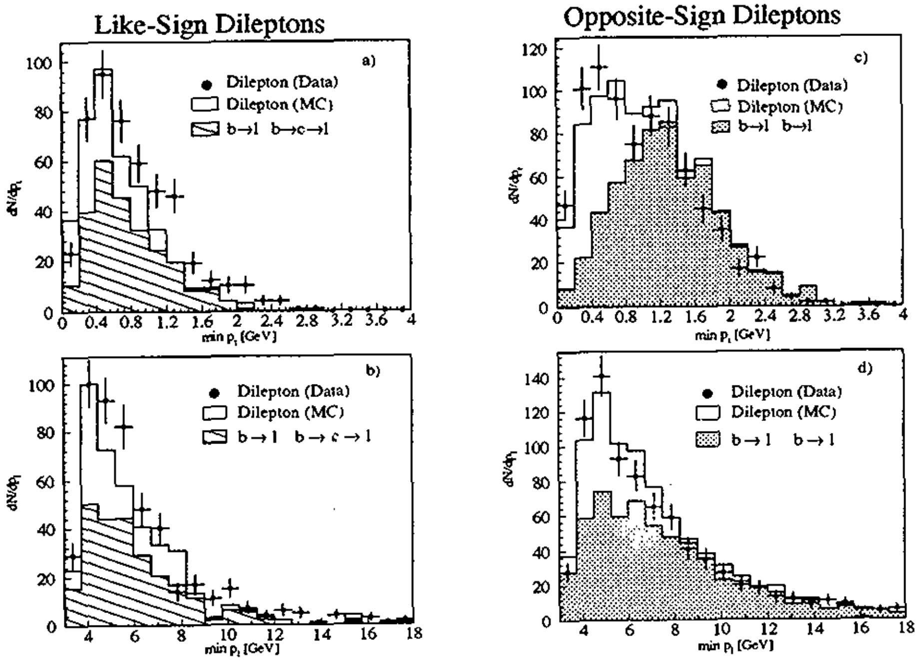

Figure 6.5: The minimum p_t and p_l for like sign (a and b) and opposite sign (c and d) dilepton events compared to the Monte Carlo expectations with no mixing. The excess of data events in a and b, and the shortage of events in c and d shows the qualitative effect of mixing.

χ_B is determined to be 0.121 ± 0.017. Separate fits give $\chi_B = 0.088 \pm 0.024$ for $\mu\mu$, $0.158 \pm$

0.050 for ee, and 0.140 ± 0.028 for eμ events. The systematic errors have been evaluated by varying parameters by their measured or estimated uncertainties. We obtain:

$$\chi_{\mathrm{B}} = 0.121 \pm 0.017\ (\mathrm{stat.}) \pm 0.006\ (\mathrm{sys.}), \tag{6.17}$$

which is in agreement with measurements from other LEP experiments [66,67].

To obtain a value of χ_s, a maximum likelihood fit to the data including the results obtained for χ_d has been performed using the relation $\chi_{\mathrm{B}} = f_d\chi_d + f_s\chi_s$. The relative fractions of B^0_d and B^0_s mesons is inferred from the relative production rate of kaons and pions. Measurements at LEP [69] and at lower energy e^+e^- colliders [70,71] correspond to a strange quark suppression factor, relative to d quarks, of $\gamma_s = f_s/f_d = 0.3$. We assume that the baryon fraction is $f_B = 0.08$, and that $f_u = f_d$. We therefore take $f_d = 0.40$ and $f_s = 0.12$. The physical constraint, $0 < \chi_d, \chi_s < 0.5$, was not imposed in the fit which yields $\chi_s = 0.46 \pm 0.21$, consistent with maximal mixing in the B^0_s-$\bar{\mathrm{B}}^0_s$ system. Imposing the physical constraint $0 < \chi_d, \chi_s < 0.5$ gives the one dimensional limit at the 90% confidence level of $\chi_s > 0.16$.

The value of χ_s is sensitive to the relative production fractions of different b hadrons. The dependence of χ_s on γ_s is shown in Figure 6.6, up to the SU(3) flavor symmetry limit $\gamma_s = 1$. The 1σ errors include a 50% uncertainty on the value of f_B. The effect of the uncertainty is a factor 5 smaller than the statistical errors. The value of χ_s is consistent with maximal mixing for any reasonable choice of the production fractions.

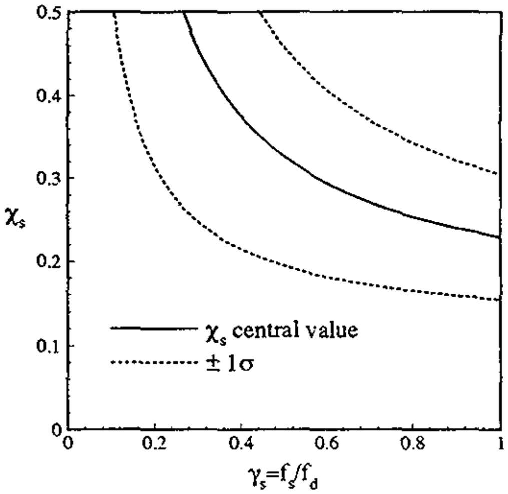

Figure 6.6: χ_s as a function of $\gamma_s = f_s/f_d$. The one σ errors include a 50% uncertainty on the value of f_B, the fraction of b baryons produced.

6.3 Weak neutral current interactions of b quarks

6.3.1 Measurement of the forward-backward charge asymmetry

The forward-backward asymmetry of quark pairs, $A_{q\bar{q}}$, produced in the $e^+e^- \to Z \to q\bar{q}$ process is sensitive to the electroweak mixing angle, $\sin^2\bar{\theta}_W$ (see chapter 8). The forward-backward asymmetry for the process $e^+e^- \rightarrow q\bar{q}$ is defined analogously to the leptonic asymmetries (see section 5.2.2):

$$A_{q\bar{q}} = \frac{\sigma_F^q - \sigma_B^q}{\sigma_F^q + \sigma_B^q} \tag{6.18}$$

where σ_F^q and σ_B^q are the cross sections in the forward and backward hemispheres with respect to the electron beam. The resulting angular distribution of the quark is

$$\frac{d\sigma}{d\cos\theta} \propto \frac{3}{8}(1+\cos^2\theta) + A_{q\bar{q}}\cos\theta, \tag{6.19}$$

where θ is the polar angle of the quark with respect to the electron beam.

We use electrons and muons from the semileptonic decay of b or c quarks to select events coming from $Z \rightarrow b\bar{b}$ and $Z \rightarrow c\bar{c}$. The c quark, with its lower mass and softer fragmentation, produces leptons with lower p and p_t than those from b quarks, but nevertheless still higher than those of leptons from the decays of the lighter quarks. As the charge of the lepton is correlated with the charge of the quark, we can use events containing these inclusive leptons to measure $A_{b\bar{b}}$ and $A_{c\bar{c}}$. We use the thrust axis of the event to give the direction of the quark and we tag its charge with the lepton charge. The thrust axis is oriented towards the hemisphere containing the negatively charged lepton (or opposite the positively charged lepton). With this convention, the thrust axis points in the direction of the b quark for $b\bar{b}$ events and in the direction of the $\bar{c}$ for $c\bar{c}$ events.

Due to mixing in the B^0-$\bar{B}^0$ system, the observed b quark asymmetry, $A_{b\bar{b}}^{obs}$, is smaller than the actual asymmetry by a factor $(1 - 2\chi_B)$. As there is no observable mixing among charm mesons, $A_{c\bar{c}}$ is measured directly.

Monte Carlo events with leptons are classified into six categories: prompt $b \rightarrow \ell$, the cascades $b \rightarrow c \rightarrow \ell$, $b \rightarrow \tau \rightarrow \ell$, and $b \rightarrow c + \bar{c} + s$ where $\bar{c} \rightarrow \ell$, prompt $c \rightarrow \ell$, and background. For brevity, we have omitted the neutrinos and other decay products in this notation. Table 6.5 shows the results of Monte Carlo studies giving the fraction of each source of leptons and background for data samples with no cut on transverse momentum and also with a cut at 1 GeV.

Category	μ		e		Asymmetry
	$p_t > 0$ GeV	$p_t > 1$ GeV	$p_t > 0$ GeV	$p_t > 1$ GeV	Dependence
1: $b \rightarrow \ell$	36.5%	70.5%	67.6%	79.8%	$A_{b\bar{b}}$
2: $b \rightarrow c \rightarrow \ell$	10.8%	6.6%	6.6%	4.3%	$-A_{b\bar{b}}$
3: $b \rightarrow \tau \rightarrow \ell$	1.8%	1.8%	2.5%	2.0%	$A_{b\bar{b}}$
4: $b \rightarrow \bar{c} \rightarrow \ell$	1.3%	0.6%	0.7%	0.4%	$A_{b\bar{b}}$
5: $c \rightarrow \ell$	16.1%	6.3%	4.3%	2.5%	$-A_{c\bar{c}}$
6: background	33.5%	14.0%	18.3%	11.1%	A_{back}

Table 6.5: Monte Carlo estimates of the fraction of each process in the data sample. Also shown is the expected asymmetry for each process.

As can be seen from table 6.5, the data at high p_t for both electrons and muons are dominated by events containing b quarks. At low p_t the muon sample has a relatively large contribution from c quarks. The requirements of the electron selection result in a reduced efficiency for low p_t events, and hence for c quark events.

To check the quality of the data, we first investigate the angular distribution for high p_t (> 1 GeV) events. In this way, we can make a direct measurement of $A_{b\bar{b}}^{obs}$. The data are corrected for angular acceptance, and the non-b quark background is subtracted. The resulting angular distribution for electron and muon events is shown in Figure 6.7. A fit is made to the form:

$$\frac{3}{8}(1+\cos^2\theta_{\rm thrust}) + A_{b\bar{b}}^{obs}\cos\theta_{thrust}. \tag{6.20}$$

The result is $A_{b\bar{b}}^{obs} = 0.062 \pm 0.013$ with $\chi^2/\text{dof} = 26/19$. This method, however, has the disadvantage that the p and p_t of the lepton are not used, thus reducing sensitivity. In addition, it is best suited to situations where the background is small, and it therefore unsuitable for a measurement of $A_{c\bar{c}}$.

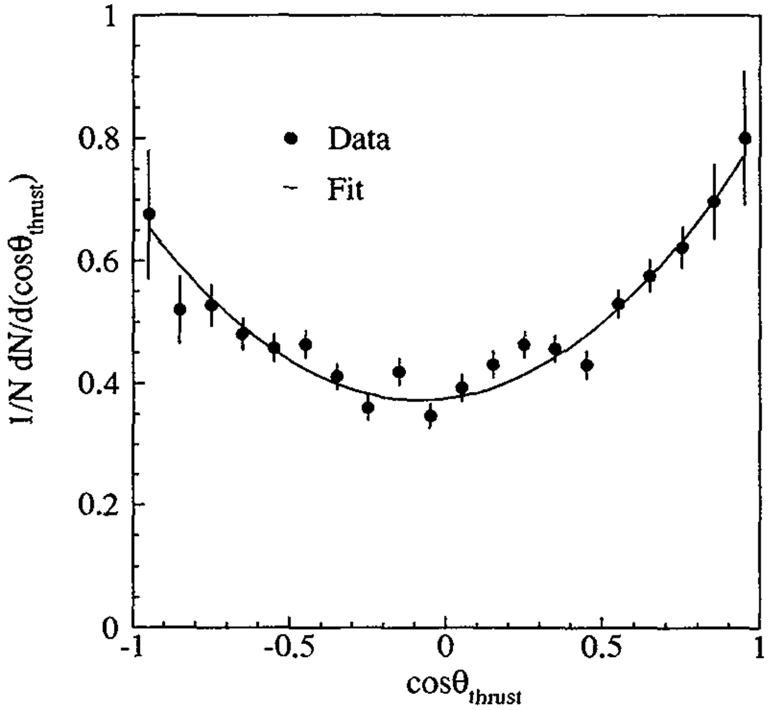

Figure 6.7: The angular distribution of the thrust axis for events containing high p_t leptons. The direction of the thrust axis has been described in the text. The points are the data, and the solid line is the result of the fit.

To use the full statistics and to improve the sensitivity, we measure $A_{b\bar{b}}$ and $A_{c\bar{c}}$ using an unbinned maximum likelihood fit in the p versus p_t plane. The fitting procedure has been described in detail in references 72 and 73. The probability for a data event to come from the various sources listed in table 6.4 is determined from the number and type of Monte Carlo events found in a rectangular box centered on the (p, p_t) values of the data event. The weights for the likelihood function are determined by the expected angular distribution given the polar angle of the thrust axis of the data event, and the asymmetry of the possible sources of the event. For sources 1, 3 and 4, the asymmetry is $A_{b\bar{b}}$, while for source 2 it is $-A_{b\bar{b}}$, as the charge of the lepton from the cascade has the opposite sign to the b quark. For source 5, it is $-A_{c\bar{c}}$.

as the thrust axis points in the direction of the $\bar{c}$ quark. In the case of dilepton events, the average asymmetries of the two leptons are used.

From a sample of $Z \rightarrow \tau^+\tau^-$ events we have estimated the charge confusion to be $(0.2\pm0.2)\%$ for muons and $(0.8 \pm 0.3)\%$ for electrons. We correct for the effects of the charge confusion, and account for its uncertainty in the systematic error.

The result of the fit for $A_{b\bar{b}}$ and $A_{c\bar{c}}$ using both inclusive muons and electrons and all center of mass energies is $A_{b\bar{b}}^{obs} = 0.066\pm0.011$ and $A_{c\bar{c}} = 0.083\pm0.038$. As the fraction of c→e events is small, the $A_{c\bar{c}}$ measurement is determined almost completely by the inclusive muon events. The correlation coefficient between $A_{b\bar{b}}^{obs}$ and $A_{c\bar{c}}$ is 20%. Separate fits for $A_{b\bar{b}}$ using the muon and electron data yield $A_{b\bar{b}}^{obs} = 0.074 \pm 0.014$ for muons, and 0.053 ± 0.019 for electrons. We have estimated the systematic error by changing the parameters by their uncertainties. The sources of the systematic error are summarized in table 6.6.

Contribution	Variation	$\Delta A_{b\bar{b}}^{obs}$	$\Delta A_{c\bar{c}}$
$b \rightarrow \ell$ branching ratio	±0.006	0.0006	0.002
$c \rightarrow \ell$ branching ratio	±0.012	0.0013	0.013
$\Gamma_{b\bar{b}}$	±10 MeV	0.0003	0.001
$\Gamma_{c\bar{c}}$	±10 MeV	0.0002	0.002
background fraction	±0.15	0.0006	0.003
background asymmetry	±0.015	0.0006	0.020
charge correlation for b quark background	±0.15	0.0004	0.001
b quark fragmentation parameter ϵ_b	±0.006	0.0002	0.002
c quark fragmentation parameter ϵ_c	±0.200	0.0006	0.004
smearing the lepton momentum $\Delta p/p$	5%	0.0001	0.001
smearing the angle between the lepton and nearest jet	$0^\circ - 1^\circ$	0.0010	0.004
uncertainty in the charge confusion correction	±0.0015	0.0002	0.001
Monte Carlo statistics		0.0035	0.009
Total		0.004	0.027

Table 6.6: Systematic errors in the $A_{b\bar{b}}^{obs}$ and $A_{c\bar{c}}$ measurements.

Our final result for $A_{c\bar{c}}$ is

$$A_{c\bar{c}} = 0.083 \pm 0.038 \text{ (stat.)} \pm 0.027 \text{ (sys.)}. \tag{6.21}$$

Due to mixing in the B^0-$\bar{B}^0$ system, the observed $b\bar{b}$ asymmetry is $A_{b\bar{b}}^{obs} = A_{b\bar{b}}(1 - 2\chi_B)$. Correcting $A_{b\bar{b}}^{obs}$ using our measured value $\chi_B = 0.121 \pm 0.017$ (stat.) $\pm$ 0.006 (sys.), we obtain

$$A_{b\bar{b}} = 0.086 \pm 0.015 \text{ (stat.)} \pm 0.007 \text{ (sys.)}. \tag{6.22}$$

As the asymmetry is predicted to depend on the center of mass energy, we have also divided our data into energies below, on, and above the Z resonance. The results for $A_{b\bar{b}}$ are shown in table 6.7 and figure 6.8. Because of limited statistics, we have not subdivided the data sample for $A_{c\bar{c}}$.

Mean $\sqrt{s}$	$A_{b\bar{b}}$
89.67 GeV	$0.025 \pm 0.051 \pm 0.007$
91.24 GeV	$0.097 \pm 0.017 \pm 0.007$
92.81 GeV	$0.062 \pm 0.042 \pm 0.007$

Table 6.7: $A_{b\bar{b}}$ for different center of mass energies. Note that the systematic error of 0.007 is common to all energies.

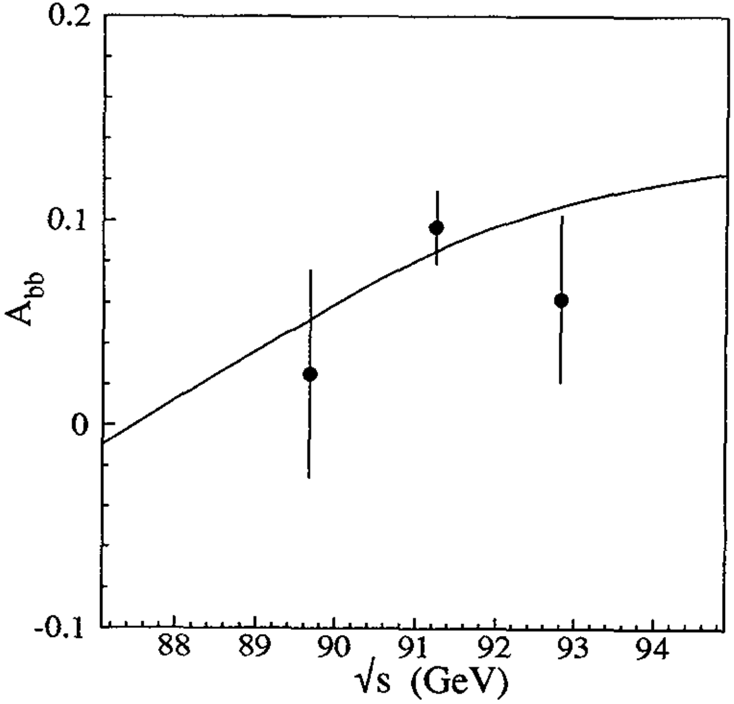

Figure 6.8: The energy dependence of $A_{b\bar{b}}$ compared to the Standard Model expectation with $\sin^2\overline{\theta}_W = 0.2336$.

Figure 6.8 shows the measured energy dependence of $A_{b\bar{b}}$ in comparison with the Standard Model expectation with $\sin^2\overline{\theta}_W = 0.2336$, as determined from these asymmetry values (see section 8.7.1). The Standard Model prediction for $A_{c\bar{c}}$ is 0.056, in good agreement with our measurement.

As can be seen in figure 6.8, the asymmetry predicted by the Standard Model is not linear as a function of energy, but rather flattens out above the Z peak due to initial state radiation. We have used ZFITTER to take this effect into account, and to recalculate the effective average center of mass energy for our complete data sample. As most of our data was taken on the Z peak, and as the effect is small, the effective average is the same as the luminosity weighted average of 91.24 GeV.

6.4 Determination of the Z partial width, $\Gamma_{b\bar{b}}$

This analysis is based on approximately 115,000 hadronic Z decays recorded in the 1990 running period [47].

In the determination of $\Gamma_{b\bar{b}}$, we perform a one parameter fit to the data, with $\Gamma_{b\bar{b}}$ as the free parameter. We obtain:

$$\Gamma_{b\bar{b}} = 394 \pm 9 \text{ MeV } (\mu + X) \tag{6.23}$$

$$\Gamma_{b\bar{b}} = 370 \pm 12 \text{ MeV } (e + X) \tag{6.24}$$

for inclusive muons and electrons, respectively. The errors are statistical only. We estimate the systematic error using the procedure described in section 6.2.2. From these studies we assign systematic errors of $\Delta\Gamma_{b\bar{b}} = 19$ MeV from the uncertainty in the branching ratios, $\mathrm{Br}(b \to \ell\nu X)$ and $\mathrm{Br}(c \to \ell\nu X)$, and $\Delta\Gamma_{b\bar{b}} = 11$ MeV for muons and $\Delta\Gamma_{b\bar{b}} = 15$ MeV for electrons from all other sources. If we perform a combined fit using the electron and muon samples, we obtain:

$$\Gamma_{b\bar{b}} = 385 \pm 7\,(\text{stat.}) \pm 11\,(\text{sys.}) \pm 19(\text{Br}) \text{ MeV}. \tag{6.25}$$

The third error gives the uncertainty from the semileptonic branching ratios. We have used the $\mathrm{Br}(b \to \ell\nu X)$ given by equation 6.7. Combining all errors in quadrature we obtain:

$$\Gamma_{b\bar{b}} = 385 \pm 23 \text{ MeV}, \tag{6.26}$$

in good agreement with the Standard Model prediction of 378 ± 3 MeV.

6.5 Production of J mesons

The J particle is expected to be dominantly produced in Z decays via the process

$$e^+e^- \to Z \to b\bar{b}; \quad b \to c\bar{c}s \to J + X. \tag{6.27}$$

The decay proceeds mainly through a color-suppressed spectator diagram, in which the c and $\bar{c}$ have to match in color. However, the magnitude of this color suppression can be reduced by QCD effects, which leads to a considerable change in the inclusive branching ratio. The branching ratio is estimated to be in the range 0.5 to 3.0% [74].

The J momentum in b hadron decays is strongly correlated with the parent particle momentum, which is sensitive to the fragmentation of the b quark. This allows us to determine the b quark fragmentation parameter using the measured J momentum distribution.

In addition to process 6.27, at LEP energies, the J particle can originate from gluon jets:

$$e^+e^- \to Z \to q\bar{q}g; \quad g \to J + X. \tag{6.28}$$

This process gives information on the interplay between the perturbative and non-perturbative effects of QCD. In addition it would be the most important process for the production of heavier vector mesons. Since again the c and $\bar{c}$ have to match in color, the process is suppressed. Theoretical estimates for the production cross section are uncertain by at least a factor of two [75,76].

The production of J particles via other processes, in particular by exclusive Z decays is predicted to be very small [77] and can be neglected.

6.5.1 Signatures of J mesons

J mesons are identified by their decays into a charged lepton pair $\mathrm{J} \to \ell^+\ell^-$ ($\ell = \mathrm{e}, \mu$). In the laboratory system, the J mesons often decay into one high momentum lepton and one low momentum lepton. We therefore select muons and electrons with a momentum larger than 2 GeV, rather than the usual 3 or 4 GeV criterion that we impose for the other analyses described in this chapter, and place less stringent cuts on the shower shape for one of the electrons. We require the opening angle between two oppositely charged lepton candidates to be smaller than 90°.

Lepton pairs that pass the above cuts can also arise from several background sources. The dominant source is the semileptonic decay of a b hadron to a c hadron, followed by the semileptonic decay of the c hadron. The background processes tend to give lepton-pair masses well below that of the J.

6.5.2 Determination of Br(Z → J + X)

The acceptance for $\mathrm{J} \to \mu^+\mu^-$ is mainly determined by the angular coverage of the muon chambers and the absorption of low momentum muons in the calorimeter and is calculated to be 0.28 ± 0.01 (stat.). The acceptance for $\mathrm{J} \to \mathrm{e}^+\mathrm{e}^-$ is determined by the angular coverage of the barrel electromagnetic calorimeter and the isolation requirements imposed by the electron selection criteria and is calculated to be 0.15 ± 0.01 (stat.). In both cases the production mechanism for the J is assumed to be via b quark decay.

Inefficiencies in the TEC, electromagnetic calorimeter and muon chambers are calculated using the data. Taking into account the correlations between the two leptons, the efficiency for finding the two muons is $\varepsilon_{\mu^+\mu^-} = 0.92 \pm 0.02$ (stat.) and for the two electrons is $\varepsilon_{\mathrm{e}^+\mathrm{e}^-} = 0.82 \pm 0.02$ (stat.).

J mesons can also result from the cascade decay of ψ' mesons and the radiative decay of χ_c mesons produced in b hadron decay [78]. From a Monte Carlo simulation, the effect of the cascade decays on the acceptance and the J momentum spectrum is negligible.

The measured invariant mass distributions of the $\ell^+\ell^-$ pairs are shown in Figure 6.9. We fit the invariant mass distribution in the mass region $2.0 < m_{\ell^+\ell^-} < 4.0$ GeV with a Gaussian for the signal and a polynomial for the background. The width of the Gaussian and the shape of the background are determined using Monte Carlo events. We use a width of 110 MeV for the $\mu^+\mu^-$ channel and 100 MeV for the $\mathrm{e}^+\mathrm{e}^-$ channel. As can be seen from the figure the shape of the background is well reproduced by the simulation. Its normalization is left free in the fit, but differs from the absolute prediction by less than 10%. We find 43 ± 8 $\mathrm{J} \to \mu^+\mu^-$ candidates and 15 ± 5 $\mathrm{J} \to \mathrm{e}^+\mathrm{e}^-$ candidates over backgrounds of 15 and 5 events, respectively.

The branching ratio Br(Z → J + X) is calculated as follows:

$$\mathrm{Br}(\mathrm{Z} \to \mathrm{J} + \mathrm{X}) = \frac{N_{\mathrm{J}}}{N_{\mathrm{h}}} \frac{\Gamma_{\mathrm{had}}}{\Gamma_{\mathrm{Z}}} \frac{1}{\mathrm{Br}(\mathrm{J} \to \ell^+\ell^-)} \tag{6.29}$$

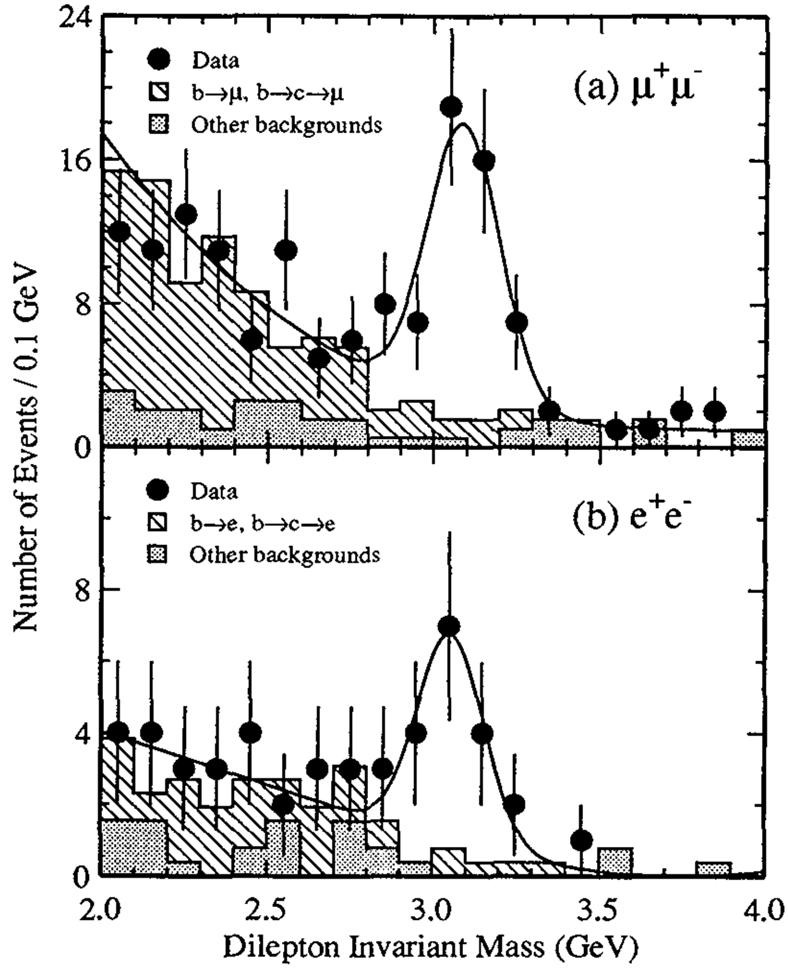

Figure 6.9: The invariant mass distributions of (a) $\mu^+\mu^-$, and (b) e^+e^- pairs. The curves are the result of the fit described in the text. The contributions from the various backgrounds are shown by the histograms.

where N_J and N_h are the corrected number of the J signal events and the total number of hadronic Z decays, respectively. Γ_had and Γ_Z are taken from the L3 measurements (see section 8.6). We use the measurement of $\mathrm{Br}(\mathrm{J} \to \ell^+\ell^-) = 0.0590 \pm 0.0015$ (stat.) $\pm\ 0.0019$ (sys.) from the MARK III experiment [79] and determine:

$$\mathrm{Br}(\mathrm{Z} \to \mathrm{J}+\mathrm{X}) = (4.5 \pm 0.8\ (\text{stat.}) \pm 0.4\ (\text{sys.})) \times 10^{-3} \text{ where } \mathrm{J} \to \mu^+\mu^- \quad (6.30)$$

$$\mathrm{Br}(\mathrm{Z} \to \mathrm{J}+\mathrm{X}) = (3.5 \pm 1.2\ (\text{stat.}) \pm 0.4\ (\text{sys.})) \times 10^{-3} \text{ where } \mathrm{J} \to e^+e^- \quad (6.31)$$

The systematic error on the selection efficiencies is estimated by varying the cuts, in particular the momentum cut which is varied from 2 to 4 GeV. We also apply extra kinematic cuts, especially for the case when the two leptons are in different jets.

Combining the two measurements and taking into account the common systematic errors, we obtain an average branching ratio:

$$\mathrm{Br}(\mathrm{Z} \rightarrow \mathrm{J}+\mathrm{X}) = (4.1 \pm 0.7\ (\mathrm{stat.}) \pm 0.3\ (\mathrm{sys.})) \times 10^{-3}. \tag{6.32}$$

We can set an upper limit on $\mathrm{Br}(\mathrm{Z} \rightarrow \mathrm{q\bar{q}g};\ \mathrm{g} \rightarrow \mathrm{J}+\mathrm{X})$ by analyzing the distribution of the angle between the J momentum and the most energetic jet in the event. The J mesons from b hadron decays tend to be inside the most energetic jet, while those from gluon jets are well separated. We generate events from the process $\mathrm{Z} \rightarrow \mathrm{q\bar{q}g};\ \mathrm{g} \rightarrow \mathrm{J+X};\ \mathrm{J} \rightarrow \ell^+\ell^-$ using the CORFUJ Monte Carlo [80]. The acceptance is determined to be 0.20 ± 0.01 for $\mathrm{J} \rightarrow \mu^+\mu^-$ and 0.12 ± 0.01 for $\mathrm{J} \rightarrow \mathrm{e^+e^-}$, including all detector efficiencies. The fraction of J mesons coming from gluon jets is determined to be:

$$f_{\mathrm{g}} = 0.03^{+0.08}_{-0.06}\ (\mathrm{stat.}) \pm 0.02\ (\mathrm{sys.}). \tag{6.33}$$

The systematic error comes from the uncertainty in the background contribution. Constraining $0 \leq f_{\mathrm{g}}$, we set an upper limit of

$$\mathrm{Br}(\mathrm{Z} \rightarrow \mathrm{q\bar{q}g};\ \mathrm{g} \rightarrow \mathrm{J}+\mathrm{X}) < 7.0 \times 10^{-4} \tag{6.34}$$

at 90% confidence level, which is close to the upper theoretical estimate.

As f_g is small, we can determine the branching ratio $\mathrm{Br}(\mathrm{b} \rightarrow \mathrm{J}+\mathrm{X})$ using the following relationship:

$$\mathrm{Br}(\mathrm{b} \rightarrow \mathrm{J}+\mathrm{X}) = \frac{\Gamma_{\mathrm{Z}}}{2 \cdot \Gamma_{\mathrm{b\bar{b}}}} \cdot (1 - f_{\mathrm{g}}) \cdot \mathrm{Br}(\mathrm{Z} \rightarrow \mathrm{J}+\mathrm{X}). \tag{6.35}$$

Using our measurements of Γ_{Z} and $\Gamma_{\mathrm{b\bar{b}}}$, we find

$$\mathrm{Br}(\mathrm{b} \rightarrow \mathrm{J}+\mathrm{X}) = (1.3 \pm 0.2\ (\mathrm{stat.}) \pm 0.2\ (\mathrm{sys.})) \times 10^{-2}. \tag{6.36}$$

This branching ratio may be compared with $(1.12 \pm 0.20) \times 10^{-2}$ obtained by experiments at CESR and DORIS [81] for $\mathrm{B_u}$ and $\mathrm{B_d}$ mesons. Taking into account the different values for $\mathrm{Br}(\mathrm{J} \rightarrow \ell^+\ell^-)$ used in the calculations, the ratio of the two branching ratios is 1.00 ± 0.24. It should be noted that in addition to the $\mathrm{B_u}$ and $\mathrm{B_d}$ mesons, also $\mathrm{B_s}$ and $\mathrm{B_c}$ mesons and b baryons are produced at LEP.

6.5.3 Measurement of the b quark fragmentation using J events

Given that the J mesons are produced predominantly in the decay of b hadrons, the measured J momentum is sensitive to the fragmentation of the b quark. We can use the J momentum distribution to determine that of the b quark.

The momentum distributions for the J meson candidates from the $\mu^+\mu^-$ and $\mathrm{e^+e^-}$ channels in the mass region $2.8 < m_{\ell^+\ell^-} < 3.4$ GeV are shown in figure 6.10. The fraction of the events that are from $\mathrm{b} \rightarrow \mathrm{J} + X$ is about 75%. The background is dominated by events with one prompt lepton and one from a cascade decay. We perform a binned maximum likelihood fit to the distributions, to extract the Peterson fragmentation parameter, ϵ_b. In the fit, the J

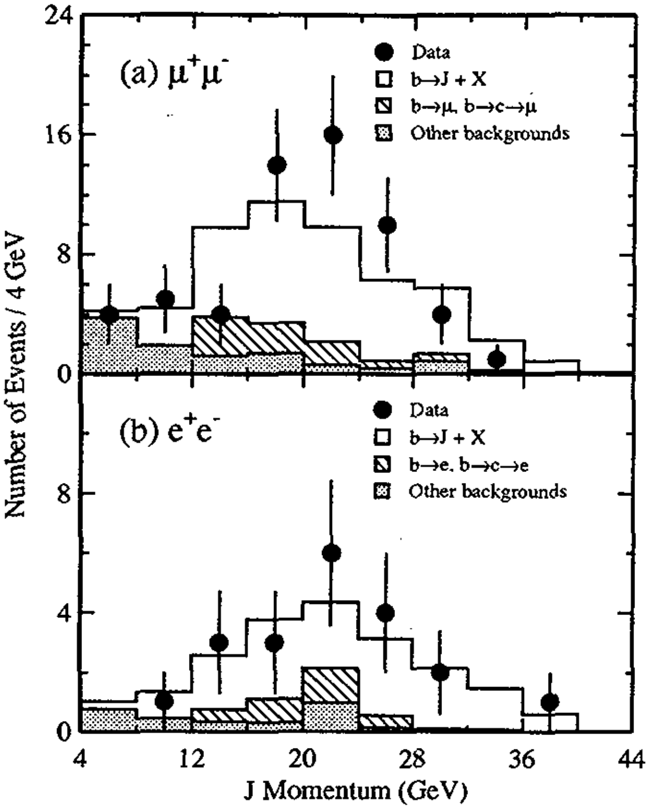

Figure 6.10: The J momentum distributions from (a) the $\mu^+\mu^-$, and (b) the e$^+$e$^-$ channels. The fit result and the background contributions are also shown.

momentum distribution and the one due to the cascade decay of the b hadron are weighted as a function of x_E by varying the parameter ϵ_b, assuming that the x_E distribution can be approximated by the Peterson function $f(x_E)$, as described in section 6.2.1. The systematic error is estimated by varying the background fractionsand selection criteria and includes the uncertainty in the fraction of events coming from gluons. We also used the EURODEC [82] package to simulate the weak decay of the b hadron produced by the JETSET program. The differences in the treatment of the b hadron decay contributes ±0.006 to the systematic error on ϵ_b.

We perform a combined fit using the inclusive e$^+$e$^-$ and $\mu^+\mu^-$ events and obtain:

$$\epsilon_b = 0.044^{+0.026}_{-0.018}\ (\text{stat.})^{+0.009}_{-0.013}\ (\text{sys.}), \tag{6.37}$$

which corresponds to the average energy fraction of b hadrons:

$$\langle x_E \rangle = 0.70 \pm 0.03\ (\text{stat.}).^{+0.02}_{-0.01}\ (\text{sys.}). \tag{6.38}$$

This result is in good agreement with the value determined in section 6.2.1.

Chapter 7

Production and Decay of Tau Leptons

In a previous chapter we have analyzed, for τ leptons produced from Z decay, the total cross-section and the forward-backward charge asymmetry (see sect. 5.3). Both these measurements reflect on the electroweak neutral current couplings of τ leptons. In this chapter we will first continue our study of these neutral current couplings by a determination of the polarization with which the τ leptons are produced in Z decay (section 7.1). Subsequently, we will use the same sample to study the decay properties of τ leptons, thus determining their coupling to the weak charged current (section 7.2).

7.1 τ polarization in Z decay

Even for unpolarized e^+e^- beams, the polarization of final state fermions f and $\bar{f}$ in the reaction $e^+e^- \rightarrow Z \rightarrow f\bar{f}$ is sensitive to the parity-violating components of the weak neutral current interaction. The average polarization $\mathcal{P}_f$

$$\mathcal{P}_f = \frac{\sigma(h=+1) - \sigma(h=-1)}{\sigma(h=+1) + \sigma(h=-1)} \tag{7.1}$$

is the asymmetry in the production of positive helicity ($h = +1$) and negative helicity ($h = -1$) fermions. For a weak neutral current containing only vector (V) and axial-vector (A) couplings, helicity conservation in the massless limit requires that the initial state e^+e^- and the final state $f\bar{f}$ can only involve fermions of opposite helicity. This implies that $\mathcal{P}_f = -\mathcal{P}_{\bar{f}}$.

In the improved Born approximation, the polarization on the peak of the Z resonance, averaged over all production angles, is given by [83]

$$\mathcal{P}_f = -\frac{2\bar{g}_V\bar{g}_A}{\bar{g}_V^2 + \bar{g}_A^2} \tag{7.2}$$

where $\bar{g}_V$ and $\bar{g}_A$ are, respectively, the effective vector and axial-vector coupling constants of fermion flavor f to the weak neutral current. $\mathcal{P}_f$ is thus sensitive to the neutral current coupling constants of the final state fermion and independent of those of the initial state electron. In the standard electroweak theory [3]

$$\mathcal{P}_\ell \simeq -2\left(1-4\sin^2\overline{\theta}_\mathrm{W}\right) \tag{7.3}$$

for $\ell = \mu, \tau$, showing the large sensitivity of $\mathcal{P}_\ell$ to the effective weak mixing angle $\sin^2\overline{\theta}_\mathrm{W}$ for leptonic final states. The measurement of $\mathcal{P}_\ell$ allows the determination of the relative sign of $\bar{g}_V$ and $\bar{g}_A$, information not otherwise accessible from observables with unpolarized e^+e^- beams.

In the case of τ lepton production, $\mathcal{P}_\tau$ can be deduced from an analysis of the kinematics of the τ decay products. The $(V-A)$ helicity structure of the weak charged current decay leads to characteristic differences in the angular distributions in the τ rest frame, or equivalently, in the laboratory frame, to differences between the energy distributions from τ leptons of opposite helicity. However, it is impossible to distinguish the effects of $\mathcal{P}_\tau$ from those of deviations from the $(V-A)$ structure of the weak charged current. In the remainder of this chapter, we will assume that no such deviations exist, in agreement with data on the helicity structure of τ decay [84].

For three-body decays ($\tau \rightarrow e\nu\nu$, $\mu\nu\nu$), the dependence of the charged lepton energy E_ℓ on $\mathcal{P}_\tau$ as a function of $x_\ell = E_\ell/E_\tau \simeq E_\ell/E_\mathrm{beam}$ is given by

$$\frac{1}{N}\frac{dN}{dx_\ell} = \frac{1}{3}\left[\left(5-9x_\ell^2+4x_\ell^3\right)+\mathcal{P}_\tau\left(1-9x_\ell^2+8x_\ell^3\right)\right]. \tag{7.4}$$

For two-body decays ($\tau \rightarrow$ hadron ν), the energy of the hadron E_h as a function of $x_\mathrm{h} = E_\mathrm{h}/E_\tau \simeq E_\mathrm{h}/E_\mathrm{beam}$ depends to lowest order linearly on $\mathcal{P}_\tau$

$$\frac{1}{N}\frac{dN}{dx_\mathrm{h}} = 1+\mathcal{P}_\tau\alpha_\mathrm{h}\left(2x_\mathrm{h}-1\right), \tag{7.5}$$

where α_h is a constant depending on the hadron type h. For the case of $\tau \rightarrow \pi\nu$, $\alpha \simeq 1$. For $\tau \rightarrow \rho\nu$, or $\mathrm{a}_1\nu$,

$$\alpha_\mathrm{h} = \frac{m_\tau^2-2m_\mathrm{h}^2}{m_\tau^2+2m_\mathrm{h}^2}, \tag{7.6}$$

where m_h is the mass of the ρ or a_1. In the latter case, the sensitivity to $\mathcal{P}_\tau$ can be enhanced by further analyzing the decays of the final state spin-1 particles [85].

7.1.1 Event selection and particle identification

We employ a selection procedure [86] which is relatively independent of the visible energy of the τ decay products, in order to minimize potential biases in rejecting backgrounds. We apply independent selection criteria in each hemisphere of the event. The hemispheres are separated by a plane perpendicular to the thrust axis. The thrust axis is calculated using the calorimetric energy only. We then proceed as follows:

First a sample of low multiplicity, back-to-back events are preselected, which consist mainly of Z decays to leptons. This preselection is designed to suppress hadronic Z decays, two-photon interactions and other backgrounds. After the preselection, the sample contains 34203 events which include more than 98% of all leptonic Z decays inside the fiducial volume defined by $|\cos\theta| < 0.7$ and a background of 5% mainly from $Z \rightarrow q\bar{q}(\gamma)$ and two-photon interactions. For the τ channels described below, each hemisphere with exactly one or three tracks and associated Z-chamber hits is considered for selection.

The final state of the τ decay in each hemisphere of the event is then identified as e, μ, π/K, ρ or a_1:

The electron identification uses matching between trajectories measured in the central tracking chamber and energy deposits in the electromagnetic calorimeter as well as the shower shape in the calorimeters. Events containing two electrons are rejected. The sample of identified electrons contains 80.5% of all $\tau \rightarrow e\nu\nu$ decays inside the fiducial region. The background contributions are 2.9% from other τ decays, 4.1% from $Z \rightarrow e^+e^-$, 0.3% from $Z \rightarrow \mu^+\mu^-$ and 0.3% from two-photon interactions.

Muons are identified using tracks measured in the muon chambers, tracking the energy deposition of particles in the calorimeters and comparing to the trajectory measured in the TEC. Events containing two muons are rejected. The sample of identified muons contains 74.5% of all $\tau \rightarrow \mu\nu\nu$ decays inside the fiducial region. The background contributions are 1.4% from other τ decays and 2.5% from $Z \rightarrow \mu^+\mu^-$.

π/K and ρ hadron candidates are first preselected by requiring that there be only one track, not identified as a muon or electron. 82% and 88% of all $\tau \rightarrow \pi\nu$ and $\rho\nu$ respectively are thus selected in the fiducial volume for further analysis. To facilitate good separation between these channels, we use a method for finding neutral clusters in the BGO which emphasizes finding π^0 showers merged with $\pi^\pm$ showers. The two one-prong channels are then separated by either rejecting or requiring additional showers compatible with the characteristics of a single π^0. The selection efficiency of the π/K selection in the fiducial volume is 63% for 1991 (figure 7.1) and 27% in 1990. The estimated background is 12.5%, 2.5% and 0.5% from other τ decays, $Z \rightarrow \mu^+\mu^-(\gamma)$ and two-photon events respectively.

Figure 7.2a shows the invariant mass of the $\pi^\pm\pi^0$ for selected ρ candidates. A fit to the distribution yields a mass of 772 ± 7 (stat.) ± 20 (sys.) MeV and a width of 163 ± 11 (stat.) $\pm$ 9 (sys.) MeV, consistent with the current world average [46]. The selection efficiency is 64.5% in the fiducial volume. The background is 17% from other τ decays and 1% from other sources.

The pion energies $E_{\pi^\pm}$ and E_{π^0} and 3-momenta $\mathbf{p}_{\pi^\pm}$ and $\mathbf{p}_{\pi^0}$ are related to the decay angles θ^*, the angle in the τ rest frame between the $\rho^\pm$ and the τ line of flight, and ψ^*, the angle in the $\rho^\pm$ rest frame between the $\pi^\pm$ and $\rho^\pm$ line of flight, by [85]

$$\cos\theta^* = \frac{4m_\tau^2}{m_\tau^2 - m_\rho^2}\frac{E_{\pi^0} + E_{\pi^\pm}}{\sqrt{s}} - \frac{m_\tau^2 + m_\rho^2}{m_\tau^2 - m_\rho^2} \tag{7.7}$$

and

$$\cos\psi^* = \frac{m_\rho}{\sqrt{m_\rho^2 - 4m_\pi^2}}\frac{E_{\pi^\pm} - E_{\pi^0}}{|\mathbf{p}_{\pi^\pm} + \mathbf{p}_{\pi^0}|} \tag{7.8}$$

Figures 7.2b and 7.2c respectively show the efficiency for $\tau^- \rightarrow \rho^-\nu_\tau$ events as a function of $\cos\theta^*$ and $\cos\psi^*$.

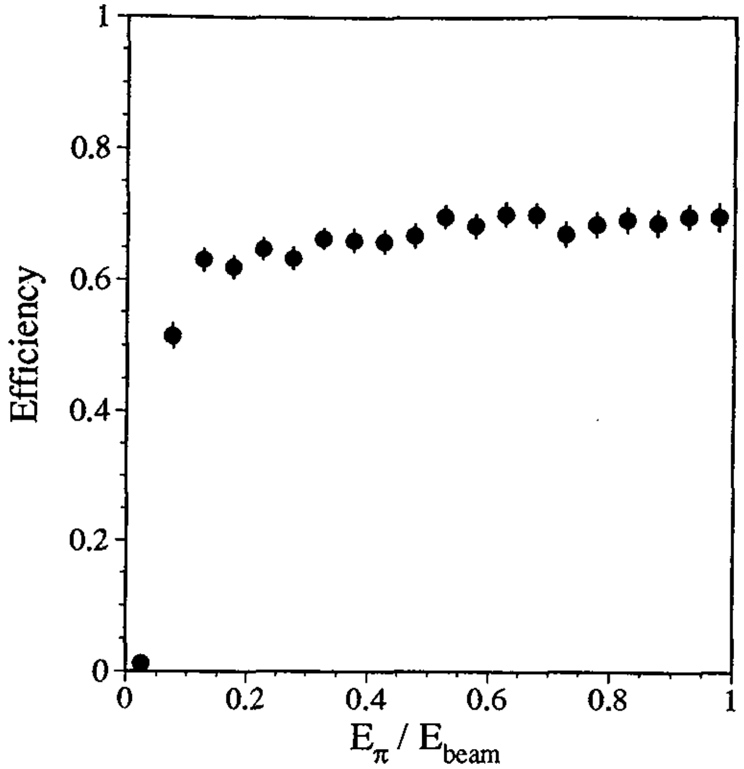

Figure 7.1: Selection efficiency of $\tau^- \rightarrow \pi^-(\mathrm{K}^-)\nu_\tau$ decays as a function of $x_\pi = E_\pi/E_{\mathrm{beam}}$ for 1991 data.

The τ decay into three charged pions, known to be dominated by the a_1 resonance subsequently decaying into $\rho^0\pi^-$, is identified by requiring three tracks in one hemisphere. Backgrounds from two-photon events are suppressed by a cut on the acolinearity of the event and from $\mathrm{q\bar{q}}$ events by requiring that the invariant mass of the three tracks is less than that of the τ. The dominant residual background, due to $\tau^- \rightarrow \pi^-\pi^+\pi^-(n\pi^0)\nu_\tau$, is removed by requiring that the energy deposition in the electromagnetic calorimeter be consistent with that expected for three charged pions. Requiring that at least one of the $\pi^+\pi^-$ combinations has an invariant mass larger than 0.5 GeV further suppresses the background from events contaminated by π^0s.

A fit is performed to combine the total calorimetric energy with the total momentum measured with the TEC to give the best estimate of the $\pi^\pm$ momenta. The $\pi^\pm$ momenta are then used to determine the quantities cos θ, the cosine of angle between the momentum of the three $\pi^\pm$ system and the τ direction of flight as determined in the rest frame of the τ, and cos ψ, the angle between the normal to the plane spanned by the three $\pi^\pm$ in their rest frame and the momentum of the three $\pi^\pm$ system. Since the normal to the plane is determined only up to a sign, only the absolute value of cos ψ is physically significant. Estimates c_θ (c_ψ) of cos θ (|cos ψ|) are determined from the measured $\pi^\pm$'s momenta using analytic approximations [87]

$$\mathrm{c}_\theta = \frac{4m_\tau^2}{m_\tau^2 - m^2}\frac{(E_1 + E_2 + E_3)}{\sqrt{s}} - \frac{m_\tau^2 + m^2}{m_\tau^2 - m^2}$$

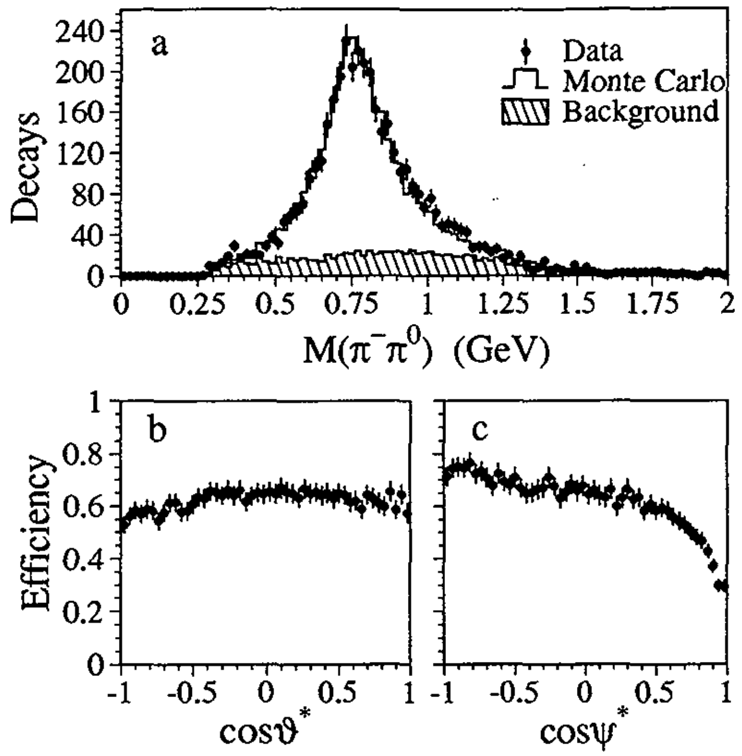

Figure 7.2: a) The invariant mass of the $\pi^{\pm}\pi^{0}$ for selected $\tau^{-} \rightarrow \rho^{-}\nu_{\tau}$ candidates compared with Monte Carlo prediction. b) The efficiency for $\tau^{-} \rightarrow \rho^{-}\nu_{\tau}$ decays as a function of $\cos\theta^{*}$ for 1991 data. c) The efficiency of $\tau^{-} \rightarrow \rho^{-}\nu_{\tau}$ decays as a function of $\cos\psi^{*}$ for 1991 data. The fall-off near $\cos\psi^{*} = 1$ corresponds to the kinematic region where the $\pi^{\pm}$ carries most of the $\rho^{\pm}$ energy and whose showers in the BGO calorimeter are merged with those of the π^{0}.

$$c_{\psi} = \frac{8m^{2}|\mathrm{p}_{1}\cdot(\mathrm{p}_{2}\times\mathrm{p}_{3})|/|\mathrm{p}_{1}+\mathrm{p}_{2}+\mathrm{p}_{3}|}{\sqrt{-\lambda(\lambda(m^{2},m_{12}^{2},m_{\pi}^{2}),\lambda(m^{2},m_{13}^{2},m_{\pi}^{2}),\lambda(m^{2},m_{23}^{2},m_{\pi}^{2}))}}$$

$$\lambda(x,y,z) = x^{2}+y^{2}+z^{2}-2xy-2yz-2zx$$

where p_{i} is the three momentum of $\pi^{\pm}$ i, m_{ij} is the invariant mass of $\pi^{\pm}$'s i and j, and m is the invariant mass of the three $\pi^{\pm}$ system. Events whose measured momenta are inconsistent with a_1 decay kinematics are rejected.

The efficiency of the a_1 selection is 37% in the fiducial volume. The estimated background is 11% mainly from other τ decays with additional π^{0}. The invariant mass distribution of selected candidates in shown in figure 7.3. The fit mass [88] is 1.186 ± 0.060 GeV, consistent with the world average [46].

The efficiencies for selection, particle identification and the estimates for the background contamination are determined using Monte Carlo simulations of the decays $\mathrm{Z} \rightarrow \tau^{+}\tau^{-}(\gamma)$, $\mathrm{e}^{+}\mathrm{e}^{-}(\gamma)$, $\mu^{+}\mu^{-}(\gamma)$ and hadrons as well as of the reactions $\mathrm{e}^{+}\mathrm{e}^{-} \rightarrow \mathrm{e}^{+}\mathrm{e}^{-}\mathrm{e}^{+}\mathrm{e}^{-}$ and $\mathrm{e}^{+}\mathrm{e}^{-}\mu^{+}\mu^{-}$ reactions [83].

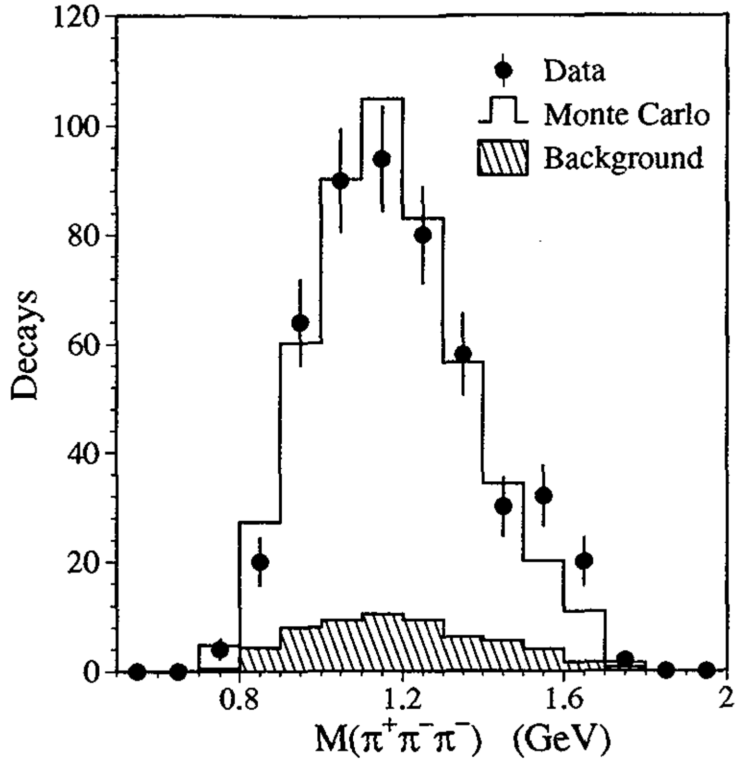

Figure 7.3: Invariant mass distribution of $\tau^- \to \pi^-\pi^+\pi^-\nu_\tau$ compared with Monte Carlo.

7.1.2 Measurement of $\mathcal{P}_\tau$

For each τ decay channel, $\mathcal{P}_\tau$ is measured by obtaining the linear combination of the $h = +1$ and $h = -1$ Monte Carlo distributions which best fits the data. For $\tau^- \to e^-\overline{\nu}_e\nu_\tau$, $\mu^-\overline{\nu}_\mu\nu_\tau$ and $\pi^-(K^-)\nu_\tau$, the energy distribution of the charged particle is used and the overall normalization and polarization are left as free parameters in a binned maximum likelihood fit. For $\tau^- \to \rho^-\nu_\tau$ and $a_1^-\nu_\tau$, multidimensional distributions are used as described below. For each decay mode, the polarization of the background from other τ decays is varied simultaneously with the polarization for the decay mode being fit. The statistical error in each channel is verified by direct calculation from the functional form of the decay distributions after including the kinematics, efficiency corrections and detector resolution. The statistical errors due to limited Monte Carlo statistics are included in the calculation of the systematic errors. A breakdown of systematic errors for each channel is given in Table 7.1 and the result for each channel is given in Table 7.2.

The decay channel $\tau^- \to e^-\overline{\nu}_e\nu_\tau$

The sum of the energies in the three most energetic BGO clusters in the hemisphere, assuming they originated from electrons and γ's, is used to estimate the energy of electron candidates.

Background from $Z \to e^+e^-(\gamma)$ is determined by selecting dielectron events which pass all the $\tau^- \to e^-\overline{\nu}_e\nu_\tau$ cuts except the cuts which reject events with identified high energy electrons

Channel	Selection	Background	Calibration	Radiative Corrections	Monte Carlo Statistics
$e^- \overline{\nu}_e \nu_\tau$	0.027	0.020	0.020	0.020	0.046
$\mu^- \overline{\nu}_\mu \nu_\tau$	0.020	0.020	0.020	0.010	0.046
$\pi^- (K^-) \nu_\tau$	0.017	0.009	0.013	0.005	0.021
$\rho^- \nu_\tau$	0.013	0.005	0.020	negligible	0.016
a_1	0.045	0.010	0.033	negligible	0.073

Table 7.1: Summary of systematic errors for all channels

Channel	$\mathcal{P}_\tau$	Stat. Error	Syst. Error
$e^- \overline{\nu}_e \nu_\tau$	-0.127	0.097	0.062
$\mu^- \overline{\nu}_\mu \nu_\tau$	-0.020	0.101	0.055
$\pi^- (K^-) \nu_\tau$	-0.148	0.046	0.033
$\rho^- \nu_\tau$	-0.152	0.035	0.029
a_1	0.105	0.164	0.093

Table 7.2: Summary for $\mathcal{P}_\tau$ and errors for all channels

in each hemisphere. A three parameter fit to the data and all backgrounds is first performed in the range $0.0 < E_{\mathrm{BGO}}/E_{\mathrm{beam}} < 1.1$ with the normalization of dielectron background as a free parameter. The dielectron background is then fixed to the fit value and a two parameter fit is performed in the range $0.0 < E_{\mathrm{BGO}}/E_{\mathrm{beam}} < 0.95$ to determine the polarization and overall normalization. The small background from two-photon events is estimated by Monte Carlo.

The systematic error from $Z \rightarrow e^+e^-(\gamma)$ background subtraction is estimated by varying its normalization by the statistical error extracted from the three parameter fit. The systematic errors from variations in the background from other τ decays are small. The accuracy of the BGO energy scale is known within 2% at 1 GeV by a study of test beam data and $e^+e^- \rightarrow e^+e^-e^+e^-$ events and within 0.3% at 45 GeV from $Z \rightarrow e^+e^-(\gamma)$ events.

The result for $\tau^- \rightarrow e^- \overline{\nu}_e \nu_\tau$ is $\mathcal{P}_\tau = -0.127 \pm 0.097$ (stat.) $\pm$ 0.062 (sys.). The electron energy spectrum together with the best fit Monte Carlo spectrum are shown in figure 7.4.

The decay channel $\tau^- \rightarrow \mu^- \overline{\nu}_\mu \nu_\tau$

The momentum measured in the muon chambers is combined with the most probable energy loss in the calorimeters to estimate the energy of muon candidates. A three parameter fit is first performed in the range $0.05 < E_\mu/E_{\mathrm{beam}} < 1.1$ with the normalization of the $Z \rightarrow \mu^+\mu^-(\gamma)$ background as an additional parameter. The background normalization is then fixed to the fitted value and a two parameter fit performed in the range $0.05 < E_\mu/E_{\mathrm{beam}} < 0.95$. All other backgrounds are estimated by Monte Carlo.

The systematic error from the $Z \rightarrow \mu^+\mu^-(\gamma)$ background is estimated by varying its normalization by the statistical error extracted from the three parameter fit. The systematic errors from variations in the background from other τ decays are small. The accuracy of the muon momentum scale is estimated to be 0.2% at 45 GeV. At lower momenta, the absolute muon

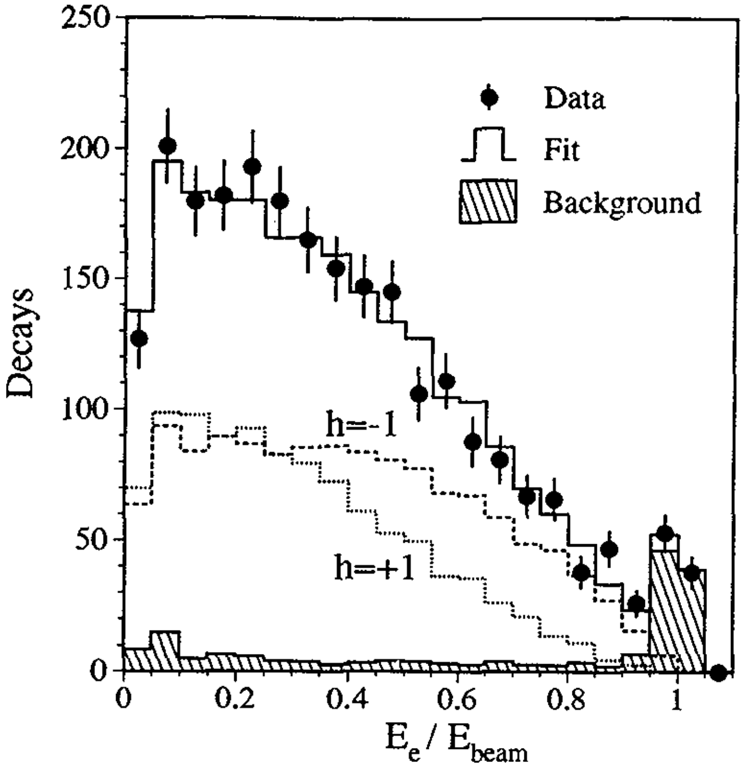

Figure 7.4: The spectrum of $\tau^- \to e^-\overline{\nu}_e\nu_\tau$ decays as a function of $x_e = E_e/E_{\text{beam}}$. Also shown is the contribution from each helicity including backgrounds for that helicity. The hatched histogram shows the total background.

momentum scale is dominated by the muon energy loss in the calorimeters which is known to within 100 MeV. The ratio of the number of muon's which have hits in three of the muon chambers to the number which have hits in two chambers was checked to ensure that the energy dependence of the efficiency is well understood and the polarization bias from this source is negligible.

The result for $\tau^- \to \mu^-\overline{\nu}_\mu\nu_\tau$ is $\mathcal{P}_\tau = -0.020\pm0.101\pm0.055$. The muon momentum spectrum together with the best fit Monte Carlo spectrum are shown in figure 7.5.

The decay channel $\tau^- \to \pi^-(K^-)\nu_\tau$

The energies deposited in the calorimeters are used to estimate the energy of the $\pi^\pm$ using the test beam calibration. This energy is combined with the momentum in the TEC to measure the most likely value of the energy assuming the presence of a single $\pi^\pm$.

The absolute energy scales of the BGO and hadron calorimeters are known within 2% each from the comparison of data and Monte Carlo energy spectra normalized to the TEC momentum for $\tau^- \to \pi^-(K^-)\nu_\tau$. The $\rho^\pm$ invariant mass from $\tau^- \to \rho^-\nu_\tau$ also shows that the shift in energy scale is less than 2% in each of the two calorimeters. The accuracy of the momentum scale in the TEC for momenta below 10 GeV is determined to be 2% by a study of the invariant mass of $K^0_S \to \pi^+\pi^-$ in $Z \to$ hadrons events and from a comparison of the momenta measured in the

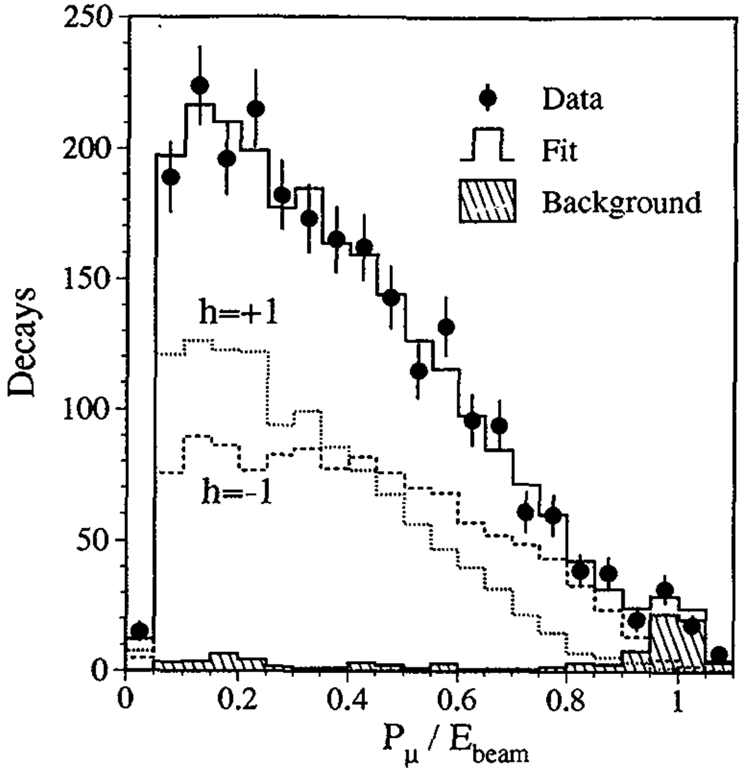

Figure 7.5: The spectrum of $\tau^- \to \mu^-\overline{\nu}_\mu\nu_\tau$ decays as a function of $x_\mu = E_\mu/E_{\rm beam}$. Also shown is the contribution from each helicity including backgrounds for that helicity. The hatched histogram shows the total background.

TEC and the muon chambers in $\tau^- \to \mu^-\overline{\nu}_\mu\nu_\tau$ decays. The systematic error due to possible differences in the data and Monte Carlo $\pi^\pm$ energy resolution is estimated by a comparison of the resolution derived independently from test beam data and Monte Carlo simulation. From this study, the $\pi^\pm$ energy resolution is parameterized as $\sigma_E/E = (55\pm5)\%/\sqrt{E(\text{ GeV})}+(8\pm1)\%$ and the uncertainty in the energy resolution is included in the systematic error.

The systematic uncertainty due to the background to $\tau^- \to \pi^-(\mathrm{K}^-)\nu_\tau$ is determined by varying the fraction of $\tau^- \to \rho^-\nu_\tau$, $\tau^- \to \mathrm{K}^{*\pm}\nu_\tau$ and $\mathrm{Z} \to \mu^+\mu^-(\gamma)$ decays by 10%, 20% and 30% respectively, accounting for statistical and systematic uncertainties in the estimation of these backgrounds in the Monte Carlo.

The result for $\tau^- \to \pi^-(\mathrm{K}^-)\nu_\tau$ is $\mathcal{P}_\tau = -0.148 \pm 0.046 \pm 0.033$. The $\pi^\pm$ energy spectrum together with the best fit Monte Carlo spectrum are shown in Fig. 7.6.

The decay channel $\tau^- \to \rho^-\nu_\tau$

$\mathcal{P}_\tau$ is determined from a two dimensional fit of $\cos\theta^*$ and $\cos\psi^*$ [85]. To take advantage of the variation of the sensitivity of $\mathcal{P}_\tau$ as a function of the $\rho^\pm$ invariant mass, the sample is divided into nine 100 MeV mass intervals from 0.35 GeV to 1.25 GeV and fitted separately in each interval.

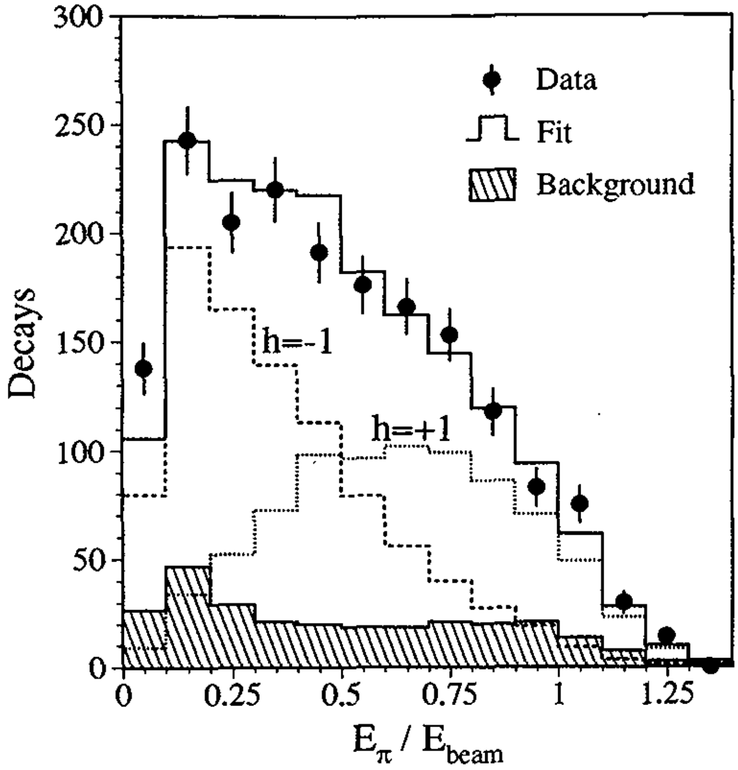

Figure 7.6: The spectrum of $\tau^- \to \pi^-(\mathrm{K}^-)\nu_\tau$ decays as a function of $x_\pi = E_\pi/E_{\mathrm{beam}}$. Also shown is the contribution from each helicity including backgrounds for that helicity. The hatched histogram shows the total background.

$\mathcal{P}_\tau$ is obtained by maximizing the likelihood function in a 20 × 20 matrix in the parameter space of $\cos\theta^*$ and $\cos\psi^*$ taking into account statistical errors in both the data and the Monte Carlo distributions. Owing to the large number of bins, we derive the probability for finding n data events in a bin given n' Monte Carlo events in the same bin for a Monte Carlo sample six times larger than the data sample assuming both the data and Monte Carlo follow a Poisson distribution. This probability is then used in a binned likelihood fit to determine $\mathcal{P}_\tau$.

Systematic errors due to the accuracy of the charged pion energy scale and due to background uncertainties are estimated using a procedure analogous to that used for the $\tau^- \to \pi^-(\mathrm{K}^-)\nu_\tau$ channel. In addition, the estimated accuracy of 1% in the energy scale of the π^0 is taken into account. The systematic error from uncertainties in the $\pi^\pm$ shower profile is estimated by a comparison of the opening angle between the $\pi^\pm$ and the π^0 in the data and in the Monte Carlo as a function of the difference in their energies in the BGO calorimeter. The bias of the central value of the fit due to limited Monte Carlo statistics is studied by fitting the data and Monte Carlo distributions to analytical formulae [87] and found to be negligible.

The fit yields $\mathcal{P}_\tau = -0.152 \pm 0.035 \pm 0.029$. Distributions of $\cos\psi^*$ together with the best fit Monte Carlo distributions are shown in Fig. 7.7 for four different ranges in $\cos\theta^*$.

As a cross check, a method using a neural network technique is applied to select the decays $\tau^- \to \rho^-\nu_\tau$ [89] with an efficiency of 54% in the fiducial volume. Since the selection is based on global energy/cluster distributions which cannot distinguish $\pi^\pm$ and π^0 in the BGO calorimeter, we can only measure the total energy of the $\rho^\pm$ (E_ρ) and the momentum of the $\pi^\pm$ ($P_{\pi^\pm}$).

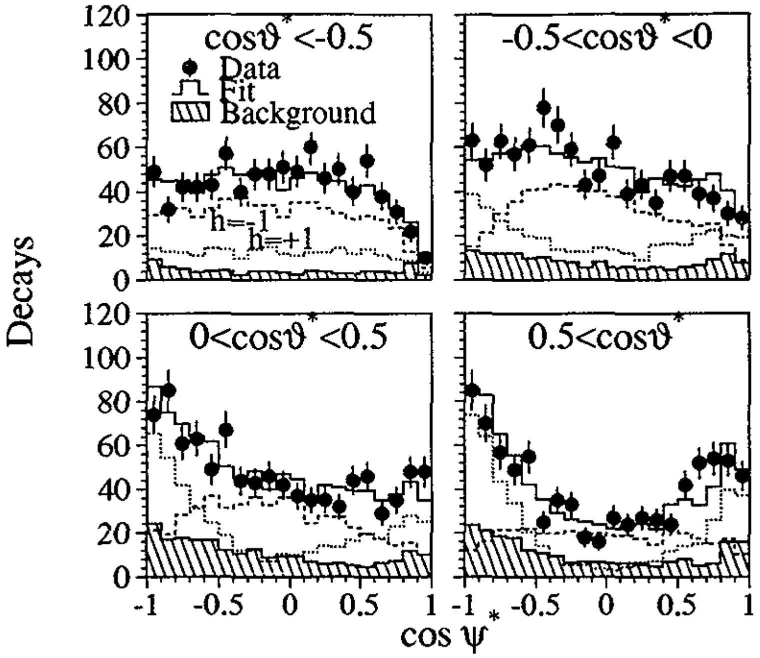

Figure 7.7: The spectra of $\tau^- \rightarrow \rho^- \nu_\tau$ decays as a function of $\cos\psi^*$ for four ranges of $\cos\theta^*$ (See text for definitions). Also shown is the contribution from each helicity including backgrounds for that helicity. The hatched histogram shows the total background.

The energy of the π^0 is then $E_{\pi^0} = E_\rho - P_{\pi^\pm}$. Using a binned maximum likelihood fit to a two dimensional distribution of $\cos\theta^*$ and $\cos\psi^*$ with 20 bins of each variable, we obtain a polarization of $P_\tau = -0.129 \pm 0.050 \pm 0.050$ which is consistent with the result above.

The decay channel $\tau^- \rightarrow \mathrm{a}_1^- \nu_\tau$

The polarization in the $\tau^- \rightarrow \mathrm{a}_1^- \nu_\tau$ channel is determined by a two dimensional fit with 20 bins in c_θ and 10 bins in c_ψ. In a manner similar to that used for the $\rho^\pm$ channel, a fit is performed taking care to account for the effects of limited Monte Carlo statistics in the likelihood function. The fit, performed for 473 decays with a three $\pi^\pm$ invariant mass less than 1.6 GeV, yields a result of $P_\tau = 0.105 \pm 0.164 \pm 0.093$.

Summary

The final results for each decay channel are summarized in Table 7.2. The weighted mean of all five decay modes is

$$\mathcal{P}_\tau = -0.132 \pm 0.026 \text{ (stat.)} \pm 0.021 \text{ (sys.)}. \tag{7.9}$$

In calculating the average, statistical correlations in events where both hemispheres are used, as well as systematic correlations in the energy calibration of $\pi^{\pm}$'s in the $\pi^-(\mathrm{K}^-)\nu_\tau$, $\rho^-\nu_\tau$ and $\mathrm{a}_1^-\nu_\tau$ channels are taken into account. All other systematic errors are assumed to be uncorrelated and are added in quadrature.

Our measurement of $\mathcal{P}_\tau$ implies that parity is violated in the neutral current process $\mathrm{Z} \rightarrow \tau^+\tau^-(\gamma)$, as has been previously found in other neutral current processes [90,91].

The above value for $\mathcal{P}_\tau$ will be used in section 8.7 to extract the effective couplings of the τ lepton to the weak neutral current and to determine the effective weak mixing angle.

7.2 τ decay properties

In this section we use the τ sample to measure the leptonic branching ratios of the τ decay and the τ lifetime. These two measurements are particularly interesting since they allow to measure the leptonic width of τ decay. The Standard Model predicts this width to have a simple relation to the muon decay width, since the matrix elements are the same and all leptons couple to the W boson with the same coupling constant. It thus allows to compare τ and μ couplings to the weak charged current. Furthermore, when comparing the leptonic width to the total width, one can extract the hadronic decay width of τ leptons. Via radiative QCD corrections, this gives a measure of the strong coupling constant $\alpha_s(m_\tau^2)$.

Z decay is a particularly clean source of τ leptons for such studies; because of the high center-of-mass energy, background contribution from low-multiplicity hadronic events are small. The good resolution of the L3 central detector yields a measurement of the τ lifetime competitive with previous high statistics determinations at lower energies [92] and other experiments at LEP [93–96]. For the determination of the lifetime we use two methods – one based on the decay length measurement and one based on the impact parameter distribution – and three samples – three-prong hadronic decays, one-prong hadronic decays and leptonic decays.

7.2.1 Determination of leptonic branching ratios

The sample of identified τ decays defined for the polarization measurement (see section 7.1) can also be used to determine the respective exclusive branching ratios. For tests of the universality of the weak charged current, the most important ones are the leptonic decays.

For this study, the $\tau^+\tau^-$ production and lepton identification criteria are basically as those used in 7.1, with the following modifications:

- $\mathrm{e}^+\mathrm{e}^- \rightarrow \mu^+\mu^-$ events are rejected by requiring muon candidates to have $p_\mu < 0.85E_{\mathrm{beam}}$, no other identified muon or minimum ionizing particle in the opposite hemisphere and an acoplanarity of more than 0.2° if the calorimetric energy is small;

Source	$\tau \rightarrow \mu\nu\nu$	$\tau \rightarrow e\nu\nu$
$\tau^+\tau^-$ selection	0.0016	0.0016
$\tau \rightarrow \ell$ selection	0.0009	0.0010
Detection efficiency	0.0022	0.0026
Acceptance	0.0025	0.0020
Background	-	0.0015
Total	0.0041	0.0038

Table 7.3: Summary of systematic errors for the leptonic branching ratios

- however, events where both τ leptons decay into muons are recovered if both muons are identified in all three layers of muon chambers, both have $p_\mu < 0.75 E_{\text{beam}}$ and no other particles are observed;
- $e^+e^- \rightarrow e^+e^-$ events are rejected by requiring that the total electromagnetic energy of the event be less than 85% of $\sqrt{s}$ and that no electron candidate has $E_e > 0.85 E_{\text{beam}}$;
- two-photon interactions are rejected by requiring a minimum total energy of 12 GeV and a minimum missing transverse momentum of 5 GeV.

We thus select a total of 2148 candidates for $\tau \rightarrow \mu\nu\nu$ and 2892 candidates for $\tau \rightarrow e\nu\nu$ with efficiencies of $(57.8 \pm 0.4)\%$ and $(74.1 \pm 0.3)\%$, respectively, inside the fiducial volume.

The background contained in the $\tau \rightarrow \mu\nu\nu$ sample is $(1.2 \pm 0.1)\%$ from non-muonic τ decays and $(0.5 \pm 0.1)\%$ from other reactions, mainly $e^+e^- \rightarrow \mu^+\mu^-$. The background for $\tau \rightarrow e\nu\nu$ is $(3.1 \pm 0.2)\%$ from non-electronic τ decays and $(2.0 \pm 0.3)\%$ from other reactions, mainly $e^+e^- \rightarrow e^+e^-$.

The branching ratios after taking into account the efficiency corrections and background subtractions are found to be

$$\begin{aligned} \mathrm{Br}(\tau \rightarrow \mu\nu_\mu\nu_\tau) &= 0.176 \pm 0.004\ (\text{stat.}) \pm 0.004\ (\text{sys.}) && (7.10) \\ \mathrm{Br}(\tau \rightarrow e\nu_e\nu_\tau) &= 0.179 \pm 0.004\ (\text{stat.}) \pm 0.004\ (\text{sys.}). && (7.11) \end{aligned}$$

The numbers given are fractions of the total number of observed τ leptons inside the fiducial region. The systematic errors are dominated by uncertainties in the estimation of acceptances and efficiencies as detailed in table 7.3. These are estimated by Monte Carlo calculation, varying acceptance boundaries as well as event and decay channel selection criteria.

The branching ratios found are in excellent agreement with the respective current world average values [46].

7.2.2 Determination of the τ lifetime

In this determination, we first measure the decay distance of the τ from its decays into three charged particles. The average position of the beam spot is used as the τ lepton's origin and the vertex determined from the decay products as its decay point. All these measurements are made in a plane transverse to the beam direction.

The average position of the beam spot in the L3 intersection point is measured for each LEP fill using hadronic events; it is determined by minimizing the sum of the squared distances of well measured high transverse momentum tracks to a common origin.

The size of the beam spot is determined from high transverse momentum tracks from the reactions $e^+e^- \to e^+e^-$ and $e^+e^- \to \mu^+\mu^-$. The distribution of their distance of closest approach (DCA) to the average beam position measures the size of the beam spot folded with the experimental resolution on both the track parameters and the average beam position. The distance between the two tracks at the average beam position, on the other hand, measures the experimental resolution on the DCA alone. By unfolding the contributions from the size of the beam spot and from the experimental resolution we obtain an effective r.m.s. beam spot size of $\sigma_x = (167 \pm 4)$ μm in the horizontal direction and $\sigma_y = (0 \pm 10)$ μm in the vertical direction. These numbers contain the uncertainty in the determination of the mean beam position.

The r.m.s. error on the distance of closest approach is $\langle \sigma_{\mathrm{DCA}} \rangle = (110 \pm 1)$ μm for particle momenta of 45 GeV when measured without further constraints. For lower momenta, a small additional contribution from multiple scattering inside the beryllium beam pipe is taken into account.

Three-prong decays

In selecting three-prong τ decays for the lifetime measurement from 1991 data, and imposing criteria on the correct assignment of charge in the hemisphere and in the total event, on track quality and on vertex determination, we obtain a total sample of 516 events. The background from other reactions in this sample is determined by Monte Carlo to be less than one event.

Figure 7.8 shows the distribution of the distance between the average position of the beam spot and the τ decay vertex — the decay distance distribution — for this sample. The sign of the decay distance is defined such that decay vertices in the τ production hemisphere carry a positive sign and those in the opposite hemisphere a negative sign. Also shown in figure 7.8 is the result of a binned maximum likelihood fit, which uses a probability density per bin proportional to the theoretical decay distance distribution folded with a Gaussian resolution function. The error on the decay distance, which enters into this convolution, is integrated over the observed error distribution, taking into account the contributions from both the size of the beam spot and the error on the decay vertex as determined from the covariance matrices of the track parameters.

The likelihood function is the product of these probability densities for all bins and is maximized with respect to the decay length λ. Using the average momentum of τ leptons in our sample of $(98.8 \pm 0.1)\%$ of the beam energy, and the observed scattering angle distribution, we thus obtain a first result for the τ lifetime

$$\tau_\tau = (0.315 \pm 0.022) \times 10^{-12}\mathrm{s}, \tag{7.12}$$

where the error is statistical only.

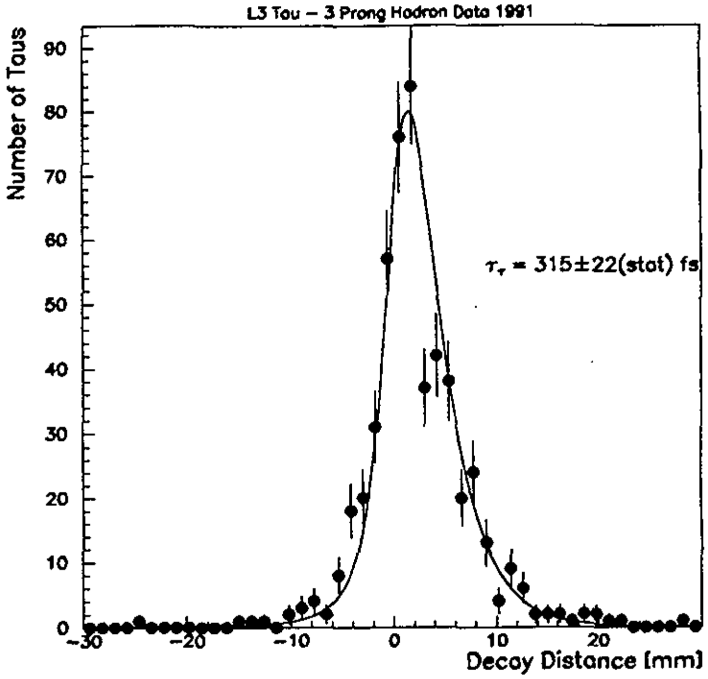

Figure 7.8: Decay length distribution for three-prong decays of the τ. Points are data, solid line is result of the fit as described in the text.

Hadronic one–prong decays

As a second, independent method we determine the τ lifetime from a measurement of the impact parameter in hadronic one-prong decays. The impact parameter δ of a track is given by the DCA to the average beam position of a fill; it is signed positive if the track intersects with the event's thrust axis in the direction of flight of the τ and negative if it intersects opposite to this direction.

The candidates for this measurement are selected in the same way as those for three-prong decays, except that exactly one track is required in each hemisphere of the event, each track must have a DCA to the average beam position of less than 2.0 mm and must not have been identified as a lepton. The sample then consists of 3372 candidates for τ decay into one charged hadron with an estimated background of $(1.35 \pm 0.70)\%$.

Figure 7.9 shows the distribution of the impact parameter δ_i for these events. To determine the average impact parameter δ, the sample is subjected to a binned maximum likelihood fit with a probability density derived from a convolution analogous to the one described above, Here, the relevant resolution is the error of the impact parameter measurement, folded with the r.m.s. size of the beam spot in the flight direction of the τ.

The conversion of the quantity δ into a τ lifetime is less direct than in the case of the decay distance measurement and proceeds via Monte Carlo simulation. For this purpose, high statistics samples of $e^+e^- \rightarrow Z \rightarrow \tau^+\tau^-$ with τ lifetimes between 0.004×10^{-12}s and 0.604×10^{-12}s were generated, the detector response simulated [83] and the simulated events run through

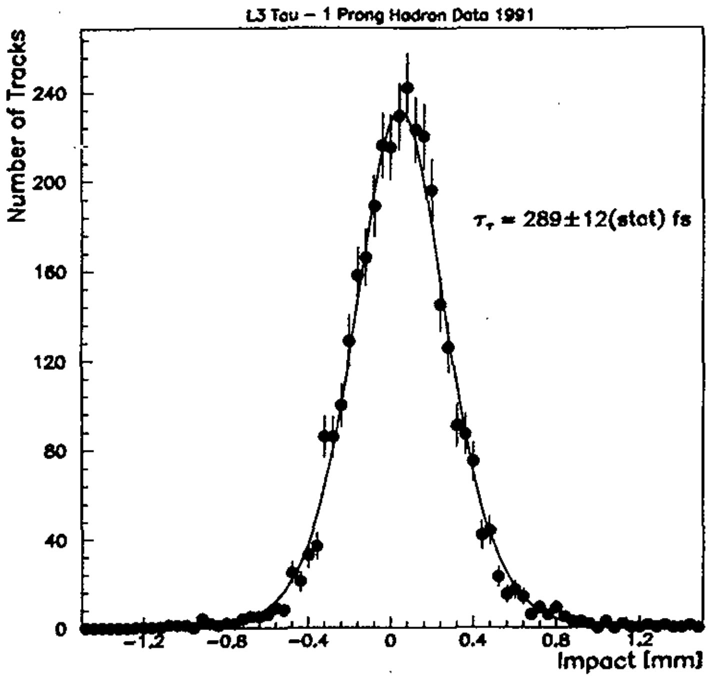

Figure 7.9: Impact parameter distribution for hadronic one-prong decays of the τ. Points are data, solid line is result of the fit as described in the text.

the same analysis as the data. The relation between the average impact parameter δ and the lifetime τ_τ is found to be linear. This method thus yields a τ lifetime

$$\tau_\tau = (0.289 \pm 0.012) \times 10^{-12}\mathrm{s}, \tag{7.13}$$

where the error is statistical only. The expected δ distribution corresponding to the best fit is overlayed on figure 7.9.

Leptonic decays

A final, independent measurement can be obtained using the leptonic decays of the τ lepton. For these decays, the transverse momenta of the leptons can be determined with high precision (1% and 2.5%, respectively) from the electromagnetic calorimeter or the muon chambers. It is thus possible to remove the uncertainty in the impact parameter due to the limited precision of curvature measurements in the TEC and to improve the impact resolution. With the momentum constraint, we obtain an impact resolution of 59μm for 45 GeV tracks. Using a sample of 1855 leptonic decays from 1991 data, we obtain the impact parameter distribution shown in figure 7.10. Performing a binned maximum likelihood fit analogous to the one for hadronic one-prong decays, we obtain a lifetime of

$$\tau_\tau = (0.287 \pm 0.017) \times 10^{-12}\mathrm{s}. \tag{7.14}$$

The error is statistical only.

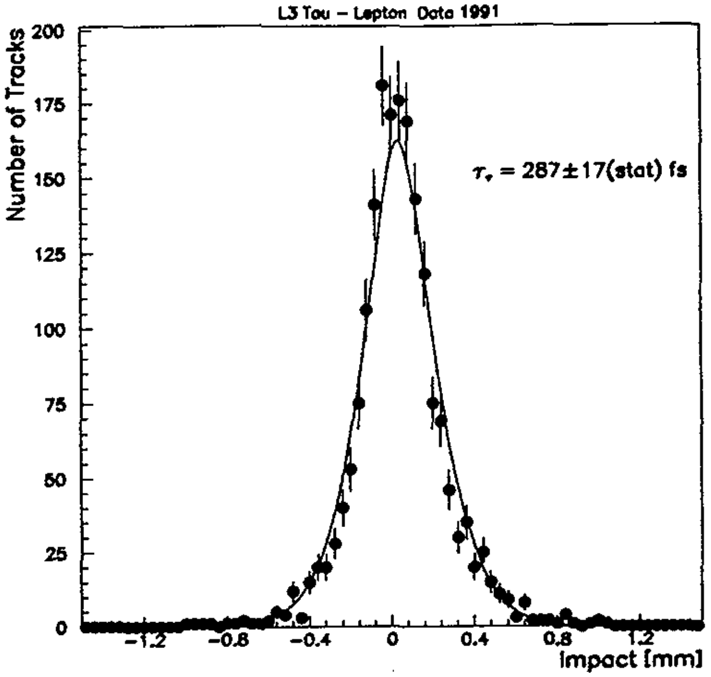

Figure 7.10: Impact parameter distribution for leptonic one-prong decays of the τ. Points are data, solid line is result of the fit as described in the text.

Since the samples for all methods are exclusive, the results can be combined. The systematic errors for the three methods are, however, correlated. Systematic errors in this measurement occur mainly by miscalibration of the central tracking chamber and by systematic under- or overestimation of the decay distance error. Varying the two main parameters of the chamber's time distance relation, i.e. the drift velocity and the zero point of the drift time measurement, by the estimated systematic uncertainties (0.3% and 5 ns, respectively) around their calibrated values, in the correlated fashion allowed by the current calibration method, we obtain a variation of the lifetime by ±10 fs. Systematically scaling the error σ of the decay length or the impact parameter in each event by a factor deviating from one by ±8% and ±3%, respectively, and varying all other parameters of the fit function by their estimated uncertainties, we observe a variation of the lifetime by ±5 fs. This error is estimated to cover uncertainties in the determination of the track parameter errors as well as systematic deviations of the single-hit position error from its estimated behavior. Lastly, the error introduced by a possible deviation from linearity, as verified by determining the lifetime in Monte Carlo samples generated with a range of lifetimes between 4 and 400 fs, is estimated to be ±3 fs. We thus conclude that these methods determine the τ lifetime with a total systematic uncertainty of $\pm 0.012 \times 10^{-12}$s.

We thus obtain a combined result for the τ lifetime

$$\tau_\tau = (0.293 \pm 0.009 \text{ (stat.)} \pm 0.012 \text{ (sys.)}) \times 10^{-12}\text{s}. \qquad (7.15)$$

As a cross check on the maximum likelihood method used in this measurement, we also determine a lifetime using the trimmed mean value of the three distributions. This estimator, which does not require a detailed model of the distributions' shape, give a lifetime value of

$(0.286 \pm 0.012) \times 10^{-12}$s, in excellent agreement with the value from the maximum likelihood fit.

Our result is smaller than the current world average of $(0.303 \pm 0.008) \times 10^{-12}$s [46], although within statistical and systematic errors. Our measurement also agrees with the theoretical expectation from the Standard Model

$$\tau_\tau = \tau_\mu \left(\frac{G_F^\mu}{G_F^\tau}\right)^2 \left(\frac{m_\mu}{m_\tau}\right)^5 \mathrm{Br}(\tau \to e\nu_e\nu_\tau) \tag{7.16}$$

where τ_μ is the measured muon lifetime and G_F^μ and G_F^τ are the Fermi coupling constants of μ and τ. This relation is affected by Standard Model radiative corrections only at the permill level [97]. Using our own result on the τ branching fraction into electrons and a recent preliminary determination of the τ mass of 1776.9 ± 0.5 MeV from BES at BEPC [98], the relation predicts a τ lifetime compatible with our measurements for equal coupling constants to the weak charged current, *i.e.* assuming $\mu - \tau$ universality. Conversely, we can convert relation 7.16 into a measurement of the coupling constant ratio; we then obtain

$$\frac{G_F^\tau}{G_F^\mu} = 0.998 \pm 0.028. \tag{7.17}$$

in agreement with $\mu - \tau$ universality for the charged current coupling constants.

Chapter 8

Determination of the Electroweak Parameters

The Glashow-Weinberg-Salam model of electroweak interactions [3], together with quantum chromodynamics [11], defines the Standard Model. In this model, the process $e^+e^- \to f\bar{f}$ is governed by γ and Z exchange. The lowest order diagrams need to be corrected for higher order electroweak and QCD contributions. The electroweak corrections can be subdivided into two parts: (i) QED corrections, which consist of diagrams with extra real or virtual photons; they are dominated by initial state radiation. (ii) Weak corrections, which involve propagator corrections, vertex corrections and box diagrams. Near the Z resonance, weak corrections can be factorized from the QED corrections.

The measurements that are carried out around the Z resonance from $e^+e^- \to f\bar{f}$ lead to a determination of the total cross sections σ, the forward-backward asymmetries A_{fb} and average polarization $\mathcal{P}_\tau$ as a function of $\sqrt{s}$ (for a general review see reference 99). From cross sections one determines m_Z, the total (Γ_Z) and partial widths (Γ_f) of the Z, while the inclusion of A_{fb} and $\mathcal{P}_\tau$ yields vector ($\bar{g}_V$) and axial-vector ($\bar{g}_A$) couplings of the Z to $f\bar{f}$ pairs.

8.1 Lowest order cross sections and asymmetries

The lowest order expression for the cross section σ of $e^+e^- \to f\bar{f}$ ($f \neq e$) with massless fermions is given by three terms : Z exchange (σ^0_Z), γ exchange (σ^0_γ) and their interference ($\sigma^0_{\gamma Z}$):

$$\sigma^0(s) = \sigma^0_Z + \sigma^0_\gamma + \sigma^0_{\gamma Z} \tag{8.1}$$

where,

$$\begin{aligned}
\sigma^0_Z &= \frac{12\pi}{m_Z^2}\frac{\Gamma_f\Gamma_e}{\Gamma_Z^2}\frac{s\Gamma_Z^2}{(s-m_Z^2)^2+m_Z^2\Gamma_Z^2} && (8.2)\\
\sigma^0_\gamma &= \frac{4\pi\alpha^2}{3s}Q_f^2 N_c^f && (8.3)\\
\sigma^0_{\gamma Z} &= -\frac{2\sqrt{2}\alpha}{3}Q_f G_F N_c^f g_{Ve} g_{Vf}\frac{(s-m_Z^2)m_Z^2}{(s-m_Z^2)^2+m_Z^2\Gamma_Z^2} && (8.4)
\end{aligned}$$

with the partial width of Z → $\mathrm{f\bar{f}}$ as

$$\Gamma_{\mathrm{f}} = \frac{G_F m_{\mathrm{Z}}^3}{6\sqrt{2}\pi}(g_{\mathrm{Vf}}^2 + g_{\mathrm{Af}}^2)N_c^{\mathrm{f}} \tag{8.5}$$

Q_{f} denotes the charge of the fermion f, the color factor N_c^{f} is 3 for quarks and 1 for leptons., G_F is the Fermi constant deduced from muon decay.

The vector (g_{V}) and axial-vector (g_{A}) couplings are defined by

$$\begin{aligned} g_{\mathrm{Vf}} &= I_3^{\mathrm{f}} - 2Q_{\mathrm{f}}\sin^2\theta_{\mathrm{W}} \\ g_{\mathrm{Af}} &= I_3^{\mathrm{f}} \end{aligned}$$

with the electroweak mixing angle

$$\sin^2\theta_{\mathrm{W}} = 1 - m_{\mathrm{W}}^2/m_{\mathrm{Z}}^2 \tag{8.6}$$

I_3^{f} is the third component of the weak isospin for the fermion f.

On the peak ($\sqrt{s} = m_{\mathrm{Z}}$), the forward-backward asymmetry A_{fb} to lowest order is given by

$$A_{\mathrm{fb}}^0 = 3 \cdot \frac{g_{\mathrm{Ve}}g_{\mathrm{Ae}}}{g_{\mathrm{Ve}}^2 + g_{\mathrm{Ae}}^2} \cdot \frac{g_{\mathrm{Vf}}g_{\mathrm{Af}}}{g_{\mathrm{Vf}}^2 + g_{\mathrm{Af}}^2} \tag{8.7}$$

The tau polarization $\mathcal{P}_\tau$ in lowest order can be expressed as

$$\mathcal{P}_\tau^0 = -\frac{2g_{\mathrm{V}\tau}g_{\mathrm{A}\tau}}{g_{\mathrm{V}\tau}^2 + g_{\mathrm{A}\tau}^2} \tag{8.8}$$

In contrast to the production of charged fermions, the reaction $\mathrm{e^+e^-} \to \nu\bar{\nu}\gamma$ is itself a higher order process. The cross section can be written as [100]

$$\frac{d^2\sigma}{dE_\gamma d\cos\theta_\gamma} = H(E_\gamma, \cos\theta_\gamma, s)\sigma_0(s') \tag{8.9}$$

where H is a radiator function for photons of energy E_γ emitted at polar angle θ_γ, s is the square of the center of mass energy, and $\sigma^0(s')$ is the reduced cross section for the process $\mathrm{e^+e^-} \to \nu\bar{\nu}$ in the new center of mass system, given by $s' = s(1 - 2E_\gamma/\sqrt{s})$. In lowest order and by approximating the W contribution by a four-point interaction, σ^0 is given by [37, 100]

$$\sigma^0(s) = \frac{G_F^2 s}{12\pi}\left(2 + \frac{N_\nu(g_{\mathrm{V}}^2 + g_{\mathrm{A}}^2)}{[1 - s/m_{\mathrm{Z}}^2]^2 + \Gamma_{\mathrm{Z}}^2/m_{\mathrm{Z}}^2} + \frac{2(g_{\mathrm{V}} + g_{\mathrm{A}})[1 - s/m_{\mathrm{Z}}^2]}{[1 - s/m_{\mathrm{Z}}^2]^2 + \Gamma_{\mathrm{Z}}^2/m_{\mathrm{Z}}^2}\right) \tag{8.10}$$

The dominant second term is proportional to the number of light neutrino families N_ν and represents the square of the amplitude for Z production. The first term arises from the square of the W exchange diagram, which contributes only to ν_e production, and the last one is due to W-Z interference. The sum of the first and third terms contributes less than 3% to the total cross section in the energy range analyzed here [100]. The contribution to σ^0 from the term proportional to N_ν remains dominant when higher-order corrections are included in the calculation.

8.2 Parameters of the Standard Model

The basic input parameters, i.e. the renormalised physical parameters of the electroweak interaction in the Standard Model are α, m_Z, m_W, m_H and the fermion masses. QCD adds one more parameter, the strong coupling constant α_s, which can be measured at LEP as discussed in section 10.2.

The fermion masses, with the exception of the top mass, and α are known with sufficient precision. The effects on the radiative corrections due to the mass of the Higgs particle are too small to be measurable. While the Z mass can be measured with high precision at LEP, the W mass cannot be determined directly at LEP at $\sqrt{s} = m_Z$. Therefore one constrains the W mass by a relation obtained from the Fermi coupling constant G_F measured in the muon decay

$$\frac{G_F}{\sqrt{2}} = \frac{\pi\alpha}{2} \cdot \frac{1}{m_Z^2 \sin^2\theta_W \cos^2\theta_W} \cdot \frac{1}{1 - \Delta r} \qquad (8.11)$$

where $\sin^2\theta_W$ is defined by

$$\sin^2\theta_W = 1 - \frac{m_W^2}{m_Z^2} \qquad (8.12)$$

and Δr takes into account the electroweak radiative corrections. With this procedure the main unknown parameters of the Standard Model are m_Z, m_t and α_s. m_Z and α_s can be measured with high precision at the Z resonance and m_t can be estimated.

8.3 Radiative Corrections

The lowest order expressions given in section 8.1 must be corrected for electroweak and QCD radiative effects. The electroweak corrections can be subdivided into two parts:

(i) QED corrections, which take into account real photon bremsstrahlung and virtual photon loops; these corrections are dominated by initial state radiation.

(ii) Weak corrections, which involve vector boson propagator corrections, vertex corrections and box diagrams with at least one vector boson exchanged [101,102].

Several programs [103–105] calculate cross sections in the Standard Model framework; they include weak radiative corrections to order $\mathcal{O}(\alpha)$. We use the analytical program ZFITTER [26] for calculating the theoretical predictions for cross sections and asymmetries. ZFITTER includes electroweak radiative corrections to $\mathcal{O}(\alpha)$ and a common exponentiation of initial and final state bremsstrahlung. Furthermore, the $\mathcal{O}(\alpha)$ corrections are supplemented with the $\mathcal{O}(\alpha, \alpha_s)$ and the leading $\mathcal{O}(\alpha^2 m_t^4/m_W^4)$ corrections from top quark insertions in the gauge boson self-energies. Comparisons have been made between cross sections as obtained from ZFITTER and other programs [103, 104] and one finds agreement between these programs within 0.5%.

8.4 Fitting Procedure and Effective Coupling Constants

For the determination of the electroweak parameters from our measurements we proceed in two ways:

a) We perform fits in the standard model framework with three lepton families and only one Higgs doublet. The free input parameters to the fit are thus m_Z, m_H and m_t. The values of $\sin^2\theta_W$, m_W and other parameters can be derived from this set. The radiative corrections can be calculated exactly up to the orders quoted previously and varied according to the values of the input parameters.

b) We determine the mass, the total width, the different partial widths of the Z and other electroweak parameters taking into account only QED radiative corrections. We call this method 'model-independent', since we do not impose relations between the measured quantities predicted by the Standard Model.

Model-independent fits are possible because the radiative corrections can be separated into QED corrections and weak corrections as mentioned in the previous section. The QED corrections, which depend on the acceptance of the detector and on cuts used in the analysis, are always taken into account for calculating the theoretical predictions. Since the weak corrections cannot be calculated exactly outside the framework of the Standard model we do not apply weak corrections, but absorb them into the definition of the fitted parameters. Thus we must interpret these as effective parameters. For this purpose, the following substitutions in the formulae given in section 8.1 are made [99]:

$$\sin^2\theta_W \longrightarrow \sin^2\overline{\theta}_W \tag{8.13}$$

$$g_{Af} \longrightarrow \bar{g}_{Af} \equiv \sqrt{\bar{\rho}}g_{Af} \tag{8.14}$$

$$g_{Vf} \longrightarrow \bar{g}_{Vf} \equiv \sqrt{\bar{\rho}}(I_3^f - 2Q_f \sin^2\overline{\theta}_W) \tag{8.15}$$

$$\rho \longrightarrow \bar{\rho} = 1 + \Delta\bar{\rho} \tag{8.16}$$

The parameter ρ is the ratio of the neutral and charge current coupling constant and is unity in the Standard Model at tree level. For the case f = b, where additional vertex corrections are important, one must replace $\bar{\rho}$ by $\bar{\rho}_b = \bar{\rho}(1 - \frac{4}{3}\Delta\bar{\rho})$ and $\sin^2\overline{\theta}_W$ by $\sin^2\overline{\theta}_W(1 + \frac{2}{3}\Delta\bar{\rho})$, where $\Delta\bar{\rho} \simeq (3G_F m_t^2)/(8\pi^2\sqrt{2})$.

The main theoretical inputs to the fitting procedure for the model-independent method are:

- initial and final state QED corrections including photon vacuum polarization;
- energy dependent Breit-Wigner shape of the Z resonance;
- use of Standard Model to calculate the $\gamma - Z$ interference term;[1]
- calculation of the t channel and the $s-t$ interference contribution for $e^+e^- \to e^+e^-$ data, using the programs ALIBABA [31] or GCR [18] which include $\mathcal{O}(\alpha^2)$ radiative corrections (see section 5.4).

---

[1] To see the effect of this term on the fitted parameters, we varied m_t in the range from 90 to 250 GeV and m_H from 60 to 1000 GeV and found that the fitted value of m_Z changes by $^{+0.5}_{-1.0}$ MeV; the change in other parameters is less than 5% of their fitted error.

8.5 Experimental systematic errors

In general, experimental systematic errors on a set of N measured quantities are correlated. This has been taken into account in the error matrix approach [106]. In this method one defines the χ^2 as

$$\chi^2 = \Delta^T V^{-1} \Delta \tag{8.17}$$

where Δ is a column vector with elements as $(\sigma^{\rm th} - \sigma^{\rm exp})$ and V is the $N \times N$ error correlation matrix between measurements. The diagonal elements of V are given by the quadratic sum of statistical and systematic errors, while the off diagonal elements are given by the product of the common systematic errors. This can be generalized also to the common systematic error between different data sets.

In addition to the experimental errors one has to take into account the errors on the center-of-mass energy. These uncertainties have been estimated by the Working Group on LEP energy [24], as discussed in section 2.11. The error on the absolute calibration of the LEP center-of-mass energy is 26 MeV for 1990, determined at $\sqrt{s} = 91.2$ GeV, 18 MeV (at $\sqrt{s} = 91.2$ GeV) for the period before and 5.3 MeV (at $\sqrt{s} = 93$ GeV) for the period after August 14, 1991. Including errors on individual beam energy values due to non-linearity, random setting errors and systematic point-to-point setting errors leads to an error of 6.3 MeV on $m_{\rm Z}$ and 4.9 MeV on $\Gamma_{\rm Z}$ originating from the LEP energy calibration [24].

8.6 Z mass, total width and partial widths

In this section we present results from 'model independent' fits to determine the mass, the total and partial widths of the Z from combined 1990 and 1991 data. This determination only uses the total cross sections for $e^+e^- \to$ hadrons, e^+e^-, $\mu^+\mu^-$ and $\tau^+\tau^-$ as a function of $\sqrt{s}$. The fitted quantities are then: $m_{\rm Z}$, $\Gamma_{\rm Z}$, $\Gamma_{\rm had}$, Γ_e, Γ_μ and Γ_τ. Values of the parameters from this fit are summarized in table 8.1.

Parameters	Six parameter fit	Four parameter fit
$m_{\rm Z}$(MeV)	$91195 \pm 6 \pm 7$ (LEP)	$91195 \pm 6 \pm 7$ (LEP)
$\Gamma_{\rm Z}$(MeV)	$2490 \pm 10 \pm 5$ (LEP)	$2490 \pm 10 \pm 5$ (LEP)
$\Gamma_{\rm had}$(MeV)	1750 ± 13	1747 ± 11
Γ_e(MeV)	83.0 ± 0.6	
Γ_μ(MeV)	82.8 ± 1.0	
Γ_τ(MeV)	84.6 ± 1.2	
Γ_ℓ(MeV)		83.1 ± 0.5

Table 8.1: *Six and four parameter fits to the cross section data of* $e^+e^- \to$ hadrons, $e^+e^-, \mu^+\mu^-$ *and* $\tau^+\tau^-$.

The mass and total width of the Z thus determined are :

$$m_{\rm Z} = 91195 \pm 6 \pm 7 \text{ (LEP) MeV} \tag{8.18}$$

$$\Gamma_{\rm Z} = 2490 \pm 10 \pm 5 \text{ (LEP) MeV} \tag{8.19}$$

where the second errors are due to uncertainties in the LEP energy.

The partial widths Γ_e, Γ_μ and Γ_τ are in good agreement with one another, supporting the hypothesis of lepton universality. In a second approach, we thus impose lepton universality. The four fitted parameters are then: m_Z, Γ_Z, Γ_{had} and Γ_ℓ. Values of the parameters from this fit are also summarized in table 8.1. They yield the following values of the hadronic and leptonic widths of the Z :

$$\Gamma_{\mathrm{had}} = 1747 \pm 11 \text{ MeV} \tag{8.20}$$
$$\Gamma_\ell = 83.1 \pm 0.5 \text{ MeV} \tag{8.21}$$

The ratio R_{had} of these two quantities is measured to be

$$R_{\mathrm{had}} = \Gamma_{\mathrm{had}}/\Gamma_\ell = 21.00 \pm 0.15 \tag{8.22}$$

It is basically independent of the top quark mass due to a cancellation of top mass terms and can be used (see chapter 10) to determine the strong coupling constant α_s.

All these results and the parameters derived in the following sections agree with the measurements of the other LEP experiments [107].

8.6.1 Number of light neutrino families

The number of light ν families, N_ν, has been obtained in the following way. The invisible width of the Z, Γ_{inv}, is defined as

$$\Gamma_{\mathrm{inv}} = \Gamma_Z - \Gamma_{\mathrm{had}} - 3\,\Gamma_\ell \tag{8.23}$$

where Γ_ℓ is the charged leptonic width as obtained from the four parameter fit (see table 8.1). From the data in table 8.1, we determine

$$\Gamma_{\mathrm{inv}} = 494.0 \pm 9.6 \text{ MeV}. \tag{8.24}$$

One can calculate N_ν simply from $(\Gamma_{\mathrm{inv}}/\Gamma_\nu)$ with Γ_ν taken from the Standard Model, but Γ_ν depends on m_t and m_H. In order to minimize the dependence on m_t and m_H we use Standard Model numbers as a ratio $(\Gamma_\ell/\Gamma_\nu)_{SM} = 0.5015 \pm 0.0007$; the small error takes into account the variation due to m_t in the range 100 to 200 GeV and m_H in the range 50 to 1000 GeV. The number of neutrinos with $m_\nu \ll m_Z/2$, is then calculated as follows:

$$N_\nu = \frac{\Gamma_{\mathrm{inv}}}{\Gamma_\ell}\left(\frac{\Gamma_\ell}{\Gamma_\nu}\right)_{\mathrm{SM}}. \tag{8.25}$$

The value of N_ν thus determined is

$$N_\nu = 2.98 \pm 0.06. \tag{8.26}$$

The error includes statistical and systematic uncertainties.

This value can be compared to the one obtained from the directly measured cross section for $e^+e^- \rightarrow \nu\bar{\nu}\gamma$ (see section 5.6). Figure 5.17 shows the measured cross section together with the expectation for different numbers of light neutrino families. The best fit to the measured cross section is obtained for

$$N_\nu = 3.14 \pm 0.24\ \text{(stat.)} \pm 0.08\ \text{(sys.)}, \tag{8.27}$$

in excellent agreement with the determination from the invisible width.

8.7 Effective weak neutral current coupling constants

Using the leptonic forward-backward asymmetries A_{fb} as well as the τ polarization $\mathcal{P}_\tau$ in addition to the total cross section data, one can determine the Z vector and axialvector couplings $\bar{g}_\mathrm{V}$ and $\bar{g}_\mathrm{A}$ to lepton pairs. Inclusion of the τ polarization significantly improves the errors obtained for $\bar{g}_\mathrm{V}$ and $\bar{g}_\mathrm{A}$ and determines the relative sign of these couplings. In the fitting procedure lepton universality is first not assumed. The nine fitted parameters are then: m_Z, Γ_Z, σ^0_had $\bar{g}_{\mathrm{Ae}}$, $\bar{g}_{\mathrm{Ve}}$, $\bar{g}_{\mathrm{A}\mu}$, $\bar{g}_{\mathrm{V}\mu}$, $\bar{g}_{\mathrm{A}\tau}$ and $\bar{g}_{\mathrm{V}\tau}$, where σ^0_had is the measured hadronic cross section on the peak corrected for photon radiation.

Parameter	Nine parameter fit	Five parameter fit
m_Z(MeV)	$91195 \pm 6 \pm 7$ (LEP)	$91195 \pm 6 \pm 7$ (LEP)
Γ_Z(MeV)	$2490 \pm 10 \pm 5$ (LEP)	$2490 \pm 10 \pm 5$ (LEP)
σ^0_had (nb)	41.34 ± 0.28	41.34 ± 0.28
$\bar{g}_{\mathrm{Ae}}$	-0.4980 ± 0.0021	
$\bar{g}_{\mathrm{Ve}}$	$-0.040^{+0.013}_{-0.011}$	
$\bar{g}_{\mathrm{A}\mu}$	$-0.4968^{+0.0050}_{-0.0037}$	
$\bar{g}_{\mathrm{V}\mu}$	$-0.048^{+0.021}_{-0.033}$	
$\bar{g}_{\mathrm{A}\tau}$	-0.5032 ± 0.0038	
$\bar{g}_{\mathrm{V}\tau}$	-0.037 ± 0.008	
$\bar{g}_\mathrm{A}$		-0.4986 ± 0.0015
$\bar{g}_\mathrm{V}$		$-0.040^{+0.006}_{-0.005}$

Table 8.2: Nine and five parameter fits to the cross section, lepton asymmetry and tau polarization data.

Results from this fit are given in the first column of table 8.2. The relative sign of the vector- and axialvector coupling to the tau is determined to be positive. Since all other signs for the coupling constants are not determined in this fit, they are asumed negative. Again, the results are in good agreement with a universal weak neutral current coupling to charged leptons. The fit is thus repeated imposing that $\bar{g}_\mathrm{V}$ and $\bar{g}_\mathrm{A}$ are the same for all charged leptons, reducing the number of free parameters to five. The result is shown in the second column of table 8.2.

Figures 5.2, 5.4, 5.5, 5.8, 5.9, 5.12, 5.14 display the fitted curves from the five parameter fit superimposed on the data. The quality of the fit is good ($\chi^2 = 82$ for 100 degrees of freedom). One sees that the value of $\bar{g}_\mathrm{V} = -0.040 \pm 0.006$ is significantly different from zero and, together with a non-vanishing value of $\bar{g}_\mathrm{A}$, indicates a parity violating component of the weak neutral current interaction. Figure 8.1 shows the region in the $\bar{g}_\mathrm{V}$ *vs.* $\bar{g}_\mathrm{A}$ plane allowed by the measurements. The Standard Model predictions are also shown in the figure.

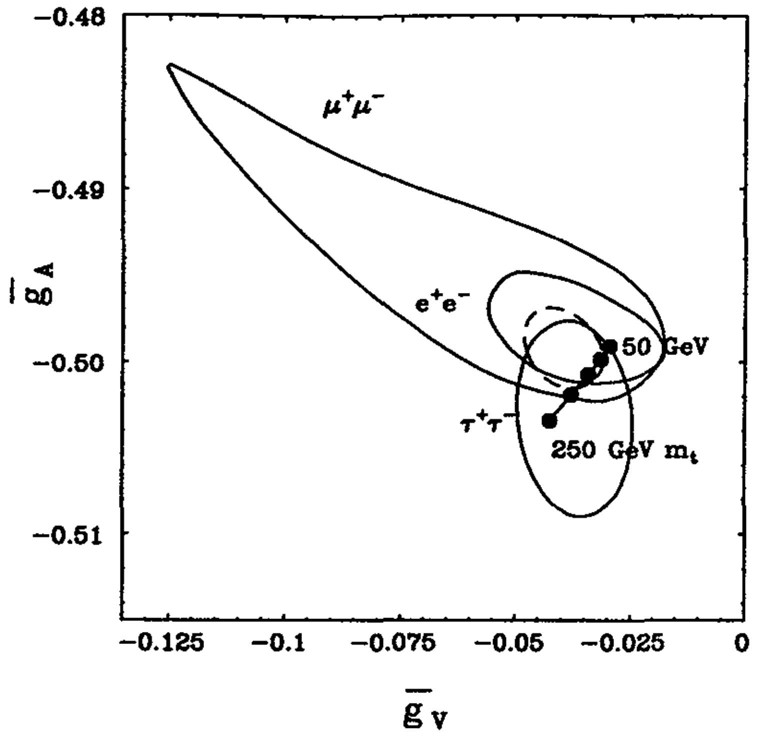

Figure 8.1: The 68% confidence level contours of $\bar{g}_V$ *vs.* $\bar{g}_A$ along with standard model predictions for different values of m_t. The dashed line corresponds to the contour asuming lepton universality.

8.7.1 Effective electroweak mixing angle

The value of $\sin^2\overline{\theta}_W$ which was introduced in section 8.3 can be determined in the following ways:

a) **Using leptonic cross section and asymmetry data:** This is done by carrying out a simultaneous fit to the cross section and lepton asymmetry data, choosing the lepton parameters as $\bar{\rho}$ and $\sin^2\overline{\theta}_W$ instead of $\bar{g}_V$ and $\bar{g}_A$. This five parameter fit gives:

$$\begin{aligned} \bar{\rho} &= 0.993 \pm 0.006 && (8.28) \\ \sin^2\overline{\theta}_W &= 0.2283 \pm 0.0032. && (8.29) \end{aligned}$$

b) **Using the value of τ polarization:** Constraining m_Z and Γ_Z to the measured values given in table 8.1, the value of $\mathcal{P}_\tau = -0.132 \pm 0.033$ as given in section 7.1 leads to $\sin^2\overline{\theta}_W = 0.2326 \pm 0.0043$.

c) **Using the value of $A_{b\bar{b}}$:** The value of $A_{b\bar{b}} = 0.086 \pm 0.017$ as given in equation 6.22 and the values of m_Z and Γ_Z as given in table 8.1 lead to a value of $\sin^2\overline{\theta}_W = 0.2336 \pm 0.0029$.

These results are summarized in figure 8.2, showing the excellent agreement between the independent methods to determine $\sin^2\overline{\theta}_W$ from asymmetry data. Carrying out a simultaneous fit to lepton asymmetry, τ polarisation and $A_{b\bar{b}}$, one obtains a value of $\sin^2\overline{\theta}_W = 0.2318 \pm 0.0021$.

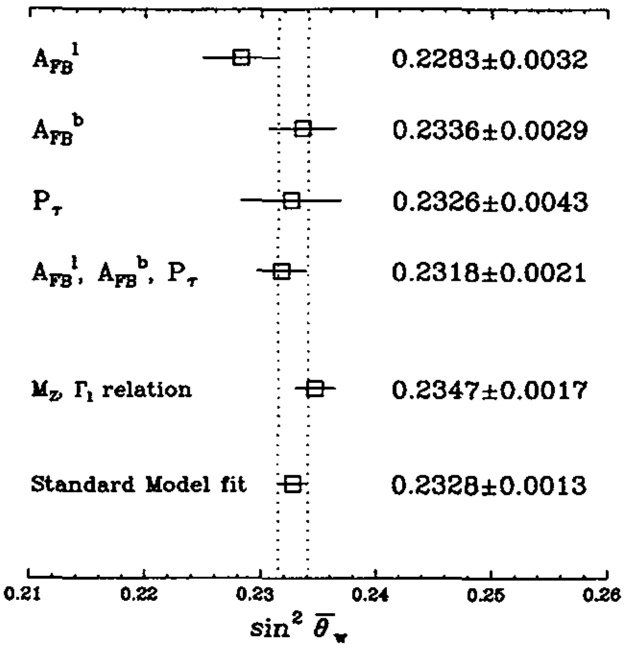

Figure 8.2: A comparison of the independent measurements of $\sin^2\overline{\theta}_W$.

These measurements can be compared to a determination of the mixing angle using the Standard Model relation between the mass and the leptonic width of the Z. In the improved Born approximation, it can be written as [108]:

$$\Gamma_\ell = \frac{\alpha(m_Z) m_Z K_{TH}}{48 \sin^2\overline{\theta}_W \cos^2\overline{\theta}_W}\left[1 + (1 - 4\sin^2\overline{\theta}_W)^2\right](1 + \frac{3\alpha}{4\pi}) \tag{8.30}$$

where K_{TH} depends mildly on the values of m_t and m_H and its value is $1.0070^{+0.0012}_{-0.0024}$ [109] with m_t and m_H in the range 90 to 200 GeV and 50 to 1000 GeV, respectively. Using the values of Γ_ℓ and m_Z from the four parameter fit, one obtains

$$\sin^2\overline{\theta}_W = 0.2347 \pm 0.0017 \pm 0.0004$$

where the second error is due to unknown top and Higgs masses. The agreement to the value obtained from asymmetries is excellent.

Finally, a joint fit to all cross section and asymmetry data in the framework of the Standard Model determines $\sin^2\overline{\theta}_W$ as a derived quantity (see section 8.8.2). One obtains a value of $\sin^2\overline{\theta}_W = 0.2328 \pm 0.0013$.

8.7.2 Quark Electroweak coupling constants

Using measurements of isolated hard photons produced in hadronic Z decays (see section 5.5), we have obtained the effective quark electroweak couplings, $c_{u,d} = 4(\bar{g}_V^2 + \bar{g}_A^2)_{u,d}$, where the subscripts u and d denote charge +2/3 (u-type) and charge −1/3 (d-type) quarks.

The general form of a distribution derived from the decay of a Z into a quark-antiquark pair, together with a photon radiated from one of the quarks, is

$$d\sigma(\mathrm{Z} \to \mathrm{q\bar{q}}\gamma) = \mathcal{F} \times \mathcal{N}, \tag{8.31}$$

with

$$\mathcal{N} = 2c_{\mathrm{u}}{Q_{\mathrm{u}}}^2 + 3c_{\mathrm{d}} \cdot {Q_{\mathrm{d}}}^2, \tag{8.32}$$

in the approximation that all quarks are massless. We determine $\mathcal{N}$ with a simultaneous fit of three direct photon distributions to the predictions of $\mathcal{O}(\alpha\,\alpha_s)$ matrix-element calculations of $\mathcal{F}$ [110], finding

$$\mathcal{N} = 1.32 \pm 0.13(\mathrm{exp.}) \pm 0.07(\mathrm{theor.}). \tag{8.33}$$

Figure 8.3 shows this result as a broad band. We combine this result with an independent constraint on the quark electroweak couplings derived from the total hadronic decay width of the Z (see section 8.6) [2]

$$2c_{\mathrm{u}} + 3c_{\mathrm{d}} = 6.736 \pm 0.047, \tag{8.34}$$

which is shown in figure 8.3 as a narrow band, and thus obtain the individual values of the u- and d-type quark electroweak couplings

$$c_{\mathrm{u}} = 0.92 \pm 0.22, \quad c_{\mathrm{d}} = 1.63 \pm 0.14. \tag{8.35}$$

These values can be compared to the electroweak quark couplings calculated within the framework of the Standard Model. Using our measurements of the effective weak mixing angle, $\bar{\theta}$, and the weak correction, $\bar{\rho}$, (see section 8.3) finding

$$c_{\mathrm{u}} = 1.145 \pm 0.007, \quad c_{\mathrm{d}} = 1.474 \pm 0.008. \tag{8.36}$$

Figure 8.3 shows this prediction as a cross. Our measurement of quark electroweak couplings from direct photons is consistent with Standard Model predictions.

8.8 Results in the framework of the Standard Model

8.8.1 Determination of the top mass

For the evaluation of the top quark mass we carry out fits to all cross section, lepton asymmetry, $\mathrm{b\bar{b}}$ asymmetry and tau polarization data simultaneously in the framework of the Standard Model. The input parameters are: m_{Z}, m_{t}, m_{H} and α_{s}. We carry out fits for three fixed values of m_{H} (50, 300 and 1000 GeV) leaving the other parameters free to be determined by the data. We find:

$$\begin{aligned} m_{\mathrm{Z}} &= 91195 \pm 9 \text{ MeV} && (8.37)\\ m_{\mathrm{t}} &= 132^{+44}_{-63} \pm 18 \text{ (Higgs) GeV} && (8.38)\\ \alpha_{\mathrm{s}} &= 0.140 \pm 0.016 && (8.39) \end{aligned}$$

The correlation between m_{t} and α_{s} is shown in figure 8.4.

---

[2] the results presented here reflect the updated lineshape parameters given in this review, and differ slightly from those in reference [33].

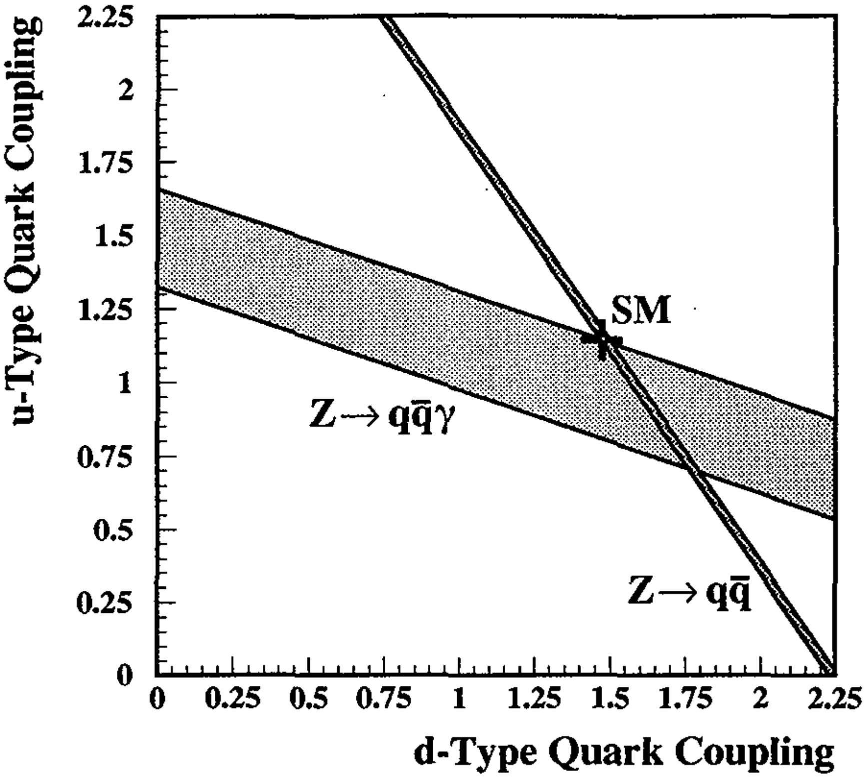

Figure 8.3: Linear constraints on the quark electroweak couplings derived from the total hadronic decay width of the Z (narrow band), and from theoretical fits to three direct photon distributions (broad band). The Standard Model values of the couplings are shown as a cross.

There is an independent determination of α_s using hadronic event topology and tau decay width data (see chapter 10) yielding $\alpha_s = 0.124 \pm 0.006$. To obtain the best precision on m_t this value of α_s is used as a constraint in our fits resulting in:

$$m_t = 152^{+36}_{-46} \pm 20 \text{ (Higgs) GeV.} \tag{8.40}$$

This result is in agreement with current limits on the top mass [111].

8.8.2 Derived quantities

From the fitted values of m_Z, m_t and α_s for a fixed value of m_H as obtained above one can derive all other quantities like $\sin^2\theta_W$, $\sin^2\overline{\theta}_W$, Δr and m_W, which we quote here for completeness.

The values of these quantities are :

$$\sin^2\theta_W = 0.227 \pm 0.005 \tag{8.41}$$

$$\sin^2\overline{\theta}_W = 0.2328 \pm 0.0013 \tag{8.42}$$

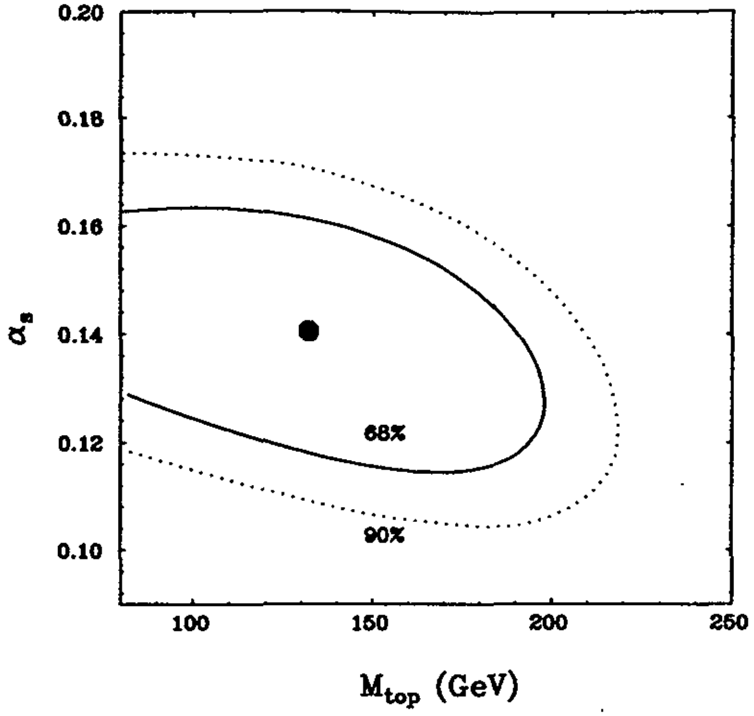

Figure 8.4: α_s *vs.* m_t contour in the standard model fit.

$$\Delta r = 0.047 \pm 0.014 \tag{8.43}$$
$$m_W = 80.2 \pm 0.3 \text{ GeV} \tag{8.44}$$

Deviation from the value of unity for the ρ parameter can occur in more general Higgs representations. Following the prescription given in reference 112, a fit to the cross section and asymmetries data leads to

$$\rho = 1.0001 \pm 0.0015(exp) \pm 0.002(m_t) \tag{8.45}$$

where the first error contains statistical and systematic uncertainties and the second accounts for variations in $m_t = 150^{+50}_{-60}$ GeV and $m_H = 300^{+700}_{-250}$ GeV. The value of ρ is consistent with the standard model value of unity.

8.9 Z resonance analysis with an S-matrix approach

The S-matrix ansatz [113, 114] is a rigorous model-independent approach to describe e^+e^- annihilation. It does not make any special assumptions on the dynamics of the hard-scattering process [114, 115], but only assumes the existence of an analytic, unitary S-matrix.

In this section we discuss results using this ansatz and compare them to those obtained in the previous sections of this chapter. A detailed description of the formalism can be found in reference 114. We start from the following parameterization of the cross section:

$$\sigma(s) = \frac{4}{3}\pi\alpha^2 \left[\frac{r_\gamma}{s} + \frac{sR + (s - m_Z^2)J}{(s - m_Z^2)^2 + m_Z^2\Gamma_Z^2} + \sum_n \frac{r_n}{m_Z^2} \left(\frac{s}{m_Z^2} - 1 \right)^n \right]. \tag{8.46}$$

The parameter r_γ describes the γ exchange, R the Z exchange and J the γZ interference terms. r_n are nonresonant contributions to the cross section. In reference [116] an extension of formula (8.46) to asymmetries is presented. The following expression results:

$$A(s) = A_0 + A_1\left(\frac{s}{m_Z^2} - 1\right) + A_2\left(\frac{s}{m_Z^2} - 1\right)^2 + \ldots \tag{8.47}$$

$A(s)$ can be the forward-backward or polarization asymmetry; however, here we cover only A_{fb}. The expressions for the first two coefficients A_0, A_1 are:

$$A_0 \sim \frac{R_{\text{fb}}}{R_{\text{tot}} + \gamma^2 r_\gamma} \approx \frac{R_{\text{fb}}}{R_{\text{tot}}}, \tag{8.48}$$

$$A_1 \sim \left[\frac{J_{\text{fb}}}{R_{\text{fb}}} - \frac{J_{\text{tot}}}{R_{\text{tot}} + \gamma^2 r_\gamma} + \frac{2\gamma^2 r_\gamma}{R_{\text{tot}} + \gamma^2 r_\gamma}\right] A_0 \approx \left[\frac{J_{\text{fb}}}{R_{\text{fb}}} - \frac{J_{\text{tot}}}{R_{\text{tot}}}\right] A_0. \tag{8.49}$$

The non-resonating quantum corrections are neglected in (8.48) and (8.49). With A_0 and A_1 all higher-order coefficients are defined by a recurrence relation. To include photonic corrections the parameters R, J, r_γ and r_n of equations 8.46), 8.48 and 8.49 have to be multiplied by s-dependent factors containing QED corrections. It should be noted that in the S-matrix approach the total width Γ_Z is not s dependent in contrast to the usual parameterization of the Breit-Wigner resonance of the Z lineshape. This leads to a transformation of Z mass m_Z to $\overline{m}_Z$ and of the total Z width Γ_Z to $\overline{\Gamma}_Z$ [114, 117]:

$$\begin{aligned} \overline{m}_Z &= [1 + (\Gamma_Z/m_Z)^2]^{-\frac{1}{2}} m_Z &\approx& \; m_Z - 34 \;\text{ MeV}, \\ \overline{\Gamma}_Z &= [1 + (\Gamma_Z/m_Z)^2]^{-\frac{1}{2}} \Gamma_Z &\approx& \; \Gamma_Z - 1 \;\text{ MeV}. \end{aligned} \tag{8.50}$$

The mass, $\overline{m}_Z$, obtained from S-matrix fits is thus shifted by about -34 MeV and the total width, $\overline{\Gamma}_Z$, by about -1 MeV.

When fitting the cross section and asymmetry data in this approach assuming lepton universality, one gets in the most general case 7 parameters, $\overline{m}_Z$, $\overline{\Gamma}_Z$, r_γ and R_{tot}^{had}, J_{tot}^{had} for hadrons and R_{tot}^{ℓ}, J_{tot}^{ℓ} for leptons. All non-resonating contributions in equation 8.46 are neglected. They are numerically small and could be considered as quantum corrections to the parameters R_{tot}, J_{tot} and r_γ. Therefore these parameters are handled with their effective values. r_γ is expressed in terms of $|\alpha^{-1}(s)|$:

$$\begin{aligned} r_\gamma &= \left|\tfrac{\alpha(s)}{\alpha}\right|^2 Q_e^2 Q_f^2 \quad \text{(for leptons)}, \\ r_\gamma &= \left|\tfrac{\alpha(s)}{\alpha}\right|^2 n_f Q_e^2 (3Q_d^2 + 2Q_u^2) \quad \text{(for hadrons)}. \end{aligned} \tag{8.51}$$

We perform a fit to cross sections and forward-backward asymmetries in two steps:

a) the γ exchange terms for leptons and hadrons are fixed using $\alpha^{-1}(s)$= 128.8;

Parameter	γ exchange term fixed	hadronic interference term fixed
$\bar{m}_Z$ (GeV)	91.151 ± 0.015	91.161 ± 0.010
$\bar{\Gamma}_Z$ (GeV)	2.489 ± 0.012	2.486 ± 0.011
R^{ℓ}_{tot}	0.140 ± 0.002	0.140 ± 0.002
J^{ℓ}_{tot}	0.036 ± 0.064	0.010 ± 0.056
R^{ℓ}_{fb}	0.004 ± 0.001	0.004 ± 0.001
J^{ℓ}_{fb}	0.672 ± 0.087	0.671 ± 0.087
$R^{\mathrm{had}}_{\mathrm{tot}}$	2.94 ± 0.03	2.93 ± 0.03
$J^{\mathrm{had}}_{\mathrm{tot}}$	0.89 ± 0.72	fixed

Table 8.3: Results of the S-matrix fit to total cross sections and forward-backward charge asymmetries.

b) the hadronic interference term $J^{\mathrm{had}}_{\mathrm{tot}}$ is fixed to its Standard Model value.

The results are shown in table 8.3. It should be noted that these results are insensitive to the value of $\alpha(s)$ used in calculating the QED contribution. This is expected because the γ exchange contributions to the cross section are very small around the Z peak. We thus fix $\alpha^{-1} = 128.8$.

The results of fit (a) for $\overline{m}_Z$ and $\overline{\Gamma}_Z$ are:

$$\overline{m}_Z = 91151 \pm 15 \text{ MeV}, \quad (8.52)$$
$$\overline{\Gamma}_Z = 2.489 \pm 12 \text{ MeV}. \quad (8.53)$$

Since the error in determining $J^{\mathrm{had}}_{\mathrm{tot}}$ is large, we fix $J^{\mathrm{had}}_{\mathrm{tot}}$ to its Standard Model value in fit (b). The mass $\overline{m}_Z$ is then shifted by +10 MeV with respect to fit (a) and its error, $\Delta\overline{m}_Z$, goes down to 10 MeV. The total width decreases by 3 MeV. Comparing the values for m_Z and $\overline{m}_Z$ in table 8.3 to the results obtained in section 8.6 (see table 8.1), we note that only when fixing the hadronic interference term in the same way as done previously, a shift of −34 MeV is observed as predicted by equation 8.50 and agreement between m_Z and $\overline{m}_Z$ is achieved. However, the measurement of the Z mass is not strictly model-independent in this case. On the other hand. the shift of $\overline{\Gamma}_Z$ with respect to Γ_Z amounts to 1 MeV with $J^{\mathrm{had}}_{\mathrm{tot}}$ free, while it grows to 3 MeV when it is fixed.

The leptonic interference term is measured for the first time. As a further cross check with the results presented in the previous sections, we use the formulae given in reference 116 to convert R^{ℓ}_{fb} and J^{ℓ}_{fb} into effective couplings. A value of $\sin^2\overline{\theta}_W = 0.227 \pm 0.004$ results for both fits, in good agreement with the determination in section 8.7.

Chapter 9

Tests of Quantum Electrodynamics

Quantum Electrodynamics (QED) is the best tested theory in physics; so far no deviation has been found. At LEP energies, QED is tested using, for example:

- processes involving only fermions and photons at the Born level, like $e^+e^- \rightarrow \gamma\gamma(\gamma)$;
- processes involving hard photon radiation, like $e^+e^- \rightarrow \ell^+\ell^-(n\gamma)$.

Tests of the first kind are reported in this chaper, while data related to tests of the latter type are presented in chapter 11.

Deviations from the QED prediction for the reaction $e^+e^- \rightarrow \gamma\gamma(\gamma)$ would imply, for example, that the electron has a finite size [118] or non-minimal couplings. In particular, an excited electron e^* might exist which couples to electrons and photons with a magnetic interaction: $\frac{e\lambda}{2m_{e^*}}\overline{\psi_{e^*}}\sigma_{\mu\nu}\psi_e F^{\mu\nu}$, where m_{e^*} is the mass of the excited electron, λ the coupling constant and $F^{\mu\nu}$ the electromagnetic field tensor [119]. The effect of such a breakdown has been parameterized [120, 118, 119, 121]. The differential cross section at the Born level, $(d\sigma/d\Omega)^0$, can be written as:

$$\sigma(\theta)^0 \equiv (d\sigma/d\Omega)^0 = \sigma(\theta)^0_{\mathrm{QED}}(1 + \delta_{\mathrm{new}}) \tag{9.1}$$

where $\delta_{\mathrm{new}} = \mp(s^2/2)(1/\Lambda_\pm^4)(1 - \cos^2\theta)$, θ is the angle of the emitted photons with respect to the beam axis, and $\Lambda_\pm$ are QED cut-off parameters.

In comparing with data, higher order contributions must be taken into account. A possible deviation between measured and calculated QED cross section, including radiative corrections, can then be written as $O(\alpha^3)$

$$\sigma(\theta)_{\mathrm{Measured}} = \sigma(\theta)^{O(\alpha^3)}_{\mathrm{QED}}(1 + \rho) \tag{9.2}$$

where ρ is a measure of a possible QED breakdown. Since radiative corrections to modified cross sections have not been calculated, we replace ρ by its Born level expression, δ_{new} .

An $e^+e^- \rightarrow \gamma\gamma(\gamma)$ event is identified by two or three clusters in the electromagnetic calorimeter without missing energy. The selection procedure is described in reference 122. It has an efficiency, for the angular range 14° < θ < 166°, of (64 ± 3)%, including losses from photon conversion, most significant in the forward-backward region, and from gaps in the detector. The integrated luminosity for the different center-of-mass energies is given in Table 9.1. This table also shows the number of events for the 1990 and 1991 runs and the measured total cross sections. The 1991 cross sections are also shown in figure 9.1 as a function of the center-of-mass energy.

$\sqrt{s}$ (GeV)	$\mathcal{L}_{int}$ 1990 (pb^{-1})	$N_{\gamma\gamma(\gamma)}$ (1990)	σ_{meas} (pb) (1990)
89.8	0.53	5	10.5 ± 4.7
91.2	2.59	43	18.4 ± 2.8
92.6	0.65	9	15.4 ± 5.1

$\sqrt{s}$ (GeV)	$\mathcal{L}_{int}$ 1991 (pb^{-1})	$N_{\gamma\gamma(\gamma)}$ (1991)	σ_{meas} (pb) (1991)
88.5	0.20	2	-
89.4	0.59	15	40.2 ± 10.4
90.3	0.47	24	80.4 ± 16.4
91.2	7.52	278	58.0 ± 3.5
92.0	0.38	11	45.1 ± 13.5
93.0	0.72	25	54.5 ± 10.9
93.7	0.53	14	41.8 ± 11.2

Table 9.1: a) The integrated luminosities as a function of the center-of-mass energies for the 1990 data (44° < θ < 136°). Also given are the number of events observed and the measured cross sections. b) The same table for the 1991 data (14° < θ < 166°).

In Table 9.2 we give the measured differential cross section for $e^+e^- \rightarrow \gamma\gamma(\gamma)$. Figure 9.2a shows the data points compared to the Born level and to the QED cross section calculated to $\mathcal{O}(\alpha^3)$. [19]. We note that radiative corrections decrease the Born QED cross section in the barrel region while increasing it in the forward-backward region. The χ^2 of the data points compared to the QED expectation is 12.3 for 9 degrees of freedom, indicating that the measured differential cross section is in agreement with the QED prediction.

We use an unbinned maximum likelihood method to set lower limits on the breakdown parameters and on the mass of an excited electron. In the former case, the probability density function is constructed by normalizing the differential cross section given above to the total cross section in our acceptance. The likelihood function is:

$$\mathcal{L} = \frac{1}{\sqrt{2\pi\sigma^2}} \exp\left(\frac{-(N_{\mathrm{obs}} - N(\Lambda))^2}{2\sigma^2}\right) \prod_{i=1}^{N_{\mathrm{obs}}} P(\theta_i, \Lambda) \qquad (9.3)$$

where Λ is the parameter under consideration, N_{obs} the observed number of events, $N(\Lambda)$ the expected number of events, and $P(\theta_i, \Lambda)$ the event probability density depending on the parameter Λ and the polar event angle θ_i. The first term corresponds to the overall normalization constraint. The error, σ, on the number of expected events includes the statistical error and the systematic error added in quadrature. We find $\Lambda_+ > 139$ GeV, $\Lambda_- > 108$ GeVat 95%

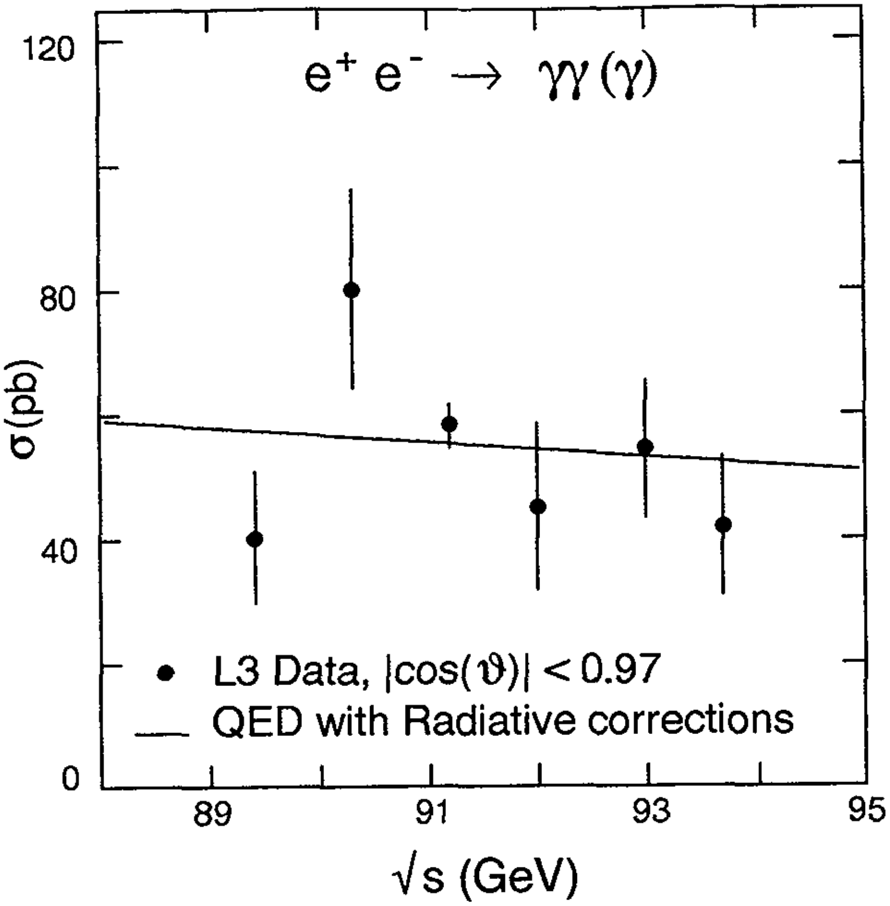

Figure 9.1: Measured cross section as a function of the center-of-mass energy for the angular region 14° < θ < 166°. QED includes radiative corrections to $O(\alpha^3)$.

$\vert\cos\theta\vert$	$N_{\gamma\gamma(\gamma)}$	$\left(\frac{d\sigma_{\text{meas}}}{d\Omega}\right)$ (pb/sr)
0.077	13	1.8 ± 0.5
0.177	23	3.3 ± 0.7
0.299	25	3.5 ± 0.7
0.435	18	2.6 ± 0.6
0.550	29	4.1 ± 0.8
0.658	52	8.2 ± 1.1
0.852	48	23.0 ± 3.3
0.906	38	28.2 ± 4.6
0.954	75	56.3 ± 6.5

Table 9.2: Differential cross sections as a function of $|\cos\theta|$ at 91.2 GeV. The $|\cos\theta|$ values given in the first column are event-weighted averages; the second column gives the number of events. Data from 1990 (44° < θ < 136°) and 1991 (14° < θ < 166°) have been combined.

confidence level. Figure 9.2b shows the ratio of the measured differential cross section to the QED prediction. The solid curves illustrate the effect of Λ_+ and Λ_-.

To set a limit on the mass of an excited electron, we use the full expression for the differential cross section given in reference 119, assuming a coupling constant $\lambda = 1$. The same functional form for the likelihood is used as in equation 9.3, with Λ replaced by m_{e^*}. We find $m_{e^*} > 127$ GeVat 95% confidence level.

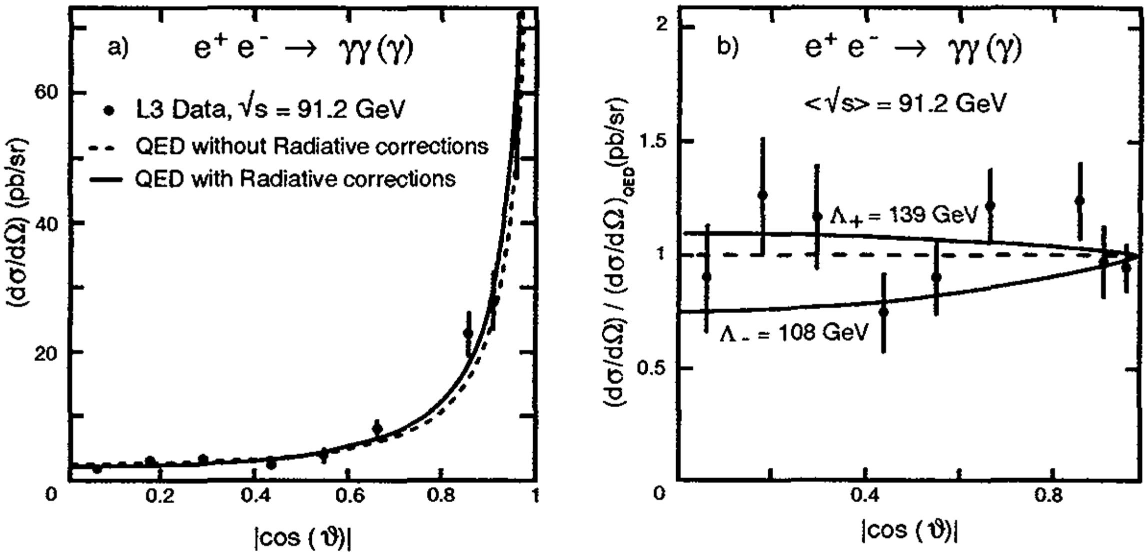

Figure 9.2: a) Measured differential cross section. The solid line gives the QED differential cross section to $\mathcal{O}(\alpha^3)$; the dashed line the Born level QED differential cross section. b) Ratio of the measured differential cross sections to the $\mathcal{O}(\alpha^3)$ QED prediction. The solid lines represent deviations expected for the lower limits on Λ_+ and Λ_-.

Chapter 10

Tests of Quantum Chromodynamics

In the last twenty years many experimental results [123–125] have been accumulated confirming the validity of Quantum Chromodynamics (QCD) [11], the theory of the strong forces. QCD is a non-abelian gauge theory with an SU(3) group structure describing the interaction of colored spin-1/2 quarks with colored spin-1 gluons. The basic Feynman diagrams are shown in figure 10.1.

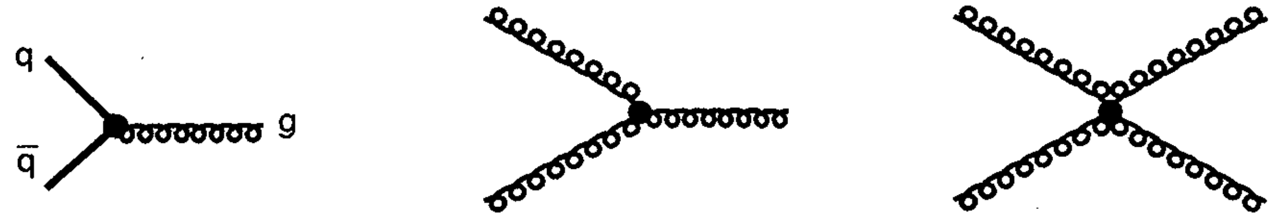

Figure 10.1: Basic QCD Feynman diagrams.

The only free parameter in this theory is the strong coupling constant α_s, which describes the strengths of both the quark-gluon coupling and the gluon self interaction. A characteristic feature of QCD is the decreasing of its coupling constant with energy, often referred to as the 'running' of α_s.

Major contributions to establishing QCD as the theory of strong interactions have come from the analysis of hadronic events in e^+e^- collisions at high energies. Milestones include the discovery of quark jets [126] and gluon jets [127], measurements confirming the gluon spin of 1 [128], the determination of the number of colors $N_C = 3$ from the total hadronic cross section [124, 129] and the measurements of the strong coupling constant α_s to second order [124, 125].

The Z resonance and its decays are ideal for QCD studies in the process $e^+e^- \rightarrow$ hadrons. The hadronic cross section is large and the background small. Hard quarks and gluons produced in hadronic events form jets, which preserve the energy and direction of the primary partons. Hadronization effects are small at such a high center of mass energy and jets are more collimated than at lower energies. Hard initial-state photon radiation is strongly suppressed. One finds at the Z pole a large number of events with 3, 4 and more jets of high energy. These clean topologies allow for a precise determination of α_s and for many other tests of QCD.

One can distinguish four separate phases in the process $e^+e^- \rightarrow$ hadrons. They correspond to different time and energy scales:

(i) Production of a $q\bar{q}$ pair (and photons) [electroweak];

(ii) Hard gluon radiation [perturbative QCD];

(iii) Fragmentation of quarks and gluons into hadrons [non-perturbative QCD];

(iv) Decays of unstable particles [electroweak and QCD].

These subprocesses are implemented in Monte Carlo event generators [130], which play an important role in the analysis of hadronic events. The study of hard gluon radiation is of primary interest here. It can be calculated perturbatively within QCD and allows for quantitative tests. Fragmentation cannot yet be calculated in QCD, but it is described by phenomenological models.

Section 10.1 describes the measurement of hadronic event shape variables and the tuning and testing of QCD models in the form of Monte Carlo generators. Section 10.2 is devoted to the precise measurement of the strong coupling constant and tests of the energy- and flavor-dependences of α_s. Studies of the fundamental properties of gluons, spin and self-coupling, are described in section 10.3. In section 10.4 we compare the measured production of isolated hard photons in hadronic events to theoretical models. Finally we present a study of gluon interference effects as predicted by QCD in section 10.5. This includes measurements of inclusive particle production, cluster multiplicities in three- and two-jet events and the string effect.

10.1 Event selection and Monte Carlo programs

To interpret measurements one has to use models describing the hadronization process and also the subsequent decays. Therefore tuning and testing of fragmentation models is the first step in the analysis of hadronic Z decays.

10.1.1 Measurement of the hadronic event structure

Events of type $e^+e^- \rightarrow$ hadrons are selected and analyzed by two independent methods: one is based on the energy measured in the electromagnetic and hadronic calorimeters, as described in chapter 5; the other one uses [45] charged tracks measured in the tracking chamber. The track measurement method is used to cross check the calorimetric method and to estimate the experimental errors. In total 250,000 events at $\sqrt{s} = 91.2$ GeV are used in this analysis.

We measure fifteen variables which characterize the shape of hadronic events [45]. Among the observables studied are thrust, major and minor [131], the heavy jet mass [132] and differential jet fractions [133, 134]. The measured distributions are corrected for detector effects, acceptance and resolution, and initial- and final-state photon radiation. The experimental uncertainties of the corrected distributions are typically a few percent per histogram bin. Figure 10.2 shows as an example the corrected major distribution. The definition of major is similar to that of thrust:

$$T = \max \frac{\sum |\vec{p}_i \cdot \vec{n}_{\mathrm{thrust}}|}{\sum |\vec{p}_i|}. \tag{10.1}$$

The major axis $\vec{n}_{major}$ is perpendicular to the thrust axis and the major value is

$$T_{\mathrm{major}} = \max \frac{\sum |\vec{p}_i \cdot \vec{n}_{\mathrm{major}}|}{\sum |\vec{p}_i|}. \tag{10.2}$$

Here p_i is the momentum of particle i in a hadronic event. For two-jet events the major value is small, while for multi-jet events T_{major} is large. The event shape distributions agree with the measurements of other LEP experiments [135–138].

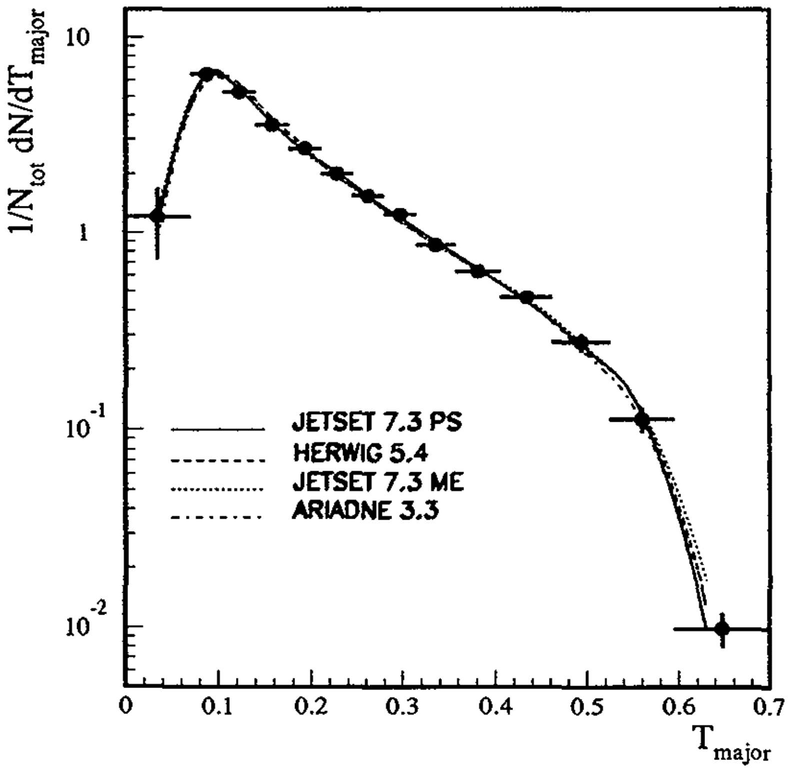

Figure 10.2: Distribution of the event shape variable major

10.1.2 Test of QCD models

A subset of the fifteen event shape distributions was used to fit free parameters in six Monte Carlo generators [22,23,139–141]. Those programs which are used most often in the analysis described in this chapter are:

- JETSET 7.3 PS [22].
  This generator simulates parton showers (PS), based on the leading-log approximation of QCD; it includes the effects of angular ordering. The probability of the first gluon branching is matched to the $O(\alpha_s)$ matrix-element calculations. Hadronization is modeled by a string which is spanned between the partons and which subsequently breaks up into hadrons. Initial- and final-state photon radiation is included in the simulation. One fit parameter is the effective parton shower scale Λ. Two additional parameters steer the longitudinal and transverse momentum distributions with respect to the jet axes.
- JETSET 7.3 ME [22].
  In addition to the parton shower option described above, JETSET can generate quarks and gluons according to the full second order QCD Matrix-Element (ME) [142]. At most four partons can be produced which are fragmented using the string model. Fit parameters are Λ_{ME} and the same two fragmentation parameters as above.
- HERWIG 5.4 [23].
  This parton shower generator incorporates a detailed simulation of QCD interference phenomena. The first gluon branching is matched to the $O(\alpha_s)$ matrix-element calculations. Also photon radiation from quarks is simulated. Hadronization is performed using a cluster model. First all gluons are split into $q\bar{q}$ pairs; subsequently, adjacent quarks and antiquarks are made to form clusters which decay into hadrons. The fit parameters are the effective scale parameter Λ and the maximum cluster mass. Clusters exceeding this threshold are forced to first decay into lower mass clusters and subsequently into hadrons.
- ARIADNE 3.3 [139].
  The perturbative QCD cascade in ARIADNE is based on the color dipole model. This parton shower simulation incorporates gluon interference phenomena. For hadronization and particle decays the JETSET string fragmentation routines are used. Fit parameters are Λ and the fragmentation parameters as in JETSET.

After the free parameters have been fitted, the distributions in the fifteen event shape variables predicted by the generators are compared to the measurements [45]. Figure 10.2 compares the measured and predicted major distribution. The parton shower models reproduce the data well. Also with the ME option in JETSET a fair overall description of the measured distributions can be achieved. However, the two-jet production rate is overestimated, while the production of multi-jet events is underestimated. All four models can describe factorial moments [143], which are calculated from the azimuthal angle of charged particles measured in the tracking chamber. The measured energy flow distribution in 3-jet events can also be reproduced.

The generators ARIADNE, HERWIG and JETSET (PS and ME) are therefore suitable to estimate hadronization corrections which are needed for the analyses described in the next sections and also in chapters 5, 6, 12 and 13.

10.2 The strong coupling constant

There are several reasons for a precise measurement of the strong coupling constant: (i) it is the only free parameter in QCD, (ii) for many tests of QCD α_s must be known, and (iii) for many electroweak tests strong corrections must be calculated precisely.

In the following sections three methods to determine α_s are described. The comparison of α_s values obtained at different energies (running) and for different quark species (flavor independence) constitute important tests of QCD. Those are described in sections 10.2.4 and 10.2.5. Finally the measured α_s values are combined in section 10.2.6.

The analyses are based on different samples of hadronic Z decays containing between 37,000 and 250,000 events selected with the cuts described in chapter 5. The statistical errors in the α_s values are therefore negligible.

10.2.1 α_s from jets and event shapes

The probability for gluon radiation off quarks is - to first order in perturbation theory - proportional to the strong coupling constant α_s. There exists a large number of observables which characterize the shape of hadronic events and which are sensitive to hard gluon radiation [133].

Among those variables is the fraction of events with three jets. This quantity has an immediate intuitive meaning and hadronization corrections are found to be small. From a comparison with the predictions of perturbative QCD α_s can be determined. We reconstruct jets out of clusters in the calorimeters by using the JADE version [34] of an invariant mass jet algorithm [144]. In this recombination scheme there is a close agreement between jet rates on parton and detector level. First the energy and direction of all clusters are determined. For each pair of clusters i and j the scaled invariant mass squared

$$y_{ij} = 2E_iE_j/E_{\mathrm{vis}}^2 \cdot (1 - \cos\theta_{ij}) \tag{10.3}$$

is evaluated. E_i and E_j are the cluster energies and θ_{ij} is the angle between clusters i and j. E_{vis} is the total energy observed in the calorimeters. The cluster pair for which y_{ij} is smallest is replaced by a pseudo-cluster k with four-momentum

$$p_k = p_i + p_j. \tag{10.4}$$

This procedure is repeated until all y_{ij} exceed a pre-set jet resolution parameter y_{cut}. The remaining pseudo-clusters are called jets. Increasing y_{cut} lowers the fraction of multi-jet events but increases the separation between the jets. The relative jet production rates $f_N = \sigma_{\mathrm{N}}/\sigma_{\mathrm{tot}}$, where N is the number of jets, are then determined as a function of the jet resolution y_{cut}. The measurements are corrected both for detector effects (resolution and acceptance) and for initial- and final-state photon radiation. The systematic experimental uncertainty in the determination

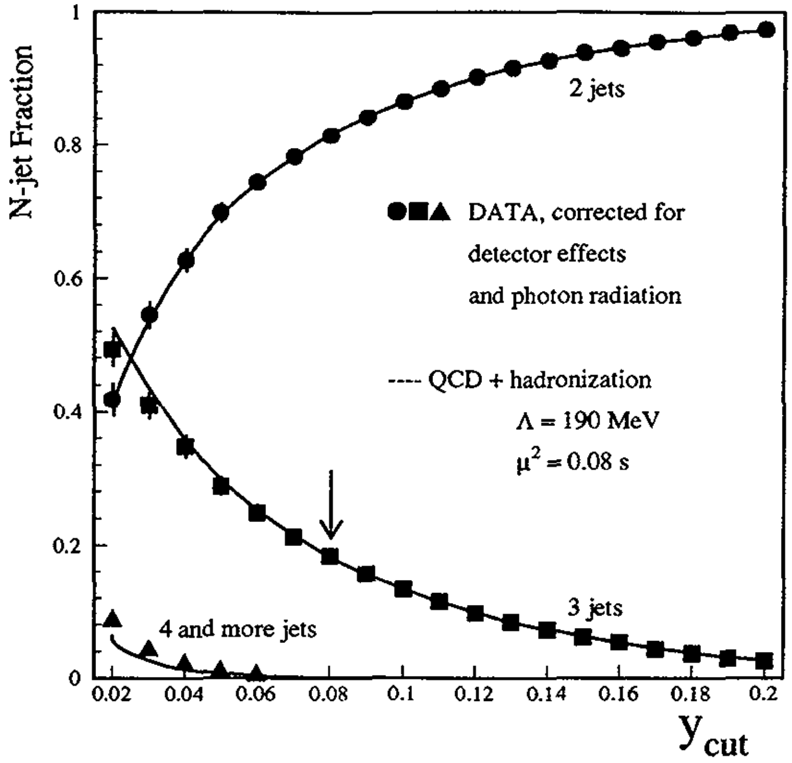

Figure 10.3: Measured jet fractions in comparison with the QCD predictions

of f_3 is estimated to be $\delta f_3/f_3 = 5\%$. Figure 10.3 shows the corrected jet fractions as a function of $y_{\rm cut}$. The dependence of the 3-jet fractions on α_s is given in second order perturbation theory by

$$f_3(\Lambda, s, \mu^2, y_{\rm cut}) = A(y_{\rm cut}) \cdot \alpha_{\rm s}(\Lambda, \mu^2) + B(y_{\rm cut}, \mu^2/s) \cdot {\alpha_{\rm s}}^2(\Lambda, \mu^2) \,. \tag{10.5}$$

where A and B are calculable functions. The renormalization scale μ^2 is not fixed in second order QCD. For the functions A and B we use the tables in reference 133, which are based on the second order QCD calculations in reference 142. The dependence of $\alpha_{\rm s}$ on $\Lambda \equiv \Lambda^{(5)}_{\overline{\rm MS}}$ is computed using the relation given in reference 145 for 5 quarks. Hadronization corrections are determined with the ME option in JETSET. They are found to be of the order of a few percent. We use the value $y_{\rm cut} = 0.08$, corresponding to an invariant mass of the two closest jets of at least 26 GeV, to derive $\alpha_{\rm s}$. For this value of $y_{\rm cut}$, the 4-jet fraction is negligible ($\approx 0.1\%$) while the 3-jet rate is:

$$f_3 = 18.4\% \pm 0.9\% \,. \tag{10.6}$$

The error is dominated by the uncertainties in the energy response factors for different detector parts. From a comparison of (10.6) to the second order QCD calculation we find

$${\alpha_{\rm s}}^{\rm jets}(m_Z) = 0.115 \pm 0.005\,({\rm exp.})\,^{+0.012}_{-0.010}\,({\rm theor.}) \tag{10.7}$$

for a renormalization scale $\mu^2/s = y_{\rm cut} = 0.08$. The theoretical error includes uncertainties due to fragmentation and jet clustering scheme dependence and due to the renormalization scale, which has been varied in the range $0.001 \leq \mu^2/s \leq 1$. The latter uncertainty, which is an estimate of the effects of yet uncalculated higher order corrections, is the dominant one. Figure 10.3 shows that the QCD calculations agree well with the measured jet fractions for $y_{\text{cut}} \geq 0.05$, where the 4-jet rate is below 1%. For smaller jet resolution parameters the measured number of events with high jet multiplicity exceeds the predicted rate. This difference indicates the importance of higher order corrections.

Also the energy-energy correlation (EEC) and its asymmetry (AEEC) [146] are observables well suited for a determination of the strong coupling constant α_s. The EEC can be defined as a histogram of all angles between any particles i, j in hadronic events weighted with the product of their energies, and averaged over N events:

$$\text{EEC}(\chi_{\text{bin}}) = \frac{1}{\Delta_{\text{bin}} \cdot N} \sum_{\text{events}}^{N} \sum_{i,j} \frac{E_i \cdot E_j}{E_{\text{vis}}^2} \delta_{\text{bin}}(\chi_{\text{bin}} - \chi_{ij}). \tag{10.8}$$

$\delta_{\text{bin}}(\chi_{\text{bin}} - \chi_{ij})$ is 1 for angles χ_{ij} inside the bin around χ_{bin} and 0 otherwise; Δ_{bin} denotes the bin width. For 2-jet events most angles are close to 0° or 180°, while events with hard gluon radiation contribute to the central region. Events of type $q\bar{q}g$ contribute asymmetrically to the EEC distribution such that the asymmetry in the energy-energy correlation

$$\text{AEEC}(\chi) = \text{EEC}(180^\circ - \chi) - \text{EEC}(\chi) \tag{10.9}$$

is positive for $\chi > 10^\circ$. We have measured both the EEC and AEEC distributions and corrected the data for detector effects, photon radiation and hadronization [147]. From a fit of the second order QCD calculations [133] to the corrected distributions the following values for the strong coupling constant are found:

$$\alpha_s{}^{\text{EEC}}(m_Z) = 0.121 \pm 0.004\,(\text{exp.})\,^{+0.011}_{-0.009}\,(\text{theor.}), \tag{10.10}$$

$$\alpha_s{}^{\text{AEEC}}(m_Z) = 0.115 \pm 0.004\,(\text{exp.})\,^{+0.008}_{-0.006}\,(\text{theor.}). \tag{10.11}$$

The three α_s values (10.7,10.10,10.11) derived from jet fractions, EEC and AEEC in second order perturbation theory agree well with each other. The estimated errors, which are dominated by theoretical uncertainties, have similar sizes. The unweighted average of the three second order α_s results is

$$\alpha_s(m_Z) = 0.118 \pm 0.004\,(\text{exp.}) \pm 0.009\,(\text{theor.}). \tag{10.12}$$

Similar results have been obtained by the other LEP collaborations [148, 136, 138].

Recently, new QCD calculations including resummation of leading- and next-to-leading-logarithms to all orders have been performed for the event shape variables thrust [149] and heavy jet mass [150], energy-energy correlations [151] and the average jet multiplicity [152] [1]. The theoretical uncertainties due to uncalculated terms are expected to be reduced with respect to second order calculations. Thrust and energy-energy correlations have been defined in equations 10.1 and 10.8, respectively. The heavy jet mass M_H is defined as [132]

$$M_H = \max[M_1(\vec{n}_T), M_2(\vec{n}_T)]\,. \tag{10.13}$$

---

[1] Recently these calculations have been performed also for 'jet broadness measures' [153].

$M_{1,2}$ are the invariant masses in the two hemispheres separated by a plane perpendicular to the thrust axis:

$$M_l^2 = \left(\sum_{\text{hemisphere } l} p_i \right)^2 , \tag{10.14}$$

where p_i is the four momentum of particle i. Here we use the normalized quantity

$$\rho = M_H^2 / E_{\text{vis}}^2 . \tag{10.15}$$

The average jet multiplicity

$$\langle n_{\text{jet}} \rangle = \frac{1}{N} \sum_{i=1}^{N} n_{\text{jet}}^i$$

is defined using the '$k_\perp$' jet algorithm [134], where N is the total number of events. The $k_\perp$ algorithm is similar to the JADE recombination scheme as described above, but the invariant mass criterion (10.3) is replaced by

$$y_{ij} = 2 \min(E_i^2, E_j^2)/E_{\text{vis}}^2 \cdot (1 - \cos\theta_{ij}). \tag{10.16}$$

The quantity y_{ij} corresponds to the scaled relative transverse momentum $k_\perp$ squared. Here we use the $k_\perp$ jet algorithm, since in this scheme (but not in the JADE scheme) the resummation of the leading and next-to-leading terms is possible [154, 134, 152]. In the new calculations all second order terms [142, 133] are included together with the leading and next-to-leading corrections. These corrections are of the form $\alpha_s{}^n \ln^m y$ with $n \geq 1$ and $m = n$ or $m = n + 1$, respectively. The generic variable y stands for the quantities $1 - T$, ρ, $(1 + \cos\chi)/2$ and y_{cut}, respectively. In the 2-jet region y is small and the corrections large. An important improvement of the new QCD calculations with respect to the second order formulæ is their ability to describe also the low y region.

Observable	$\alpha_s(m_Z)$	Exp. Err.	Theor. Err.
Thrust	0.118	± 0.004	$^{+0.008}_{-0.006}$
Heavy Jet mass	0.124	± 0.003	$^{+0.007}_{-0.005}$
EEC	0.135	± 0.003	$^{+0.005}_{-0.007}$
$\langle n_{\text{jet}} \rangle$	0.132	± 0.003	$^{+0.006}_{-0.004}$

Table 10.1: α_s values and errors derived from event shape variables

We have determined α_s values from a fit to the four corrected distributions (thrust, heavy jet mass, energy-energy correlations and average jet multiplicity) [155]. The results are summarized in table 10.1. Figure 10.4 shows the QCD fit in comparison with the measured ρ distribution. In all cases a good fit is obtained. The experimental uncertainties in table 10.1 are determined by repeating the α_s determination for different energy response factors and unfolding methods, and by using tracks instead of calorimetric clusters. The theoretical error includes both hadronization uncertainties and the estimated error due to the approximations made in the perturbative QCD calculations. The fragmentation uncertainty is estimated as

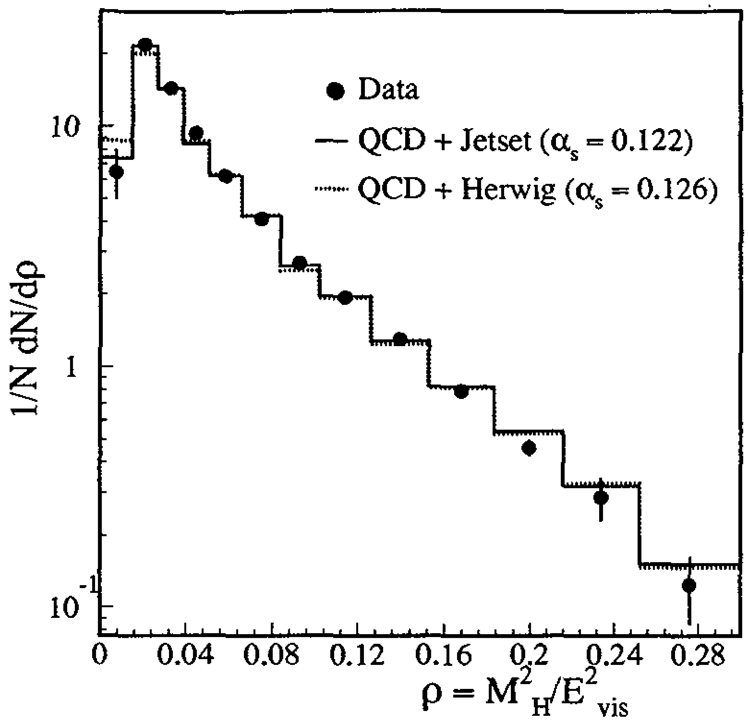

Figure 10.4: Distribution of the scaled heavy jet mass squared ρ

half the difference of the α_s values obtained using JETSET and HERWIG for the hadronization correction. The uncertainty in α_s due to approximations in the perturbative calculations is estimated by repeating the α_s fit for different values of the renormalization scale in the interval $0.5\sqrt{s} \leq \mu \leq 2\sqrt{s}$.

The values for the strong coupling constant given in table 10.1 agree, within errors, with the α_s values based on the new calculations published by other LEP collaborations [138, 156].

To obtain a combined value for the strong coupling constant we take the unweighted average of the first three α_s values of table 10.1 and obtain $\alpha_s = 0.125 \pm 0.003\,(\text{exp.})$. Since in the calculation of the average jet multiplicity some terms are missing [157], we do not include the last α_s value in table 10.1 in our combined result. We estimate the total theoretical error, due to both the approximations in the higher order corrections and hadronization effects, independently from the estimate of the theoretical error in table 10.1, and from the spread of the three α_s values from thrust, heavy jet mass and EEC, yielding ±0.008. The two estimates agree well. We conservatively assign the larger one as the theoretical uncertainty on our α_s determination. The combined result is therefore

$$\alpha_s(m_Z) = 0.125 \pm 0.003\,(\text{exp.})\ \pm 0.008\,(\text{theor.}). \qquad (10.17)$$

Here we have assumed that the experimental uncertainties in the three α_s values are fully correlated.

A better determination of the theoretical uncertainties will become possible when the new calculation techniques have been applied to more event shape variables.

The value of 0.125 agrees within errors with the result 0.118 obtained using second order

QCD calculations (see equation 10.12).

10.2.2 α_s from the hadronic Z width

The QCD correction to the hadronic Z width can be measured directly from the ratio of the hadronic and leptonic partial widths of the Z boson. In the Standard Model, this is given by

$$R_{\mathrm{had}} \equiv \Gamma_{\mathrm{had}}/\Gamma_\ell = R^0_{\mathrm{had}} \cdot (1+\delta_{\mathrm{QCD}}). \tag{10.18}$$

The factor $R^0_{\mathrm{had}} = \Gamma^0_{\mathrm{had}}/\Gamma_\ell = 19.95 \pm 0.02$ can be calculated from the vector and axial-vector coupling constants $\bar{g}_{\mathrm{V}}$ and $\bar{g}_{\mathrm{A}}$ of the quarks and leptons [26] (see chapter 8), with $N_{\mathrm{C}} = 3$ as the number of colors. Here Γ^0_{had} stands for the hadronic width without QCD corrections ($\alpha_s = 0$). R^0_{had} depends only slightly on the top and Higgs masses, since most m_t and m_{H} dependent corrections are common to Γ^0_{had} and Γ_ℓ. The error of ± 0.02 corresponds to a variation of m_t between 100 and 200 GeV and m_{H} in the range from 60 to 1000 GeV.

The QCD correction can be cast in the form [158]

$$\delta_{\mathrm{QCD}} = 1.05\frac{\alpha_s}{\pi} + 0.9(\frac{\alpha_s}{\pi})^2 - 13(\frac{\alpha_s}{\pi})^3, \tag{10.19}$$

where the recently calculated third order correction [159], the charm and bottom mass effects and the top mass dependence [160] are taken into account. Theoretical uncertainties in δ_{QCD} are expected to be as small as 2% [161]. This translates into an uncertainty of $\Delta\alpha_s \approx 0.002$, a precision unmatched by any other method for the determination of the strong coupling constant. However, since the QCD correction to the hadronic Z width is small ($\approx 4\%$), a high experimental precision is required in order to determine the strong coupling constant with a precision comparable to that of α_s from the event topology.

From our value $R_{\mathrm{had}} = 21.00 \pm 0.15$ (see equation 8.22) one gets

$$\alpha_s(m_{\mathrm{Z}}) = 0.155 \pm 0.023, \tag{10.20}$$

where the error is dominated by experimental uncertainties.

Also the total width of the Z is in principle a measure of the QCD correction δ_{QCD}. However, Γ_{Z} depends strongly on the top quark mass. From a combined fit of all cross section and asymmetry data one can determine m_t and α_s simultaneously, as described in chapter 8. That result, which is more model dependent than the α_s value derived here, is consistent with the value (10.20).

If one uses the value of α_s as derived from the event topology, the number of colors can be determined from the measured value of R_{had}. The result is $N_{\mathrm{C}} = 3.03 \pm 0.02$.

10.2.3 α_s from τ decays

The hadronic decay width of the τ lepton can also be used to measure α_s. The ratio of the hadronic and leptonic decay widths

$$R_\tau \equiv \Gamma^\tau_{\mathrm{had}}/\Gamma^\tau_\ell = B^\tau_{\mathrm{had}}/B^\tau_\ell = R^0_\tau \cdot (1+\delta^\tau_{\mathrm{QCD}}) \tag{10.21}$$

where B^{τ}_{had} and B^{τ}_{ℓ} are the hadronic and leptonic branching ratios, is defined in analogy to equation (10.18). The QCD correction, $\delta^{\tau}_{\mathrm{QCD}}$, is related to δ_{QCD} as defined in equation 10.19. The perturbative part [159] is therefore known to $\mathcal{O}({\alpha_s}^3)$, and non-perturbative effects are found to be small [162–164]. The factor $R^0_{\tau} = 3.03 \pm 0.01$ contains the color factor $N_{\mathrm{C}} = 3$ and small corrections from the Cabibbo-Kobayashi-Maskawa matrix-elements, electroweak radiative corrections and non-perturbative QCD corrections. For the perturbative QCD correction as a function of the strong coupling constant at the mass of the τ lepton we use the calculations given in reference 164.

We measure R_{τ} from the leptonic branching ratios,

$$R_{\tau} = \frac{1 - B_e - B_{\mu}}{B_e}. \tag{10.22}$$

Alternatively one can determine B_e from the τ lifetime. using the Standard Model relation

$$\tau_{\tau} = \tau_{\mu} \cdot \left(\frac{m_{\mu}}{m_{\tau}}\right)^5 \cdot B_e \tag{10.23}$$

and $B_{\mu} = 0.973 \cdot B_e$. Here we use the recently measured value of $m_{\tau} = 1776.9 \pm 0.5$ MeV [98].

From our measured branching fractions (see section 7.2) we obtain

$$R_{\tau}^{\text{branching fraction}} = 3.61 \pm 0.15. \tag{10.24}$$

With our measured τ lifetime $\tau_{\tau} = (293 \pm 15)$ fs (see section 7.2) we determine

$$R_{\tau}^{\text{lifetime}} = 3.60 \pm 0.29. \tag{10.25}$$

The results (10.24) and (10.25) agree with each other. From the weighted average

$$R_{\tau} = 3.61 \pm 0.13 \tag{10.26}$$

we obtain for the strong coupling constant at the τ mass

$$\alpha_s(m_{\tau}) = 0.35 \pm 0.06\,(\text{exp.}) \pm 0.03\,(\text{theor.}). \tag{10.27}$$

The theoretical uncertainty due to missing higher order terms is estimated as the difference between the results obtained using the perturbative calculations in references 163 and 164. The uncertainty due to non-perturbative effects is found to be negligible [162–164], however additional corrections may be necessary [165].

10.2.4 Running of α_s

We present two independent analyses which quantitatively confirm the running of the strong coupling constant as predicted by QCD.

Firstly, we compare the α_s values at $\mu = m_{\tau}$ derived from the hadronic width of the τ lepton (10.30) with the average of the two α_s values at $\mu = m_{\mathrm{Z}}$ obtained from Z decays (equations 10.17 and 10.20). The corresponding numbers

$$\alpha_s(m_{\tau} = 1.78\ \text{GeV}) = 0.35 \pm 0.07 \quad \text{(from } \tau \text{ decays)} \tag{10.28}$$
$$\alpha_s(m_{\mathrm{Z}} = 91\ \text{GeV}) = 0.129 \pm 0.008 \quad \text{(from Z decays)} \tag{10.29}$$

differ by a factor 2.7 ± 0.6. Extrapolating the first α_s value from $\mu = m_\tau$ to m_Z assuming the energy dependence as predicted by QCD [166] yields

$$\alpha_s(m_Z) \quad = 0.121 \pm 0.006\,(\text{exp.}) \pm 0.003\,(\text{theor.}) \qquad (\text{from } \tau \text{ decays}). \tag{10.30}$$

The agreement of this result from τ decays with the value from Z decays shows that QCD describes the running of α_s quantitatively. Note that the relative errors for α_s shrink with increasing energy scale μ since the absolute value of the slope of the function $\alpha_s(\mu)$ increases with α_s.

Secondly, figure 10.5 shows the 3-jet fraction for $y_{\text{cut}} = 0.08$ measured in e^+e^- annihilation for center of mass energies between 14 and 60 GeV [34, 167] and at 91 GeV [144, 135, 168, 138]. In leading order the 3-jet rate is proportional to the strong coupling constant α_s. The energy dependence is reproduced by QCD. An energy independent strong coupling constant can be ruled out from the comparison of all measured 3-jet fractions.

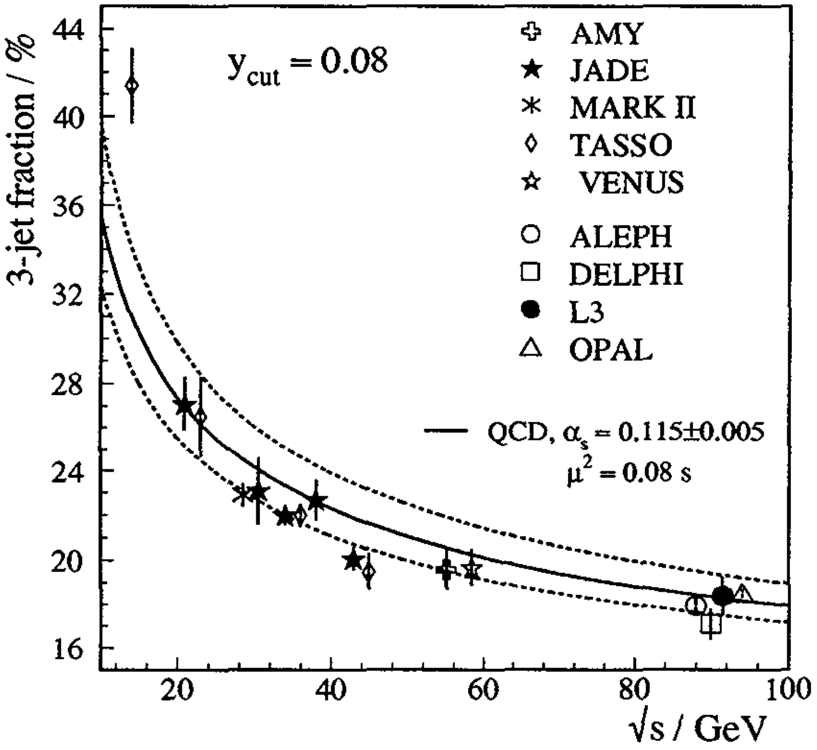

Figure 10.5: Energy dependence of the 3-jet fraction in e^+e^- annihilation. The solid and dashed lines correspond to the QCD prediction for $\alpha_s = 0.115 \pm 0.005$.

The results presented in this section demonstrate unambiguously the running of α_s as predicted by QCD, and provide therefore indirect evidence for the gluon self-coupling.

10.2.5 Flavor-independence of α_s

We have compared the strong coupling constants for bottom quarks and for the light flavors u, d, s, and c [169].

At the Z pole the fraction of bottom events in the hadron sample is 22% (see chapter 6). The b quark content can be enhanced by selecting hadronic events with muons or electrons from semileptonic decays of b hadrons as described in section 6.1. In a hadron sample of 110,000 events we find 1,800 events with muons of momenta above 4 GeV and p_t with respect to the nearest jet exceeding 1.5 GeV. For electrons, the corresponding number is 1,100 events for momenta above 3 GeV and p_t above 1.0 GeV. In the inclusive lepton sample $(87 \pm 3)\%$ of the events contain bottom quarks.

The 3-jet rates, in the total sample of hadronic events and in the sample enriched in b quarks, are measured as described in section 10.2.1. One gets for the ratio of 3-jet fractions at $y_{\text{cut}} = 0.05$, after corrections for detector, hadronization and bottom mass effects:

$$\frac{f_3^\ell}{f_3^{\text{had}}} = 1.00 \pm 0.03\ (\text{stat.}) \pm 0.04\ (\text{sys.}). \qquad (10.31)$$

Knowing the bottom content in the two data sets, one can calculate the ratio of α_s values for b quarks and the lighter species:

$$\alpha_s{}^{\text{b}}/\alpha_s{}^{\text{udsc}} = 1.00 \pm 0.08. \qquad (10.32)$$

Here the quarks u,d,s,c are assumed to have the same coupling strengths. This result agrees with the QCD expectation of one. The precision is significantly better than that achieved previously in e^+e^- experiments [170].

10.2.6 Summary of α_s measurements

Figure 10.6 compares the $\alpha_s(m_Z)$ values (10.17, 10.20, 10.30) obtained from event shapes, the QCD correction to the hadronic Z width and from τ decays. It has to be stressed that these determinations are independent. In case of R_{had} and R_τ the error is dominated by experimental uncertainties, while in the case of the α_s value from the event topology, theoretical errors are dominant.

The weighted mean value of the three α_s numbers is

$$\alpha_s(m_Z) = 0.124 \pm 0.005. \qquad (10.33)$$

This result corresponds to [145]

$$\Lambda^{(5)}_{\overline{MS}} = 310^{+90}_{-80}\ \text{MeV}. \qquad (10.34)$$

With a relative precision of 4%, the α_s value measured by L3 is one of the most precise determinations of the strong coupling constant. Our $\Lambda_{\overline{MS}}$ value agrees with the values measured in other processes, such as Υ decay, deep-inelastic lepton-nucleon scattering and $p\bar{p}$ collisions. It also agrees with results obtained in e^+e^- collisions at center of mass energies between 14 and 65 GeV [161, and references therein].

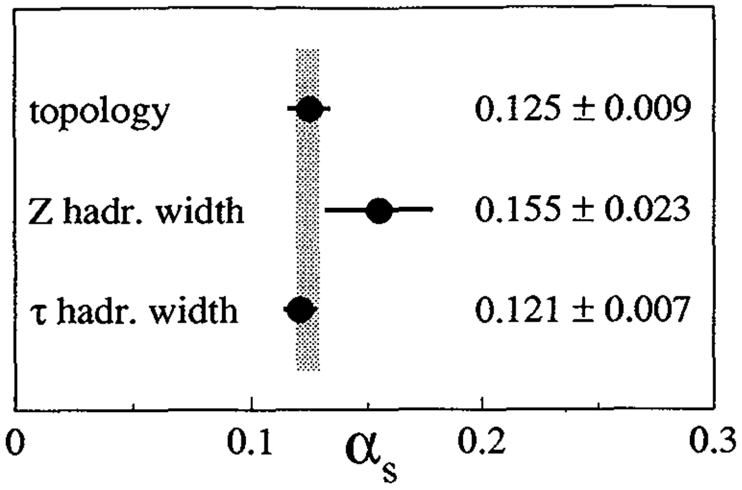

Figure 10.6: Summary of $\alpha_s(m_Z)$ measurements

10.3 Measurement of gluon properties

With α_s known, all second order QCD matrix-element calculations can be tested by comparing the measured jet distributions in 3- and 4-jet events to the theory. The measurements are used to determine the gluon spin and to show that the gluon self-coupling exists.

10.3.1 3-jet events and gluon spin

We have selected 43,000 events with three jets using the JADE clustering scheme with a jet resolution parameter of $y_{\text{cut}} = 0.02$, corresponding to a jet pair mass of 13 GeV or more [171].

For unpolarized beams, an event of type ($e^+e^- \rightarrow 3$ jets) can be described by four independent kinematical variables (apart from the jet masses). They can be chosen as:

x_1 = energy of the first jet normalized to the beam energy ;

x_2 = energy of the second jet normalized to the beam energy;

θ = polar angle of the first jet with respect to the e^- direction;

χ = angle between the jet plane and a plane spanned by the first jet and the beam.

The energy fractions x_i are determined from the angles between jets after projection onto the event plane. Here no distinction between quark, antiquark and gluon jets is made. We refer to the most energetic jet as the first jet, *i.e.* $x_1 > x_2 > x_3$ and $x_1 + x_2 + x_3 = 2$. The distributions in those four variables are sensitive to the gluon spin (0 or 1).

We have measured for our 3-jet sample the jet energy distributions and the event orientation as well as the two-dimensional distributions in the variables x_2, x_3 and $\cos\theta$, χ. We have also studied the y_{cut} dependence of distributions in the four kinematical variables. The experimental precision is about 5%. All measurements can be reproduced by the second order

QCD calculations (with gluon spin of 1) [142,22,172]. We have compared our measurements also to the predictions of a first order spin-0 gluon model [22,173]. The scalar gluon model can not reproduce the measurements. As an example the x_3 distribution is shown in figure 10.7. It

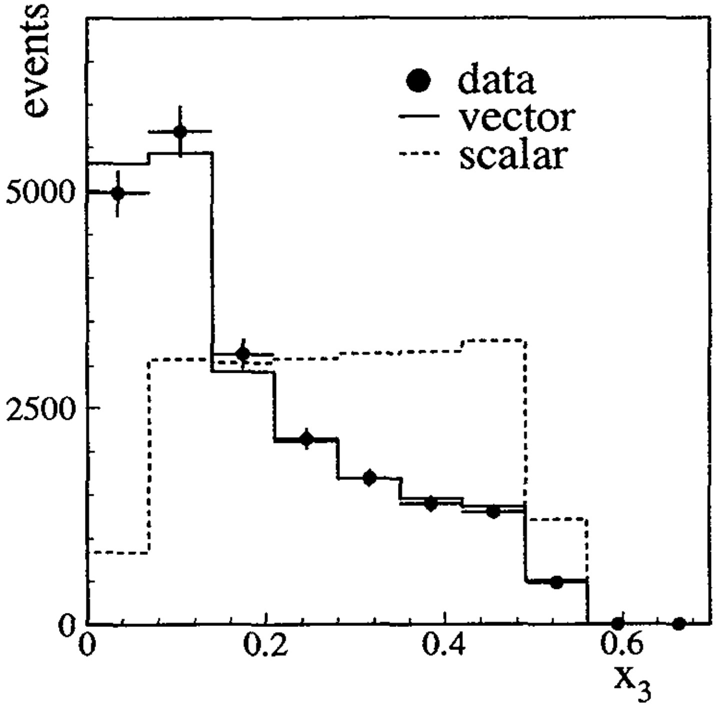

Figure 10.7: Distribution of scaled energy of second jet x_3

is based on events with transition values y_{23}, for which a 3-jet configuration turns into a 2-jet event, in the range $0.02 \leq y_{23} \leq 0.05$. The data are corrected for detector effects. The theoretical curves include hadronization corrections and are normalized to the number of data events. The spin-0 gluon model is clearly ruled out. Also from the study of the event orientation alone the hypothesis of scalar gluons can be excluded [171].

Our results agree with those obtained by other experiments at the Z resonance [174]. The spin-0 model has been ruled out already from analyses of other reactions [175], and also from e^+e^- data at lower energies [128]. However, at LEP the differences between the two models are much bigger, and the QCD predictions can be tested with a higher precision.

10.3.2 4-jet events and gluon self-coupling

One of the essential features of QCD is the self-interaction of gluons, a consequence of its non-abelian nature. We performed tests of QCD which are sensitive to the gluon self-coupling in $e^+e^- \rightarrow$ hadrons. They are based on a study of angular correlations in 4-jet events [176].

QCD predicts two classes of 4-jet events which correspond to the processes

$$Z \rightarrow q\bar{q}gg \tag{10.35}$$

and

$$Z \to q\bar{q}q\bar{q} \tag{10.36}$$

at parton level. The corresponding generic Feynman diagrams are shown in figure 10.8. The first

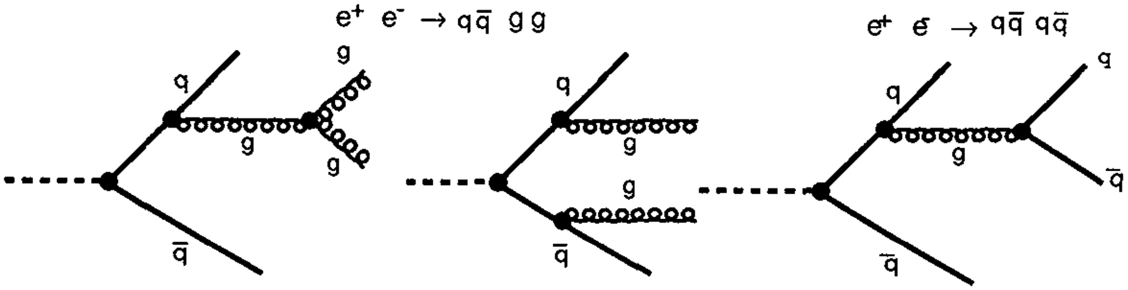

Figure 10.8: Feynman diagrams for 4-jet production

graph for $q\bar{q}gg$ events contains a three-gluon vertex. An alternative model without self-coupling of the spin-1 gluons can be constructed with three color degrees of freedom for the quarks [177]. Here only the double bremsstrahlung diagrams contribute to the process $e^+e^- \to q\bar{q}gg$.

Different variables have been proposed that are sensitive to the differences between QCD and the abelian model [178, and references therein]. All of them are based on angular correlations between the four energy ordered jets. The two most energetic jets are likely to correspond to the primary quarks.

We have measured these angular variables using 4,200 events with four jets defined by the JADE jet algorithm with a resolution parameter of $y_{\rm cut} = 0.02$. The corrected and normalized distribution of the Bengtsson-Zerwas angle $\chi_{\rm BZ}$ [179] is shown in figure 10.9. The quantity $\chi_{\rm BZ}$ is the angle between the plane spanned by the two most energetic jets and the plane containing the other two jets. The measurements are compared to the predictions of QCD and the abelian model. The data are corrected for detector effects. Corrections for hadronization and particle decays are included in the theoretical curves. The theoretical uncertainties (bands in figure 10.9) are estimated by comparing angular distributions determined from a matrix-element calculation to those from a parton shower generator. The measurements are reproduced by QCD, while the predictions of the abelian model are clearly incompatible with the data. The same conclusions can be drawn from the study of other angular variables [176].

Similar studies have been performed by other LEP experiments [180] and for smaller event samples at $\sqrt{s} \approx 60$ GeV [181].

10.4 Isolated hard photons in hadronic events

We have studied the production of energetic final-state photons in hadronic Z decays [35]. Photons, like gluons, can be emitted from the primary quarks; however, photons differ from gluons in that they appear directly in the final state without undergoing a complex evolution into hadrons.

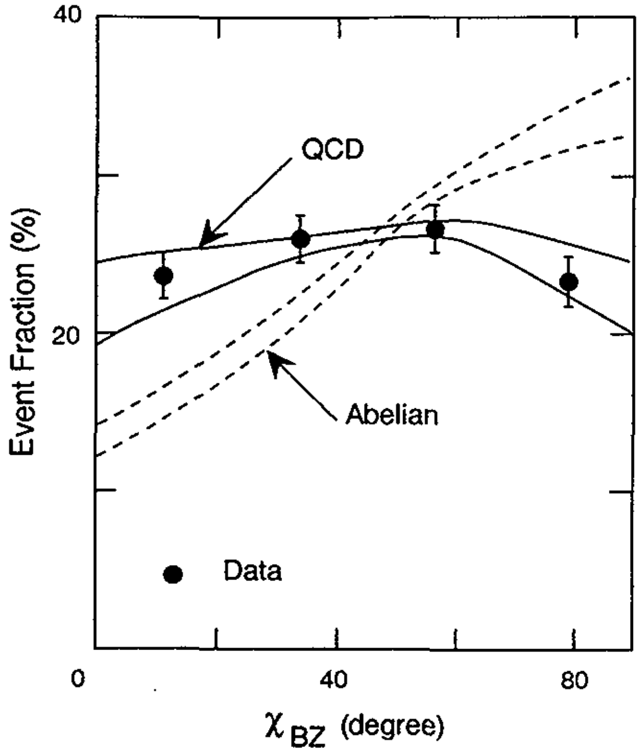

Figure 10.9: Distribution of the Bengtsson-Zerwas angle χ_{BZ}

We analyze a sample of 320,000 hadronic events measured at the Z peak and select photon candidates as described in section 5.5. This selection leaves 3202 events. We compare measured distributions to three event generators and to an $\mathcal{O}(\alpha\alpha_s)$ matrix-element calculation [182,110]. All the generators, JETSET 7.3, HERWIG 5.4, and ARIADNE 4.02 [183], use the leading-logarithms method (including matrix-elements to lowest order) of calculating the direct photon contribution. For the matrix-element calculation [110]. an effective first order α_s value of 0.17 was used. The dependence on the strong coupling is small; setting $\alpha_s = 0$ changes the predicted total rate of hard photons by only a few percent. We use the Standard Model predictions for the electroweak coupling constants of quarks with a value of $\sin^2\theta_W$ as determined in chapter 8.

The measured photon energy spectrum is shown in figure 10.10 and compared to model predictions. The data are corrected for detector effects, acceptance, initial-state radiation and neutral hadron background [35]. The matrix-element calculation describes the data well [33]. We observe a good general agreement between our measurements and the predictions and we cannot discriminate between them. Our result agrees with those of other LEP collaborations [36].

10.5 Particle production and gluon interference effects

Analytical QCD calculations predict gluon interference , affecting particle spectra and multiplicities and the particle production between jets. In the following sections we present our measurements and compare them to the corresponding QCD calculations.

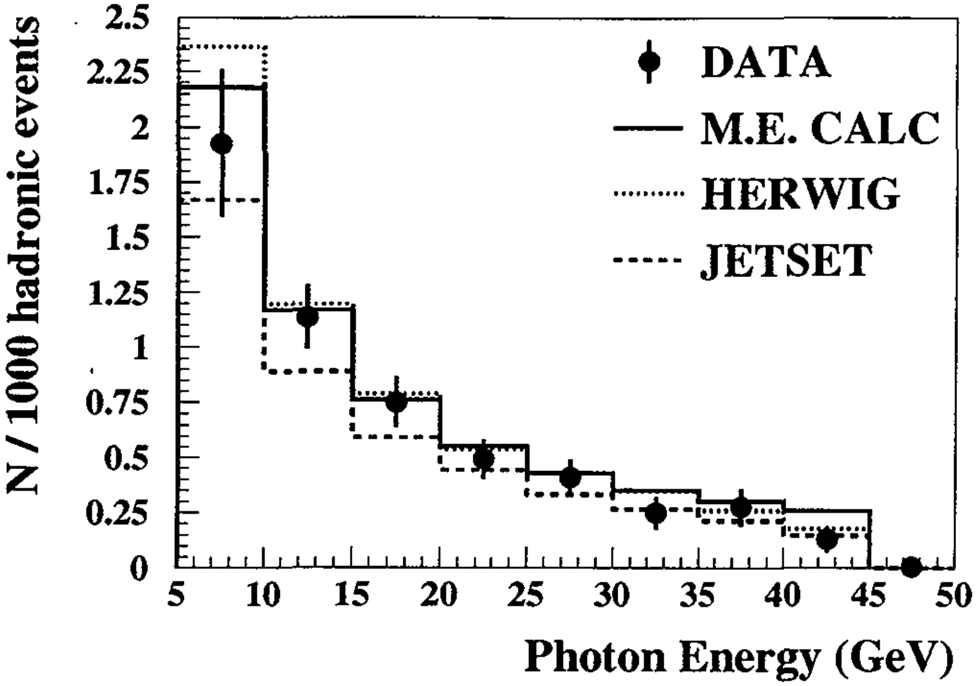

Figure 10.10: Energy distribution for isolated photons in hadronic events. The error bars indicate the total experimental uncertainties. The spectrum predicted by the ARIADNE program (not shown) is very close to the result of the matrix element calculation.

10.5.1 Inclusive particle production

We have measured inclusive particle production in hadronic events and compared the momentum spectra to the predictions of QCD calculations. Neutral pions and η mesons are reconstructed from photon pairs measured in the electromagnetic calorimeter [184, 185]. Charged particles are reconstructed using the central tracking chamber [184].

There are two approaches to calculate the inclusive momentum spectra within perturbative QCD: 1) Monte Carlo parton shower generators based on leading-log calculations including gluon coherence and including hadronization and particle decays, and 2) analytical calculations in the Modified Leading-Log Approximation (MLLA), summing double and single leading-log contributions, and including coherence effects [186]. In this case it is assumed that the calculated parton spectra can be compared directly to the momentum distribution of measured hadrons (Local Parton Hadron Duality, LPHD) [186, 187].

A striking prediction of perturbative QCD concerning the inclusive momentum spectra is a reduction of the number of soft gluons due to destructive interference [188]. This behavior can be studied best in terms of the variable $\xi_p = \ln(1/x_p)$, where x_p is the ratio of the particle momentum to the beam energy. The QCD calculations predict a maximum in the ξ_p distribution [186, 189, 190]. The differential cross section at high values of ξ_p is reduced due to soft gluon interference. The position of the maximum, ξ_p^*, is expected to move to higher values with increasing center of mass energy. For massive particles the spectrum is modified such that the peak position is shifted to lower values. Thus one expects that for η mesons with a mass of 549 MeV, ξ_p^* should be smaller than that for π^0 mesons with a mass of 135 MeV.

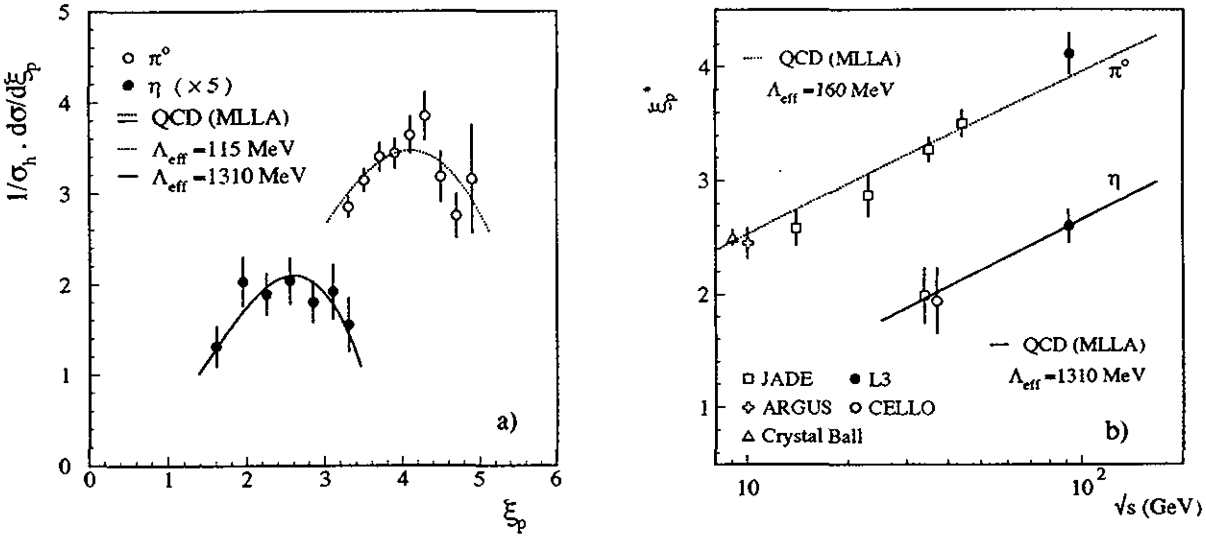

Figure 10.11: a) Inclusive ξ_p spectra for π^0 and η, b) position of the maximum in the ξ_p distributions for π^0 and η

Hadronic events are selected as described in chapter 5. The π^0 and charged particle analyses are based on 112,000 events, while the study of inclusive η production uses 297,000 events. Photons are recognized as isolated and confined clusters in the barrel part of the electromagnetic calorimeter. The photon direction is determined assuming the photon to originate at the interaction point. For the π^0 analysis, the energy of each photon must exceed 130 MeV, for the η analysis the cut is at 500 MeV. The finite granularity of the electromagnetic calorimeter sets a lower bound of $\sim 6°$ on the opening angle of detected pairs of photons, which effectively limits the energy of the observed π^0 (η) mesons decaying into non-overlapping photons to less than 3(10) GeV.

The invariant mass distribution of all photon pairs in the kinematic region $0.0075 < x_p < 0.065$ is shown in figure 2.8. The fit to the mass distribution, indicated by a solid line, is the sum of a Gaussian function and a third order polynomial. The π^0 peak has a width of $\sigma = 7.1$ MeV. In the η analysis all photons entering into a two photon combination with invariant mass compatible with the π^0 mass are excluded. The resulting $\gamma\gamma$ invariant mass distribution in the kinematic region $0.035 < x_p < 0.225$ is shown in figure 2.8. The width of the η peak is $\sigma = 16.1$ MeV. To measure the differential cross sections the observed meson yields in the data are corrected, as a function of momentum, for detector effects and initial- and final-state photon radiation. The detection efficiencies are found to be between 2% and 6% for π^0's. The η detection efficiencies, including the 38.9% branching ratio of the η meson into two photons, are found to be approximately 1%.

The inclusive momentum distribution for charged particles is determined from the tracks measured in the central tracking chamber. The x_p and ξ_p distributions are corrected for detector effects, photon radiation and decays of particles with an average lifetime longer than $5 \cdot 10^{-10}$ s.

We measure the average number of charged particles per hadronic event to be $\langle n_{\mathrm{ch}} \rangle = 20.8 \pm 0.5$. Assuming the form of the spectra as predicted by JETSET to extrapolate our measured π^0 and η cross sections to the full x_p range we find $\langle n_{\pi^0} \rangle = 9.8 \pm 0.7$ and $\langle n_\eta \rangle = 1.1 \pm 0.2$ for the average π^0 and η multiplicities per event. The numbers for charged particles and η mesons agree with those determined by other LEP experiments [191,192].

The ξ_p distributions for π^0, η and charged particles are compared to the predictions of the MLLA QCD calculation [186], which can be written in the form:

$$\frac{1}{\sigma_{\mathrm{h}}} \frac{d\sigma}{d\xi_p} = N(\sqrt{s}) \cdot f(\sqrt{s}, \Lambda_{\mathrm{eff}}, \xi_p). \tag{10.37}$$

There are only two free parameters in this expression; an overall normalization factor N, which describes the hadronization and depends on the center of mass energy and on the particle type; and an effective scale parameter Λ_{eff} (not directly related to $\Lambda_{\overline{\mathrm{MS}}}$). Formula (10.37) is valid in the range $1 < \xi_p < \ln(0.5\sqrt{s}/\Lambda_{\mathrm{eff}})$.

We fit expression (10.37) to our data in a range of ξ_p of about ±1 around the position ξ_p^* of the maximum. We obtain:

$$\begin{aligned} \pi^0 :\ \Lambda_{\mathrm{eff}} &= 115 \pm 38 \text{ MeV} \qquad \xi_p^* = 4.11 \pm 0.18 \qquad (10.38) \\ \eta :\ \Lambda_{\mathrm{eff}} &= 1310 \pm 270 \text{ MeV} \qquad \xi_p^* = 2.60 \pm 0.15 \qquad (10.39) \\ \text{charged particles} :\ \Lambda_{\mathrm{eff}} &= 220 \pm 20 \text{ MeV} \qquad \xi_p^* = 3.71 \pm 0.05. \qquad (10.40) \end{aligned}$$

ξ_p^* is the position of the maximum as calculated from (10.37). The QCD predictions for $\sqrt{s} =$ 91 GeV based on the fitted parameters are compared in figure 10.11a to the measured ξ_p spectra for π^0 and η. The peak position shifts to smaller values with increasing particle mass, as predicted by QCD.

In order to study the energy dependence of the inclusive ξ_p distributions, we determined Λ_{eff} and N by fitting the MLLA function (10.37) as described above, for all the available π^0, η spectra between 9 and 91 GeV which cover the peak region [184, 185, 193, 194]. The corresponding peak positions ξ_p^* are shown in figure 10.11b for π^0 and η mesons. The measurements are consistent with the QCD formula (10.37). The Λ_{eff} values used for the QCD calculations for π^0 in figure 10.11b are obtained from a fit to all data points. Also the peak positions for charged particles for center of mass energies between 14 and 91 GeV [184,194] are reproduced by QCD. Our analysis shows that the MLLA calculations including gluon interference together with the LPHD hypothesis describe the form, energy and particle mass dependence of the inclusive ξ_p spectra.

10.5.2 Multiplicities in 3- and 2-jet events

We measure the ratio of cluster multiplicities in 3- and 2- jet samples. The latter events are due to fragmentation of two quarks whereas three jet final states are due to one additional hard gluon. If one naively assumes that the multiplicity is directly related to the color charge, one would expect the multiplicity ratio in 3-jet ($q\bar{q}g$) relative to 2-jet ($q\bar{q}$) events to be $(2C_F + C_A)/2C_F = 17/8$, where $C_F = 4/3$ and $C_A = 3$ are the color charges of quark and gluon, respectively. This ratio has been calculated [195] in the framework of perturbative QCD, including leading and next-to-leading terms to all orders.

Jets are reconstructed using the $k_\perp$ algorithm [134], see section 10.2.1 . We choose a fixed value of y_{cut} ($y_1 = 0.01$) to select exclusive 3- and 2-jet samples. Then, using the same algorithm but a smaller value of y_{cut}, y_0, we determine the cluster multiplicity in the 3- and 2-jet samples. We thus obtain two sets of measurements M_2 and M_3 which are the average cluster multiplicities at a cluster resolution y_0 in events that consist of precisely two and three jets, respectively, at jet resolution y_1.

We have studied the average multiplicities in 3-jet and 2-jet events and the ratio. These measurements are corrected for detector effects, acceptance and resolution, and for initial- and final-state photon radiation, on a bin-by-bin basis using the JETSET 7.3 Monte Carlo program. The systematic errors on each corrected data point are due to uncertainties in the detector simulation and biases from the Monte Carlo program. Statistical uncertainties are negligible.

The corrected distribution of the multiplicity ratio is shown in figure 10.12 in comparison with the QCD calculations [195]. The theoretical calculations agree with the experimental data. We show in the same figure the ratio as predicted by a model without gluon interference [196]. The prediction rises monotonically with decreasing y_0 and fails to reproduce the measurements. In the QCD calculations the decrease of M_3/M_2 with decreasing y_0 below the value of 1.5 is due to a suppression of the gluon jet contribution to the cluster multiplicity in 3-jet events. The suppression is due to soft gluon interference. Our analysis shows that inclusion of these coherence effects in the calculations are needed to describe our measurements, and that the naive expectation for the ratio M_3/M_2 of $17/8 = 2.125$ is not supported by our data.

10.5.3 String effect

More than ten years ago it was observed for the first time that in events of type $e^+e^- \to 3$ jets at $\sqrt{s} \approx 30$ GeV fewer particles are produced in between the q and $\bar{q}$ jets in comparison to the other two inter-jet regions [197]. This observation was confirmed by other e^+e^- experiments [198, 199, 45]. This asymmetry in the particle flow in the 3-jet plane was predicted in the context of the string fragmentation model [200], and can also be explained by analytical QCD calculations including coherence effects [201].

We present here a comparison of the energy flow in 3-jet events of the types $q\bar{q}g$ and $q\bar{q}\gamma$ which confirms the string effect in a model independent way. We select $q\bar{q}g$ 3-jet events by clustering jets with the JADE algorithm [34] using $y_{\text{cut}} = 0.05$ and requiring three jets. After energy ordering the first jet comes most probably from a quark. An inclusive muon with a momentum exceeding 4 GeV (see chapter 6) is required in one of the two other jets, thus tagging it as a quark jet. With a probability of about 85% the remaining third jet stems from a gluon. Events with two hadronic jets and one isolated photon with $E_\gamma \geq 5$ GeV are selected as

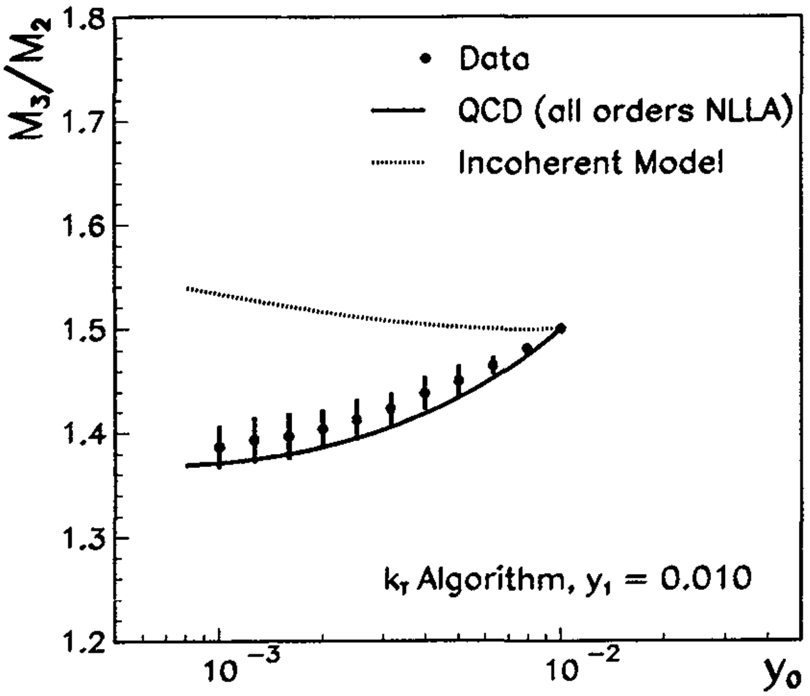

Figure 10.12: Multiplicity ratio M_3/M_2 as function of y_0 in comparison with the predictions of QCD calculations and a model without gluon interference effects (Incoherent Model).

described in section 10.4. In both cases we restrict ourselves to events where the angle between the two quark jets is in the range 152° to 168°. In total we select 82 $q\bar{q}\gamma$ and 590 $q\bar{q}g$ events.

The energy flow in the 3-jet event plane is measured as the energy weighted distribution of the angles of all calorimetric clusters with respect to the axis of the first jet. Figure 10.13 compares the energy flow for the $q\bar{q}g$ events and $q\bar{q}\gamma$ events. The quark jets appear at angles around 0° and 160° and the gluon or photon between 200° and 320°. In the angular region between the two quark jets a clear depletion is visible in case of $q\bar{q}g$ events. The ratio of the integrals of the energy flows for $q\bar{q}\gamma$ and $q\bar{q}g$ events in the range $56° < \Phi < 112°$ is measured to be 1.8 ± 0.3. The error includes both statistical and systematic uncertainties. We have verified that the energy flow distribution is not biased by requiring a high momentum muon in the event: a comparison of energy ordered 3-jet events without muons to those including a muon shows no difference within statistical errors. Both the JETSET 7.3 and HERWIG 5.4 parton shower Monte Carlo programs reproduce our measurements.

10.6 Summary

We have performed a precise measurement of the strong coupling constant, the only free parameter in Quantum Chromodynamics. The average of the values obtained from the topol-

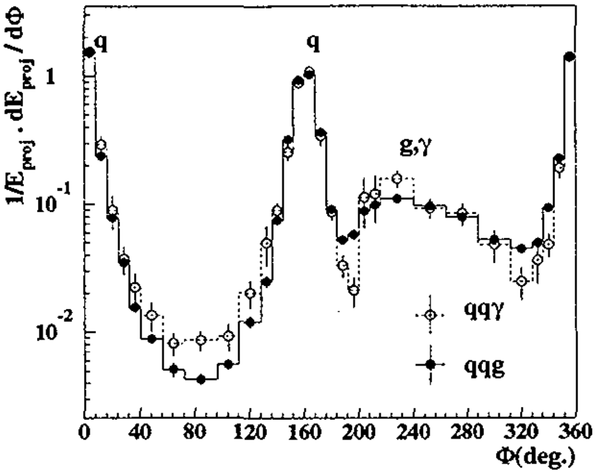

Figure 10.13: Comparison of energy flow in $q\bar{q}\gamma$ and $q\bar{q}g$ events. The measurements are shown both in the form of points with statistical error bars and in the form of a histogram

ogy of hadronic Z decays, the ratio of the hadronic and leptonic Z widths and τ decays is $\alpha_s(m_Z) = 0.124 \pm 0.005$.

We have tested the fundamental properties of QCD. The running of α_s is confirmed by the comparison of α_s values at $\mu = m_\tau$ and $\mu = m_Z$, and by the measured $\sqrt{s}$ dependence of the 3-jet fraction. The strong coupling strength for bottom quarks is found to agree with that of the lighter quarks. Many distributions for 3-jet and 4-jet events have been measured; they are reproduced by QCD. Alternative models with scalar gluons or without gluon self interaction are ruled out.

String and cluster fragmentation models describe hadronic events, including topologies with isolated hard photons. All distributions at the hadron level are reproduced by QCD Monte Carlo programs. The direct photon production in hadronic Z decays can be described by $\mathcal{O}(\alpha\alpha_s)$ matrix-element calculations. Analytical QCD calculations including soft gluon interference effects describe the measured inclusive particle spectra and the ratio of multiplicities in 3- and 2-jet events. A comparison of the energy flows in $q\bar{q}\gamma$ and $q\bar{q}g$ events confirms the string effect.

Chapter 11

Leptonic Final States with Hard Photons

Photon radiation from the initial and final state leptons is the known source for hard and isolated photon production. The process is described by QED and can be accurately simulated by Monte Carlo programs. Leptonic events with photons are easily identified [202]. Therefore, $\ell^+\ell^-(n\gamma)$ events can be used to test QED. An excess in $\ell^+\ell^-(n\gamma)$ events would imply new physics. The data used in this analysis are collected from the 1990, 1991 and 1992 runs corresponding to a total integrated luminosity of 40 pb^{-1} and a sample of 1,600,000 Z bosons produced at center-of-mass energies ranging from 88.2 to 93.8 GeV.

Electrons and photons are identified by their shower characteristics in the electromagnetic calorimeter. Electrons are distinguished from photons by the presence of tracks in the central tracking chamber. Muons are identified and measured in the muon chambers. Taus are identified by their one- and three-prong decays. Leptons are required to have visible energies above 3.0 GeV. In addition, the polar angles of electrons, muons and taus must be within the fiducial volumes defined by $|\cos\theta_e| < 0.74$, $|\cos\theta_\mu| < 0.80$, and $|\cos\theta_\tau| < 0.74$, respectively. Photons are required to fulfill $|\cos\theta_\gamma| < 0.9$ and to have an energy above 1.0 GeV. In order to have a reliable energy measurement and to reduce background from tau decays, photons are required to be at least 8° away from electrons, 5° from muons, and 15° from taus. The total number of selected events in each channel is shown in table 11.1.

number	Data				MC Expectations			
of photons	e^+e^-	$\mu^+\mu^-$	$\tau^+\tau^-$	$\ell^+\ell^-$	e^+e^-	$\mu^+\mu^-$	$\tau^+\tau^-$	$\ell^+\ell^-$
$n \geq 0$	31351	28854	22400	82605	—	—	—	—
$n \geq 1$	2412	2270	1150	5832	2147	2279	1178	5604
$n \geq 2$	94	109	41	244	74	92	32	198

Table 11.1: Numbers of $\ell^+\ell^-(n\gamma)$ events in the data together with the expected numbers from the Monte Carlo. The Monte Carlo expectations are normalized to the corresponding number of data events with $n \geq 0$.

To compare the measured distributions with the expectation from QED, we use the Monte Carlo program YFS3 as described in reference 203. The program generates events of the type

$e^+e^- \to \mu^+\mu^-(n\gamma)$ according to the Yennie-Frautschi-Suura scheme [204] with multiple colinear and soft photon radiation in both the initial and final states. It includes the additional leading-log terms for one or two hard photons. The cross section for the production of events with hard and isolated photons as calculated by the program has been found to be in good agreement with the exact $\mathcal{O}(\alpha^2)$ matrix element calculations [205]. The program is adequate to describe the $e^+e^- \to \tau^+\tau^-(n\gamma)$ process since only photons with energies greater than 1.0 GeV and opening angles with respect to the nearest tau direction greater than 15° are considered, so that tau mass effects are negligible. The t channel contribution to the $e^+e^- \to e^+e^-(n\gamma)$ process is not modeled by YFS3. Instead we use the pure s channel distributions for comparisons with $e^+e^-(n\gamma)$ data. The expected number of events from Monte Carlo is shown in table 11.1. In the following comparisons, the contributions from the three lepton flavors are combined.

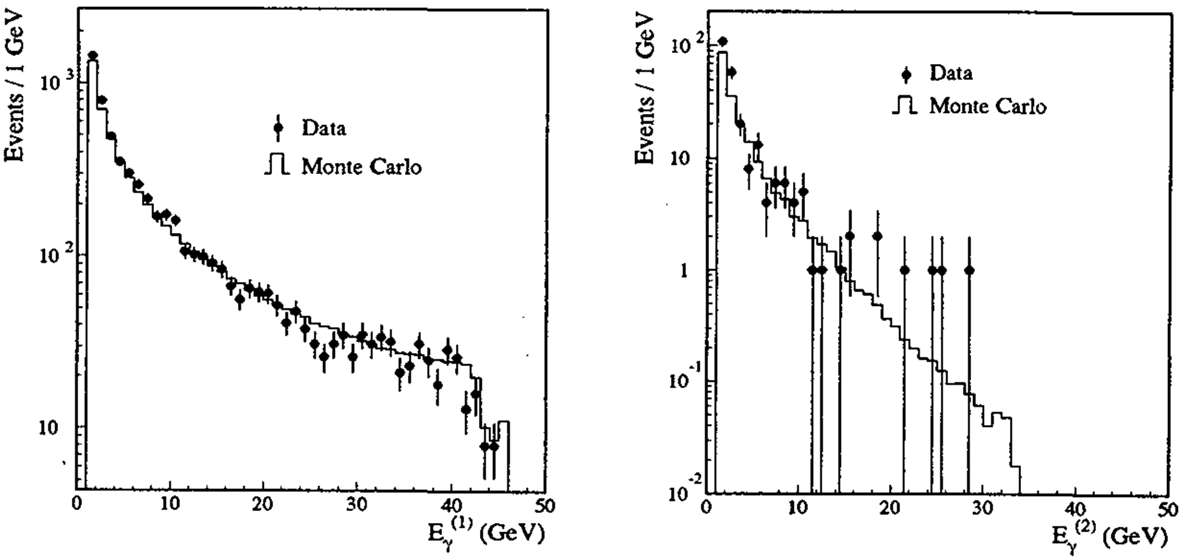

Figure 11.1: (a) The energy distribution of the most energetic photon for the selected $\ell^+\ell^-$ events with one or more photons. (b) The energy distribution of the second most energetic photon for the selected $\ell^+\ell^-$ events with at least two photons.

The energy distribution of the most energetic photon for events with one or more photons in the final state is compared with the prediction of the YFS3 Monte Carlo program in Fig. 11.1(a). Fig. 11.1(b) shows the energy spectrum of the second most energetic photon for events with at least two photons. Fig. 11.2 shows the comparison with the Monte Carlo for the angle between the most energetic photon and the nearest charged lepton for events with one or more photons. The Monte Carlo distributions in these figures are obtained from a high statistics sample corresponding to approximately 10^7 $e^+e^- \to \mu^+\mu^-(n\gamma)$ events. These are generator level events selected with criteria similar to those used for the $\ell^+\ell^-(n\gamma)$ events in the data. The distributions are normalized to the expected number of events obtained from the fully simulated Monte Carlo events shown in table 11.1. As shown in the table and in the figures, the predicted Monte Carlo distributions for events with one or more photons are in good agreement with the data in both the shape and the normalization. We note that the Monte Carlo underestimates e^+e^- events with photons. The underestimation is due to the fact that the Monte Carlo simulation does not include the t channel contribution for e^+e^- production.

Fig. 11.3 shows the $m_{\gamma\gamma}$ distribution for events with at least two photons compared with the prediction of the Monte Carlo program. The Monte Carlo distribution is obtained from the same high statistics $e^+e^- \to \mu^+\mu^-(n\gamma)$ sample used for Fig. 11.1 and is normalized in the same manner. Four data events have an invariant mass of the photon pair clustering around 60 GeV. Three are $\mu^+\mu^-\gamma\gamma$ events and the fourth is an $e^+e^-\gamma\gamma$ event. These events have the following measured photon pair masses: $m_{\gamma\gamma} = 58.8 \pm 0.6$, 59.0 ± 0.6, 62.0 ± 0.6, 60.0 ± 0.6 GeV. QED does not predict clustering of $m_{\gamma\gamma}$ around 60 GeV and we determine the probability for observing four or more events around 60 GeV due to a fluctuation in our data. We simulate 10^6 $m_{\gamma\gamma}$ distributions with the number of events in each simulation normalized to the total number $\ell^+\ell^-\gamma\gamma$ events in the data. The instances of events clustering within a single mass bin of $\Delta m_{\gamma\gamma} = 5$ GeV are counted. This bin width corresponds to eight times the $m_{\gamma\gamma}$ measurement error at 60 GeV. The probability for observing four or more clustered events, all with $m_{\gamma\gamma} >$ 50 GeV, is found to be $\mathcal{O}(10^{-2})$. The photon pairs could arise from the decay of a massive particle. However, a fluctuation cannot be ruled out. More data are needed to ascertain the origin of these event.

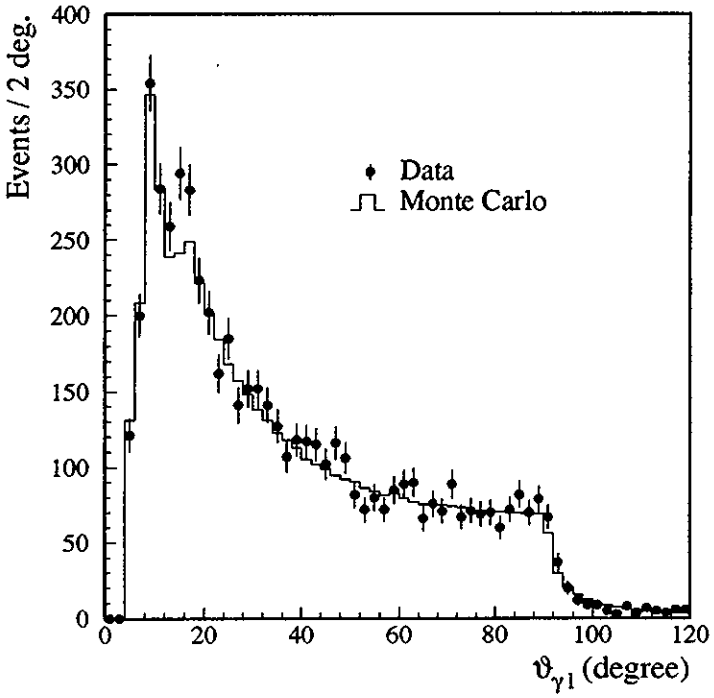

Figure 11.2: The angle distribution of the most energetic photon with respect to the nearest lepton for the selected $\ell^+\ell^-$ events with at least one photon. The structure at 15° in the data is caused by $\tau^+\tau^-(n\gamma)$ events and is not reproduced by the Monte Carlo for $\mu^+\mu^-(n\gamma)$ events for which the angular resolution is better.

Events of the type $e^+e^- \to \nu\bar{\nu}\gamma\gamma$ have also been searched for in the data collected from 1991 and 1992 runs, applying similar requirements on the photons and requiring the polar angle of the direction of missing momentum to be greater than 25.8° with respect to the beam axis. No event is found with $m_{\gamma\gamma} > 10$ GeV. It should also be noted that, with different isolation criteria and in a data sample of approximately 450,000 Z events corresponding to an integrated luminosity of 13 pb^{-1}, no hadronic event containing isolated photon pair with $m_{\gamma\gamma} > 40$ GeV

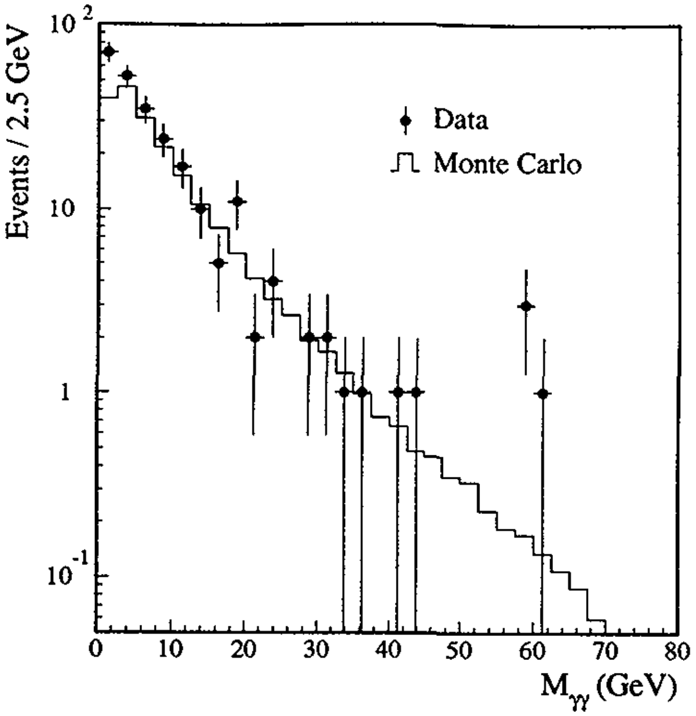

Figure 11.3: $m_{\gamma\gamma}$ distribution of the data for $\ell^+\ell^-$ events with two or more photons compared to the expectation from the Monte Carlo.

has been observed in our data [35].

Chapter 12

Search for the Higgs Boson

12.1 The Higgs boson in the Standard Model

In the Standard Model [3] the Z and $W^{\pm}$ bosons acquire mass through the Higgs mechanism [12], which, in its minimal formulation, predicts the existence of one neutral scalar boson H^0. The H^0 coupling to both vector bosons and fermions is predicted by the theory, while the value of its mass is not predicted. If the Higgs boson is lighter than the Z, it can be produced in Z decays through the bremsstrahlung process [206]:

$$e^+e^- \to Z \to H^0 + Z^* \to H^0 + f\bar{f}. \tag{12.1}$$

In the Standard Model the cross section for this process is known as a function of the Higgs mass [207]. Higher order electroweak corrections have been taken into account using the improved Born approximation [101] and accounting for radiative corrections to the ZZ^*H^0 vertex [208]. The effect of initial state photon radiation has been computed using an exponentiation technique [209].

The Higgs decay partial widths into fermions are also well established for masses of the H^0 greater than 2 GeV [210]. Since the Higgs coupling to fermions is proportional to the fermion mass, the Higgs decays predominantly into $b\bar{b}$ for masses above 11 GeV, although the branching ratios into $c\bar{c}$ and $\tau^+\tau^-$ are not negligible [210]. In the mass range from 4 to 11 GeV, decays into $\tau^+\tau^-$ and $c\bar{c}$ dominate. Between 2 and 4 GeV it will decay mainly into $s\bar{s}$. Below 2 GeV non-perturbative effects make the prediction of the branching ratios less firm [210]. In this last region, the experimental Higgs search should be independent of the decay modes. Below the $2m_\mu$ threshold the Higgs can decay only into two electrons or two photons. In this case the Higgs width is very small and consequently its lifetime can be so long that it can decay outside the detector.

Before the startup of LEP, the Higgs boson H^0 has been searched in very different reactions [211–218]. The most stringent limit, $m_{H^0} > 5$ GeV, comes from the CUSB experiment [216], searching for the reaction $\Upsilon \to \gamma H^0$. However, no exclusion so far was complete mainly due to uncertainties in the computation of expected production rates involving hadron physics. Only the range 1.2 MeV $< m_{H^0} <$ 50 MeV was excluded at 90% confidence level [212].

Here we report our search for the Standard Model Higgs boson using data samples from 1990 and 1991 LEP runs corresponding to a total of 408,000 Z hadronic decays and an integrated luminosity of 17.5 pb^{-1} at center of mass energies between 88.2 and 94.3 GeV.

12.1.1 Search in the mass range $m_{\mathrm{H}^0} < 2m_\mu$

For masses of the Higgs boson below the $\mu^+\mu^-$ threshold its lifetime would be of order picoseconds and it would decay predominantly into an $\mathrm{e}^+\mathrm{e}^-$ pair. We have searched for such very low mass Higgs Boson in the channel $\mathrm{e}^+\mathrm{e}^- \to \ell^+\ell^-\mathrm{H}^0$ with $\ell = \mathrm{e}$ or μ where the Higgs boson decays into two charged particles either inside or outside the volume of the electromagnetic calorimeter. For the former case, the event signature is a pair of acoplanar, isolated and very energetic leptons accompanied by at least two additional tracks associated with energy clusters in the calorimeters. For the latter case the events are characterized by a pair of acoplanar and energetic leptons with no other detected particle balancing the missing momentum.

Three events have been found satisfying these criteria. The expected background is 4.3 ± 0.4 events, from the reaction $\mathrm{e}^+\mathrm{e}^- \to \mathrm{e}^+\mathrm{e}^-\gamma$, where the photon reaches the hadronic calorimeter without leaving a signal in the electromagnetic calorimeter.

12.1.2 Search in the mass range $2m_\mu < m_{\mathrm{H}^0} < 2$ GeV

We have searched for a low mass Higgs boson decaying into muons or hadrons. The main backgrounds with a similar signature are four fermion final state processes and radiative dileptons with a photon converting in material in or in front of the central tracking chamber.

Event signature is the presence a pair of acoplanar, isolated and very energetic leptons accompanied by at least two additional tracks associated with energy clusters in the calorimeters. In order to reject photon conversions, the vertex of the Higgs candidate decay products should be closer than 20 mm to the beam spot in the transverse plane.

Six events have been found which satisfy the above requirements: 2 in the $\mathrm{e}^+\mathrm{e}^- \to \mathrm{e}^+\mathrm{e}^-+\mathrm{X}$ channel and 4 in the $\mathrm{e}^+\mathrm{e}^- \to \mu^+\mu^-+\mathrm{X}$ channel. The expected background is 5.8 ± 1.2 events from $\mathrm{e}^+\mathrm{e}^- \to \mathrm{e}^+\mathrm{e}^-\mu^+\mu^-$ and 1.9 ± 0.2 events from $\mathrm{e}^+\mathrm{e}^- \to \mu^+\mu^-\mu^+\mu^-$.

12.1.3 Search in the mass range $2 < m_{\mathrm{H}^0} < 15$ GeV

In this mass region the Higgs decay products will appear as one or more hadronic jets. We have searched for events with a pair of energetic, isolated and acolinear electron or muons accompanied by hadronic jets consisting of more than two particles each. There are no candidates where the mass recoiling against the lepton pair is below 15 GeV.

We have also searched for events of the kind $\mathrm{e}^+\mathrm{e}^- \to \nu\bar{\nu}\mathrm{H}^0$ characterized by the presence of a single jet, two acolinear jets or many acoplanar jets and large missing energy.

The selection efficiencies for all channels are summarized in table 12.1 as a function of the Higgs mass. We find no candidate satisfy these criteria. From a Monte Carlo simulation of all background processes we expect to find less than one event.

Higgs mass (GeV)	2	5	9	15
efficiency for $e^+e^- \rightarrow H^0\nu\bar{\nu}$	0.24	0.37	0.35	0.44
efficiency for $e^+e^- \rightarrow H^0e^+e^-$	0.226	0.408	0.518	0.526
efficiency for $e^+e^- \rightarrow H^0\mu^+\mu^-$	0.246	0.275	0.318	0.462

Table 12.1: Selection efficiencies as a function of Higgs boson mass for all analyzed production channels

12.1.4 Search in the mass range $m_{H^0} > 15$ GeV

We have searched for the Higgs boson with a mass above the $b\bar{b}$ threshold in the channels:

$$\begin{aligned}
e^+e^- &\rightarrow (H^0 \rightarrow q\bar{q})(Z^* \rightarrow \nu\bar{\nu}),\\
e^+e^- &\rightarrow (H^0 \rightarrow q\bar{q})(Z^* \rightarrow \mu^+\mu^-),\\
e^+e^- &\rightarrow (H^0 \rightarrow q\bar{q})(Z^* \rightarrow e^+e^-),\\
e^+e^- &\rightarrow (H^0 \rightarrow q\bar{q})(Z^* \rightarrow \tau^+\tau^-)\\
e^+e^- &\rightarrow (H^0 \rightarrow \tau^+\tau^-)(Z^* \rightarrow q\bar{q}).
\end{aligned}$$

The final state $(H^0 \rightarrow q\bar{q})(Z^* \rightarrow q\bar{q})$, although dominant, is very difficult to separate from four-jet QCD background, and has not been considered in the analysis.

Events of the kind $e^+e^- \rightarrow \ell^+\ell^-q\bar{q}$ are selected by requiring two isolated leptons recoiling against a high multiplicity hadronic system. Isolation criteria for the leptons are designed to reject heavy flavor double semileptonic decays in events like $e^+e^- \rightarrow b\bar{b} \rightarrow \ell^+\ell^-+X$. In table 12.2 the high mass Higgs detection efficiencies for the different channels studied are summarized. For the $H^0e^+e^-$ and the $\tau^+\tau^-q\bar{q}$ channels we quote efficiencies for the 1990 and the 1991 setup. The efficiency for the 1990 data is lower due to the lower geometrical acceptance of the electromagnetic calorimeter which did not include the endcaps. For the $H^0\nu\bar{\nu}$ and the $H^0\mu^+\mu^-$ channels the efficiencies are the same in 1990 and 1991.

Two events passed the selection criteria. One is an $e^+e^- \rightarrow e^+e^-+X$ event observed at $\sqrt{s} = 88.4$ GeV. The event is shown in Figure 12.1. Its main parameters are: mass recoiling against the final state $e^+e^- = 31.4 \pm 1.5$ GeV, mass(e^+e^-)$= 46.8 \pm 1.9$ GeV, measured mass of the hadronic system = 23 GeV; this last value is consistent with the Monte Carlo expectation of 28.7 ± 4.3 GeV for the decay of a Higgs boson with mass 31.4 GeV.

Higgs mass (GeV)	30	40	50	55	60
$H^0\nu\bar{\nu}$ channel	36.4	60.6	59.0	50.3	37.4
$H^0e^+e^-$ channel (1991)	58.2	55.2	52.2	50.5	49.4
$H^0e^+e^-$ channel (1990)	45.5	38.0	35.0	32.0	29.0
$H^0\mu^+\mu^-$ channel	62.6	61.2	61.6	60.6	55.4
$(H^0 \to \tau^+\tau^-)(Z^* \to q\bar{q})$ (1991)	3.8	10.2	15.8	17.6	15.0
$(H^0 \to \tau^+\tau^-)(Z^* \to q\bar{q})$ (1990)	2.4	5.4	9.4	12.4	8.8
$(H^0 \to q\bar{q})(Z^* \to \tau^+\tau^-)$ (1991)	14.6	8.6	4.0	2.2	1.4
$(H^0 \to q\bar{q})(Z^* \to \tau^+\tau^-)$ (1990)	8.0	4.2	2.2	1.4	1.2

Table 12.2: Selection efficiencies (in %) for Higgs events in the different channels. The efficiencies for the $H^0\nu\bar{\nu}$ and $H^0\mu^+\mu^-$ channels are the same for 1990 and 1991 data.

The second candidate is an $e^+e^- \to \mu^+\mu^- + X$ event observed at $\sqrt{s} = 91.3$ GeV. This event is shown in Figure 12.2. Its main parameters are: mass recoiling against $\mu^+\mu^- = 70.4 \pm 0.7$ GeV, mass$(\mu^+\mu^-) = 6.5 \pm 0.2$ GeV, measured mass of the hadronic system = 61.6 GeV; this last value is consistent with the Monte Carlo expectation of 65.7 ± 6.2 GeV for the decay of a Higgs boson with mass 70.4 GeV.

Both events are consistent with the four fermion background $e^+e^- \to \ell^+\ell^- q\bar{q}$ for which we expect a total of 3.3±0.4 events from both channels.

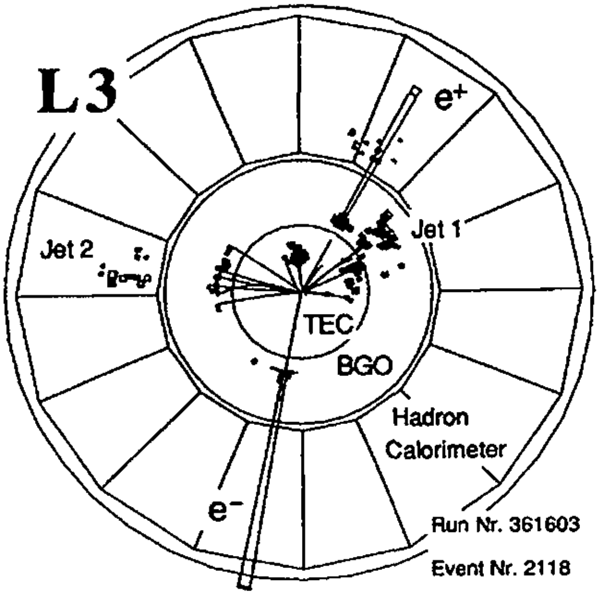

Figure 12.1: The candidate for $e^+e^-H^0$ production shown in the plane perpendicular to the beam direction.

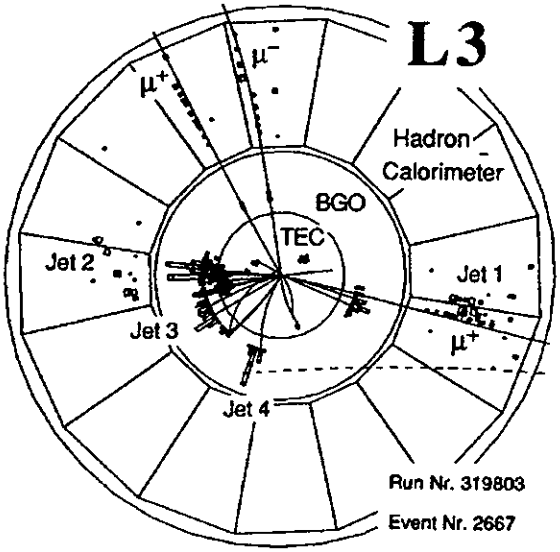

Figure 12.2: The candidate for $\mu^+\mu^-\mathrm{H}^0$ production shown in the plane perpendicular to the beam direction. Only the inner detector is drawn.

$\mathrm{H}^0\nu\bar{\nu}$ events are characterized by large missing energy and momentum imbalance due to the undetected neutrinos from the Z^* decay. The heavy quarks from the Higgs decay receive a Lorentz boost leading to two acoplanar jets, which mainly populate one hemisphere with a rather low energy deposit in the other. The direction of the missing energy points far away from the quark jets. In contrast, in $\mathrm{e}^+\mathrm{e}^- \rightarrow \mathrm{q}\bar{\mathrm{q}}$ events which are the main source of background, the two jets from the $\mathrm{q}\bar{\mathrm{q}}$ system are typically coplanar with the beam axis. Any missing energy is mostly due to the jet energy resolution and undetected neutrinos within the jets. As a consequence, the missing energy direction is close to one of the jet axes for background events.

The search for Higgs candidates has been carried out based on the above signatures. Selection criteria are designed to reject all events from the background channels while maintaining a high detection efficiency for the Higgs boson (see table 12.2). No events pass the selction cuts. The uncertainty in the selection efficiency has been studied by changing the detector calibration constants within their errors and by using two different hadronization models in the Monte Carlo. The effect of the changes in the calibration was found to be less than 1.5% of the detection efficiency for a 50 GeV Higgs mass. The selection efficiencies predicted using the JETSET 7.3 [22] and HERWIG 5.3 [23] fragmentation schemes agree with each other. In addition, we have studied $\mathrm{q}\bar{\mathrm{q}}\gamma$ events which, after eliminating the γ from the reconstruction, have a topology similar to the $\mathrm{H}^0\nu\bar{\nu}$ signal [219]. For these events we compared all the variables used in the analysis and found good agreement between the data and the Higgs Monte Carlo. From these studies we conclude that our efficiencies have a relative uncertainty of less than 1.5%.

12.1.5 Mass limits

Figure 12.3 shows the number of expected events at the upper end of the mass range from 30 to 60 GeV. The 95% confidence level upper limit, also shown in the figure, was obtained with the likelihood function for the two candidates, taking into account the number of expected events from the background and the experimental mass measurement errors. In the region around 50 GeV, the total number of expected events from all channels has a systematic uncertainty of 2.6%, which is also included. We thus obtain a lower limit on the mass of a Standard Model Higgs boson of:

$$m_{\mathrm{H}^0} > 52 \text{ GeV} \tag{12.2}$$

at the 95 % confidence level.

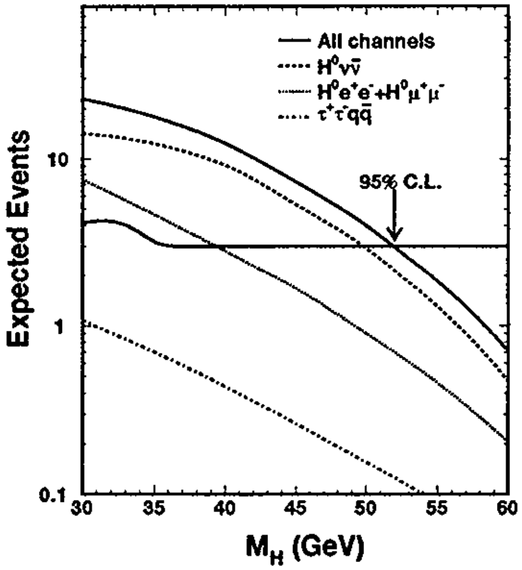

Figure 12.3: Number of events expected in the different channels. The 95% confidence level line is shown and the Higgs mass limit at 95% confidence level is indicated.

12.1.6 Higgs boson decay into two photons

In the Standard Model, the Higgs cannot couple to photons at tree level; however, the $\mathrm{H}^0 \rightarrow \gamma\gamma$ decay proceeds via one-loop diagrams involving charged fermions and W bosons. Since the Standard Model cross-section for this process is extremely low at LEP energies, an anomalous signal of hadronic events with two high energy photons can be a strong indication of new physics. As mentioned in section 10.4, we have found 4 data events with a pair of hard isolated photons. We use the PYTHIA 5.6 Monte Carlo [220] to simulate Higgs events with the Higgs decaying into two photons. The $\gamma\gamma$ invariant mass resolution is $\approx 6\%$ for $\mathrm{M_H}$=10 GeV and is better than 2% for $\mathrm{M_H} > 30$ GeV. Using this estimate for the resolution, we find that the 4 data events fall in different $\gamma\gamma$ invariant mass bins. The acceptance varies from 19% to 35% over the range $10 < m_{\mathrm{H}} < 70$ GeV.

The 95% confidence level upper limit for $\sigma(e^+e^- \rightarrow H^0 + \text{hadrons}) \times \text{Br}(H^0 \rightarrow \gamma\gamma)$ is plotted in Figure 12.4. The limit is several orders of magnitude above the Standard Model prediction.

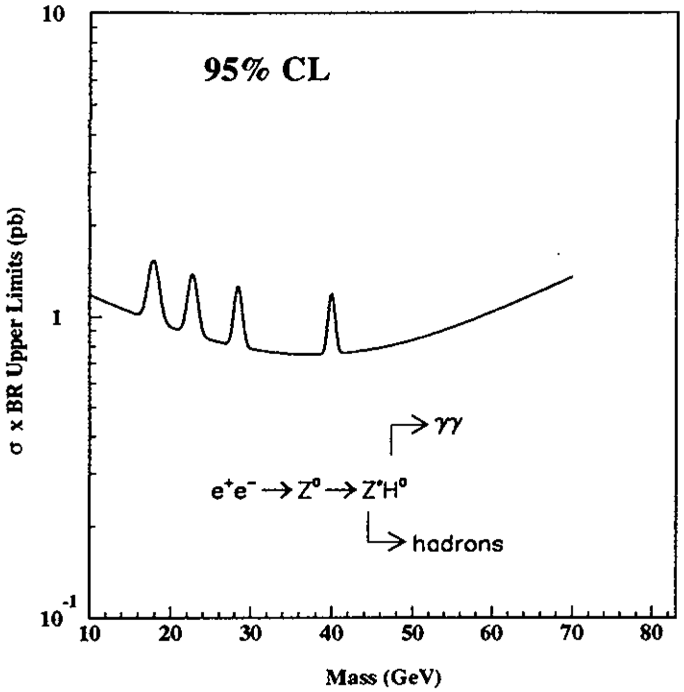

Figure 12.4: Upper limit at the 95 % confidence level on $\sigma(e^+e^- \rightarrow H^0 + \text{hadrons}) \times \text{Br}(H^0 \rightarrow \gamma\gamma)$ as a function of m_{H^0}.

12.2 Search for non-minimal Higgs bosons

A two-doublet extension of the minimal Standard Model would have a richer Higgs particle spectrum and would add new phenomena to the Standard Model physics. The general theoretical background is summarized in reference 221. Briefly, the Higgs sector of a two-doublet model contains 5 physical Higgs bosons: one neutral CP-odd scalar, A^0, two neutral CP-even scalars, H^0 and h^0, and two charged scalars, $H^\pm$. The masses of the Higgs bosons, the mixing angle, α, between the two neutral scalar Higgs fields and the ratio of the vacuum expectation values of the two Higgs doublets, $\tan\beta$, are free parameters. The Higgs production processes near the Z resonance are:

a) bremsstrahlung ($Z \rightarrow Z^*h^0$ or $Z \rightarrow Z^*H^0$);

b) neutral pair production ($Z \rightarrow h^0A^0$ or $Z \rightarrow H^0A^0$); and

c) charged pair production ($Z \rightarrow H^+H^-$).

A detailed presentation of this work is given in [222, 223]. In this section, we first investigate Higgs boson production in a general two-doublet model. We then derive limits in the Minimal Supersymmetric Standard Model (MSSM).

12.2.1 Neutral Higgs bosons in the two-doublet Higgs model

The cross section for process (a) is proportional to $\sin^2(\beta-\alpha)$, while the cross section of process (b) is proportional to $\cos^2(\beta-\alpha)$. If, for a set of parameters, one cross section vanishes, the other dominates.

Limit on $\sin^2(\beta-\alpha)$

Searches for Higgs boson bremsstrahlung in the mass range 0 to 60 GeV constrain the quantity $\sin^2(\beta-\alpha)$ of the two-doublet Higgs model. The Higgs boson couplings to the up-and down-type fermions may be enhanced or suppressed compared to the predictions in the minimal Standard Model and depend on the unknown free parameters of the Higgs sector. The limits on Standard Model Higgs boson production as quoted in section 12.1 can thus be converted into a limit on $\sin^2(\beta-\alpha)$, as shown in Figure 12.5. The effects of changes in the selection efficiencies at production thresholds are clearly visible. The further structure in the exclusion contour is due to the few candidate events. Their number is in agreement with the expectations from four-fermion background.

Excluded Region in the $(m_{\mathrm{h}}, m_{\mathrm{A}})$ plane

Limits on the contribution of pair-produced Higgs to Γ_{Z} give an upper limit on the quantity $\cos^2(\beta-\alpha)$. From our line-shape data.a limit on additional contributions to Γ_{Z} is set at 35 MeV (see section 13.1). A mass pair $(m_{\mathrm{h}},m_{\mathrm{A}})$ is excluded if the corresponding upper limit on $\sin^2(\beta-\alpha)$ from the bremsstrahlung process is lower than the lower limit coming from the pair production process. The process $\mathrm{h}^0 \to \mathrm{A}^0\mathrm{A}^0$ has been searched for using methods analogous to the search for Standard Model Hiss bosons (see section 12.1). The cuts have been adjusted and a similar detection efficiency has been reached. The small variations of these efficiencies are visible in the exclusion plots as discontinuities in the region where $\mathrm{h}^0 \to \mathrm{A}^0\mathrm{A}^0$ decays are allowed. The resulting exclusion plot is shown in Figure 12.6.

12.2.2 Search for neutral Higgs pair-production

Signatures resulting from the following expected Higgs decay modes are investigated: $\mathrm{h}^0/\mathrm{A}^0 \to \tau^+\tau^-$, $\mathrm{h}^0/\mathrm{A}^0 \to \mathrm{b\bar{b}}$, $\mathrm{h}^0 \to \mathrm{A}^0\mathrm{A}^0$. Searches for 4 jet, 6 jet, $\tau\tau$ jet jet and 4 τ signatures are performed. No signal has been observed in any of these channels. Figure 12.7 shows the excluded regions in the $(m_{\mathrm{h}},m_{\mathrm{A}})$ plane for branching ratio limits on:

$$\frac{\Gamma(\mathrm{Z} \to \mathrm{h}^0\mathrm{A}^0 \to \tau^+\tau^-\tau^+\tau^-)}{\Gamma(\mathrm{Z} \to \mathrm{q\bar{q}})}. \tag{12.3}$$

The limits for the $\mathrm{Z} \to \mathrm{h}^0\mathrm{A}^0 \to \tau^+\tau^-\mathrm{b\bar{b}}$ process are shown in Figure 12.8 and the limits for the $\mathrm{Z} \to \mathrm{h}^0\mathrm{A}^0 \to \mathrm{b\bar{b}b\bar{b}}$ process are shown in Figure 12.9.

The process $\mathrm{Z} \to \mathrm{h}^0\mathrm{A}^0 \to \mathrm{A}^0\mathrm{A}^0\mathrm{A}^0 \to \mathrm{b\bar{b}b\bar{b}b\bar{b}}$ can dominate if $m_{\mathrm{h}} > 2m_{\mathrm{A}}$. The 95% confidence level limit on the branching ratio in the mass range $18 \leq m_{\mathrm{A}} \leq 27$ GeV and

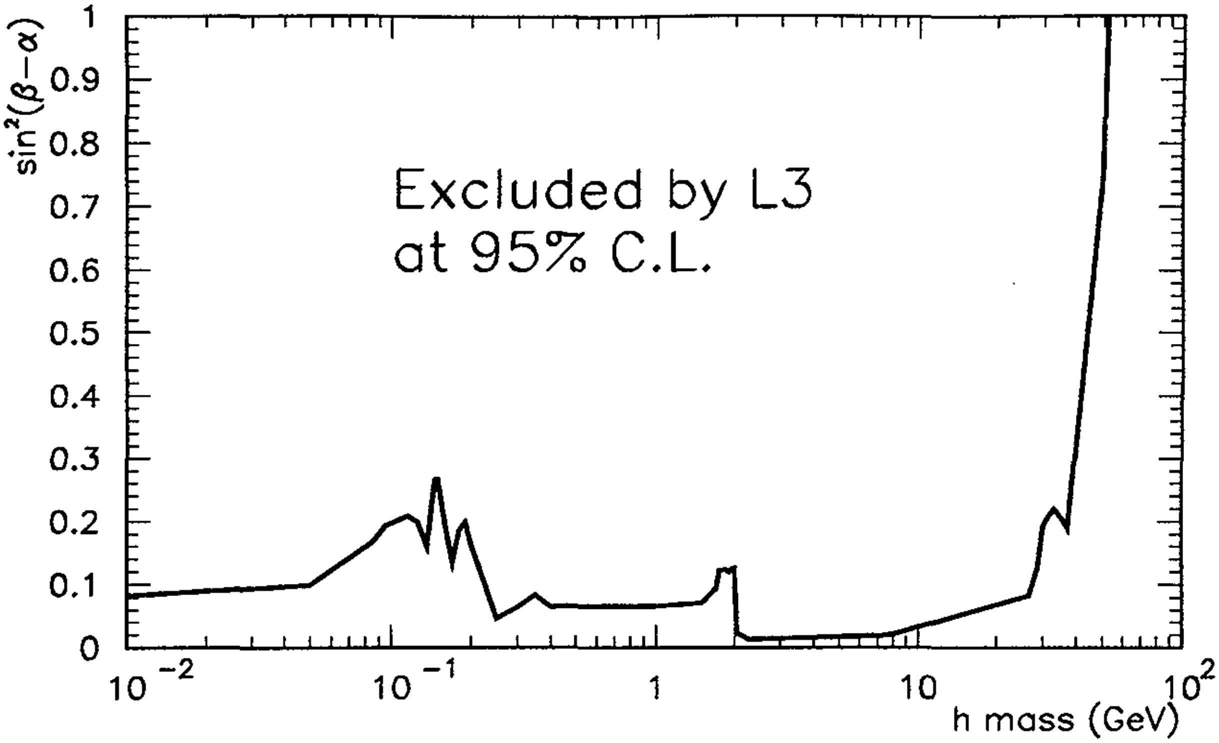

Figure 12.5: Limit on $\sin^2(\beta - \alpha)$ of the two-doublet Higgs model.

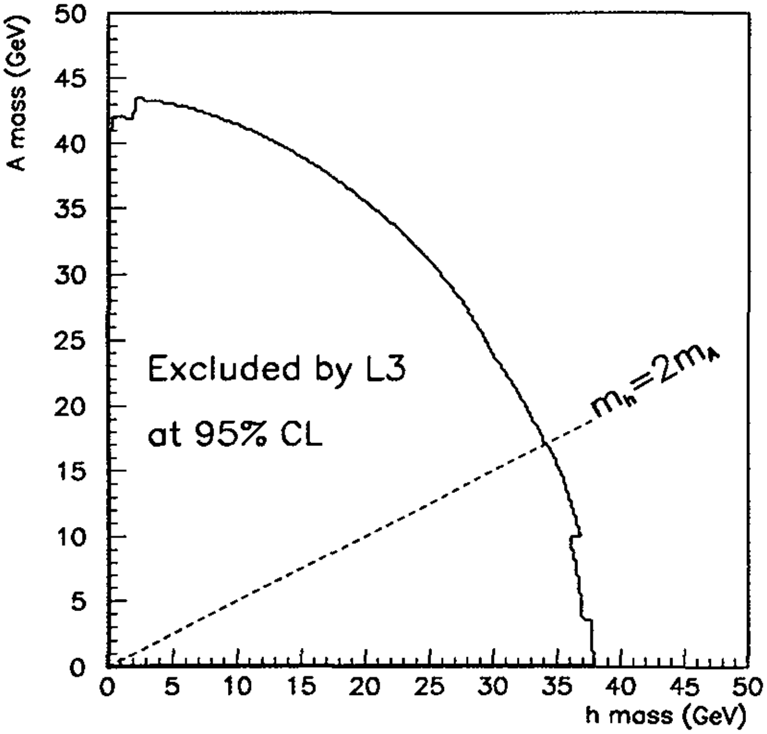

Figure 12.6: Exclusion in the (m_h, m_A) plane of the two-doublet Higgs model.

$m_h > 2m_A$ is:

$$\frac{\Gamma(Z \to b\bar{b}b\bar{b}b\bar{b})}{\Gamma(Z \to q\bar{q})} \leq 9.4 \times 10^{-4}. \tag{12.4}$$

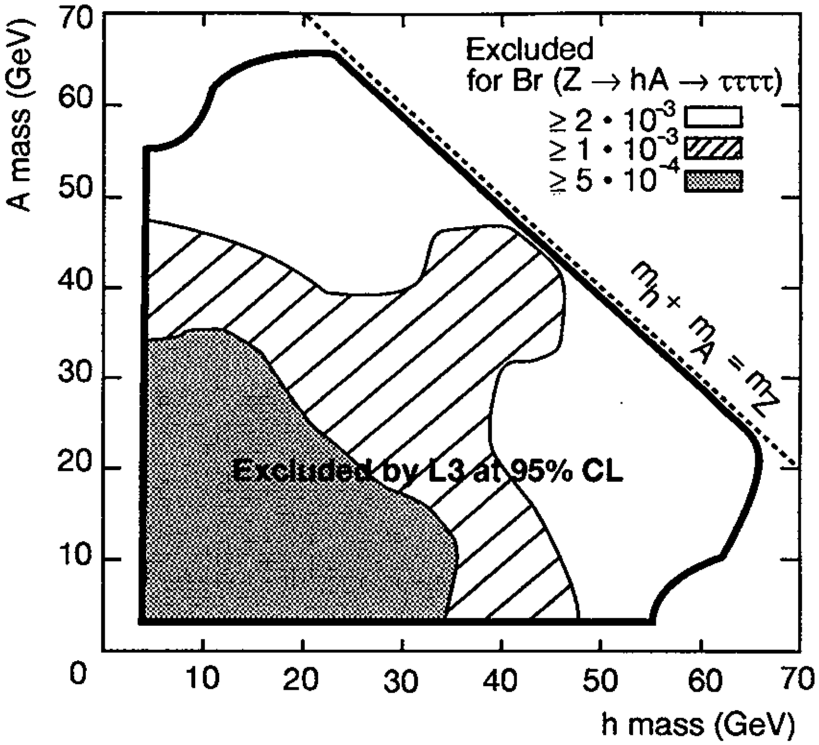

Figure 12.7: Regions of the (m_h,m_A) plane excluded at 95% CL for values of the branching ratio $\Gamma(Z \rightarrow h^0A^0 \rightarrow \tau^+\tau^-\tau^+\tau^-)/\Gamma(Z \rightarrow q\bar{q}) \geq 5 \times 10^{-4}$ (dark region), 1×10^{-3} (hatched region) and 2×10^{-3} (region inside thick contour line).

12.2.3 Search for charged Higgs pair-production

The partial width for Z decay into a charged Higgs pair depends only on the mass of the charged Higgs [221]. Searches for the three processes relevant at LEP-I are performed: $Z \rightarrow H^+H^- \rightarrow \tau^+\nu\tau^-\nu$, $\tau\nu cs$, $c\bar{s}\bar{c}s$. No Higgs signal has been observed. The search in the hadronic decay channel is the most difficult one due to an irreducible $Z \rightarrow q\bar{q}$ background. A lower Higgs mass limit of 41 GeV, independent of the Higgs branching ratio, is obtained. Figure 12.10 shows the 95% CL mass limit on charged Higgs bosons as a function of their leptonic branching ratio obtained from the search in the three channels.

12.2.4 Interpretation in the Minimal Supersymmetric Standard Model

The results obtained in previous sections can be combined to set mass limits on the neutral Higgs bosons in the Minimal Supersymmetric Standard Model. In this two-doublet model, the parameters $\tan\beta$ and α are directly related to m_H and m_A at tree level. The tree level model also predicts that $m_H < m_A$, $m_H < m_W$, and $m_{H^\pm} > m_Z$.

Radiative corrections, however, can modify these predictions. The main effects of radiative corrections can be extracted by making the following two assumptions [101]: a) that all Supersymmetric partners are degenerate in mass and do not mix and b) the leading top mass term

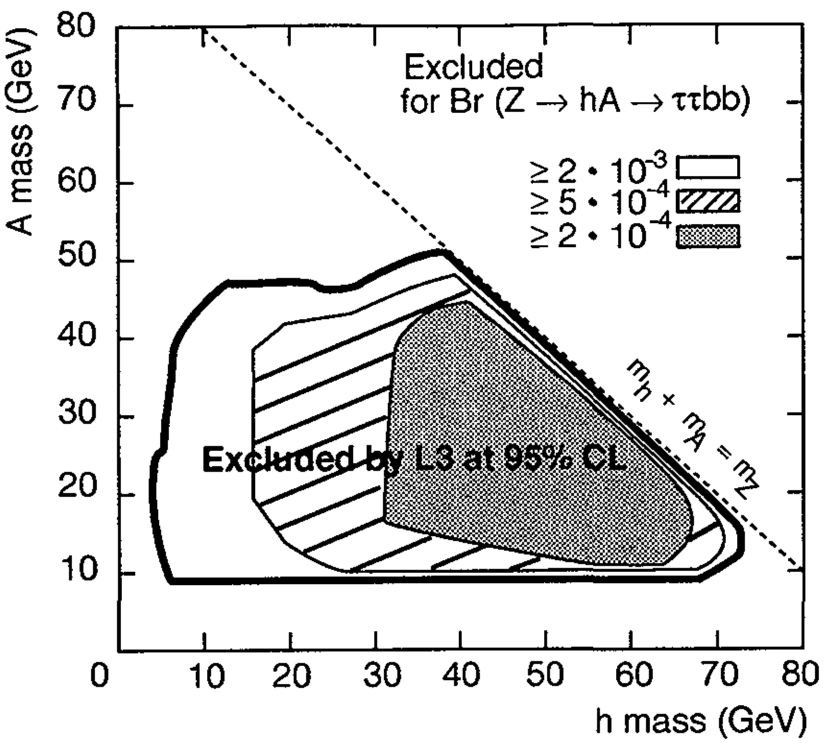

Figure 12.8: Regions of the (m_h,m_A) plane excluded at 95% CL for values of the branching ratio $\Gamma(Z \to h^0A^0 \to \tau^+\tau^-b\bar{b})/\Gamma(Z \to q\bar{q}) \geq 2 \times 10^{-4}$ (dark region), 5×10^{-4} (hatched region) and 2×10^{-3} (region inside thick contour line). The analysis has been performed for $h^0 \to \tau^+\tau^-$ and $A^0 \to b\bar{b}$.

in the radiative correction expression, ${m_t}^4$, is dominant. With these assumptions, the effects of radiative corrections can be summarized with a single dimensionless parameter, ϵ, for a given top mass m_t and $m_{\tilde{t}}$, the mass of the supersymmetric partner of the top quark:

$$\epsilon \equiv \frac{3\alpha/\sin^2\theta_W}{2\pi}\frac{{m_t}^4}{m_W^2 m_Z^2}\ln(\frac{m_{\tilde{t}}^2}{{m_t}^2}). \tag{12.5}$$

For $\epsilon = 0$ the tree level relations are preserved. For large ϵ, the neutral boson mass limits and the relationships between the masses and α and $\tan\beta$ are altered [101]. The charged Higgs remains too massive to be produced at LEP I. We allow a conservative range of the top and stop masses:

$$90 < m_t < 250 \text{ GeV}, \quad m_t < m_{\tilde{t}} < 1000 \text{ GeV}, \tag{12.6}$$

corresponding to an ϵ range of $0 < \epsilon < 1.45$.

After radiative corrections, two (m_h,m_A) pairs may correspond to one given (m_A,$\tan\beta$) pair. A point in the $m_H m_A$-plane is only excluded if all the corresponding (m_A,$\tan\beta$) values are excluded for a range of $\tan\beta$ from 1 to 50 and for any value of ϵ from 0 to 1.45. Figure 12.11 shows the region excluded in the $m_H m_A$-plane by a combination of the direct searches for neutral Higgs bosons and the limit on the Z width.

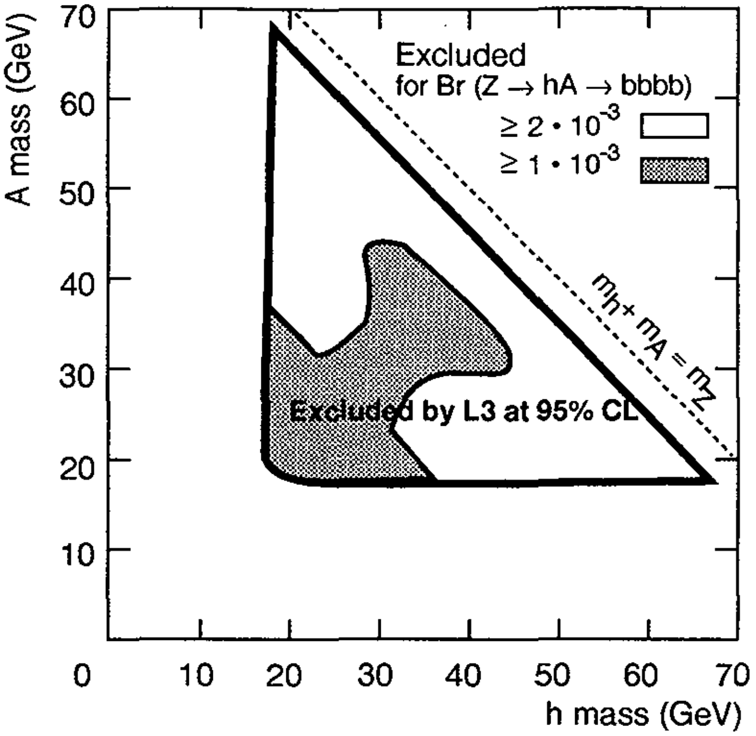

Figure 12.9: Regions of the (m_h,m_A) plane excluded at 95% CL for values of the branching ratio $\Gamma(Z \to h^0A^0 \to b\bar{b}b\bar{b})/\Gamma(Z \to q\bar{q}) \geq 1 \times 10^{-3}$ (dark region), 2×10^{-3} (region inside thick contour line).

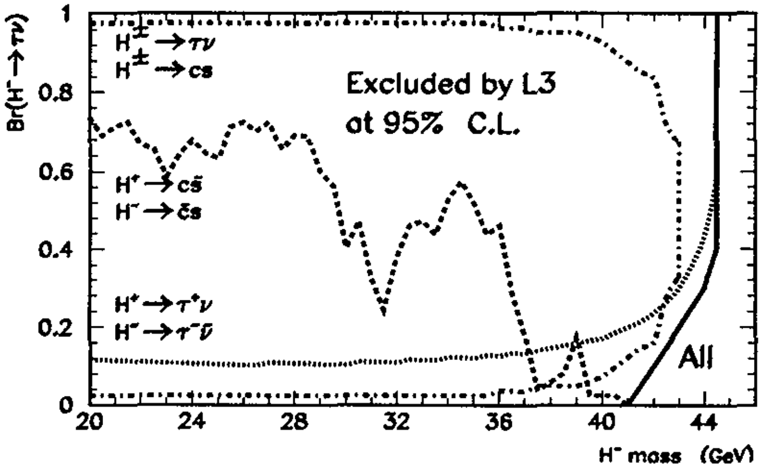

Figure 12.10: Excluded regions of pair-produced charged Higgs bosons as a function of the charged Higgs mass and the leptonic Higgs branching fraction. The thick contour line determines the combined mass limit.

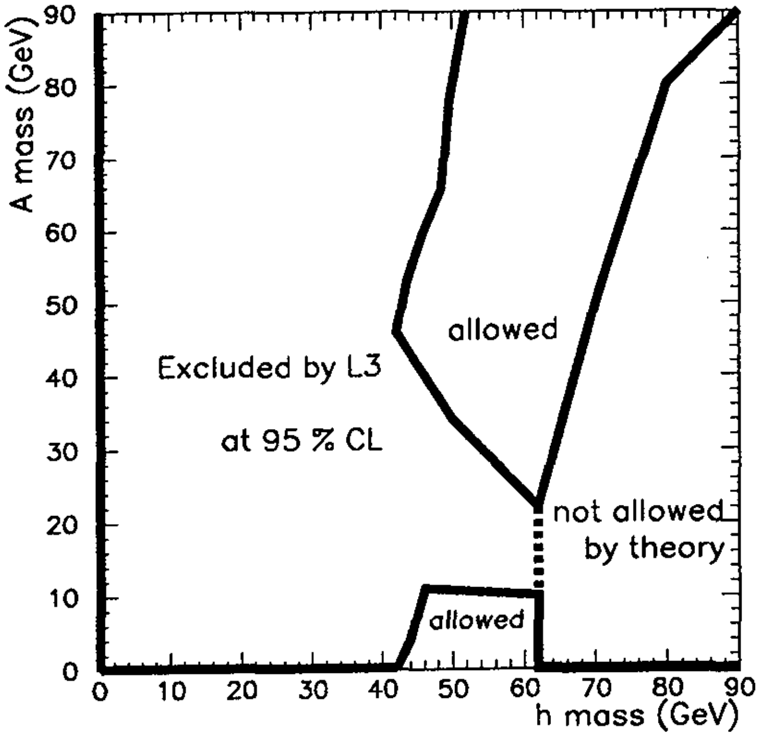

Figure 12.11: Excluded regions in the (m_h,m_A) plane at 95% CL in the MSSM, independent of radiative corrections.

Chapter 13

Search for New Particles and New Interactions

e^+e^- collisions at LEP provide an ideal data sample in which to search for physics beyond the Standard Model, because the energy is high and production cross sections are large. In this chapter we describe the search for new particles using the data sample collected during the 1990 and 1991 LEP running periods using a total integrated luminosity of 17.5 pb^{-1}.

One can broadly classify our search methods into three categories:

- indirect searches that quantify how much room is left for new physics by the precise measurements of Z properties (see chapters 5 and 8);
- direct searches for new particles among the decay products of the Z;
- direct searches for new particle production by non-resonant QED channels.

13.1 Limits from line shape measurements

A hypothetical Z decay mode, $Z \to X$ will contribute to the total Z width, Γ_Z, by its partial width $\Gamma_Z^X \equiv \Gamma(Z \to X)$. If all final states X are undetected, Γ_Z^X will contribute to the invisible Z width, Γ_{inv}.

To obtain conservative limits on the new physics, we use values $m_t = 91$ GeV, $m_H = 1000$ GeV, and $\alpha_s = 0.115$, which are compatible with our measurements (see chapters 8 and 10) and give lower values for Γ_Z and Γ_{inv} in the Standard Model. From the ZFITTER program [26], we obtain the following predictions for this set of parameters: $\Gamma_Z = 2472$ MeV and $\Gamma_{\mathrm{inv}} = 498$ MeV. These values serve as lower bounds on the theoretical prediction. The limit on the decay width due to new physics is then obtained by the following procedure: Assuming the measurements of Γ_Z and Γ_{inv} have Gaussian errors, the probability distribution above the theoretical bound is renormalized to 100% confidence level. The renormalized distribution is then divided such that the area above the dividing line contains 5% of the distribution. The one-sided 95% confidence level upper limit on new physics is then given by the difference between the dividing line and the lower bound. In this way we obtain the following upper limits on the contribution $\Delta\Gamma_Z$ of new physics to the total Z width and $\Delta\Gamma_{inv}$ to the invisible Z width:

$$\begin{aligned} \Delta\Gamma_Z &< 35.1 \text{ MeV} \qquad (13.1) \\ \Delta\Gamma_{inv} &< 16.2 \text{ MeV} \qquad (13.2) \end{aligned}$$

at the 95% confidence level. Limits on the mass of new sequential quarks and leptons, and supersymmetric particles, obtained using these results, are listed in table 13.1.

It should be noted that these limits can be substantially weaker if some conspiracy between different channels exists. For instance, all Z widths would be reduced by radiative corrections due to the existence of fermions with electroweak vector coupling to the Z and with mass just above the production threshold in Z decay. A chargino of 50 GeV mass [224] would decrease the Z widths by about 0.6%. In this case the limits derived from width measurements would be weaker.

Limits (GeV) (95% C.L.)	From Γ_Z $\Delta\Gamma_Z < 35.1$ MeV	From Γ_{inv} $\Delta\Gamma_{inv} < 16.2$ MeV
M_U	41.8	
M_D	44.7	
M_L	30.2	
M_N		45.2
$M_{\tilde{\nu}}$		37.1
$M_{\tilde{u}}$	35.3	
$M_{\tilde{d}}$	36.8	
$M_{\tilde{H}^\pm}$	44.0	
$M_{\tilde{W}^\pm}$	45.5	

Table 13.1: 95% confidence level limits on the masses of new particles obtained from the Z widths limits. The particles are the sequential up- and down-type quarks (U and D), charged and neutral leptons (L and N) with standard weak isospin assignment, neutrino and quark supersymmetric partners ($\tilde{\nu}$, $\tilde{u}$ and $\tilde{d}$), and the supersymmetric partners of the charged Higgs and the W ($\tilde{H}^\pm$ and $\tilde{W}^\pm$).

13.2 Limits on an additional heavy gauge boson Z′

Most candidates for unifying theories predict additional gauge bosons, thus leading in a natural way to the extension of the Standard Model with new, heavy neutral gauge bosons [225]. The measurement of the Standard Model parameters with high accuracy as performed at LEP allows the search for possible deviations with sensitivity to new phenomena.

Direct searches for Z′ production have been performed at $p - \bar{p}$ colliders [226]. Here we investigate virtual effects of a Z′ on the Z resonance. The Z′ influences mainly the couplings of the Z to fermions, provided the mixing angle θ_M between Z and Z′ is non-zero. It should be noted, that measurements near $\sqrt{s} = m_Z$ are ideal to search for Z-Z′ mixing. Limits for θ_M and the Z′ mass, $m_{Z'}$, can be derived from analyses based on the energy dependence of cross sections and asymmetries of Z final states [227].

The models considered are based on symmetry breaking of the superstring-inspired E6 group and on a left-right symmetric extension of the Standard Model [228]. Both the E6 and the left-right model contain a parameter, denoted as θ_6 and α_{LR}, respectively, which effectively fixes the couplings of the Z′ to fermions. Special cases of the E6 model are known as the χ, ψ and η models, with values of $\theta_6 = 0°$, $90°$ and $-52.24°$, respectively.

13.2.1 Modifications to standard cross sections

For the analysis, the results of a common treatment of γ, Z and Z′ exchange, QED corrections, and weak loops within the extended theory are used [227]. The influence of the Z′ exchange is taken into account in Born approximation. In the on-mass-shell renormalization scheme the vector boson masses and their mixing angle are related to

$$\tan^2\theta_M = \frac{m_Z^2 - m_{Z^0}^2}{m_{Z'}^2 - m_Z^2} \qquad (13.3)$$

$$m_Z^2 = \frac{m_W^2}{\cos^2\theta_W}, \qquad (13.4)$$

where m_Z would be the mass of the Z in the absence of mixing. In equation 13.3 a minimal extension of the Standard Model is supposed, i.e. only one Higgs doublet is assumed.

13.2.2 Fitting procedure

The fits were performed with a special code ZEFIT [227, 26]. As input, the cross sections for the hadronic and leptonic final states and the forward-backward charge asymmetries A_{fb} as a function of $\sqrt{s}$ are used (see chapter 5). The free parameters of the fit are the Standard Model parameters, θ_M and $m_{Z'}$. We assume m_H=300 GeV and α_s= 0.12. The top quark mass is left as a free parameter except for the direct CDF constraint $m_t > 91$ GeV [111]. Statistical and systematic errors are taken into account as described in chapter 8.

13.2.3 Results

The dependence on θ_M was investigated as a function of the model parameters θ_6 and α_{LR}. For all models considered, the values of the mixing angle θ_M obtained were compatible with zero. In figures 13.2 and 13.3 the 95% confidence level limits of θ_M as a function of θ_6 and α_{LR} are shown for different values of $m_{Z'}$. Here the top quark mass has been fixed to m_t = 150 GeV. Fig. 13.1 shows the allowed contour in the $m_{Z'}$ vs θ_M plane for 95% confidence level in the χ model. The contours for the other models are similar.

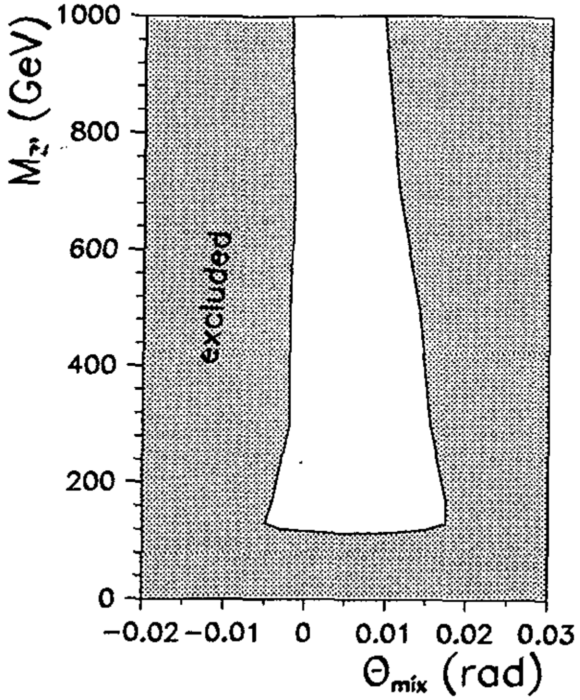

Figure 13.1: The 95% C. L. allowed region in the $m_{Z'}$ vs θ_M plane in the χ model.

The lower limits for $m_{Z'}$ are 117 GeV, 118 GeV and 100 GeV for the χ, ψ and η models, respectively. θ_M is limited to the interval from -0.04 to +0.04 at $m_{Z'}$ masses around 200 GeV and values of θ_6 near that of the η model. In all other cases and for larger Z′ masses, the mixing angle θ_M has allowed values between -0.010 and +0.015.

13.3 Search for isodoublet heavy charged and neutral leptons

Mass limits on sequential charged and neutral heavy leptons obtained from the total and invisible Z width have been already given in section 13.1. More stringent limits can be obtained from a direct search for stable charged leptons and unstable neutral leptons. Unstable sequential charged leptons with a mass lower then $m_Z/2$ are ruled out by the absence of a neutrino with mass lower than $m_Z/2$. This analysis [229] was based on data collected between March and June 1990 corresponding to an integrated luminosity of about 2.23 pb^{-1}.

13.3.1 Search for unstable neutral leptons

In the following analysis we consider the case that the charged lepton is heavier ,and the associated neutrino lighter than $m_Z/2$. Then the neutrinos will be produced in pairs in Z decays.

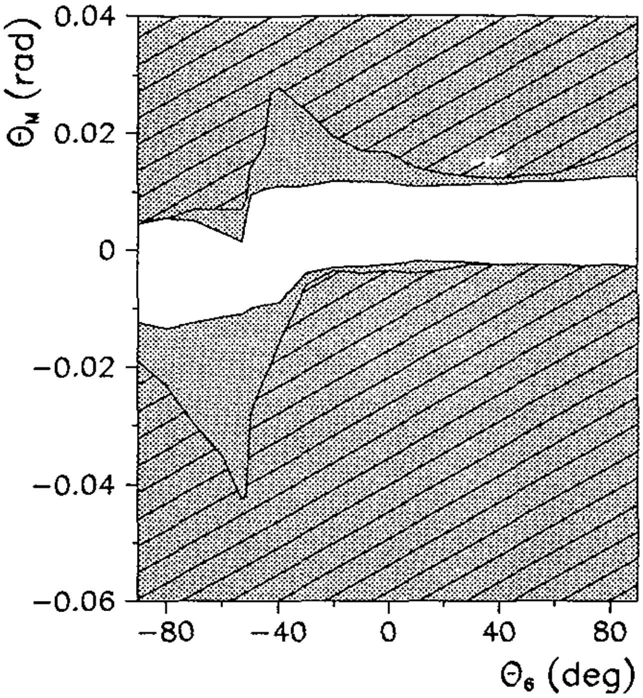

Figure 13.2: The 95% C. L. upper and lower limits of θ_M as a function of the E6 model angle θ_6 for $m_{Z'} \geq 200$ GeV (hatched area) and for $m_{Z'} \geq 700$ GeV (shaded area).

Heavy neutrinos can only decay via the charged current process $L^0 \rightarrow \ell^{\pm}W^{\mp *}$ if flavor mixing exists between leptons. The decay amplitude contains a mixing parameter V_{ℓ,L^0} for the transition from L^0 to the light charged lepton ℓ. The neutral lepton decay width (for Dirac type) is given by:

$$\Gamma(L^0 \rightarrow \ell^{\pm}W^{\mp *}) = 9|V_{\ell,L^0}|^2 \frac{G_F^2 m_{L^0}^5}{192\pi^3}$$

The decay width is a factor two larger for Majorana leptons, since the transitions $L^0 \rightarrow \ell^+$ and $L^0 \rightarrow \ell^-$ occur with equal probability. The factor 9 takes into account the $W^{\pm *}$ decay channels into $\mu\nu$, $e\nu$, $\tau\nu$, ud, cs. The mean decay path of the heavy neutral lepton is given by

$$l_{L^0} = \beta\gamma\tau_{L^0} \propto \beta|V|^{-2}m_{L^0}^{-6},$$

where $|V|^2 = |V_{e,L^0}|^2 + |V_{\mu,L^0}|^2 + |V_{\tau,L^0}|^2$. We have restricted our search to mean decay paths that are smaller than 1 cm to obtain a high detection and reconstruction efficiency. This corresponds to a lifetime smaller than 60 ps for $m_{L^0} = 40$ GeV. It implies that the limits of the direct search for neutral lepton decays are only valid for mixing parameters $|V|^2 > 6.2 \times 10^{-8}$ at $m_{L^0} = 20$ GeV and $|V|^2 > 5.1 \times 10^{-10}$ at $m_{L^0} = 40$ GeV.

We have searched for heavy neutral lepton events with isolated leptons, not compatible with $\mu^+\mu^-$, e^+e^- or $\tau^+\tau^-$ or heavy quark decays. No candidates were found. The selection efficiencies for neutral leptons are about 46% for decays into electrons and muons, and 14% for decays into taus. They vary less than 4% in the mass range from 20 GeV to 44 GeV.

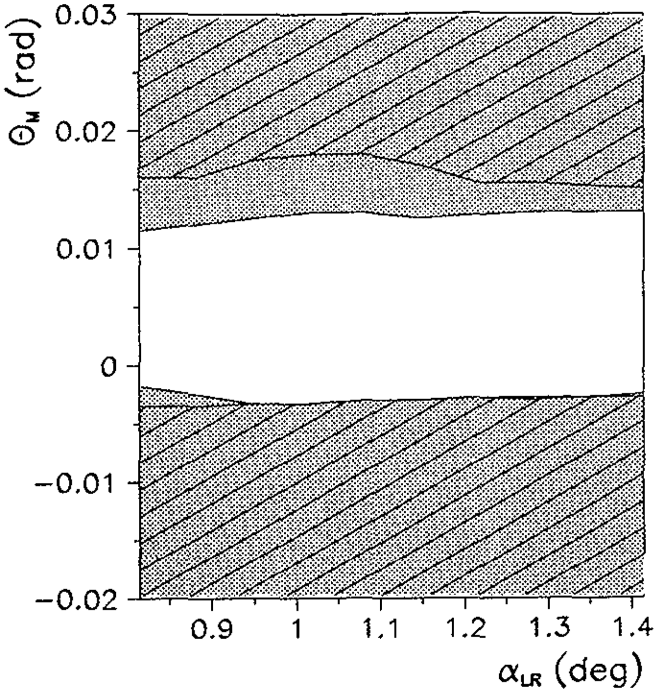

Figure 13.3: The 95% C. L. upper and lower limits of θ_M as a function of the left-right model parameter α_{LR} for $m_{Z'} \geq 200$ GeV (hatched area) and for $m_{Z'} \geq 700$ GeV (shaded area).

Combining this result with our limits from the Z width we obtain mass limits for Dirac leptons for various dominant decay modes, within the limits on $|V|$ as specified above:

$m_{\mathrm{L}^0} > 46.5$ GeV for $\mathrm{L}^0 \rightarrow \mathrm{e} + \mathrm{W}^*$
$m_{\mathrm{L}^0} > 46.5$ GeV for $\mathrm{L}^0 \rightarrow \mu + \mathrm{W}^*$
$m_{\mathrm{L}^0} > 46.4$ GeV for $\mathrm{L}^0 \rightarrow \tau + \mathrm{W}^*$

For Majorana leptons the mass limits are:

$m_{\mathrm{L}^0} > 45.5$ GeV for $\mathrm{L}^0 \rightarrow \mathrm{e} + \mathrm{W}^*$
$m_{\mathrm{L}^0} > 45.5$ GeV for $\mathrm{L}^0 \rightarrow \mu + \mathrm{W}^*$
$m_{\mathrm{L}^0} > 45.1$ GeV for $\mathrm{L}^0 \rightarrow \tau + \mathrm{W}^*$

13.3.2 Search for stable charged leptons

Pair production of new stable charged leptons would appear as two back-to-back charged tracks of low momentum in the muon chambers. As the mass of the particles increases, the dE/dx energy loss in the inner detector increases. Only for masses up to about 38 GeV the heavy lepton is able to reach the outer muon chambers; for masses larger than 43 GeV it will not be able to penetrate the electromagnetic calorimeter. In the mass region below 38 GeV we obtain limits in searching for an excess in the rate of $e^+e^- \rightarrow \mu^+\mu^-$. In the mass region above 38 GeV we have looked for events with two back-to-back tracks in the central tracking chamber having either a time of flight compatible with a low velocity particle or a large energy loss in the electromagnetic calorimeter.

We search for heavy leptons in the mass region below 38 GeV by repeating the muon pair selection [230] with modified cuts on the particle momentum and time-of-flight. We obtain a one-sided 95% C.L. limit on the production of heavy leptons of $\Gamma_{\rm LL} < 5.4$ MeV. This rules out stable heavy leptons below 38 GeV.

The search for stable charged leptons heavier than 38 GeV is carried out by looking for two back-to-back tracks in the central tracking chamber with large energy loss in the electromagnetic calorimeter. No event with such a signature was found. The acceptance varied from 49% at 38 GeV to 33% at 44.5 GeV. We expect 158, 78, 16 events at $m_{\rm L} = 38.0$ GeV, $m_{\rm L} = 41.0$ GeV, and $m_{\rm L} = 44.0$ GeV, respectively. Basing our 95% C.L. limit on three expected events we exclude the mass range $38.0 < m_{\rm L} < 44.6$ GeV in this study. Combined with the above limit we exclude therefore a new stable charged lepton with $m_{\rm L} < 44.6$ GeV at 95% confidence level.

13.4 Search for isosinglet neutral heavy leptons

We search for neutral heavy leptons that are isosinglets under the Standard $SU(2)_L$ gauge group. Such neutral heavy leptons are expected in many extensions of the Standard Model. We have searched for three types of heavy leptons N_e, N_μ, N_τ associated with the three neutrino types ν_e, ν_μ, ν_τ. In this search, one isosinglet neutral heavy lepton N_ℓ is assumed to be associated with each generation of light neutrinos via the mixing amplitude U_ℓ. We do not consider mixing of the light neutrinos with higher isodoublet states (sequential leptons) nor the possibility of mixing among light neutrinos (as discussed in reference 231). However, an interpretation of our results in such models is straightforward. Also, the large mass difference between the light and heavy neutrinos allows us to ignore oscillations [231].

The mixing between the isosinglet neutral lepton and its associated isodoublet neutrino allows single production to occur in Z decays:

$$Z \rightarrow N_\ell \bar{\nu}_\ell \tag{13.5}$$

The production cross section is reduced from the neutrino pair production cross-section by a phase-space factor and by the square of the mixing amplitude. It can be written as [231, 232]:

$$\mathrm{Br}(Z \rightarrow \bar{\nu}_\ell N_\ell) = \mathrm{Br}(Z \rightarrow \nu_\ell \bar{\nu}_\ell)|U_\ell|^2 (1 - \frac{m_{\rm N}^2}{m_{\rm Z}^2})^2 (1 + \frac{1}{2}\frac{m_{\rm N}^2}{m_{\rm Z}^2}) \tag{13.6}$$

where U_ℓ is the mixing amplitude, $m_{\rm N}$ the mass of N_ℓ. In contrast to Z decay into sequential isodoublet neutral leptons where pair production is dominant, single production dominates here because the corresponding pair production cross section is suppressed relative to the single production cross section by an additional $|U_\ell|^2$ factor, which is expected to be small [232].

Isosinglet neutral leptons decay via the neutral or charged weak currents:

$$\mathrm{N}_\ell \to \mathrm{Z}^*\nu \quad \text{and} \quad \mathrm{Z}^* \to \mathrm{ee}, \mu\mu, \tau\tau, \nu\nu, \mathrm{qq} \tag{13.7}$$
$$\mathrm{N}_\ell \to \mathrm{W}^*\ell \quad \text{and} \quad \mathrm{W}^* \to \mathrm{e}\nu, \mu\nu, \tau\nu, \mathrm{qq}' \tag{13.8}$$

To calculate the branching ratios of these decays into the final states, we use the formulae from references 231, 232. For most of the mass range, the dominant decay mode is via charged currents, with one charged lepton and two quarks in the final state, which is about 50% of the total rate. For low N_τ masses, the dominant decay mode is via the neutral current mainly with one neutrino and two quarks in the final state.

The mean decay length is a function of the mixing parameter $|U_\ell|^2$ and the mass. It is given by:

$$L_\mathrm{N} = \beta\gamma c\tau_\mathrm{N} \propto \beta |U_\ell|^{-2} m_\mathrm{N}^{-6}, \tag{13.9}$$

This implies that the decay can occur far from the interaction point if the particle has a low mass or a very small mixing. We consider in our searches also the case where the decay occurs inside the electromagnetic or hadronic calorimeter, at decay lengths of up to 2 meters.

13.4.1 Event signatures and selection

Because of the Lorentz boost in the laboratory frame, the decay signature depends on the mass of the isosinglet lepton. For low mass, we have mainly monojet events, while for high mass, two or more jets are dominant.

Search for monojets

By searching for monojet events with charged particles, we cover all visible decay modes of an isosinglet lepton of mass $m_\mathrm{N} \leq$ 15 GeV. The details of the selection criteria are discussed in reference 233. We are then left with 2 events from data, while we expect 0.6 ± 0.4 events from $\mathrm{Z} \to \tau^+\tau^-(\gamma)$ decays.

As mentioned above, low masses or small mixing amplitudes U_ℓ can result in decays far from the interaction point. We also select events with a monojet without charged particles visible in the central tracking chamber. We find two candidates in the data and we expect 0.6 ± 0.6 events from conventional sources.

Search for two acoplanar jets

This event topology consists of a pair of acoplanar and acolinear jets with large missing energy and transverse momentum imbalance. This search covers all decay modes containing a neutrino in the final state for the mass region $m_\mathrm{N} \geq$ 15 GeV and the modes containing hadrons and a lepton for the mass region 15 GeV $\leq m_\mathrm{N} \leq$ 50 GeV. Backgrounds to this topology come from conventional Z decays where some energy is either unseen or not well measured.

After applying all cuts [233], one event is left in the data while we expect 0.2 ± 0.2 from $Z \rightarrow \tau^+\tau^-(\gamma)$ decay.

Search for isolated leptons in multijet events

By selecting hadronic events with an isolated lepton, we search for the ℓqq decay modes in the mass region ≥ 50 GeV. The main background to this topology comes from the semileptonic decays of heavy quarks. Radiative hadronic decays $Z \rightarrow q\bar{q}\gamma$, where a hard photon converts in the beam pipe, can also fake an isolated electron.

We select events with three or more reconstructed jets. The acoplanarity between the two most energetic jets has to be greater than 30°.

After applying our selection cuts to the data, we find a total of 42 candidates in the three decay modes. The number of data events and the Monte Carlo background expectations are shown in Table 13.2.

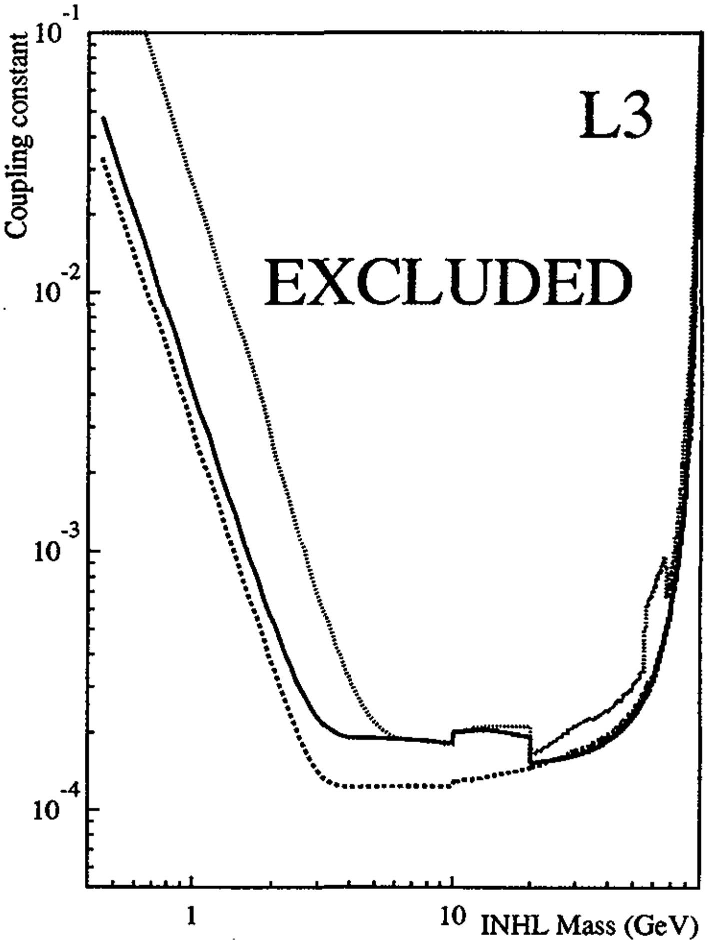

Figure 13.4: The 95% C.L. upper limit on the mixing amplitude $\mid U_\ell \mid^2$ as a function of the mass of the isosinglet neutral heavy lepton. The solid line is the limit for N_e, the dashed line is the limit for N_μ and the dotted line is for N_τ.

Decay Mode	Data	Monte-Carlo
eqq	6	7 ± 2
μqq	10	7 ± 2
τqq	26	23 ± 3

Table 13.2: List of selected events in data and Monte-Carlo.

13.4.2 Results

We calculate the 95% confidence level upper limit on the square of the mixing amplitude and the branching ratio for each generation. The upper limit for the mixing amplitude as a function of the mass is shown in Fig. 13.4. The mixing term $|U_\ell|^2$ is constrained to be less than 2×10^{-4} for the mass range $3 < m_{\mathrm{N}} < 50$ GeV. The limit can be expressed as $\mathrm{Br}(\mathrm{Z} \to \bar{\nu}_\ell \mathrm{N}_\ell) < 3 \times 10^{-5}$ for masses from 3 GeV up to m_{Z}.

13.5 Search for supersymmetric particles

Supersymmetry [234] is one of the most appealing extension of the Standard Model. Supersymmetry models predict the existence of two scalar partners $\tilde{\mathrm{f}}_L$ and $\tilde{\mathrm{f}}_R$ for each fermion f, associated with its two helicity states. In a similar manner, the super-partners of the photon, $\mathrm{W}^\pm$, Z, and Higgs particles are predicted as photino $\tilde{\gamma}$, wino $\tilde{\mathrm{W}}^\pm$, zino $\tilde{\mathrm{Z}}$, and Higgsinos respectively. In these models, a minimum of two Higgs doublets are needed such that one doublet gives masses only to the up-type quarks and leptons and the other one only to the down-type fermions. The search for Higgs particles required by supersymmetry has been discussed in section 12.2. Supersymmetry must be broken since no super-partner degenerated in mass with its ordinary particle has been observed. Consequently, the photino, zino, and neutral Higgsinos mix to form four Majorana-type mass eigenstates called neutralinos ($\tilde{\chi}$, $\tilde{\chi}_2$, $\tilde{\chi}_3$, $\tilde{\chi}_4$), while wino and the charged Higgsino mix to form two mass eigenstates called charginos ($\tilde{\chi}^\pm$, $\tilde{\chi}_2^\pm$). In addition, a new quantum number called R-parity [235] is introduced with R=+1 for ordinary particles and R=-1 for their super-partners. In most supersymmetry models, R-parity is conserved. As a result, supersymmetric particles are produced in pairs and the lightest supersymmetric particle (LSP) is neutral and stable, i.e. interacts weakly with matter. In the searches described below, we assume that the lightest neutralino ($\tilde{\chi}$) is the LSP and that R-parity is conserved.

13.5.1 Scalar leptons

The super-partners of charged leptons could be produced in pair in Z decays:

$$\mathrm{e}^+\mathrm{e}^- \to \mathrm{Z} \to \tilde{\ell}^+\tilde{\ell}^- \to \ell^+\ell^-\tilde{\chi}\tilde{\chi}$$

Due to different radiative corrections, the mass of right-handed $\tilde{\ell}$ is expected to be smaller than that of the left-handed $\tilde{\ell}$. In the search discussed below, mass degeneracy between left- and right-handed $\tilde{\ell}$ is thus not assumed. The results are conservatively given for that of right-handed $\tilde{\ell}$.

Pair production of light scalar charged leptons with $\ell^+\ell^-\tilde{\chi}\tilde{\chi}$ final state would appear as two back-to-back ordinary leptons with missing energy in the detector. Therefore, $\ell^+\ell^-\tilde{\chi}\tilde{\chi}$ events are indistinguishable from of $\tau^+\tau^-$ decays of the Z. The production of light $\tilde{\ell}$ would then result in an excess in the $\tau^+\tau^-$ sample. We select $\tau^+\tau^-$-type events using the criteria similar to those described in chapter 5. However, the requirement on the acolinearity angle between two taus is removed. In addition, each tau-jet is required to have at least one and at most three associated tracks. From the measured $\Gamma_{\tau\tau}$ and following the same procedure described in section 13.1, we exclude scalar electrons and muons below 17 GeV if $m_{\tilde{\chi}} < 15$ GeV and scalar taus below 13 GeV if $m_{\tilde{\chi}} < 10$ GeV.

Pair production and subsequent decay of heavy $\tilde{\ell}$ would appear as an acolinear di-lepton event with large missing energy. To select these events, the following selection criteria are applied:

1. There should be two jets in the events. Each jet is required to have at least one and at most three associated charged tracks. The energy of the jets is required to be less than 30 GeV.
2. The opening angle in the $r - \phi$ plane (coplanarity) between the two jets must be smaller than 170°.
3. The momentum imbalance is required to be larger than 4.0 GeV and its direction is required to be 45° away from the beam line.
4. No track should lie within a 45° half-opening angle cone in the azimuthal angle along the momentum imbalance direction.
5. No calorimeter cluster with energy greater than 300 MeV should lie within a 45° half-opening angle cone centered along the momentum imbalance direction.

Two events have been found satisfying these requirements: one e^+e^- and one $\mu^+\mu^-$ event, both compatible with the expected rate from two-photon processes. Figure 13.5 shows the 95% confidence level excluded region in the $m_{\tilde{\ell}}, m_{\tilde{\chi}}$ plane for the three scalar lepton species, $\tilde{e}$, $\tilde{\mu}$ and $\tilde{\tau}$, after combining the results for light $\tilde{\ell}$.

In contrast to the scalar charged leptons, there is only one scalar partner to the left-handed neutrino. The production ($e^+e^- \to Z \to \tilde{\nu}\bar{\tilde{\nu}}$) and subsequent decay ($\tilde{\nu} \to \nu\tilde{\chi}$) of scalar neutrinos would result in a decay width of the Z into invisible channels greater than the Standard Model predictions for three neutrino families. As shown in section 13.1, such scalar neutrinos are excluded for masses up to 37.1 GeV. However, the masses of scalar neutrinos of all three flavors are nearly degenerate in many models. From the same procedure and assuming mass degeneracy, we can exclude the existence of scalar neutrinos for masses below 41.8 GeV.

13.5.2 Charginos

Charginos can be pair produced in Z decays if their masses are smaller than $m_Z/2$. The $Z\tilde{\chi}^+\tilde{\chi}^-$ coupling is expected to be very large. The Z partial width decay into $\tilde{\chi}^+\tilde{\chi}^-$ is almost equal to

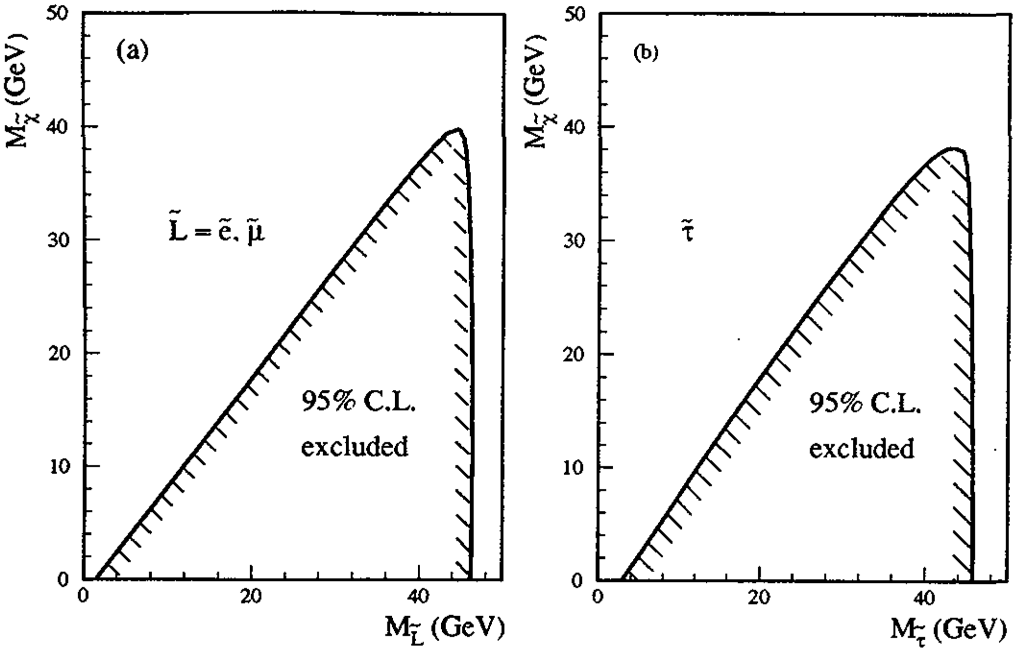

Figure 13.5: 95% confidence level excluded region in the $m_{\tilde{\ell}}, m_{\tilde{\chi}}$ plane for the three scalar lepton species: (a) ẽ and $\tilde{\mu}$ (b) $\tilde{\tau}$.

the leptonic partial width Γ_ℓ if the chargino is a pure higgsino (the supersymmetric partner of the $H^{\pm}$).and can be as large as $9\Gamma_\ell$ in case the chargino is a pure wino (the supersymmetric partner of the $W^{\pm}$). Therefore, independent of its decay and field content, the lightest chargino is excluded for masses up to 44 GeV from the measurement of the total Z decay width as shown in section 13.1.

13.6 Search for compositeness

Compositeness [236] could answer many fundamental questions left open by the Standard Model, such as the fermion mass spectrum. In these models, quarks, leptons and gauge bosons are all composite with an associated energy scale Λ. One natural consequence of compositeness is the existence of excited states, f^*, of known fermions f. An excited fermion will then decay into its ground state by radiating a photon or a gluon.

At e^+e^- colliders, excited fermions can be produced in pairs ($e^+e^- \rightarrow f^*f^*$) or singly ($e^+e^- \rightarrow ff^*$). While in the first case the f^* mass is limited to masses less than the beam energy, in the second case it can reach mass regions close to the center of mass energy.

We have also searched for a possible signature of the composite nature of the Z which could manifest itself through a radiative decay into a lower mass resonance or a large branching ratio into three photons.

13.6.1 Excited charged leptons

We have studied the processes $e^+e^-\to\ell^+\ell^-\gamma\gamma$, $e^+e^-\to\ell^+\ell^-\gamma$ where ℓ can be an electron, a muon or a tau [237, 238]. Since the excited electron production is completely dominated by very small angle reactions due to the t channel photon exchange, we have also studied the process $e^+e^- \to (e^\pm)e^\mp\gamma$, in which one of the electrons escapes detection.

Here the Z and γ are assumed to couple to spin $\frac{1}{2}$ excited lepton pairs in the same way as to ordinary lepton pairs. The lowest order pair-production cross section can be found in reference 239. The differential and total cross section for single f* production can be found in reference 240. We assume that the f* current follows the standard SU(2)×U(1) form, with its own coupling constant λ. Both for the single and pair production, a reduction factor due to the effect of initial state radiation is taken into account in our calculations.

Selection of $e^+e^-\to \ell^+\ell^-\gamma(\gamma)$ events follows closely the selection of the corresponding $e^+e^-\to \ell^+\ell^-$ events for the Z lineshape measurement (see chapter 5). In addition we require that:

1) one (or two) identified photons with an energy of at least 10 GeV each must be detected;

2) the angle between the two leptons must be smaller than 170°;

3) the angle between the photon and any of the two leptons must be larger than 10°.

To select events of the type $e^+e^- \to e^\pm e^{*\mp} \to (e^\pm)e^\mp\gamma$ with one electron in the beam pipe we require that the event contains only one electron and only one photon each of which have an energy greater than 5 GeV and an angle between them lower than 170°. The missing momentum vector should point towards the beam direction within 20°.

From the pair production searches we can exclude the presence of any excited charged lepton up to a mass of 45.6 GeV independently of the coupling constant λ. Figure 13.6 shows the limit on λ/m_{ℓ^*} as a function of the mass of the excited leptons obtained from the single production searches.

A limit on the mass of an excited electron of $m_{e^*} > 127$ GeV at 95% confidence level has also been set from the measurement of the $e^+e^- \to \gamma\gamma$ cross section as described in chapter 9.

13.6.2 Excited neutrinos

The cross section of single ν^* production can be calculated using the same effective Lagrangian. Since the Z contribution is dominant within the energy range investigated at LEP, we can neglect the γ and $W^\pm$ contributions which are less than 1% [241].

An excited neutrino ν^* can decay into a γ or a virtual Z plus a neutrino, or a virtual W, or even a real W if m_{ν^*} is greater than m_W, plus a charged lepton. We performed the two following studies [242]:

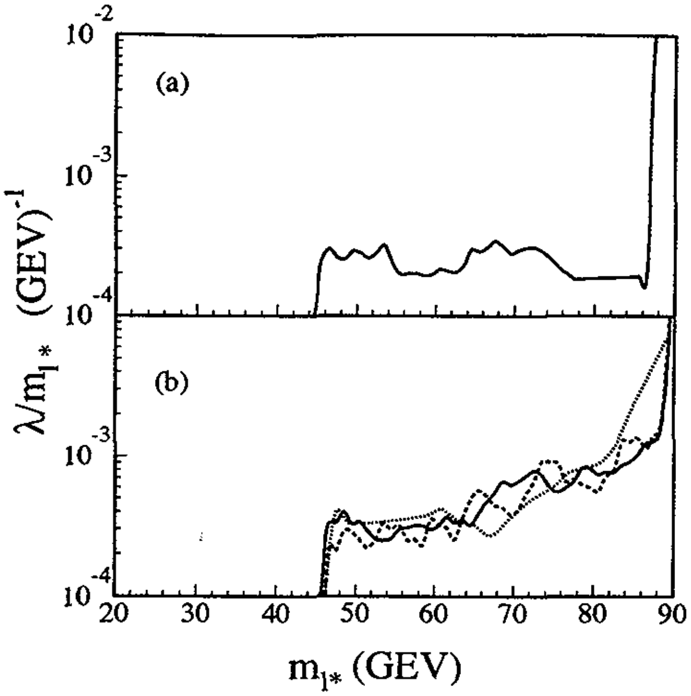

Figure 13.6: 95% confidence level upper limit on the coupling constant λ/m_{ℓ^*} as a function of the mass of the excited leptons obtained from the single production searches. a) from the $e^+e^- \to ee^* \to (e)e\gamma$ search b) from the $e^+e^- \to \ell^+\ell^-\gamma(\gamma)$ search. Full line $\ell = e$, dashed line $\ell = \mu$ and dotted line $\ell = \tau$.

1. If we impose a standard SU(2)×U(1) current, the $\gamma\nu\nu^*$ coupling vanishes and $\nu^* \to \nu Z$ and $\nu^* \to eW$ are the only decay modes allowed (we assume the lowest mass excited neutrino to be in the electron family). Since the branching ratio to the W channel decay is expected to be 71%, independent of the ν^* mass, and the W signature is much clearer than the one of the Z decays, we will investigate only the W channel. The visible final state is an electron plus two jets if the W decays hadronically or an electron plus another lepton if the W decays leptonically.
2. If the $\gamma\nu\nu^*$ coupling exists [243], the decay $\nu^* \to \nu\gamma$ would have a branching ratio in excess of 99% [244]. Hence the W and Z channel decays can be neglected. The event signature is a single energetic photon.

Figure 13.7 shows the upper limit of λ/m_{ν^*} at 95% C.L. as a function of m_{ν^*}. Independently of the existence of the $\gamma\nu\nu^*$ coupling, the excited neutrino is excluded at the 95% C.L. for a mass less than 91 GeV if the $Z\nu\nu^*$ coupling is the same as the $Z\nu\nu$ coupling, i.e. $\lambda = 1$.

13.6.3 Excited quarks

An excited quark mainly decays into a quark and a photon or a gluon. If we assume that the coupling λ/m_{q^*} is the same for the vertex $qq^*\gamma$ and qq^*g, the branching ratios would be only

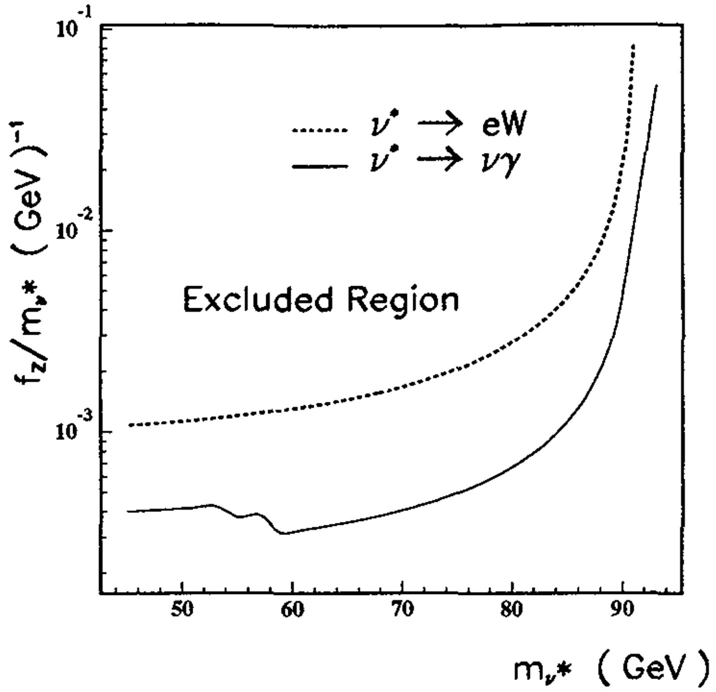

Figure 13.7: 95% confidence level upper limit on $\lambda/m_{\nu*}$ as a function of the mass of the excited neutrino obtained from the single production searches.

dependent on α and α_s, respectively. Neglecting the decays $q^* \rightarrow qZ$ and $q^* \rightarrow q'W$, the decay channel $q^* \rightarrow q\gamma$ has 8% branching ratio while the decay channel $q^* \rightarrow qg$ has 92% branching ratio [236].

Events of the kind $e^+e^- \rightarrow qqg(g)$, are characterized by the presence of three or four well separated hadronic jets and are therefore contained in the Z → hadrons sample used for the lineshape measurement (see chapter 5). Jets are reconstructed using the Jade [34] algorithm with a resolution parameter $y_{cut} = 0.02$ (see chapter 10). Out of the 115000 hadronic events collected during the 1990 running period, 50413 three jet and 8736 four jet events are retained for the $e^+e^- \rightarrow qqg$ and the $e^+e^- \rightarrow qqgg$ analysis, respectively.

Four jets are further combined into two pairs of jets, (i,j) and (k,l) by taking the combination which gives the smallest difference between two invariant masses, in order to satisfy the hypothesis of the production and decay of two identical states. We have used energy conservation constraints to improve the resolution for jet pair masses. In order to reduce the contribution from standard QCD processes we require the following:

1. The lowest energy jet should have at least 10 GeV. This is to remove preferentially QCD events with gluon radiation.
2. $P_{in}^2 > 4$ GeV^2 for four jet events and $P_{in}^2 > 8$ GeV^2 for three jet events, where P_{in}^2 is defined as the square of the momentum component of a cluster in the event plane and perpendicular to the jet axis averaged over the number of clusters. The event plane is defined by the thrust and major axes.

Four jet events are further constrained requiring:

- $(E_i + E_j - \sqrt{s/2})^2 + (E_k + E_l - \sqrt{s/2})^2 < 25$ GeV^2, where $E_{i,j,k,l}$ are the energies of the individual jets and (i, j) and (k, l) denote the two jet pairs chosen.
- $|\cos\vartheta_{ij} - \cos\vartheta_{kl}| < 0.4$. The two opening angles $\vartheta_{i,j}$ and $\vartheta_{k,l}$ are defined as the angles between the jets in each jet-pair system in the Z rest frame.

The number of events passing those cuts is consistent with the QCD Monte Carlo predictions from JETSET [22] and HERWIG [23].

From the pair production searches we can exclude the presence of any excited quark up to a mass of 45.6 GeV independently of the coupling constant λ and for a branching ratio Br(q* → qg) larger than 17% for a down-type quark and larger than 25% for an up-type quark. Figure 13.8 shows the limit on λ/m_{q^*} as a function of the mass of the excited quarks obtained from the single production searches.

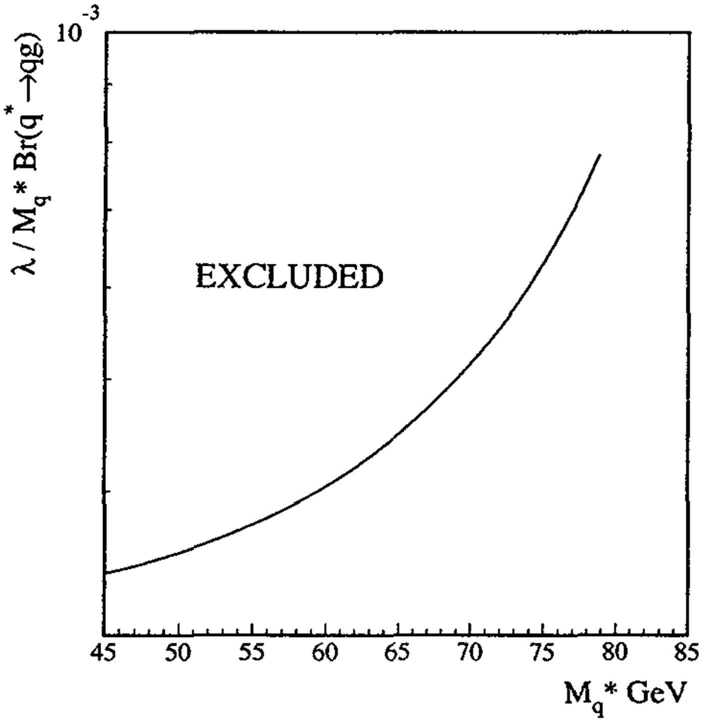

Figure 13.8: 95% confidence level limit on $\lambda/m_{q^*} \times \mathrm{Br}(q^* \to qg)$ as a function of the mass of the excited quarks obtained from the single production searches.

We have also searched for q* decaying into qγ using the $e^+e^- \to$ hadrons $+ \gamma$ data sample described in chapter 10.

To study the pair production process, we search this sample for events with two photons passing our cuts. We find 4 events. Our efficiency varies between 21% and 36% for $M_{q^*} > 15$ GeV depending on the q* mass. From this, we set a 95% confidence level upper limit on $\sigma(e^+e^- \to Z \to q^*q^*) \times \mathrm{Br}^2(q^* \to q\gamma) < 2$ pb. Assuming standard fermion couplings to the Z and using all 5 flavors, the production cross section can be calculated and we extract a limit on Br($q^* \rightarrow q\gamma$) $< 4\%$ for m_{q^*} up to 45 GeV.

To investigate single q^* production, we search for a peak in the γ-jet invariant mass spectrum, considering only those events which are made up of a photon and exactly two hadronic jets. After imposing the constraints of energy and momentum conservation, Monte-Carlo simulations [245] predict a γ-jet invariant mass resolution better than 2 GeV, independent of M_{q^*}. We use a bin size of 4 GeV to scan for a peak in the γ-jet invariant mass spectrum and the background is estimated by fitting a smooth curve to the data. The acceptance, calculated from the signal Monte-Carlo and including the 4 GeV binning efficiency, varies with q^* mass from 27% at 80 GeV to 41% at 50 GeV. This gives a 95% confidence level upper limit on $\sigma(e^+e^- \rightarrow Z \rightarrow q^*q) \times \mathrm{Br}(q^* \rightarrow q\gamma)$ shown as a function of m_{q^*} in Fig. 13.9.

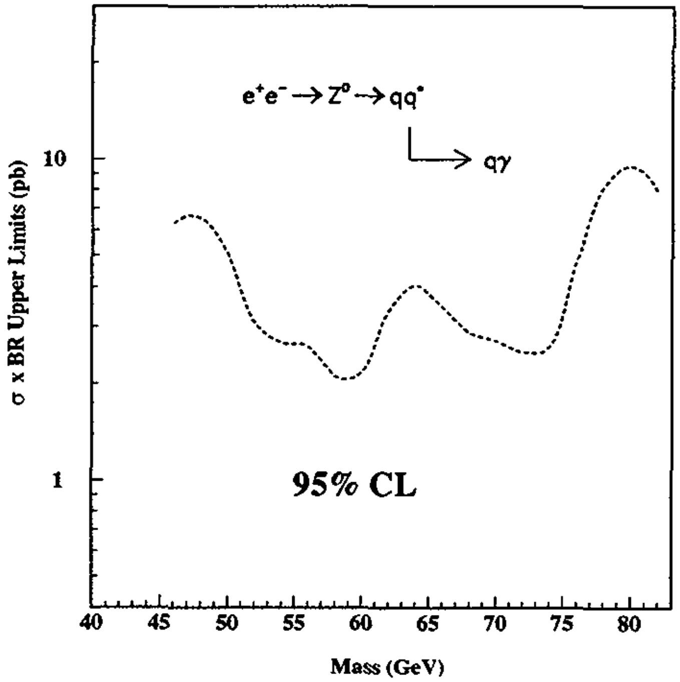

Figure 13.9: Upper limit at the 95 % confidence level for $\sigma(e^+e^- \rightarrow Z \rightarrow q^*q) \times \mathrm{Br}(q^* \rightarrow q\gamma)$.

13.6.4 Radiative decays of the Z

An excess of $e^+e^- \rightarrow \gamma\gamma\gamma$ events would be a clear signature of new physics [122]. In the Standard Model, the decay of the Z to three photons has an expected branching ratio of about 7×10^{-10} [246]. In composite models, the Z may couple to photons through its charged constituents [236]. The three photons in the final state may be separated from the QED process $e^+e^- \rightarrow \gamma\gamma(\gamma)$ by their distinct topology. For example, the energy of the less energetic photon for a QED event is preferentially low and it is emitted in the forward-backward direction. The selection of three photon final states has been described in the chapter 9. We found 10 events while from QED we expect 12 $e^+e^- \rightarrow \gamma\gamma(\gamma)$ events. We note here that the anomalous term which could couple Z to photons has a negligible effect away from the Z pole [236]. Therefore for our analysis we only consider events on the Z peak. We found 5 events on the Z peak where from QED we expect 8.6. Using Poisson statistics we set an upper limit on the branching ratio of the reaction $Z \rightarrow \gamma\gamma\gamma$ of $Br(Z \rightarrow \gamma\gamma\gamma) < 3.3 \times 10^{-5}$.

We have also searched for the radiative decay of the Z into a narrow, high mass resonance Y [35]. The signature expected for this channel is a monochromatic photon plus jets. We make use of the high precision photon energy measurement of the L3 detector to calculate the mass of the particles recoiling against the photon. The resolution of the recoil mass is determined from the photon energy resolution and is better then 2% for $M_Y > 50$ GeV. We scan the recoil mass spectrum of the data using a mass window given by $\Delta M_Y = 0.03(s - M_Y^2)/M_Y$ The bin size, ΔM_Y, has been chosen so that more than 80% of the signal from a narrow resonance would be confined to a single bin in the recoil mass spectrum. The background is estimated by fitting a smooth curve to the data, thus avoiding the uncertainties coming from Monte-Carlo background predictions. We find no statistically significant excess. The acceptance of our cuts, as determined from the signal Monte-Carlo, varies from 33% at M_Y=35 GeV to 24% at M_Y=85 GeV. The 95% confidence level upper limit on $\sigma(e^+e^- \rightarrow Z \rightarrow Y\gamma) \times Br(Y \rightarrow \text{hadrons})$ is shown in Fig. 13.10 as a function of m_Y.

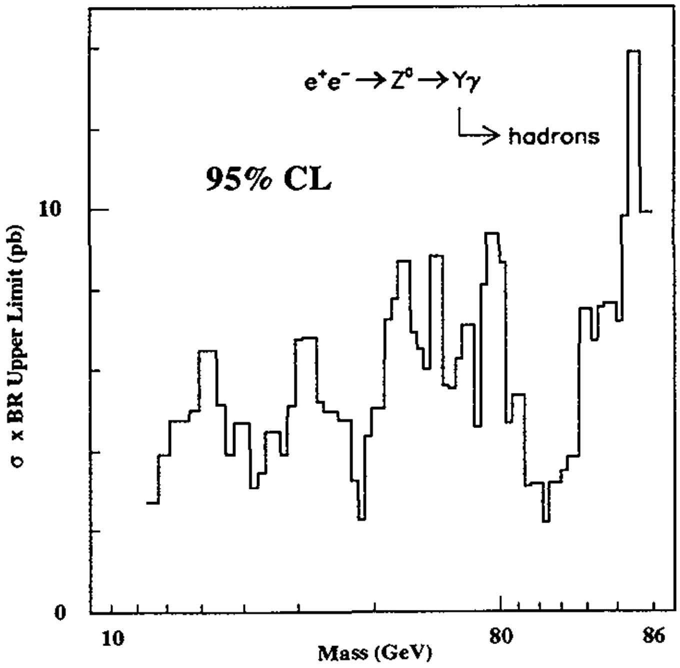

Figure 13.10: Upper limit at the 95% confidence level for $\sigma(e^+e^- \rightarrow Z \rightarrow Y\gamma) \times Br(Y \rightarrow \text{hadrons})$ as a function of m_Y.

13.7 Z decay into a photon and a scalar meson

We searched for rare or forbidden decays in the Standard Model: $Z \rightarrow \pi^0\gamma$, $Z \rightarrow \eta\gamma$ and $Z \rightarrow \gamma\gamma$ [122]. The Z, since it is a spin 1 boson, is not allowed to decay into two photons [247]. However some theories predict a large coupling of the Z to $\pi^0\gamma$ or $\eta\gamma$ [248]. The $\pi^0\gamma$ and $\gamma\gamma$ decay modes would leave the same signature in the detector and the total acceptance for either mode is 73%. This includes geometrical acceptance and selection efficiency. The case of $Z \rightarrow \eta\gamma$ is different because we only considered the decay of η into $3\pi^0$ and 2γ which accounts for 71% of its decay products. The total acceptance for $Z \rightarrow \eta\gamma$ is therefore 52%. A systematic error of 3% on the acceptance was taken into account. We obtained the following upper limits at 95% confidence level :

$$\begin{array}{lll}
\Gamma(Z \rightarrow \eta\gamma) < 0.44 \ \text{MeV} & \text{or} & \text{Br} < 1.8 \times 10^{-4} \\
\Gamma(Z \rightarrow \pi^0\gamma) < 0.31 \ \text{MeV} & \text{or} & \text{Br} < 1.2 \times 10^{-4} \\
\Gamma(Z \rightarrow \gamma\gamma) < 0.31 \ \text{MeV} & \text{or} & \text{Br} < 1.2 \times 10^{-4}.
\end{array}$$

13.8 Flavor changing neutral currents

In the Standard Model lepton flavor is conserved. However, there is no gauge principle requiring this conservation law. Different models [249–253], beyond the Standard Model, allow processes which violate lepton flavor conservation. In theories where such violation arises through mixing with new particles [249,251], the branching ratio for such processes, e.g. $Z \rightarrow \mu\tau$, can be as large as 10^{-4}. The observation of such decays would be a clear indication of physics beyond the Standard Model. We have searched for the three lepton flavor violating processes $Z \rightarrow \mu\tau$, $Z \rightarrow e\tau$ and $Z \rightarrow e\mu$ [254]. The major backgrounds for all these processes is $Z \rightarrow \tau^+\tau^-$, where either one or both of the taus decay leptonically. We reduce this background by requiring that at least one lepton momentum is very close to the beam energy. Leptons are identified in a manner similar to the one used for the lineshape measurements (see chapter 5), with additional criteria to reject electrons and muons which could mimic hadronic tau decays. We use the longitudinal shower profile in the calorimeters and reject all events with a shower consistent with a minimum ionizing particle opposite to a muon, or consistent with an electromagnetic energy deposit larger then 30 GeV opposite to an electron.

Figures 13.11 and 13.12 show the measured electron energy and muon momentum spectra compared with the Monte Carlo expectation for the background and a $Z \rightarrow e\tau$ and $Z \rightarrow \mu\tau$ signal. The candidates found, 1, 1 and 0 in the $Z \rightarrow \mu\tau$, $Z \rightarrow e\tau$, and $Z \rightarrow e\mu$ channels respectively, are consistent with the expected background. We set the following limits for these decays:

$$\text{Br}(Z \rightarrow \mu\tau) < 2.9 \times 10^{-5}, \tag{13.10}$$

$$\text{Br}(Z \rightarrow e\tau) < 3.0 \times 10^{-5}, \text{ and} \tag{13.11}$$

$$\text{Br}(Z \rightarrow e\mu) < 1.5 \times 10^{-5} \tag{13.12}$$

at the 95% confidence level.

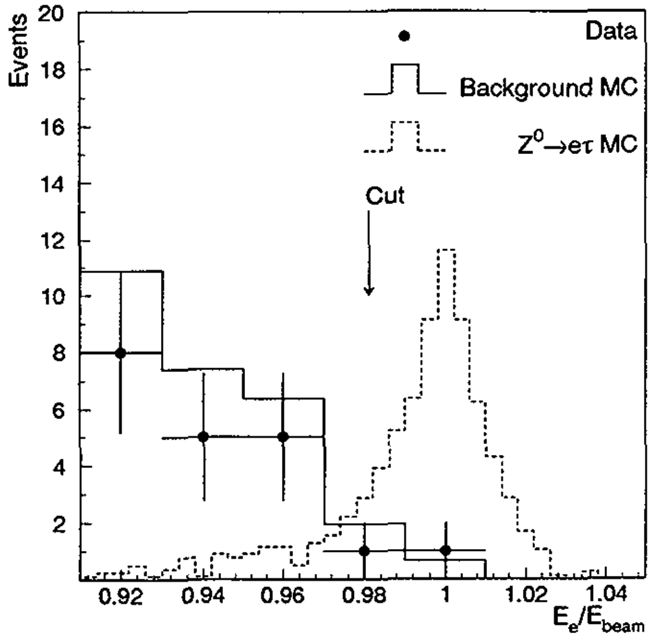

Figure 13.11: The distribution of the electron energy (E_e) for the data, Monte Carlo background, and signal Z $\rightarrow$ $e\tau$ Monte Carlo. The normalization for the signal Monte Carlo is arbitrary. The arrow represents the cut on electron energy used in this analysis.

13.9 Leptoquarks

Leptoquarks are bosons of special interest, since they are predicted by many theories [255] beyond the Standard Model, as in grand unification models (SU(5), SO(10)), superstring (E6), technicolor or composite models. The quantum numbers and couplings of the leptoquarks are specific to each theory and therefore their production and decay depend on the particular assumptions. All possible assignments of charge and weak isospin to leptoquarks with SU(3)×SU(2)×U(1) invariant couplings are given in reference 256. The coupling to leptons and quarks implies a fractional electrical charge (multiples of $1/3e$). The color triplet leptoquarks carry baryon and lepton numbers. Low leptoquark masses of order 100 GeV are expected in theories with conserved baryon and lepton numbers; especially in the case where one has three types of leptoquarks, one for each family [257].

In our search [258] we limit ourselves to pair-produced scalar leptoquarks, D. The cross-section is given in reference 259 :

$$\frac{d\sigma}{d\cos\theta} = \frac{3\pi\alpha^2}{8s}\beta^3(1-\cos^2\theta)\sum_{j=L,R}|C_j|^2, \qquad (13.13)$$

where $\beta = \sqrt{1-(4m_{\mathrm{D}}^2/s)}$ is the velocity of the leptoquark, m_{D} is the mass of the leptoquark, and C_j contains the propagators and the known couplings for a given leptoquark charge Q_{D}.

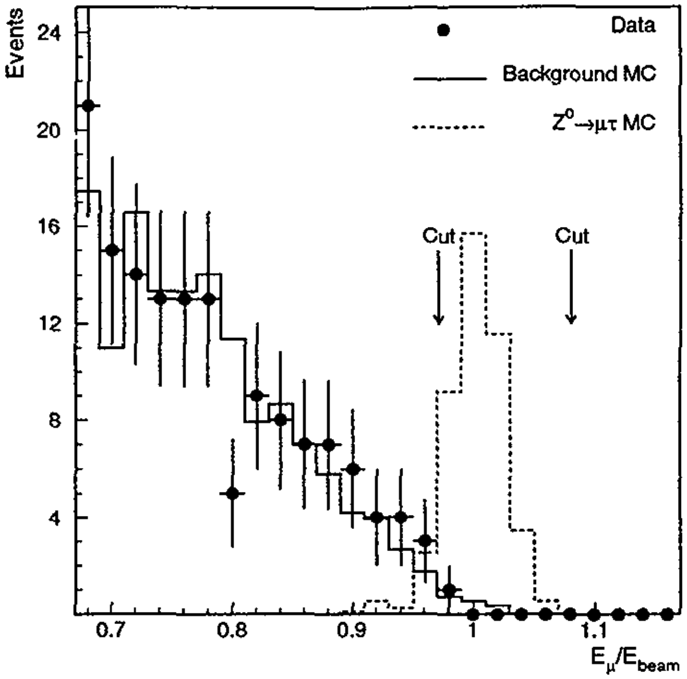

Figure 13.12: The distribution of the muon energy (E_μ) for the data, Monte Carlo background, and signal Z $\rightarrow$ $\mu\tau$ Monte Carlo. The normalization for the signal Monte Carlo is arbitrary. The arrows represent the cuts on muon energy used in this analysis.

Contributions to the cross section due to the photon exchange or the possible Z′ (for E(6) type leptoquarks, see section 13.2) in the s channel are neglected, since they are relatively small in the region of the Z resonance. The t channel contribution (with a coupling put equal to e) is also ignored [260, 259]. Initial state radiation, which has been taken into account in the event rate estimation, reduces the cross section by about 30%.

In this analysis we assume one leptoquark for each family with an electric charge of -1/3 or 2/3 which decays into a quark and a lepton belonging to the same family [261, 262]. The selected channels are listed in table 13.3. The event signature is two isolated leptons and two jets.

Here we update our previous results [258] with the data collected during the 1991 LEP running period. The total integrated luminosity of 17.5 pb^{-1} corresponds to 408,000 hadronic Z decays. Similar limits have been published by other LEP experiments [263]. UA2 [264] obtained a lower mass limit of 67 GeV (95% confidence level) for a scalar leptoquark decaying with a 50% branching ratio into a quark and an electron.

We search in the following channels:

$$e^+e^- \rightarrow e^+e^-X, \quad \mu^+\mu^-X, \quad \tau^+\tau^-X, \quad \nu\bar{\nu}X.$$

The signature of a leptoquark event would consist of two leptons and two jets. In order to determine the acceptance for leptoquark events, we generate events in the mass range 20 to

45 GeV. The fragmentation is performed according to the JETSET 7.3 [22] prescription. The resulting acceptances near the kinematical limit for the different reaction channels are listed in table 13.3. The most important contribution to the background is due to hadronic events. The criteria used to select the leptoquark candidate events are described in detail in reference 258.

We find that one data event survives in the $\nu\bar{\nu}q\bar{q}$ channel, where the expected background is 0.2 events from $Z \rightarrow \tau^+\tau^-$. The number of expected leptoquark pairs has been calculated according to eqn. 13.13. The rate of events has been determined assuming the same weak isospin ($I_3 = 0$) for the $Q_{\rm D} = +2/3$ as for the $Q_{\rm D} = -1/3$ leptoquarks. Expected production rates for $Q_{\rm D} = +2/3$ leptoquarks are higher than those for $Q_{\rm D} = -1/3$ leptoquarks.

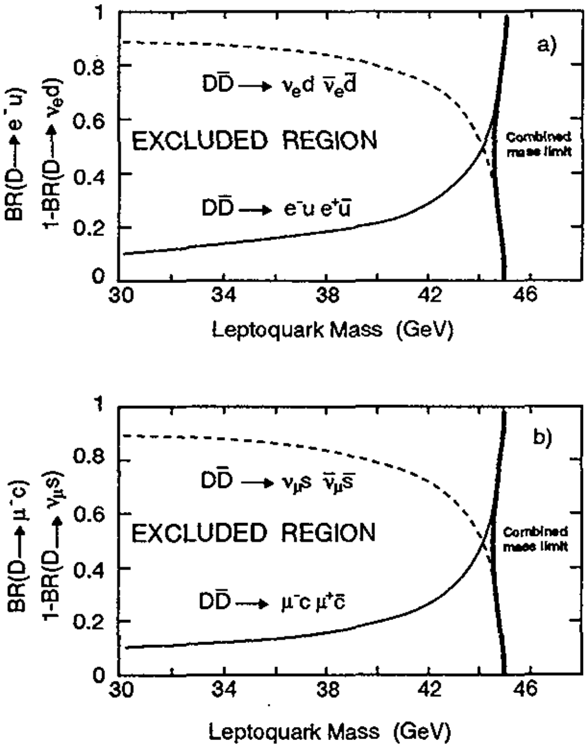

Figure 13.13: The excluded region at the 95% confidence level in terms of the mass and branching ratios, Br, for the decay modes of the leptoquarks belonging to the a) electron and b) muon family ($Q_{\rm D} = -\frac{1}{3}$). The mass limit found by combining the two decay modes is also shown.

In Figure 13.13 we show the excluded region as a function of the mass and the $D \rightarrow \ell q$ and $D \rightarrow \nu_\ell q$ branching ratios for $Q_{\rm D} = -1/3$. By combining results from the complementary decay modes, within the same family, we obtain the combined leptoquark mass limits at the 95% confidence level, also shown in Figure 13.13. The branching-ratio independent mass limit is then given by the minimum of the combined limits and is presented in Table 13.3. We obtain a conservative lower mass limit of 44.4 GeV for the first and second family leptoquarks. Because of the high mass of the top quark, decays of leptoquarks associated with the third family have only one allowed decay mode for the mass region under study, namely $D \rightarrow \tau^+ b$, if no mixing is allowed. In this particular case where the charge of the leptoquark equals 2/3 and the branching ratio is unity, the lower mass limit is 44.6 GeV at the 95% confidence level.

Single leptoquark production in Z decays [261] or via $e\gamma \rightarrow D\bar{u}$ predicts a small number of events assuming the Yukawa coupling is identical to the electromagnetic coupling. We determine our acceptances for single, isotropic production of leptoquarks with masses of 50 to 70 GeV. Acceptances between 30% and 50% are found for the e^+e^-X, $\mu^+\mu^-X$ and $\nu\bar{\nu}X$ channels. No candidates are found. Upper limits on the products of the branching ratio and the cross section, 0.71, 0.64 and 0.58 pb for the three channels respectively, at the 95% confidence level.

channel	Q_{D}	acceptance near the kinematic limit [%]	leptoquark mass limit [GeV]
$\mathrm{DD} \rightarrow \mathrm{e}^-\mathrm{u}\mathrm{e}^+\bar{\mathrm{u}}$	$-1/3$	39±2	44.4
$\mathrm{D}\bar{\mathrm{D}} \rightarrow \nu_{\mathrm{e}}\mathrm{d}\bar{\nu}_{\mathrm{e}}\bar{\mathrm{d}}$	$-1/3$	64±2	
$\mathrm{DD} \rightarrow \mu^-\mathrm{c}\mu^+\bar{\mathrm{c}}$	$-1/3$	46±2	44.5
$\mathrm{D}\bar{\mathrm{D}} \rightarrow \nu_\mu\mathrm{s}\bar{\nu}_\mu\bar{\mathrm{s}}$	$-1/3$	64±2	
$\mathrm{DD} \rightarrow \mathrm{e}^+\mathrm{d}\mathrm{e}^-\mathrm{d}$	$+2/3$	39±2	45.2
$\mathrm{D}\bar{\mathrm{D}} \rightarrow \bar{\nu}_{\mathrm{e}}\mathrm{u}\nu_{\mathrm{e}}\bar{\mathrm{u}}$	$+2/3$	64±2	
$\mathrm{DD} \rightarrow \mu^+\mathrm{s}\mu^-\bar{\mathrm{s}}$	$+2/3$	46±2	45.2
$\mathrm{D}\bar{\mathrm{D}} \rightarrow \bar{\nu}_\mu\mathrm{c}\nu_\mu\bar{\mathrm{c}}$	$+2/3$	64±2	
$\mathrm{DD} \rightarrow \tau^+\mathrm{b}\tau^-\mathrm{b}$	$+2/3$	7.0±1.	44.6

Table 13.3: Experimental acceptances near the kinematic limit and the 95% confidence level lower mass limits for pair-produced leptoquarks. The mass limits are independent of branching ratios.

Chapter 14

Summary and Conclusions

In this report we have presented results from the L3 experiment at LEP obtained during its first three years of operation. The accumulated statistics corresponds to about half a million observed decays of the Z boson. The major results are the following:

- *Measurements of the properties of the Z.* The mass, total and partial widths of the Z have been measured, for most decay channels to a precision better than 1%. These measurements allowed us to determine the number of light neutrino families from the width into unobserved final states, $N_\nu = 2.98 \pm 0.06$. This result is in agreement with a direct measurement from the reaction $e^+e^- \to \nu\bar{\nu}\gamma$, $N_\nu = 3.14 \pm 0.27$.

- *Measurements of the weak neutral current couplings.* The cross sections for lepton and hadron production at the Z resonance, the forward-backward asymmetries in leptonic decays and $Z \to b\bar{b}$, as well as the mean polarization of τ leptons have been measured. These measurements result in independent determinations of the Z coupling constants to fermions. No deviation from universality is observed, and all data are well described by the Standard Model relations among coupling constants, with a value of the effective weak mixing angle $\sin^2\overline{\theta}_W = 0.2328 \pm 0.0013$.

- *Measurements of the properties of b quarks and b hadrons.* Large, clean samples of Z decays into b quarks have been identified. Electroweak neutral current production and charged current decay of b quarks are found to be in agreement with Standard Model expectations. From a measurement of the forward-backward charge asymmetry we have determined $\sin^2\overline{\theta}_W = 0.2336 \pm 0.0029$. The average leptonic branching ratio and the lifetime of b hadrons produced in Z decays allow a determination of the Cabibbo-Kobayashi-Maskawa matrix element $|V_{cb}|$. Mixing between B^0 and $\bar{B}^0$ mesons, as observed through like-sign dileptons in hadronic events, is found with a value of the mixing parameter $\chi_B = 0.121 \pm 0.018$.

- *Measurements of the properties of τ leptons.* The average polarization of τ leptons has been measured using five different decay channels. The ratio of the effective vector and axial-vector coupling constants of the weak neutral current to τ leptons is determined to be $\bar{g}_{V\tau}/\bar{g}_{A\tau} = 0.068 \pm 0.017$. This is in agreement in sign and magnitude with the prediction of the Standard Model and determines $\sin^2\overline{\theta}_W = 0.2326 \pm 0.0043$. The lifetime and leptonic branching ratios of τ lepton decays agree with the expectation for a universal weak charged current interaction. The τ thus behaves as a standard sequential lepton.

- *Tests of QED.* Quantum electrodynamics has been tested at very short distances using the reaction $e^+e^- \rightarrow \gamma\gamma$. Good agreement of the rate and kinematics for this reaction with the QED predictions was observed. We have set limits on cut-off parameters at the electromagnetic vertex with values of order 120 GeV.

- *Measurements of the properties of hadron production.* A large number of hadronic final states produced in Z decays has been observed. Many precision tests of QCD have been performed using this sample. Most prominently, independent measurements of the strong coupling constant α_s based on event shapes, the hadronic Z width and hadronic τ decays are all consistent with a value of $\alpha_s(m_Z^2) = 0.124 \pm 0.005$, and support the running of the coupling constant over a large range of momentum transfer. The value of α_s is flavor-independent and experimental evidence for the gluon self-coupling was obtained. The shape of hadronic events and the rate of two-, three- and four-jet events are well described by calculations using second order QCD matrix elements or parton showers. In particular, different QCD models have been tested using hard isolated photon radiation in hadronic events. The momentum spectra of charged pions, π^0 and η and their evolution with center of mass energy are in agreement with QCD expectations.

- *Leptonic final states with hard photons.* Four events in the reaction $e^+e^- \rightarrow \ell^+\ell^-\gamma\gamma$ cluster at an invariant mass of the photon pair around 60 GeV. The probability for a statistical fluctuation to produce such a high mass cluster is estimated to be of order 10^{-2}. These photons could arise from the decay of a massive particle. More data are needed to ascertain the origin of these events.

- *Search for Higgs bosons.* We have searched for the Higgs boson of the minimal Standard Model by examining all the decay channels of the Z which would involve this particle, and the many different Higgs decay channels. The complete mass range from 0 to 52 GeV has been excluded. No signal has been observed for Higgs bosons belonging to a non-minimal Higgs multiplet. In the case of a two-doublet Higgs model, large fractions of the kinematically accessible region have been excluded. Pair produced charged Higgs bosons have not been observed; independently of the decay channel, a lower limit of 41 GeV has been placed on their mass.

- *Search for new particles and interactions.* No indications for the existence of new particles or new interactions have so far been observed by L3. Stringent limits for many such new phenomena have been obtained. Upper limits of the order of a few percent have been set on a possible admixture of an additional Z′ to the weak neutral current, together with lower limits on a possible Z′ mass of order 110 GeV. Decays of the Z by flavor changing neutral current interactions have been limited to branching ratios of a few times 10^{-5}. No new sequential heavy leptons or isosinglet neutral heavy leptons were found up to the kinematic limit. No sign of the rich spectrum of new particles as predicted by supersymmetry was observed. No indication of compositeness of the known charged leptons, neutrinos and quarks, for example by the production of excited states e^*, μ^*, τ^*, ν^* or q^*, was found. No leptoquarks decaying into a charged lepton or neutrino and a quark were observed.

With these results obtained by L3 in the first round of experimentation at LEP, thorough tests of the standard gauge theory of electroweak and strong interactions have been achieved. Through statistically and systematically accurate results, predicted relations among natural constants and their evolution with momentum transfer are verified. Gauge theories are thus probed at the one-loop level. The emphasis of the L3 detector on high accuracy measurements of leptons, photons and jets has proven to be a powerful design concept both in the measurement of standard physics reactions and in the search for new phenomena.

In the future, an increase in statistics at the Z resonance will allow more precise measurements on the above mentioned subjects and increase our sensitivity to new phenomena. While some of the results are still limited by statistics, larger samples will also allow more thorough investigations of the systematics involved.

At LEP 200, with an energy increase to reach of order 200 GeV in the center of mass system, experiments will be sensitive to higher mass scales. Another fundamental aspect of non-Abelian gauge theories, gauge boson self-coupling and gauge cancellation, will be put to experimental test. The LEP program will thus cover all basic experimental aspects of the electroweak neutral current interaction.

Acknowlegements

We wish to express our gratitude to the CERN accelerator division for the excellent performance of the LEP machine. We acknowledge the contributions of all the engineers and technicians who have participated in the construction and maintenance of this experiment. We also wish to thank all former collaborators who have left L3 for their valuable contributions. Those of us who are not from member states thank CERN for its hospitality and help. We acknowledge the support of all the funding agencies which contributed to this experiment.

The L3 Collaboration:

O.Adriani,[14] M.Aguilar-Benitez,[23] S.Ahlen,[9] J.Alcaraz,[15] A.Aloisio,[26] G.Alverson,[10] M.G.Alviggi,[26] G.Ambrosi,[31]
Q.An,[16] H.Anderhub,[45] A.L.Anderson,[13] V.P.Andreev,[35] L.Antonov,[39] D.Antreasyan,[7] P.Arce,[23] A.Arefiev,[25]
A.Atamanchuk,[35] T.Azemoon,[3] T.Aziz,[1,8] P.V.K.S.Baba,[16] P.Bagnaia,[34] J.A.Bakken,[33] L.Baksay,[41] R.C.Ball,[3]
S.Banerjee,[8] J.Bao,[5] R.Barillère,[15] L.Barone,[34] A.Baschirotto,[24] R.Battiston,[31] A.Bay,[17] F.Becattini,[14] U.Becker,[13,45]
F.Behner,[45] J.Behrens,[45] Gy.L.Bencze,[11] J.Berdugo,[23] P.Berges,[13] B.Bertucci,[31] B.L.Betev,[39,45] M.Biasini,[31]
A.Biland,[45] G.M.Bilei[31] R.Bizzarri,[34] J.J.Blaising,[4] G.J.Bobbink,[15,2] R.Bock,[1] A.Böhm,[1] B.Borgia,[34] M.Bosetti,[24]
D.Bourilkov,[28] M.Bourquin,[17] D.Boutigny,[4] B.Bouwens,[2] E.Brambilla,[26] J.G.Branson,[36] I.C.Brock,[32] M.Brooks,[21]
A.Bujak,[42] J.D.Burger,[13] W.J.Burger,[17] J.Busenitz,[41] A.Buytenhuijs,[28] X.D.Cai,[16] M.Capell,[20] M.Caria,[31]
G.Carlino,[26] A.M.Cartacci,[14] R.Castello,[24] M.Cerrada,[23] F.Cesaroni,[34] Y.H.Chang,[13] U.K.Chaturvedi,[16]
M.Chemarin,[22] A.Chen,[47] C.Chen,[6] G.M.Chen,[6] H.F.Chen,[18] H.S.Chen,[6] M.Chen,[13] W.Y.Chen,[47] G.Chiefari,[26]
C.Y.Chien,[5] M.T.Choi,[40] S.Chung,[13] C.Civinini,[14] I.Clare,[13] R.Clare,[13] T.E.Coan,[21] H.O.Cohn,[29] G.Coignet,[4]
N.Colino,[15] A.Contin,[7] X.T.Cui,[16] X.Y.Cui,[16] T.S.Dai,[13] R.D'Alessandro,[14] R.de Asmundis,[26] A.Degré,[4] K.Deiters,[43]
E.Dénes,[11] P.Denes,[33] F.DeNotaristefani,[34] M.Dhina,[45] D.DiBitonto,[41] M.Diemoz,[34] H.R.Dimitrov,[39] C.Dionisi,[34,15]
L.Djambazov,[45] M.T.Dova,[16] E.Drago,[26] D.Duchesneau,[17] P.Duinker,[2] I.Duran,[37] S.Easo,[31] H.El Mamouni,[22]
A.Engler,[32] F.J.Eppling,[13] F.C.Erné,[2] P.Extermann,[17] R.Fabbretti,[43] M.Fabre,[43] S.Falciano,[34] S.J.Fan,[38] O.Fackler,[20]
J.Fay,[22] M.Felcini,[15] T.Ferguson,[32] D.Fernandez,[23] G.Fernandez,[23] F.Ferroni,[34] H.Fesefeldt,[1] E.Fiandrini,[31] J.Field,[17]
F.Filthaut,[28] G.Finocchiaro,[34] P.H.Fisher,[5] G.Forconi,[17] T.Foreman,[2] K.Freudenreich,[45] W.Friebel,[44] M.Fukushima,[13]
M.Gailloud,[19] Yu.Galaktionov,[25,13] E.Gallo,[14] S.N.Ganguli,[15,8] P.Garcia-Abia,[23] D.Gele,[22] S.Gentile,[34,15]
S.Goldfarb,[10] Z.F.Gong,[18] E.Gonzalez,[23] A.Gougas,[5] D.Goujon,[17] G.Gratta,[30] M.Gruenewald,[30] C.Gu,[16]
M.Guanziroli,[16] J.K.Guo,[38] V.K.Gupta,[33] A.Gurtu,[8] H.R.Gustafson,[3] L.J.Gutay,[42] K.Hangarter,[1] B.Hartmann,[1]
A.Hasan,[16] D.Hauschildt,[2] C.F.He,[38] J.T.He,[6] T.Hebbeker,[1] M.Hebert,[36] G.Herten,[13] A.Hervé,[15] K.Hilgers,[1] H.Hofer,[45]
H.Hoorani,[17] G.Hu,[16] G.Q.Hu,[38] B.Ille,[22] M.M.Ilyas,[16] V.Innocente,[15] H.Janssen,[15] S. Jezequel,[4] B.N.Jin,[6] L.W.Jones,[3]
A.Kasser,[19] R.A.Khan,[16] Yu.Kamyshkov,[29] P.Kapinos,[35,44] J.S.Kapustinsky,[21] Y.Karyotakis,[15] M.Kaur,[16]
S.Khokhar,[16] M.N.Kienzle-Focacci,[17] J.K.Kim,[40] S.C.Kim,[40] Y.G.Kim,[40] W.W.Kinnison,[21] D.Kirkby,[30] S.Kirsch,[44]
W.Kittel,[28] A.Klimentov,[13,25] A.C.König,[28] E.Koffeman,[2] O.Kornadt,[1] V.Koutsenko,[13,25] A.Koulbardis,[35]
R.W.Kraemer,[32] T.Kramer,[13] V.R.Krastev,[39,31] W.Krenz,[1] A.Krivshich,[35] H.Kuijten,[28] K.S.Kumar,[12] A.Kunin,[12,25]
G.Landi,[14] D.Lanske,[1] S.Lanzano,[26] P.Lebrun,[22] P.Lecomte,[45] P.Lecoq,[15] P.Le Coultre,[45] D.M.Lee,[21] I.Leedom,[10]
C.Leggett,[3]J.M.Le Goff,[15] R.Leiste,[44] M.Lenti,[14] E.Leonardi,[34] X.Leytens,[2] C.Li,[18,16] H.T.Li,[6] P.J.Li,[38] J.Y.Liao,[38]
W.T.Lin,[47] Z.Y.Lin,[18] F.L.Linde,[15] B.Lindemann,[1] L.Lista,[26] Y.Liu,[16] W.Lohmann,[44,15] E.Longo,[34] Y.S.Lu,[6]
J.M.Lubbers,[15] K.Lübelsmeyer,[1] C.Luci,[34] D.Luckey,[7,13] L.Ludovici,[34] L.Luminari,[34] W.Lustermann,[44] J.M.Ma,[6]
W.G.Ma,[18] M.MacDermott,[45] P.K.Malhotra,[8†] R.Malik,[16] A.Malinin,[25] C.Maña,[23] M.Maolinbay,[45] P.Marchesini,[45]
F.Marion,[4] A.Marin,[9] J.P.Martin,[22] L.Martinez-Laso,[23] F.Marzano,[34] G.G.G.Massaro,[2] K.Mazumdar,[8] P.McBride,[12]
T.McMahon,[42] D.McNally,[45] M.Merk,[32] L.Merola,[26] M.Meschini,[14] W.J.Metzger,[28] Y.Mi,[19] G.B.Mills,[21] Y.Mir,[16]
G.Mirabelli,[34] J.Mnich,[1] M.Möller,[1] B.Monteleoni,[14] R.Morand,[4] S.Morganti,[34] N.E.Moulai,[16] R.Mount,[30] S.Müller,[1]
A.Nadtochy,[35] E.Nagy,[11] M.Napolitano,[26] F.Nessi-Tedaldi,[45] H.Newman,[30] C.Neyer,[45] M.A.Niaz,[16] A.Nippe,[1]
H.Nowak,[44] G.Organtini,[34] D.Pandoulas,[1] S.Paoletti,[14] P.Paolucci,[26] G Pascala,[34] G.Passaleva,[14,31] S.Patricelli,[26]
T.Paul,[5] M.Pauluzzi,[31] C.Paus,[1] F.Pauss,[45] Y.J.Pei,[1] S.Pensotti,[24] D.Perret-Gallix,[4] J.Perrier,[17] A.Pevsner,[5]
D.Piccolo,[26] M.Pieri,[15] P.A.Piroué,[33] F.Plasil,[29] V.Plyaskin,[25] M.Pohl,[45] V.Pojidaev,[25,14] H.Postema,[13] Z.D.Qi,[38]
J.M.Qian,[3] K.N.Qureshi,[16] R.Raghavan,[8] G.Rahal-Callot,[45] P.G.Rancoita,[24] M.Rattaggi,[24] G.Raven,[2]
P.Razis,[27]K.Read,[29] D.Ren,[45] Z.Ren,[16] M.Rescigno,[34] S.Reucroft,[10] A.Ricker,[1] S.Riemann,[44] B.C.Riemers,[42] K.Riles,[3]
O.Rind,[3] H.A.Rizvi,[16] F.J.Rodriguez,[23] B.P.Roe,[3] M.Röhner,[1] S.Röhner,[1] L.Romero,[23] J.Rose,[1] S.Rosier-Lees,[4]
R,Rosmalen,[28] Ph.Rosselet,[19] W.van Rossum,[2] S.Roth,[1] A.Rubbia,[13] J.A.Rubio,[15] H.Rykaczewski,[45] M.Sachwitz,[44]
J.Salicio,[15] J.M.Salicio,[23] G.S.Sanders,[21] A.Santocchia,[31] M.S.Sarakinos,[13] G.Sartorelli,[7,16] M.Sassowsky,[1]
G.Sauvage,[4] V.Schegelsky,[35] D.Schmitz,[1] P.Schmitz,[1] M.Schneegans,[4] H.Schopper,[46] D.J.Schotanus,[28] S.Shotkin,[13]
H.J.Schreiber,[44] J.Shukla,[32] R.Schulte,[1] S.Schulte,[1] K.Schultze,[1] J.Schwenke,[1] G.Schwering,[1] C.Sciacca,[26] I.Scott,[12]
R.Sehgal,[16] P.G.Seiler,[43] J.C.Sens,[15,2] L.Servoli,[31] I.Sheer,[36] D.Z.Shen,[38] S.Shevchenko,[30] X.R.Shi,[30] E.Shumilov,[25]
V.Shoutko,[25] D.Son,[40] A.Sopczak,[36] C.Spartiotis,[5] T.Spickermann,[1] P.Spillantini,[14] R.Starosta,[1] M.Steuer,[7,13]
D.P.Stickland,[33] F.Sticozzi,[13] H.Stone,[33] K.Strauch,[12] B.C.Stringfellow,[42] K.Sudhakar,[8] G.Sultanov,[16] L.Z.Sun,[18,16]
H.Suter,[45] J.D.Swain,[16] O.Syben,[1] A.A.Syed,[28] X.W.Tang,[6] L.Taylor,[10] G.Terzi,[24] Samuel C.C.Ting,[13] S.M.Ting,[13]
M.Tonutti,[1] S.C.Tonwar,[8] J.Tóth,[11] A.Tsaregorodtsev,[35] G.Tsipolitis,[32] C.Tully,[33] K.L.Tung,[6] J.Ulbricht,[45]
L.Urbán,[11] U.Uwer,[1] E.Valente,[34] R.T.Van de Walle,[28] I.Vetlitsky,[25] G.Viertel,[45] P.Vikas,[16] U.Vikas,[16] M.Vivargent,[4]
H.Vogel,[32] H.Vogt,[44] I.Vorobiev,[25] A.A.Vorobyov,[35] L.Vuilleumier,[19] M.Wadhwa,[4] W.Wallraff,[1] C.Wang,[13]
C.R.Wang,[18] G.H.Wang,[32] X.L.Wang,[18] Y.F.Wang,[13] Z.M.Wang,[16,18] A.Weber,[1] J.Weber,[45] R.Weill,[19] T.J.Wenaus,[20]
J.Wenninger,[17] M.White,[13] C.Willmott,[23] F.Wittgenstein,[15] D.Wright,[33] S.X.Wu,[16] B.Wysłouch,[13] Y.Y.Xie,[38]
J.G.Xu,[6] Z.Z.Xu,[18] Z.L.Xue,[38] D.S.Yan,[38] B.Z.Yang,[18] C.G.Yang,[6] G.Yang,[16] C.H.Ye,[16] J.B.Ye,[18] Q.Ye,[16] S.C.Yeh,[47]
Z.W.Yin,[38] J.M.You,[16] N.Yunus,[16] M.Yzerman,[2] C.Zaccardelli,[30] P.Zemp,[45] M.Zeng,[16] Y.Zeng,[1] D.H.Zhang,[2]
Z.P.Zhang,[18,16] B.Zhou,[9] G.J.Zhou,[6] J.F.Zhou,[1] R.Y.Zhu,[30] A.Zichichi,[7,15,16] B.C.C.van der Zwaan.[2]

---

1 I. Physikalisches Institut, RWTH, W-5100 Aachen, FRG[§]
III. Physikalisches Institut, RWTH, W-5100 Aachen, FRG[§]
2 *National Institute for High Energy Physics, NIKHEF, NL-1009 DB Amsterdam, The Netherlands*
3 University of Michigan, Ann Arbor, MI 48109, USA
4 Laboratoire d'Annecy-le-Vieux de Physique des Particules, LAPP,IN2P3-CNRS, BP 110, F-74941 Annecy-le-Vieux CEDEX, France
5 Johns Hopkins University, Baltimore, MD 21218, USA
6 Institute of High Energy Physics, IHEP, 100039 Beijing, China
7 INFN-Sezione di Bologna, I-40126 Bologna, Italy
8 Tata Institute of Fundamental Research, Bombay 400 005, India
9 Boston University, Boston, MA 02215, USA
10 Northeastern University, Boston, MA 02115, USA
11 Central Research Institute for Physics of the Hungarian Academy of Sciences, H-1525 Budapest 114, Hungary[‡]
12 Harvard University, Cambridge, MA 02139, USA
13 Massachusetts Institute of Technology, Cambridge, MA 02139, USA
14 *INFN* Sezione di Firenze and University of Florence, I-50125 Florence, Italy
15 European Laboratory for Particle Physics, CERN, CH-1211 Geneva 23, Switzerland
16 World Laboratory, FBLJA Project, CH-1211 Geneva 23, Switzerland
17 University of Geneva, CH-1211 Geneva 4, Switzerland
18 Chinese University of Science and Technology, USTC, Hefei, Anhui 230 029, China
19 University of Lausanne, CH-1015 Lausanne, Switzerland
20 Lawrence Livermore National Laboratory, Livermore, CA 94550, USA
21 Los Alamos National Laboratory, Los Alamos, NM 87544, USA
22 Institut de Physique Nucléaire de Lyon, IN2P3-CNRS,Université Claude Bernard, F-69622 Villeurbanne Cedex, France
23 Centro de Investigaciones Energeticas, Medioambientales y Tecnologicas, CIEMAT, E-28040 Madrid, Spain
24 INFN-Sezione di Milano, I-20133 Milan, Italy
25 Institute of Theoretical and Experimental Physics, ITEP, Moscow, Russia
26 INFN-Sezione di Napoli and University of Naples, I-80125 Naples, Italy
27 Department of Natural Sciences, University of Cyprus, Nicosia, Cyprus
28 University of Nymegen and NIKHEF, NL-6525 ED Nymegen, The Netherlands
29 Oak Ridge National Laboratory, Oak Ridge, TN 37831, USA
30 California Institute of Technology, Pasadena, CA 91125, USA
31 INFN-Sezione di Perugia and Universitá Degli Studi di Perugia, I-06100 Perugia, Italy
32 Carnegie Mellon University, Pittsburgh, PA 15213, USA
33 Princeton University, Princeton, NJ 08544, USA
34 INFN-Sezione di Roma and University of Rome, "La Sapienza", I-00185 Rome, Italy
35 Nuclear Physics Institute, St. Petersburg, Russia
36 University of California, San Diego, CA 92093, USA
37 Dept. de Fisica de Particulas Elementales, Univ. de Santiago, E-15706 Santiago de Compostela, Spain
38 Shanghai Institute of Ceramics, SIC, Shanghai, China
39 Bulgarian Academy of Sciences, Institute of Mechatronics, BU-1113 Sofia, Bulgaria
40 Center for High Energy Physics, Korea Advanced Inst. of Sciences and Technology, 305-701 Taejon, Republic of Korea
41 University of Alabama, Tuscaloosa, AL 35486, USA
42 *Purdue University, West Lafayette, IN 47907, USA*
43 Paul Scherrer Institut, PSI, CH-5232 Villigen, Switzerland
44 DESY-Institut für Hochenergiephysik, O-1615 Zeuthen, FRG
45 Eidgenössische Technische Hochschule, ETH Zürich, CH-8093 Zürich, Switzerland
46 University of Hamburg, W-2000 Hamburg, FRG
47 High Energy Physics Group, Taiwan, China

[§] Supported by the German Bundesministerium für Forschung und Technologie
[‡] Supported by the Hungarian OTKA fund under contract number 2970.
[†] Deceased.

Bibliography

[1] Gargamelle Collab., F.J. Hasert *et al.*, Phys. Lett. **46 B** (1973) 121.

[2] UA1 Collab., G. Arnison *et al.*, Phys. Lett. **122 B** (1983) 103.

[3] S.L. Glashow, Nucl. Phys. **22** (1961) 579;
S. Weinberg, Phys. Rev. Lett. **19** (1967) 1264;
A. Salam, "Elementary Particle Theory", Ed. N. Svartholm, Stockholm, "Almquist and Wiksell" (1968), 367.

[4] C. Camilleri *et al.*, Physics with Very High Energy e^+e^-Colliding Beams, Preprint CERN/76-18, CERN, 1976.

[5] SLAC Linear Collider Conceptual Design Report, Preprint SLAC-PUB-229, SLAC, 1980.

[6] M. Bourquin *et al.*, Preprint 86-02, ECFA, 1981.

[7] ALEPH Collab., D. Decamp *et al.*, Nucl. Inst. Meth. **A 294** (1990) 121.

[8] DELPHI Collab., P. Aarnio *et al.*, Nucl. Inst. Meth. **A 303?** (1991) 233.

[9] L3 Collab., B. Adeva *et al.*, Nucl. Inst. Meth. **A 289** (1990) 35.

[10] OPAL Collab, K. Ahmet *et al.*, Nucl. Inst. Meth. **A 305** (1991) 275.

[11] M. Gell-Mann, Acta Phys. Austriaca , Suppl. **IX** (1972) 733;
H. Fritzsch and M. Gell-Mann, 16th International Conference on High Energy Physics, Batavia, 1972; editors J.D. Jackson and A. Roberts, National Accelerator Laboratory (1972);
H. Fritzsch, M. Gell-Mann and H. Leytwyler, Phys. Lett. **B 47** (1973) 365;
D.J. Gross and F. Wilczek, Phys. Rev. Lett. **30** (1973) 1343;
D.J. Gross and F. Wilczek, Phys. Rev. **D 8** (1973) 3633;
H.D. Politzer, Phys. Rev. Lett. **30** (1973) 1346;
G. 't Hooft, Nucl. Phys. **B 33** (1971) 173.

[12] P. W. Higgs, Phys. Lett. **12** (1964) 132, Phys. Rev. Lett. **13** (1964) 508 and Phys. Rev. **145** (1966) 1156;
F. Englert and R. Brout, Phys. Rev. Lett. **13** (1964) 321.

[13] A.Bay *et al.*, The Xenon Monitor of the L3 Electromagnetic Calorimeter, Preprint UGVA-DPNC 1992/01-150, University of Geneva. 1992, submitted to NIM.

[14] The working group on LEP energy and the LEP collaborations ALEPH, DELPHI, L3 and OPAL, "Measurement of the mass of the Z-boson and the energy calibration of LEP", Preprint, CERN, 1993, to be published in Phys. Lett. **B**.

[15] The L3 detector simulation is based on GEANT Version 3.14.
See R. Brun *et al.*, "GEANT 3", CERN DD/EE/84-1 (Revised), September 1987.
The GHEISHA program (H. Fesefeldt, RWTH Aachen Report PITHA 85/02 (1985)) is used to simulate hadronic interactions.

[16] S. Jadach and B.F.L. Ward, Phys. Rev. **D 40** (1989) 3582.

[17] S. Jadach *et al.*, Phys. Lett. **B 268** (1991) 253;
S. Jadach *et al.*, Comp. Phys. Comm. **70** (1992) 305.

[18] M. Caffo *et al.*, in "Z Physics at LEP 1", CERN 89-08, eds G. Altarelli,R. Kleiss and C. Verzegnassi (CERN, Geneva, 1989) Vol. 1, p. 171;
M. Greco, Riv. Nuov. Cim. **11** (1988) 1.

[19] F.A. Berends and R. Kleiss, Nucl. Phys. **B 186** (1981) 22.

[20] L3 Collab., O. Adriani *et al.*, Phys. Lett. **B 292** (1992) 463.

[21] L3 Collab., B. Adeva *et al.*, Z. Phys. **C 51** (1991) 179.

[22] T. Sjöstrand, Comp. Phys. Comm. **39** (1986) 347;
T. Sjöstrand and M. Bengtsson, Comp. Phys. Comm. **43** (1987) 367.

[23] G. Marchesini and B. Webber, Nucl. Phys. **B 310** (1988) 461;
G. Marchesini *et al.*, Comp. Phys. Comm. **67** (1992) 465.

[24] The working group on LEP energy, L. Arnaudon *et al.*, "The Energy Calibration of LEP in 1991", Preprint CERN-PPE/92-125, CERN, 1992.

[25] S. Jadach, B.F.L. Ward and Z. Was, Comp. Phys. Comm. **66** (1991) 276.

[26] D. Bardin et al., FORTRAN package ZFITTER, and preprint CERN–TH. 6443/92;
D. Bardin et al., Z. Phys. **C 44** (1989) 493;
D. Bardin et al., Nucl. Phys. **B 351** (1991) 1;
D. Bardin et al., Phys. Lett. **B 255** (1991) 290.

[27] M. Böhm, A. Denner and W. Hollik, Nucl. Phys. **B 304** (1988) 687.

[28] F.A. Berends, R. Kleiss and W. Hollik, Nucl. Phys. **B 304** (1988) 712.

[29] J.H. Field and T. Riemann, private communication;
W. Beenakker in Proceedings of the Joint International Lepton-Photon Symposium & Europhysics Conference on High Energy Physics, Geneva, Switzerland 1991. Vol. 1, p. 28;
M. Cacciari *et al.*, Phys. Lett. **B 286** (1992) 387.

[30] M. Cacciari *et al.*, Phys. Lett. **B268** (1991) 441;
M. Cacciari *et al.*, Phys. Lett. **B279** (1992) 384;
M. Cacciari *et al.*, Phys. Lett. **B286** (1992) 387.

[31] W. Beenakker, F.B. Berends and S.C. van der Marck, Nucl. Phys. **B 349** (1991) 323.

[32] E. Laermann *et al.*, Nucl. Phys. **B 207** (1982) 205;
P. Mättig and W. Zeuner, Z. Phys. **C 52** (1991) 31.

[33] L3 Collab., O. Adriani *et al.*, Determination of Quark Electroweak Couplings from Direct Photon Production in Hadronic Z Decays, Preprint CERN-PPE/92-209, CERN, 1992, to be published in Physics Letters B.

[34] JADE Collab., W. Bartel *et al.*, Z. Phys. **C 33** (1986) 23;
JADE Collab., S. Bethke *et al.*, Phys. Lett. **B 213** (1988) 235.

[35] L3 Collab., O. Adriani *et al.*, Phys. Lett. **B 292** (1992) 472.

[36] ALEPH Collab., D. Decamp *et al.*, Phys. Lett. **B 264** (1991) 476;
ALEPH Collab., D. Buskulic *et al.*, "Measurement of Prompt Photon Production in Hadronic Z^0 Decays", CERN Preprint CERN-PPE/92-143;
DELPHI Collab., P. Abreu *et al.*, Z. Phys. **C 53** (1992) 555;
OPAL Collab., M.Z. Akrawy *et al.*, Phys. Lett. **B 246** (1990) 285;
OPAL Collab., G. Alexander *et al.*, Phys. Lett. **B 264** (1991) 219;
OPAL Collab., P.D. Acton *et al.*, Z. Phys. **C 54** (1992) 193.

[37] A.D. Dolgov, L.B. Okun and V.I. Zakharov, Nucl. Phys. **B 41** (1972) 197;
E. Ma and J. Okada, Phys. Rev. Lett. **41** (1978) 287 and erratum ibid. **41** (1978) 1759;
K.J. Gaemers, R. Gastmans and F.M. Renard, Phys. Rev. **D 19** (1979) 1605;
G. Barbiellini, B. Richter and J. Siegrist, Phys. Lett. **B 106** (1981) 414.

[38] M. Chen, C. Dionisi, M. Martinez and X. Tata, Phys. Rev. **159** (1988) 201.

[39] ALEPH Collab., D. Decamp *et al.*, Z. Phys. **C 53** (1991) 1;
DELPHI Collab., P. Abreu *et al.*, Nucl. Phys. **B 367** (1991) 511;
L3 Collab., B. Adeva *et al.*, Z. Phys. **C 51** (1991) 179;
OPAL Collab., G. Alexander *et al.*, Z. Phys. **C 52** (1991) 175.

[40] D. Karlen, Nucl. Phys. **B 289** (1987) 23.

[41] R.Miquel, C. Mana and M. Martinez, Z. Phys. **C 48** (1990) 309;
F.A. Berends *et al.*, Nucl. Phys. **B 301** (1988) 583.

[42] O. Nicrosini and L. Trentadue, Nucl. Phys. **B 318** (1989) 1.

[43] L3 Collab., B. Adeva *et al.*, Phys. Lett. **B 275** (1992) 209.

[44] OPAL Collab, M.Z. Akrawy *et al.*, Z. Phys. **C 50** (1991) 373.

[45] L3 Collab., B. Adeva *et al.*, Z. Phys. **C 55** (1992) 39.

[46] Particle Data Group, Phys. Lett. **B 239** (1990) VII.113, We have averaged the PETRA and PEP measurements according to the procedure used by the Particle Data Group.

[47] L3 Collab., B. Adeva *et al.*, Phys. Lett. **B 261** (1991) 177.

[48] C. Peterson *et al.*, Phys. Rev. **D 27** (1983) 105.

[49] L3 Collab., B. Adeva *et al.*, Phys. Lett. **B 270** (1991) 111.

[50] CLEO Collab., A. Bean *et al.*, Phys. Rev. Lett. **58** (1987) 183;
ARGUS Collab., H. Albrecht *et al.*, Phys. Lett. **B232** (1989) 554;
MARK II Collab., G. Abrams *et al.*, Phys. Rev. Lett. **64** (1990) 1095.

[51] J. Kühn and P. Zerwas, "Heavy Flavors at LEP I" Preprint MPI-PAE/PTh 49/89, Max Planck Institute, Munich. A shortened version is available as J. Kühn and P. Zerwas in "Z Physics at LEP 1", CERN 89-08, ed. G. Altarelli *et al.*, (CERN, Geneva, 1989), volume 1, p. 267.

[52] N. Cabibbo, Phys. Rev. Lett. **10** (1963) 531,
M.Kobayashi and K.Maskawa, Prog. Theo. Phys. **49** (1973) 652.

[53] C.S. Kim and A.D. Martin, Phys. Lett. **B 225** (1989) 186.

[54] G. Alterelli, N. Cabibbo, G. Carbó, L. Maiani and G. Martinelli, Nucl. Phys. **B 208** (1982) 365.

[55] ARGUS Collab., H. Albrecht *et al.*, Phys. Lett. **B 249** (1990) 359.

[56] CLEO Collab., R. Fulton *et al.*, Phys. Rev. Lett. **64** (1990) 16.

[57] ARGUS Collab., H. Albrecht *et al.*, Phys. Lett. **B 255** (1991) 297.

[58] UA1 Collab., C. Albajar *et al.*, Phys. Lett. **B 186** (1987) 247, erratum *ibid.* **B 197** (1987) 565.

[59] UA1 Collab., C. Albajar *et al.*, Phys. Lett. **B 262** (1991) 171.

[60] CDF Collab., F. Abe *et al.*, Phys. Rev. Lett. **67** (1991) 3351.

[61] ARGUS Collab., H. Albrecht *et al.*, Phys. Lett. **B 192** (1987) 245.

[62] CLEO Collab., M. Artuso *et al.*, Phys. Rev. Lett. **62** (1989) 2233.

[63] ARGUS Collab., H. Albrecht *et al.*, Z. Phys. **C 55** (1992) 357.

[64] L3 Collab., B. Adeva *et al.*, Phys. Lett. **B 252** (1990) 703.

[65] Mark II Collab., J.F. Kral *et al.*, Phys. Rev. Lett. **64** (1990) 1211.

[66] ALEPH Collab., D. Decamp *et al.*, Phys. Lett. **B 258** (1991) 236.

[67] OPAL Collab, P.D. Acton *et al.*, Phys. Lett. **B 276** (1992) 379.

[68] L3 Collab., B. Adeva *et al.*, Phys. Lett. **B 288** (1992) 395.

[69] OPAL Collab, G. Alexander *et al.*, Phys. Lett. **B 264** (1991) 467.

[70] JADE Collab., W. Bartel *et al.*, Z. Phys. **C 20** (1983) 187.

[71] TASSO Collab., M. Althoff *et al.*, Z. Phys. **C 27** (1985) 27.

[72] L3 Collab., B. Adeva *et al.*, Phys. Lett. **B 252** (1991) 713.

[73] L3 Collab., O. Adriani *et al.*, Phys. Lett. **B 292** (1992) 454.

[74] J.H. Kühn, S. Nussinov and R. Rückl, Z. Phys. **C 5** (1980) 117;
J.H. Kühn and R. Rückl, Phys. Lett. **B 135** (1984) 477;
M. B. Wise, Phys. Lett. **B 89** (1980) 229;
T. DeGrand and T. Toussaint, Phys. Lett. **B 89** (1980) 256;
P. H. Cox *et al.*, Phys. Rev. **D 32** (1985) 1157;
I. Bigi and A. Sanda, Nucl. Phys. **B 193** (1981) 98.

[75] G. C. Branco, H. P. Nilles and K. H. Streng, Phys. Lett. **B 85** (1979) 269.

[76] K. Hagiwara, A. D. Martin and W. J. Stirling, Phys. Lett. **B 51** (1991) 517.

[77] B. Guberina, J.H. Kühn, R.D. Peccei and R. Rückl, Nucl. Phys. **B 174** (1980) 317.

[78] ARGUS Collab., H. Albrecht *et al.*, Phys. Lett. **B 277** (1992) 209.

[79] MARK-III Collab., Phys. Rev. Lett. **68** (1992) 282.

[80] W. J. Stirling, CORFUJ Monte Carlo program, private communication.

[81] CLEO Collab., M.S. Alam *et al.*, Phys. Rev. **D 34** (1986) 3279;
ARGUS Collab., H. Albrecht *et al.*, Phys. Lett. **B 199** (1987) 451;
CRYSTAL BALL Collab., W. Maschmann *et al.*, Z. Phys. **C 46** (1990) 555.

[82] A. Ali and B. van Eijk, in "Z Physics at LEP 1", CERN Report CERN 89-08, eds G. Altarelli,R. Kleiss and C. Verzegnassi (CERN, Geneva, 1989) Vol. 3, p. 226.

[83] S. Jadach, Z. Was *et al.*, in "Z Physics at LEP 1", CERN Report CERN 89-08, eds G. Altarelli,R. Kleiss and C. Verzegnassi (CERN, Geneva, 1989) Vol. 1, p. 235 and references therein.

[84] ARGUS Collab., H. Albrecht *et al.*, Phys. Lett. **249 B** (1990) 278.

[85] K. Hagiwara, A. D. Martin, D. Zeppenfeld, Phys. Lett. **B235** (1990) 198;
A. Rougé, Z. Phys. **C48** (1990) 75.

[86] L3 Collab., O. Adriani *et al.*, Phys. Lett. **B 294** (1992) 466.

[87] A. Rougé, in Workshop on Tau Lepton Physics, Orsay 1990, ed. M. Davier and B. Jean-Marie, (Edition Frontieres, 1991), p. 213.

[88] M. G. Bowler, Phys. Lett. **B 182** (1986) 400;
M. Feindt, Z. Phys. **C 48** (1990) 681;
J. H. Kühn and A. Santamaria, Z. Phys. **C 48** (1990) 445;
L. M. Barkov, *et al.*, Nucl. Phys. **B 256** (1985) 365.

[89] V. Innocente, Y.F. Wang and Z.P. Zhang, Nucl. Inst. Meth. **A323** (1992) 647.

[90] C.Y. Prescott *et al.*, Phys. Lett. **77 B** (1978) 347.

[91] C.Y. Prescott *et al.*, Phys. Lett. **84 B** (1979) 524.

[92] JADE Collab., C. Kleinwort *et al.*, Z. Phys. **C 42** (1989) 7;
TASSO Collab., W. Braunschweig *et al.*, Z. Phys. **C 39** (1988) 331;
MARK II Collab., D. Amidei *et al.*, Phys. Rev. **D 37** (1988) 1750;
ARGUS Collab., H. Albrecht *et al.*, Phys. Lett. **B 199** (1987) 580;
CLEO Collab., C. Bebek *et al.*, Phys. Rev. **D 36** (1987) 690;
HRS Collab., S. Abachi *et al.*, Phys. Rev. Lett. **59** (1987) 2519;
MAC Collab., H. R. Band *et al.*, Phys. Rev. Lett. **59** (1987) 415;
MAC Collab., E. Fernandez *et al.*, Phys. Rev. Lett. **54** (1985) 1624.

[93] ALEPH Collab., D. Decamp *et al.*, Phys. Lett. **B 279** (1992) 411.

[94] DELPHI Collab., P. Abreu *et al.*, Phys. Lett. **B 267** (1991) 422.

[95] L3 Collab., B. Adeva *et al.*, Phys. Lett. **B 265** (1991) 451.

[96] OPAL Collab, P.D. Acton *et al.*, Phys. Lett. **B 273** (1991) 355.

[97] W.J. Marciano and A. Sirlin, Phys. Rev. Lett. **61** (1988) 1815.

[98] BES Collab., J.Z. Bai *et al.*, Phys. Rev. Lett. **69** (1992) 3021.

[99] "Z Physics at LEP", CERN 89-08, ed. G. Altarelli, R. Kleiss and C. Verzegnassi, (CERN, Geneva, 1989).

[100] L. Trentadue *et al.*, in "Z Physics at LEP 1", CERN Report CERN 89-08, eds G. Altarelli,R. Kleiss and C. Verzegnassi (CERN, Geneva, 1989) Vol. 1, p. 129.

[101] M. Consoli, W. Hollik and F. Jegerlehner, in "Z Physics at LEP 1", CERN Report CERN 89-08, eds G. Altarelli,R. Kleiss and C. Verzegnassi (CERN, Geneva, 1989) Vol. 1, p. 7.

[102] M. Böhm and W. Hollik, in "Z Physics at LEP 1", CERN 89-08, ed. R. Kleiss G. Altarelli and C. Verzegnassi, (CERN, Geneva, 1989), volume 1, p. 203.

[103] G. Burgers, in "Polarisation at LEP", CERN Report CERN 88-06, ed. G. Alexander *et al.*(CERN, Geneva, Switzerland) 1988, p.121.

[104] F.A. Berends *et al.*, in "Z Physics at LEP 1", CERN Report CERN 89-08, eds G. Altarelli,R. Kleiss and C. Verzegnassi (CERN, Geneva, 1989) Vol. 1, p. 89.

[105] D.C. Kennedy *et al.*, Nucl. Phys. **B 321** (1989) 83.

[106] H.J. Behrend *et al.*, Phys. Lett. **B183** (1987) 400.
W. de Boer, Nucl. Inst. Meth. **A278** (1989) 687.

[107] ALEPH Collab., D. Decamp et al., Z. Phys. **C53** (1992) 1;
DELPHI Collab., P. Abreu et al., Nucl. Phys. **B367** (1991) 511;
OPAL Collab., G. Alexander et al., Z. Phys. **C52** (1991) 175;
OPAL Collab., P.D. Acton et al., CERN/PPE/93-03, submitted to Z. Phys C.

[108] S. Banerjee and S.N. Ganguli, "Estimation of the QED coupling constant α,at $\sqrt{s} = m_Z$", CERN-PPE/92-165 (1992).

[109] S. Banerjee and S.N. Ganguli, "Determination of factors K_{eff}", L3 internal note 1246, September 1992.

[110] D. Kirkby, "QCD Corrections to Isolated Hard Photon Production in e^+e^- Annihilation", CALTECH Preprint CALT-68-1822 (1992).

[111] CDF Collab., F. Abe *et al.*, Phys. Rev. **D 43** (1991) 664.

[112] P. Langacker and M. Luo, *Phys. Rev.* **D44** (1991) 817.

[113] A. Borrelli *et al.*, Nucl. Phys. **B 333** (1990) 357.

[114] A. Leike, T. Riemann and J. Rose, Phys. Lett. **B 273** (1991) 513.

[115] S. Willenbrock and G. Valencia, Phys. Lett. **B 259** (1991) 373.

[116] T. Riemann, Phys. Lett. **B 293** (1992) 451.

[117] D. Bardin, A. Leike, T. Riemann and M. Sachwitz, Phys. Lett. **B 206** (1988) 539.

[118] F.M. Renard, Phys. Lett. **B 116** (1982) 264.

[119] A. Litke, Harvard Univ., Ph.D Thesis (1970) unpublished.

[120] R. P. Feynman, Phys. Rev. **74** (1948) 939.

[121] F.E. Low, Phys. Rev. Lett. **14** (1965) 238.

[122] L3 Collab., O. Adriani *et al.*, Phys. Lett. **B 288** (1992) 404.

[123] J.I. Friedman and H.W. Kendall, Ann. Rev. Nucl. Sci. **22** (1972) 203;
J.I. Friedman, Rev. Mod. Phys. **63** (1991) 615;
L. DiLella, Ann. Rev. Nucl. Sci. **35** (1985) 107;
R.K. Ellis and W.J. Stirling, "QCD and Collider Physics", Fermilab Report FERMILAB-Conf-90-164-T;
G. Altarelli, Ann. Rev. Nucl. Sci. **39** (1989) 357.

[124] MARK J Collab., B. Adeva *et al.*, Phys. Rep. **109** (1984) 131.

[125] A. Ali and F. Barreiro in "High Energy Electron Positron Physics", editors A. Ali and P. Söding, World Scientific (1988), p. 611;
P. Mättig, Phys. Rep. **177** (1989) 142.

[126] R.F. Schwitters *et al.*, Phys. Rev. Lett. **35** (1975) 1320;
G. Hanson *et al.*, Phys. Rev. Lett. **35** (1975) 1609.

[127] MARK J Collab., D.P. Barber *et al.*, Phys. Rev. Lett. **43** (1979) 830;
TASSO Collab., R. Brandelik *et al.*, Phys. Lett. **B 86** (1979) 243;
PLUTO Collab., C. Berger *et al.*, Phys. Lett. **B 86** (1979) 418;
JADE Collab., W. Bartel *et al.*, Phys. Lett. **B 91** (1980) 142.

[128] TASSO Collab., R. Brandelik *et al.*, Phys. Lett. **B 97** (1980) 453;
PLUTO Collab., C. Berger *et al.*, Phys. Lett. **B 97** (1980) 459;
CELLO Collab., H.-J. Behrend *et al.*, Phys. Lett. **B 110** (1982) 329;
R. Clare (MARK J Collab.), "QCD Properties of Jets", MIT Ph.D. Thesis (1982).

[129] G. d'Agostini, W. de Boer and G. Grindhammer, Phys. Lett. **B 229** (1989) 160;
R. Marshall, Z. Phys. **C 43** (1989) 595;
V. Branchina *et al.*, Phys. Rev. Lett. **65** (1990) 3237;
V. Branchina *et al.*, Phys. Rev. **D 46** (1992) 75.

[130] T. Sjöstrand, Int. J. Mod. Phys. **A 3** (1988) 751;
T. Sjöstrand *et al.*, in "Z Physics at LEP1", CERN Report CERN 89-08, eds G. Altarelli,R. Kleiss and C. Verzegnassi (CERN, Geneva, 1989) Vol. 3, p. 143.

[131] S. Brandt *et al.*, Phys. Lett. **12** (1964) 57;
E. Farhi, Phys. Rev. Lett. **39** (1977) 1587;
MARK J Collab., D.P. Barber *et al.*, Phys. Rev. Lett. **43** (1979) 830.

[132] L. Clavelli, Phys. Lett. **B 85** (1979) 111;
MARK II Collab., A. Peterson *et al.*, Phys. Rev. **D 37** (1988) 1;
TASSO Collab., W. Braunschweig *et al.*, Z. Phys. **C 45** (1989) 11.

[133] Z. Kunszt and P. Nason in "Z Physics at LEP1", CERN Report CERN 89-08, eds G. Altarelli,R. Kleiss and C. Verzegnassi (CERN, Geneva, 1989) Vol.1, p. 373.

[134] N. Brown and W.J. Stirling, Z. Phys. **C 53** (1992) 629;
S. Catani *et al.*, Phys. Lett. **B 269** (1991) 432;
S. Bethke *et al.*, Nucl. Phys. **B 370** (1992) 310.

[135] ALEPH Collab., D. Buskulic *et al.*, Z. Phys. **C 55** (1992) 209.

[136] DELPHI Collab., P. Abreu *et al.*, Z. Phys. **C 54** (1992) 45.

[137] OPAL Collab., M.Z. Akrawy *et al.*, Z. Phys. **C 47** (1990) 505.

[138] OPAL Collab., P.D. Acton *et al.*, Z. Phys. **C 55** (1992) 1.

[139] U. Pettersson, "ARIADNE: A Monte Carlo for QCD Cascades in the Color Dipole Formulation", Lund Preprint LU TP 88-5 (1988);
L. Lönnblad, "ARIADNE 3: A Monte Carlo for QCD Cascades in the Color Dipole Formulation", Lund Report LU TP 89-10 (1989).

[140] K. Kato and T. Munehisa, Phys. Rev. **D 36** (1987) 61;
K. Kato and T. Munehisa, Comp. Phys. Comm. **64** (1991) 67.

[141] R. Odorico, Nucl. Phys. **B 228** (1983) 381;
R. Odorico, Comp. Phys. Comm. **32** (1984) 139, and erratum ibid. **34** (1985) 43;
R. Odorico, "COJETS 6.23: a Monte Carlo Simulation Program for $\bar{p}-p$, $p-p$ and e^+e^- Annihilation", Bologna Preprint DFUB 92/6.

[142] R.K. Ellis, D.A. Ross and A.E. Terrano, Nucl. Phys. **B 178** (1981) 421.

[143] A. Białas and R. Peschanski, Nucl. Phys. **B 273** (1986) 703;
A. Białas and R. Peschanski, Nucl. Phys. **B 308** (1988) 857.

[144] L3 Collab., B. Adeva *et al.*, Phys. Lett. **B 248** (1990) 464.

[145] Particle Data Group, Phys. Rev. **D 45** (1992) III.54.

[146] Y.L. Dokshitser, D.I. Dyakonov and S.I. Troian, Phys. Lett. **78** (1978) 290;
C.L. Basham *et al.*, Phys. Rev. Lett. **41** (1978) 1585;
C.L. Basham *et al.*, Phys. Rev. **D 17** (1978) 2298;
C.L. Basham *et al.*, Phys. Rev. **D 19** (1979) 2018.

[147] L3 Collab., B. Adeva *et al.*, Phys. Lett. **B 257** (1991) 469.

[148] ALEPH Collab., D. Decamp *et al.*, Phys. Lett. **B 255** (1991) 623;
ALEPH Collab., D. Decamp *et al.*, Phys. Lett. **B 257** (1991) 479.

[149] S. Catani *et al.*, Phys. Lett. **B 263** (1991) 491.

[150] S. Catani, G. Turnock and B.R. Webber, Phys. Lett. **272** (1991) 368.

[151] J.C. Collins and D.E. Soper, Nucl. Phys. **B 193** (1981) 381;
J.C. Collins and D.E. Soper, Nucl. Phys. **B 197** (1982) 446 and erratum ibid. **B 213** (1983) 545;
J.C. Collins and D.E. Soper, Nucl. Phys. **B 284** (1987) 253;
J. Kodaira and L. Trentadue, Phys. Lett. **B 123** (1983) 335;
G. Turnock, "Energy-Energy Correlation Distribution in e^+e^- Annihilation", Cavendish Preprint Cavendish-HEP-92/3 (1992).

[152] S. Catani *et al.*, Nucl. Phys. **B 377** (1992) 445.

[153] S. Catani, G. Turnock and B.R. Webber, Phys. Lett. **B 295** (1991) 269.

[154] N. Brown and W.J. Stirling, Phys. Lett. **B 252** (1990) 657.

[155] L3 Collab., O. Adriani *et al.*, Phys. Lett. **B 284** (1992) 471.

[156] ALEPH Collab., D. Decamp *et al.*, Phys. Lett. **B 284** (1992) 163.

[157] S. Catani and B.R. Webber, private communication (1992).

[158] T. Hebbeker, "QCD correction to Γ_{had}", Aachen Report PITHA 91/08 (revised version).

[159] L.R. Surguladze and M.A. Samuel, Phys. Rev. Lett. **66** (1991) 560 and erratum ibid. **66** (1991) 2416;
S.G. Gorishny, A.L. Kataev and S.A. Larin, Phys. Lett. **B 259** (1991) 144.

[160] B.A. Kniehl and J.H. Kühn, Nucl. Phys. **B 329** (1990) 547;
A. Djouadi, J.H. Kühn and P.M. Zerwas, Z. Phys. **C 46** (1990) 411;
K.G. Chetyrkin and J.H. Kühn, Phys. Lett. **B 248** (1990) 359.

[161] T. Hebbeker, Phys. Rep. **217** (1992) 69.

[162] S. Narison and A. Pich, Phys. Lett. **B 211** (1988) 183;
E. Braaten, Phys. Rep. **D 39** (1989) 1458;
M.A. Samuel and L.R. Surguladze, Phys. Rev. **D 44** (1991) 1602.

[163] E. Braaten, S. Narison and A. Pich, Nucl. Phys. **B 373** (1992) 581.

[164] F. Le Diberder and A. Pich, Phys. Lett. **286** (1992) 147;
F. Le Diberder and A. Pich, Fortran program to calculate R_τ (1992), private communication.

[165] G. Altarelli, "QCD and Experiment: Status of α_s", CERN Preprint CERN-TH.6623/92.

[166] A. Petermann, "α_s Extrapolation with Analytic Thresholds", CERN Preprint CERN-TH.6487/92.

[167] TASSO Collab., W. Braunschweig *et al.*, Phys. Lett. **B 214** (1988) 286;
MARK II Collab., S. Bethke *et al.*, Z. Phys. **C 43** (1989) 325;
AMY Collab., I.H. Park *et al.*, Phys. Rev. Lett. **62** (1989) 1713;
VENUS Collab., K. Abe *et al.*, Phys. Lett. **B 240** (1990) 232.

[168] DELPHI Collab., P. Abreu *et al.*, Phys. Lett. **B 247** (1990) 167.

[169] L3 Collab., B. Adeva *et al.*, Phys. Lett. **B 271** (1991) 461.

[170] TASSO Collab., W. Braunschweig *et al.*, Z. Phys. **C 42** (1989) 17.

[171] L3 Collab., B. Adeva *et al.*, Phys. Lett. **B 263** (1991) 551.

[172] J.G. Körner and G.A. Schuler, Z. Phys. **C 26** (1985) 559;
J.G. Körner, G.A. Schuler and F. Barreiro, Phys. Lett. **B 188** (1987) 272;
G.A. Schuler and J.G. Körner, Nucl. Phys. **B 325** (1989) 557.

[173] E. Laermann, K.H. Streng and P.M. Zerwas, Z. Phys. **C 3** (1980) 289 and erratum ibid. **C 52** (1991) 352;
K. Koller *et al.*, Z. Phys. **C 6** (1980) 131.

[174] OPAL Collab., G. Alexander et al, Z. Phys. **C 52** (1991) 543;
DELPHI Collab., P. Abreu *et al.*, Phys. Lett. **B 274** (1992) 498.

[175] K. Koller and H. Krasemann, Phys. Lett. **B 88** (1979) 119;
UA1 Collab., G. Arnison *et al.*, Phys. Lett. **B 136** (1984) 294;
UA2 Collab., P. Bagnaia *et al.*, Phys. Lett. **B 144** (1984) 283;
N. Artega-Romero, A. Nicolaidis and J. Silva, Phys. Rev. Lett. **52** (1984) 172.

[176] L3 Collab., B. Adeva *et al.*, Phys. Lett. **B 248** (1990) 227.

[177] K.J.F. Gaemers and J.A.M. Vermaseren, Z. Phys. **C 7** (1980) 81.

[178] S. Bethke, A. Ricker and P.M. Zerwas, Z. Phys. **C 49** (1991) 59.

[179] M. Bengtsson and P.M. Zerwas, Phys. Lett. **B 208** (1988) 306.

[180] OPAL Collab., M.Z. Akrawy *et al.*, Z. Phys. **C 49** (1991) 49;
DELPHI Collab., P. Abreu *et al.*, Phys. Lett. **B 255** (1991) 466;
ALEPH Collab., D. Decamp *et al.*, Phys. Lett. **B 284** (1992) 151.

[181] AMY Collab., I.H. Park *et al.*, Phys. Rev. Lett. **62** (1989) 1713;
VENUS Collab., K. Abe *et al.*, Phys. Rev. Lett. **66** (1991) 280.

[182] G. Kramer and B. Lampe, Phys. Lett. **B 269** (1991) 179;
Z. Kunszt and Z. Trócsányi, "QCD Corrections to Photon Production in Association with Hadrons in e^+e^- Annihilation", ETH Zürich Preprint ETH-TH/92-26;
E.W.N. Glover and W.J. Stirling, Phys. Lett. **B 295** (1992) 128.

[183] L. Lönnblad, Comp. Phys. Comm. **71** (1992) 15.

[184] L3 Collab., B. Adeva *et al.*, Phys. Lett. **B 259** (1991) 199.

[185] L3 Collab., O. Adriani *et al.*, Phys. Lett. **B 286** (1992) 403.

[186] Y.L. Dokshitser and S.I. Troian, "Nonleading Perturbative Corrections to the Dynamics of Quark-Gluon Cascades and Soft Hadron Spectra in e^+e^- Annihilation", Leningrad Preprint LNPI-922 (1984);
Y.I. Azimov *et al.*, Z. Phys. **C 27** (1985) 65;
Y.I. Azimov *et al.*, Z. Phys. **C 31** (1986) 213;
V.A. Khoze, Y.L. Dokshitser and S.I. Troian, "Color Coherence in QCD Jets", Lund Preprint LU TP 90-12.

[187] D. Amati and G. Veneziano, Phys. Lett. **B 83** (1979) 87.

[188] A.H. Mueller, Phys. Lett. **B 104** (1981) 161;
A. Bassetto *et al.*, Nucl. Phys. **B 207** (1982) 189;
B.I. Ermolaev and V.S. Fadin, JETP Lett. **33** (1981) 285;
Y.L. Dokshitser, V.S. Fadin and V.A. Khoze, Phys. Lett. **B 115** (1982) 242.

[189] A.H. Mueller, Nucl. Phys. **B 213** (1983) 85;
A.H. Mueller, Nucl. Phys. **B 228** (1983) 351.

[190] C.P. Fong and B.R. Webber, Phys. Lett. **B 229** (1989) 289;
C.P. Fong and B.R. Webber, Nucl. Phys. **B 355** (1991) 54.

[191] DELPHI Collab., P. Abreu *et al.*, Z. Phys. **C 52** (1991) 271;
ALEPH Collab., D. Decamp *et al.*, Phys. Lett. **B 273** (1991) 181;
OPAL Collab., P.D. Acton et al, Z. Phys. **C 53** (1992) 535.

[192] ALEPH Collab., D. Buskulic *et al.*, Phys. Lett. **B 292** (1992) 210.

[193] JADE Collab., W. Bartel *et al.*, Phys. Lett. **B 130** (1983) 454;
JADE Collab., W. Bartel *et al.*, Z. Phys. **C 28** (1985) 343;
ARGUS Collab., H. Albrecht *et al.*, Z. Phys. **C 46** (1990) 15;
CELLO Collab., H.J. Behrend *et al.*, Z. Phys. **C 47** (1990) 1;
CRYSTAL BALL Collab., C. Bieler *et al.*, Z. Phys. **C 49** (1991) 225;
JADE Collab., W. Bartel *et al.*, Z. Phys. **C 46** (1990) 1 and erratum ibid, **C 47** (1990) 676.

[194] MARK II Collab., J.F. Patrick *et al.*, Phys. Rev. Lett. **49** (1982) 1232;
JADE Collab., W. Bartel *et al.*, Z. Phys. **C 20** (1983) 187;
HRS Collab., D. Bender *et al.*, Phys. Rev. **D 31** (1985) 1;
TASSO Collab., W. Braunschweig *et al.*, Z. Phys. **C 47** (1990) 187;
OPAL Collab., M.Z. Akrawy *et al.*, Phys. Lett. **B 247** (1990) 617;
DELPHI Collab., P. Abreu *et al.*, Phys. Lett. **B 275** (1992) 231.

[195] S. Catani *et al.*, Nucl. Phys. **B 383** (1992) 419.

[196] B.R. Webber, private communication (1992).

[197] JADE Collab., W. Bartel *et al.*, Phys. Lett. **B 101** (1981) 129.

[198] JADE Collab., W. Bartel *et al.*, Z. Phys. **C 21** (1983) 37;
JADE Collab., F. Ould-Saada *et al.*, Z. Phys. **C 39** (1988) 1;
TPC Collab., H. Aihara *et al.*, Z. Phys. **C 28** (1985) 31;
TPC/Two-Gamma Collab., H. Aihara *et al.*, Phys. Rev. Lett. **57** (1986) 945;
TASSO Collab., M. Althoff *et al.*, Z. Phys. **C 29** (1985) 29;
MARK II Collab., P.D. Sheldon *et al.*, Phys. Rev. Lett. **57** (1986) 1398.

[199] OPAL Collab., M.Z. Akrawy *et al.*, Phys. Lett. **B 261** (1991) 334.

[200] B. Andersson, G. Gustafson and T. Sjöstrand, Phys. Lett. **B 94** (1980) 211;
B. Andersson, G. Gustafson and T. Sjöstrand, Z. Phys. **C 6** (1980) 235.

[201] Y.I. Azimov *et al.*, Phys. Lett. **B 165** (1985) 147;
Y.I. Azimov *et al.*, Jad. Fiz. **43** (1986) 149.

[202] L3 Collab., O. Adriani *et al.*, Phys. Lett. **B 295** (1992) 337.

[203] S. Jadach and B.F.L. Ward, Phys. Lett **B 274** (1992) 470.

[204] D.R.Yennie, S.C. Frautschi and H. Suura, Annals of Physics **13** (1961) 379.

[205] W.J. Stirling, Phys. Lett. **B 271** (1991) 261;
S. Jadach *et al.*, Phys. Rev. **D 42** (1990) 2977;
S. Jadach, E. Richter-Wąs and B.F.L. Ward, private communication.

[206] B.L. Ioffe and V.A. Khoze, "What can be expected from experiments on colliding e^+e^- beams with ≈ 100 GeV ?", Sov. J. Part. Nucl. **9** (1978) 50;
J. D. Bjorken in "Proceedings of the 1976 SLAC Summer Institute on Particle Physics, Stanford", Ed. M. C. Zipf, (Stanford Linear Accel. Center, Stanford, 1976), SLAC-PUB-1866 (1977) 1;
J. Finjord, Phys.Scripta **21** (1980) 143.

[207] F.A. Berends and R. Kleiss, Nucl. Phys. **B 260** (1985) 32.

[208] B.A. Kniehl, Phys. Lett. **B 282** (1992) 249.

[209] F.A. Berends W.L. van Neerven and G.J.H. Burgers, Nucl. Phys. **B 297** (1988) 429.

[210] P. J. Franzini et al., in "Z Physics at LEP 1", CERN 89-08, eds G. Altarelli,R. Kleiss and C. Verzegnassi (CERN, Geneva, 1989) Vol. 2,p. 59 and references therein.

[211] I. Beltrami *et al.*, Nucl. Phys. **A 451** (1986) 679.

[212] N.C. Mukhopadhyay *et al.*, Phys. Rev. **D 29** (1984) 565.

[213] M. Davier and H. Nguyen Ngoc, Phys. Lett. **B 229** (1989) 150.

[214] G.D. Barr *et al.*, Phys. Lett. **B 235** (1990) 356.

[215] CLEO Collab., M.S. Alam *et al.*, Phys. Rev. **D 40** (1989) 712.

[216] P. Franzini *et al.*, Phys. Rev. **D 35** (1987) 2883.

[217] SINDRUM Collab., S. Egli *et al.*, Phys. Lett. **B 222** (1989) 533.

[218] P. Yepes, Phys. Lett. **B 227** (1989) 182.

[219] L3 Collab., B. Adeva *et al.*, Phys. Lett. **B 257** (1991) 450.

[220] H.U. Bengtsson, T. Sjöstrand, Comp. Phys. Comm. **46** (1987) 43.

[221] S. Dawson, J.F. Gunion, H.E. Haber and G.L. Kane, The Physics of the Higgs Bosons: Higgs Hunter's Guide, Addison Wesley, Menlo Park, 1989.

[222] L3 Collab., O. Adriani *et al.*, Phys. Lett. **B 294** (1992) 457.

[223] L3 Collab., O. Adriani *et al.*, Search for Non-Minimal Higgs Bosons in Z Decays, Preprint CERN-PPE/92-163, CERN, 1992, to be published in Zeitschrift für Physik C.

[224] R. Barbieri, M. Frigeni and F. Caravaglios, Phys. Lett. **B 279** (1992) 169.

[225] J. L. Hewett, T. G. Rizzo, *Phys. Reports* **C 183** (1989) 193; P. Langacker, M. Luo, A. K. Mann, *Rev. Mod. Phys.* **64** (1992) 87; and references therein.

[226] CDF Collab., F. Abe *et al.*, Phys. Rev. Lett. **68** (1992) 1463.

[227] A. Leike, S. Riemann, T. Riemann, Phys. Lett. **B 291** (1992) 187.

[228] R. W. Robinett, Phys. Rev. **D 26** (1982) 2388;
R. W. Robinett, J. L. Rosner, Phys. Rev. **D 26** (1982) 2396;
R. W. Robinett, J. L. Rosner, Phys. Rev. **D 25** (1982) 3036 and erratum ibid. **D 27** (1983) 679;
C. N. Leung, J. L. Rosner,Phys. Rev. **D 29** (1982) 2132.

[229] L3 Collab., B. Adeva *et al.*, Phys. Lett. **B 251** (1990) 321.

[230] L3 Collab., B. Adeva *et al.*, Phys. Lett. **B 250** (1990) 183.

[231] M. Gronau, C. Leung and J. Rosner, Phys. Rev. **D 29** (1984) 2539.

[232] M. Dittmar, M.C. Gonzalez-Garcia, A. Santamaria and J.W.F. Valle, Nucl. Phys. **B 332** (1990) 1.

[233] L3 Collab., O. Adriani *et al.*, Phys. Lett. **B 295** (1992) 371.

[234] Y.A. Golfand and E.P. Likhtman, Sov. Phys. JETP **13** (1971) 323;
D.V. Volkhov and V.P. Akulov, Phys. Lett. **B 46** (1973) 109;
J. Wess and B. Zumino, Nucl. Phys. **B 70** (1974) 39;
P. Fayet and S. Ferrara, Phys. Rep. **C 32** (1977) 249;
A. Salam and J. Strathdee, Fortschr. Phys. **26** (1978) 57.

[235] P. Fayet, Nucl. Phys. **B 90** (1975) 104;
A. Salam and J. Strathdee, Nucl. Phys. **B 87** (1975) 85.

[236] Boudjema *et al.*, in "Z Physics at LEP 1", CERN Report CERN 89-08, eds G. Altarelli,R. Kleiss and C. Verzegnassi (CERN, Geneva, 1989) Vol. 2, p. 188 and references therein.

[237] L3 Collab., B. Adeva *et al.*, Phys. Lett. **B 247** (1990) 177.

[238] L3 Collab., B. Adeva *et al.*, Phys. Lett. **B 250** (1990) 205.

[239] H. Baer *et al.*, in "Physics at LEP", CERN Report CERN 86-02, ed. J. Ellis and R. Peccei, (CERN, Geneva, 1986), Vol. 1, p. 297.

[240] K. Hagiwara *et al.*, Z. Phys. **C 29** (1985) 115.

[241] H. Terazawa *et al.*, Phys. Lett. **B 112** (1982) 387.

[242] L3 Collab., B. Adeva *et al.*, Phys. Lett. **B 252** (1990) 525.

[243] L.B. Okun, M.B. Voloshin and M.I. Vysotskii, Sov. Phys. JETP **64** (1986) 446 and erratum ibid. **65** (1987) 209;
M.B. Voloshin, Phys. Lett. **209 B** (1988) 360.

[244] F. Boudjema and A. Djouadi, Phys. Lett. **B 240** (1990) 485.

[245] Y.F. Wang, Ph.D. Thesis, Univ. of Florence, 1992 (unpublished);
F.A. Berends and P.H. Daverfeldt, Nucl. Phys. **B272** (1986) 131.

[246] I.J. van der Bij and E.W.N. Glover (Conveners), in "Z Physics at LEP 1", CERN Report CERN 89-08, eds G. Altarelli,R. Kleiss and C. Verzegnassi, Vol. 2, p. 1.

[247] C.N. Yang, Phys. Rev. **77** (1950) 242.

[248] M. Jacob, T. T. Wu, Phys. Lett. **232B** (1989) 529 ;
G. B. West, Mod. Phys. Lett. **5 A** (1990) 2281 ;
S. Ghosh, D. Chatterjee, Mod. Phys. Lett. **5 A** (1990) 1493.

[249] T.K. Kuo and N. Nakagawa, Phys. Rev. **D 32** (1985) 306.

[250] J. Bernabeu *et al.*, Phys. Lett. **B 187** (1987) 303.

[251] G. Eilam and T.G. Rizzo, Phys. Lett. **B 188** (1987) 91.

[252] M.J.S. Levine, Phys. Rev. **D 36** (1987) 1329.

[253] J. Bernabeu and A. Santamaria, Phys. Lett. **B 197** (1987) 418.

[254] L3 Collab., B. Adeva *et al.*, Phys. Lett. **B 271** (1991) 453.

[255] J. Pati and A. Salam, Phys. Rev. **D 10** (1974) 275;
S. Dimopoulos, Nucl. Phys. **B 168** (1980) 69;
C.H. Albright, Phys. Rev. **D 29** (1984) 2595;
B. Schrempp and F. Schrempp, Nucl. Phys. **B 242** (1984) 203;
V.D. Angelopoulos *et al.*, Nucl. Phys. **B 292** (1987) 59.

[256] W. Buchmüller, R. Rückl and D. Wyler, Phys. Lett. **B 191** (1990) 442.

[257] W. Buchmüller and D.Wyler, Phys. Lett. **B 177** (1987) 377;
J.L. Hewett and S. Pakvasa, Phys. Lett. **B 227** (1989) 178.

[258] L3 Collab., B. Adeva *et al.*, Phys. Lett. **B 261** (1991) 169.

[259] D. Schaile and P.M. Zerwas, Proceedings of the Workshop on Physics at Future Accelerators, CERN Report CERN 87-07, (CERN, Geneva, 1987), Vol. II, p. 251.

[260] F.M. Renard, "Basics of electron positron collisions", ed. Frontieres, 1981, p.64.
J.L. Hewett and T.G. Rizzo, Phys. Rev. **D36** (1987) 3367 and references therein.

[261] N.D. Tracas and S.D.P. Vlassopulos, Phys. Lett. **B 220** (1989) 285.

[262] B. Schrempp and F. Schrempp, Phys. Lett. **B 153** (1985) 101.

[263] OPAL Collab., G. Alexander et al., Phys. Lett. **B 263** (1991) 123;
ALEPH Collab., D. Decamp et al., Phys. Rep. **216** (1992) 253;
DELPHI Collab., P. Abreu et al., Phys. Lett. **B 275** (1992) 222;.

[264] UA2 Collab., J. Alitti *et al.*, Phys. Lett. **B 274** (1991) 507.